

FILE COPY

DO NOT REMOVE

NBSIR 76-848

# SEMI-ANNUAL REPORT ON MATERIALS RESEARCH IN SUPPORT OF SUPERCONDUCTING MACHINERY

---

RECEIVED

DATE 11/10/77  
OTP

R. P. Reed, J. G. Hust, M. B. Kasen, H. M. Ledbetter, H. I. McHenry,  
D. T. Read, R. E. Schramm, L. L. Sparks, and R. L. Tobler

Cryogenics Division  
Institute for Basic Standards  
National Bureau of Standards  
Boulder, Colorado 80302

October 1976

Prepared for :  
Advanced Research Projects Agency  
1400 Wilson Boulevard  
Arlington, Virginia 22209



NBSIR 76-848

## **SEMI-ANNUAL REPORT ON MATERIALS RESEARCH IN SUPPORT OF SUPERCONDUCTING MACHINERY**

---

R. P. Reed, J. G. Hust, M. B. Kasen, H. M. Ledbetter, H. I. McHenry,  
D. T. Read, R. E. Schramm, L. L. Sparks, and R. L. Tobler

Cryogenics Division  
Institute for Basic Standards  
National Bureau of Standards  
Boulder, Colorado 80302

October 1976

Prepared for :  
Advanced Research Projects Agency  
1400 Wilson Boulevard  
Arlington, Virginia 22209



---

U.S. DEPARTMENT OF COMMERCE, Elliot L. Richardson, Secretary  
James A. Baker, III, Under Secretary  
Dr. Betsy Ancker-Johnson, Assistant Secretary for Science and Technology  
NATIONAL BUREAU OF STANDARDS, Ernest Ambler, Acting Director





SEMI-ANNUAL REPORT ON MATERIALS RESEARCH

IN SUPPORT OF SUPERCONDUCTING MACHINERY

Sponsored by  
Advanced Research Projects Agency  
ARPA Order No. 2569  
Program Code 4D10  
August 10, 1975 - October 1, 1976

Program Director  
Dr. E. C. van Reuth  
Materials Sciences  
Advanced Research Projects Agency  
1400 Wilson Boulevard  
Arlington, Virginia 22209

Program Manager  
Dr. R. P. Reed  
Cryogenics Division  
Institute for Basic Standards  
National Bureau of Standards  
Boulder, Colorado 80302

The views and conclusions contained in this document are those of the authors and should not be interpreted as necessarily representing the official policies, either expressed or implied, of the Advanced Research Projects Agency or of the U.S. Government.

### Abstract

Results are reported of a six-month study, ending September 1976, on candidate materials for superconducting-machinery components. The results cover five areas--advanced composites, elastic properties, fatigue resistance and fracture toughness, magnetothermal conductivity, and thermal conductivity. Material properties were studied over the temperature range 4 to 300 K. Materials studied include: aluminum alloy 5083, copper-0.3 cadmium-0.3 tin, copper-28 nickel, iron-48 nickel, 3.5 Ni and 9 Ni steels, titanium-4 aluminum-6 vanadium, titanium-5 aluminum-2.5 tin, stainless steel 21-6-9, several austenitic stainless steels of the 300 series, 300-grade maraging steel, phenolformaldehyde, and the composites boron/aluminum, boron/epoxy, graphite/epoxy, and niobium-titanium/copper. Some notable results of the study are: anomalous elastic properties of stainless steel 21-6-9 due to a Néel transition; complete sets of elastic constants for two composites, B/Al and NbTi/Cu; thermal conductivities of Ti-6Al-4V and Fe-48Ni are reduced by a magnetic field while those of Cu-0.5 Sn and Cu-28Ni are unaffected; a screening method for composites of possible cryogenic use; general trends regarding temperature effects on the fracture toughness and fatigue-crack-growth resistances of structural alloys are correlated with crystal structure class; and the tensile-yield-strength and fracture-toughness data for fourteen commercial structural alloys at 4 K and 295 K are compared demonstrating an inverse relationship between these properties and indicating the optimum combination of properties that are technologically possible. Also, the materials and properties studied experimentally during the three-year program are summarized.

This work was supported by the Advanced Research Projects Agency of the U.S. Department of Defense.

Key words: Aluminum alloys; composites; elastic properties; engineering materials; fatigue; fracture; iron alloys; cryogenic temperatures; maraging steels; mechanical properties; nickel alloys; phenolformaldehyde; stainless steels; superconducting machinery; thermal conductivity; titanium alloys.

	Page
ADVANCED COMPOSITES	
M. B. Kasen, R. E. Schramm, and D. T. Read . . . . .	1
ELASTIC PROPERTIES	
H. M. Ledbetter and D. T. Read . . . . .	19
Orthorhombic elastic constants of an NbTi/Cu composite superconductor	
H. M. Ledbetter and D. T. Read . . . . .	23
Temperature dependence of the elastic constants of an NbTi/Cu superconducting composite	
D. T. Read and H. M. Ledbetter . . . . .	48
Low-temperature elastic properties of a 300-grade maraging steel	
H. M. Ledbetter . . . . .	66
Low-temperature elastic properties of a precipitation- hardened copper alloy	
H. M. Ledbetter . . . . .	84
Elastic properties of a boron-aluminum composite at low temperatures	
D. T. Read and H. M. Ledbetter . . . . .	100
Anomalous low-temperature elastic behavior of a nitrogen- strengthened chromium-manganese stainless steel	
H. M. Ledbetter . . . . .	117
FRACTURE MECHANICS PARAMETERS	
R. L. Tobler, H. I. McHenry, R. P. Reed, and R. E. Schramm . .	133
Fracture mechanics parameters for a 5083-0 aluminum alloy at low temperatures	
R. L. Tobler and R. P. Reed . . . . .	135
Tensile and fracture behavior of a nitrogen-strengthened, chromium-nickel-manganese stainless steel at cryogenic temperatures	
R. L. Tobler and R. P. Reed . . . . .	162
Cryogenic tensile, fatigue, and fracture parameters for a solution-annealed maraging steel	
R. L. Tobler, R. P. Reed, and R. E. Schramm . . . . .	188
Cryogenic effects on the fracture mechanics para- meters of ferritic nickel-alloy steels	
R. L. Tobler . . . . .	214
Note on the fracture properties of Fe-49Ni at cryogenic temperatures	
H. I. McHenry and R. E. Schramm . . . . .	244
Fatigue crack growth resistance of structural alloys at cryogenic temperatures	
R. L. Tobler and R. P. Reed . . . . .	256
Fracture of structural alloys at temperatures approaching absolute zero	
R. L. Tobler . . . . .	279
MAGNETOTHERMAL CONDUCTIVITY	
L. L. Sparks . . . . .	287
THERMAL CONDUCTIVITY	
J. G. Hust . . . . .	305

### Disclaimer

Tradenames of equipment and materials are used in this report for clarity and to conform with standard usage in the scientific and engineering literature. Selection of materials for discussion and examination with regard to application in superconducting machinery is based on properties reported in the literature, and must be regarded as preliminary and tentative. In no case does such selection imply recommendation or endorsement by the National Bureau of Standards, nor does it imply that the material or equipment is necessarily the best available for the purpose.

SEMI-ANNUAL REPORT ON MATERIALS RESEARCH  
IN SUPPORT OF SUPERCONDUCTING MACHINERY

ADVANCED COMPOSITES

M. B. Kasen, R. E. Schramm, and D. T. Read

Cryogenics Division  
Institute for Basic Standards  
National Bureau of Standards  
Boulder, Colorado 80302

October 1976

NBS COMPOSITE-MATERIALS STUDIES DURING ARPA-SPONSORED  
PROGRAM, SEPTEMBER 1973 TO SEPTEMBER 1976

Subject	ARPA Report No.
Literature Review	1, 2, (4), (5)*
Cryostat Construction	1
Tensile Test Procedures	2, 3, 4
Shear Test Procedures	3, 4
Compression Test Procedures	5
Fatigue Test Procedures	6
Tensile Data, Boron-Epoxy	2, 3, 4
Tensile Data, Boron-Aluminum	3, 4
Tensile Data, Graphite-Epoxy	3, 4
Tensile Data, Glass-Epoxy	4
Tensile Data, Kevlar-Epoxy	4
Shear Data, Boron-Epoxy	4
Shear Data, Boron-Aluminum	3, 4
Shear Data, Graphite-Epoxy	4
Shear Data, Glass-Epoxy	4
Compression Data, Boron-Epoxy	5
Compression Data, Boron-Aluminum	5
Compression Data, Graphite-Epoxy	5
Compression Data, Glass-Epoxy	5
Tensile Fatigue Data, Boron-Epoxy	6
Tensile Fatigue Data, Boron-Aluminum	6
Compression Fatigue Data, Boron-Epoxy	6

\*Numbers in parentheses refer to report numbers in which reprint versions of the manuscripts occur. Other numbers refer to pre-print versions.



## Summary: Advanced Composites

A comparison has been made between the wearout rates of  $[0/\pm 45/0]_S$  boron-epoxy and boron-aluminum composites in low-cycle fatigue at 295 K and 76 K. Using degradation of modulus as the wearout criterion, these preliminary data indicate that cryogenic temperatures have a negligible effect on either tensile or compressive fatigue performance of boron-epoxy. A similar indication was obtained for boron-aluminum in tensile fatigue.

## Contents: Advanced Composites

	Page
1.0 Review . . . . .	3
2.0 Phase III: Fatigue of Composites at Cryogenic Temperatures . .	3
2.1 Introduction . . . . .	3
2.2 Experimental Procedures . . . . .	4
2.3 Results and Discussion . . . . .	5
2.4 Conclusions . . . . .	6
3.0 References . . . . .	7
Appendix 1: List of Symbols . . . . .	8

### 1.0 Review

Work on this project was initiated by preparing state-of-the-art reviews on the mechanical and thermal properties of structural composites at cryogenic temperatures (1-3). These reviews suggested that boron-aluminum, boron-epoxy, graphite-epoxy, glass-epoxy and Kevlar 49-epoxy composites warranted further study to characterize key static mechanical properties at cryogenic temperatures. This work was undertaken in a previous experimental portion of the ongoing study (9).

Phase I of the experimental work involved development of apparatus and procedures for obtaining the required data. Phase II encompassed the static characterization work. All of the above work has been completed and has been reported in prior Semi-Annual Reports (see summary table at beginning of this section). Phase III addresses the question of the effect that cryogenic temperatures have on the performance of composite materials under fatigue loading and is the subject of this report.

## 2.0 Phase III: Fatigue of Composites at Cryogenic Temperatures

### 2.1 Introduction

The ability of composite structures to withstand cyclic stresses at cryogenic temperatures is crucial to their suitability for use in rotating cryogenic machinery. Very little is presently known on this subject. The few studies that have been undertaken indicate that the fatigue life of glass-cloth-epoxy composites is improved by cooling to cryogenic temperatures, although the overall performance remains unimpressive (4). NBS tests of uniaxial glass-epoxy straps indicate that they are fit for service as thermal stand-offs transitioning from 4 K to 295 K in a superconducting generator (5). The only data known to the authors on the fatigue performance of advanced composites at cryogenic temperatures is restricted to low-cycle hydrostatic testing of filament-wound pressure vessels (6-7).

It is unfortunate that there exists no body of theory permitting prediction of crossply composite fatigue performance from systematically determined uniaxial properties, as is the case for the static mechanical properties. Each layup of a particular type composite must therefore be looked upon as a distinct material having a unique S-N curve. To a large extent, this

problem arises due to the differing strain to failure of the fiber and the matrix. Where the strain capability of the fiber exceeds that of the matrix and where the fiber is of low modulus as is the case for glass-epoxy, the matrix will fracture at relatively low stress levels, even when stressed in the uniaxial fiber direction. This leads to increased damping, fiber-matrix debonding and to relatively poor fatigue performance. Conversely, where the fiber has a low strain capability and high modulus, as with graphite or boron, the fatigue performance in the uniaxial fiber direction is excellent, as the matrix remains intact until fiber fracture. Advanced composites tested in the uniaxial longitudinal direction have almost flat S-N curves at room temperature. However, when advanced composites are crossplied, the failure mode in fatigue becomes a complex function of the anisotropy of a particular layup as well as of the constituent properties, composite quality and other variables.

The above considerations made it evident that the conventional S-N curve approach to studying composite fatigue would be unproductive in the present program. An alternative approach was to seek to answer the more general question of the extent to which cryogenic temperatures affect the fatigue performance of state-of-the-art composites developed for service at and above room temperature. The development of an efficient means of accomplishing this would permit screening of existing composites for further cryogenic study and might well pinpoint some composite types so insensitive to temperature as to allow existing room temperature fatigue data to be used to predict cryogenic fatigue performance. This report describes the attempts made to achieve this goal.

## 2.2 Experimental Procedures

Composites begin to wear out when the magnitude of a cyclic applied stress exceeds the elastic limit of any component. Wearout is manifested by an increase in damping (increased internal friction) and in a decrease in modulus. The initial objective of the present work was to determine if modulus changes could be used as a criterion for assessing the state of internal damage in a  $[0/\pm 45/0]_s$  5.6 mil boron-epoxy specimen subjected to tensile-tensile and to compressive-compressive low-cycle fatigue at 295 K and 76 K, and in a similar boron-aluminum composite in tensile-tensile fatigue.

The selected composites consisted of eight plies of 0.014 cm (5.6 mil) boron in a matrix of PR-286 epoxy or 6061 aluminum. The commercial suppliers reported 52.1% and 48.4% nominal fiber volume fraction for the boron-epoxy and the boron-aluminum, respectively. Loads were always applied along the  $0^\circ$  fiber direction. This layup was selected to provide reasonable fatigue performance due to the  $0^\circ$  plies while providing wearout by virtue of the inability of the  $\pm 45^\circ$  plies to sustain the loads.

Specimen configurations were similar to those previously used for static tension and compression studies, Table 1. Sufficient thickness to avoid column bending failure in compression was obtained by removing the scrim cloth and bonding two thickness of boron-epoxy to give 16 plies.

The tensile specimen gripping system which had proved adequate for static testing (8) was inadequate for fatigue, as the specimen tended to pull out of the grips. The 0.16 cm (0.06 in) Ti-6Al-4V serrated gripping plates were replaced with 0.64 cm (0.25 in) thick Inconel X-750 plates, and the 0.48 cm (0.19 in) stainless steel pressure plates were increased to 0.64 cm (0.25 in) thickness. Provisions were made for passing a 0.64 cm (0.25 in) diameter bolt through the grip system and specimen. This bolt was torqued to 16 N·m (12 ft·lb), while the twelve pressure screws on the sides of each grip were torqued to 8 N·m (6 ft·lb) each.

The compressive test fixture developed for static use (9) proved adequate



for the fatigue program. However, the titanium pull rods failed under fatigue and were replaced with stainless steel.

As previously in this study, specimen strain was monitored by gages bonded to the specimen surface. Tensile fatigue specimens had both longitudinal and Poisson's gages, while only a longitudinal gage was used for the compression fatigue specimens. Debonding of the gages was not a problem.

Static mechanical properties of the composite were determined in tension and compression at 295 K and 76 K using methods previously described (9). Fatigue studies utilized a closed-loop electrohydraulic machine, specially adapted for cryogenic work. All tests were run at 30 Hz using a sinusoidal wave form. The experimental procedure was similar to that of Williams, et al. (10). A static stress-strain curve was initially obtained, after which a dynamic stress-strain curve was obtained for comparison. To obtain the dynamic stress-strain curve, we first fatigued ( $R = 0.1$ ) the specimen for 25,000 cycles at a maximum stress ( $\sigma_{\max}$ ) that was a small fraction of the ultimate strength. Near the end of this fatigue increment a peak-reading DVM was used to measure the maximum strain ( $\epsilon_{\max}$ ). After fatigue, a quasi-static loading gave the modulus ( $E_f$ ). The maximum fatigue stress was then increased for another 25,000 cycles and another set of measurements. These stress increases were repeated until specimen fracture.

The 295 K tests were run in ambient air. A small temperature increase ( $\sim 10^\circ\text{C}$ ) was observed after the first few steps, remaining relatively stable for the remainder of the step sequence. The 76 K tests were run immersed in liquid nitrogen.

An attempt was made to measure modulus and damping changes by dynamic methods during several tensile fatigue tests of the boron-epoxy and boron-aluminum composite materials at 295 K and at 76 K. Piezoelectric transducers were attached to opposite ends of the specimen-grip system; one was driven with an electrical signal of variable frequency, and the voltage across the other was monitored as the output signal. This allowed the specimen-grip-load train system to be scanned for mechanical resonances over a 0.5-15 kHz range between load steps.

### 2.3 Results and Discussion

Static mechanical properties are given in Table 2. Table 3 compares these data with values of tensile strength and moduli predicted by the rule of mixtures, using uniaxial and  $\pm 45^\circ$  data obtained earlier in this program from the same type composites. The boron-epoxy properties follow the rule of mixtures very well in both strength and modulus. Boron-aluminum follows the rule reasonably well in strength. However, the measured modulus substantially exceeds the predicted value, reflecting the non-linearity between stress and strain in crossplied boron-aluminum composite materials.

Results of the dynamic stress-strain, low-cycle fatigue program appear in Table 4 and in summary in Figs. 1-3. In each of these Figures, plot (a) reflects the strain determined dynamically during a given run, while plot (b) reflects quasi-static strain determined from the slope of a stress-strain curve obtained between each fatigue step. If the dynamic tensile modulus remains unchanged throughout a test, a plot of  $\sigma_{\max}/\sigma_{tu}$  vs.  $\epsilon_{\max}/\epsilon_{tu}$  should have a slope of 1.0 for a composite with a linear stress-strain curve to fracture. (See Appendix 1 for definition of symbols.) The same is true for the dynamic compressive modulus. Likewise, a plot of  $E_f/E_0$  vs.  $\epsilon_{\max}/\epsilon_{tu}$  should have a constant value of 1.0 if the static modulus is unchanging. The same is true for the static compressive modulus. Therefore, deviations from these values were considered as indicators of the extent to which damage was being incurred during the fatigue program.

Fig. 1 (a) indicates that the dynamic tensile modulus of the  $[0/\pm 45/0]_S$

boron-epoxy was not affected by cyclic loading up to about 76% of its static ultimate strength at either 295 K or 76 K. However, Fig. 1 (b) indicates that a small decrease in static tensile modulus did occur at both temperatures.

The compression fatigue data of Fig. 2 show more scatter than does the tensile data. Nevertheless, Fig. 2 (a) indicates that the dynamic compression modulus is relatively unaffected by cyclic loading below about 60% of its ultimate compressive strength. The data suggest that a modulus reduction may occur at higher stress levels. Test temperature appears irrelevant. Fig. 2 (b) indicates that the static compressive modulus does decline with cyclic loading; in some specimens, the decline began at very low stress levels. Again, no temperature dependence of the modulus change was evident.

Most of the compressive data were obtained by cycling at 30 Hz with 25,000 cycles per increment of stress. As reported on Table 5, several runs were also made at 15 Hz and at 10,000 cycles per increment without a significant difference in result.

The limited amount of data obtained on  $[0/\pm 45/0]_S$  boron-aluminum during dynamic stress-strain, low-cycle fatigue testing in tension is reported on Table 4 and summarized in Fig. 3. The displacement of the data above the line of slope 1.0 in Fig. 3 (a) does not reflect cyclic stiffening. Rather, it reflects an increase in the slope of the initial part of the stress-strain curve due to the initial cycle to the preload limit indicated on the Figure for the purpose of determining the static modulus. During the cyclic test, the modulus follows the steeper initial slope up to the preload limit, after which it continues at a lesser slope of approximately 1.0, causing the observed displacement of the plotted data. This is an illustration of the non-linearity characteristic of cross-plyed boron-aluminum composites. Fig. 3 (a) therefore suggests that the cyclic tensile loading up to about 82% of the static ultimate strength had no significant effect on the dynamic tensile modulus. Fig. 3 (b) indicates that the tensile modulus was likewise unaffected. The temperature of testing appears irrelevant.

Attempts to measure modulus and damping changes by resonance methods during the dynamic stress-strain, low-cycle fatigue program produced inconsistent results. Several maxima of the amplitude of the output signal voltage, each corresponding to a mechanical resonance in the specimen-grip-load train system were observed in the 5-15 KHz range. In most of the tests, the observed frequencies and amplitudes did not exhibit systematic behavior as a function of load step number (increasing stress increment). The boron-aluminum specimen tested at 76 K (specimen 1-3) did exhibit systematic behavior. Fig. 4 shows the frequency (x axis) and amplitudes (y axis) of several resonances after the load step indicated by the numeral at the data point. These load steps correspond to the increasing stress levels for specimen 1-3 listed on Table 4. The systematic decrease in resonance amplitude at those frequencies indicates that damping in this specimen was increased significantly by stress cycling, while the absence of large systematic changes in resonance frequencies indicates that the modulus change was not large, in agreement with Fig. 3 (b). The failure to observe similar systematic behavior in test at 295 K indicates that the damping in the specimens before fatiguing, the sensitivity of the apparatus, or both change significantly on cooling to 76 K.

## 2.4 Conclusions

A dynamic stress-strain, low-cycle fatigue method has shown itself capable of detecting composite wearout as revealed by modulus changes in a  $[0/\pm 45/0]_S$  boron-epoxy specimen. However, the method was found to lack the sensitivity required for purposes of screening composite systems for use at cryogenic temperatures. The data suggest that static and dynamic moduli differ, the static modulus providing the most sensitivity to composite wearout. It is

probable that the method would produce more useful results with a composite layup less forgiving in fatigue, i.e., a  $[0/\pm 45]$  or a  $[\pm 45]$  orientation.

The wearout rate in boron-epoxy appears to be greater in compression fatigue than in tension fatigue both at 295 K and 76 K, although the substantially larger scatter in data in compression tends to obscure this difference.

The wearout rate as measured by modulus decrease in the  $[0/\pm 45/0]_S$  boron-epoxy composite used in this study was the same at 76 K as at 295 K. This suggests that the room temperature fatigue data on boron-epoxy composites might serve as a criteria for cryogenic service. However, these preliminary indications must be complimented by additional test work.

Results of the study indicate that  $[0/\pm 45/0]_S$  boron-aluminum performs well in low-cycle tensile fatigue. No difference in performance was detected between tests conducted at 295 K and at 76 K.

Attempts to use an in-situ dynamic resonance method for evaluating composite wearout was for the most part unsuccessful. However, partial success with a boron-aluminum specimen fatigued in tension at 76 K suggests that the method might prove very useful when apparatus and procedures are perfected.

### 3.0 References

1. Kasen, M. B., "Properties of Filamentary-Reinforced Composites at Cryogenic Temperatures," Composite Reliability, ASTM STP 580, American Society for Testing and Materials, 1975, pp. 586-611.
2. Kasen, M. B., "Mechanical and Thermal Properties of Filamentary-Reinforced Structural Composites at Cryogenic Temperatures. I: Glass-Reinforced Composites," Cryogenics, 15 (6), 1975, pp. 327-349.
3. Kasen, M. B., "Mechanical and Thermal Properties of Filamentary-Reinforced Structural Composites at Cryogenic Temperatures. II: Advanced Composites," Cryogenics, 15 (12), 1975, pp. 701-722.
4. Brink, N. O., "Determination of the Performance of Plastic Laminates under Cryogenic Temperatures," ASD-TDR-62-794, Air Force Systems Command, WPAFB, Ohio (August 1962) AD 288944.
5. Tobler, R. L. and Read, D. T., "Fatigue Resistance of a Uniaxial S-Glass/Epoxy Composite at Room and Liquid Helium Temperatures," J. Compos. Mater. 10, 32 (1976).
6. Hanson, M. P., "Tensile and Cyclic Fatigue Properties of Graphite Filament-Wound Pressure Vessels at Ambient and Cryogenic Temperatures," NASA TN D-5354, National Aeronautics and Space Administration, Lewis Research Center, Cleveland, Ohio (1969) (N69-31300) (identical to SAMPE 15, 249).
7. Alfring, R. J., Morris, E. E., Landes, R. E., "Cycle-Testing of Boron Filament-Wound Tanks," NASA CR-72899, National Aeronautics and Space Administration, Lewis Research Center A(1971) (N71-38023).
8. Kasen, M. B. and Schramm, R. E., "Advanced Composites," in Semi-Annual Technical Reports on Materials Research in Support of Superconducting Machinery - II; R. P. Reed, A. F. Clark, E. C. van Reuth (Eds.); Nat. Bur. Stds., Boulder, CO; October 1974; ADA004586.



9. Schramm, R. E. and Kasen, M. B., "Advanced Composites," in Semi-Annual Technical Reports on Materials Research in Support of Superconducting Machinery - V; R. P. Reed, A. F. Clark, E. C. van Reuth (Eds.); Nat. Bur. Stds., Boulder, CO; April 1976.
10. Williams, R. S., Reifsnider, K. L., Stinchcomb, W. W., and Turgay, H. T., "The Effect of Frequency and Strain Amplitude on the Fatigue Damage of Boron/Epoxy Fiber-Reinforced Composite Materials," AFOSR-TR-75-1387, AFOSR, Arlington, VA, April 1975, ADA 015479.

#### APPENDIX 1: LIST OF SYMBOLS

$E$	Elastic modulus measured from quasi-static loading.
$E_o$	Elastic modulus measured prior to fatigue.
$E_f$	Elastic modulus measured after fatigue.
$R$	Ratio of minimum to maximum stress during fatigue cycle.
$\epsilon^{cu}$	Maximum strain measured in quasi-static loading (compression).
$\epsilon^{tu}$	Maximum strain measured in quasi-static loading (tension).
$\epsilon_{max}$	Maximum strain measured during fatigue.
$\sigma^{cu}$	Maximum stress measured in quasi-static loading (compression).
$\sigma^{tu}$	Maximum stress measured in quasi-static loading (tension).
$\sigma_{max}$	Maximum stress measured during fatigue.
$\nu$	Poisson's ratio measured in quasi-static loading.
$\nu_o$	Poisson's ratio measured prior to fatigue.
$\nu_f$	Poisson's ratio measured after fatigue.

Table 1. Nominal specimen dimensions.

Specimen	Length		Width		Thickness		Gage Length	
	cm	in	cm	in	cm	in	cm	in
Tension	25.4	10.0	2.54	1.0	0.142	0.056	15.2	6.0
Compression	10.2	4.0	0.406	0.160	0.279	0.110	1.3	0.5

Table 2. Static mechanical properties

Test Temp. (K)	E		$\nu$	$\sigma^u$		$\epsilon^u\%$
	$10^9 \text{ N/m}^2$	$10^6 \text{ psi}$		$10^8 \text{ N/m}^2$	$10^3 \text{ psi}$	
<u>[0/±45/0]<sub>s</sub> Boron-Epoxy</u>						
			<u>Tension</u>			
295	120	17.4	0.755	7.62	110	0.65
295	119	17.2	0.692	7.60	110	0.68*
295	122	17.7	0.806	<u>8.10</u>	<u>117</u>	<u>0.71</u>
76	117	17.0	0.551	8.56	124	0.70
76	133	19.3	0.540	<u>8.61</u>	<u>125</u>	<u>0.70</u>
4	134	19.4	0.580	**	**	**
4	133	19.3	0.561	8.87	129	0.71
			<u>Compression</u>			
295	102	14.8		12.4	180	1.20
295	101	14.7		9.7	<u>141</u>	<u>1.08</u>
<u>[0/±45/0]<sub>s</sub> Boron-Aluminum</u>						
			<u>Tension</u>			
295	178	25.8	0.295	7.74	112	0.54*
295	179	26.0	0.287	8.53	124	0.60*
295	180	26.0	0.305	<u>7.61</u>	<u>110</u>	<u>0.58</u>
295	159	23.0	0.415	<u>6.34</u>	92	0.51
76	163	23.6	0.350	<u>8.14</u>	118	<u>0.68</u>
4	166	24.0	0.314	8.47	123	0.72*

\* Grip Fracture

\*\* No fracture

Underlined values used in calculating data on Figs. 1-3 and Table 5.

Table 3. Comparison between measured properties of  $[0/+45/0]_S$  boron-epoxy and boron-aluminum and properties predicted by the rule of mixtures.

Material	295 K		76 K		295 K		76 K	
	Predicted $\sigma^{tu}$	Measured $\sigma^{tu}$	Predicted $\sigma^{tu}$	Measured $\sigma^{tu}$	Predicted $E^t$	Measured $E^t$	Predicted $E^t$	Measured $E^t$
Boron-epoxy	128	110-117	130	124-125	17.4	17.4-17.7	17.8	17.0-19.3
Boron-aluminum	119	92-124	146	118	16.3	23.0-26.0	16.3	23.6

$\sigma^{tu} = 10^3$  psi,  $E^t = 10^6$  psi

Table 4. Results or dynamic  $\sigma$ - $\epsilon$  tests.

	Fatigue Cycles $10^3$	Dynamic		Static		$\frac{\sigma_{\max}}{\sigma_{tu}}$	$\frac{\epsilon_{\max}}{\epsilon_{tu}}$	$\frac{E_f}{E_0}$
		$\sigma_{\max}$ $10^8 \text{ N/m}^2$	$\epsilon_{\max}$ %	$E$ $10^9 \text{ N/m}^2$	$\nu$			
Boron-Epoxy, specimen 1-8, 76 K, $\sigma_{tu} = 8.61 \times 10^8$ $\text{N/m}^2$ , $\epsilon_{tu} = 0.70\%$ , 30 Hz, Tension	0	--	--	130	0.578	--	--	1.00
	25	0.50	0.05	132	0.573	0.06	0.07	1.02
	50	1.01	0.09	132	0.553	0.12	0.13	1.02
	75	1.51	0.13	132	0.563	0.18	0.19	1.02
	100	2.02	0.17	132	0.568	0.23	0.24	1.02
	125	2.53	0.21	128	0.563	0.29	0.30	0.98
	150	3.03	0.24	126	0.563	0.35	0.34	0.97
	175	3.53	0.29	126	0.580	0.41	0.41	0.97
	200	4.04	0.33	125	0.597	0.47	0.47	0.96
	225	4.54	0.38	124	0.589	0.53	0.54	0.95
	250	5.05	0.41	123	0.593	0.59	0.59	0.95
	275	5.56	0.46	122	0.587	0.65	0.66	0.94
	300	6.06	0.50	120	0.608	0.70	0.71	0.92
	325	6.56	0.52	132	0.641	0.76	0.74	1.02
Boron-Epoxy, specimen 1-3, 295 K, $\sigma_{tu} = 8.10 \times 10^8$ $\text{N/m}^2$ , $\epsilon_{tu} = 0.71\%$ , 30 Hz, Tension	0	--	--	117	0.703	--	--	1.00
	25	0.50	0.05	116	0.712	0.06	0.07	0.99
	50	1.00	0.09	115	0.698	0.12	0.13	0.98
	75	1.50	0.13	115	0.693	0.19	0.18	0.98
	100	2.51	0.23	117	0.715	0.31	0.32	1.00
	125	3.51	0.31	113	0.717	0.43	0.44	0.97
	150	4.01	0.36	113	0.713	0.50	0.51	0.97
	175	4.51	0.40	113	0.728	0.56	0.56	0.97
	200	5.01	--	113	0.740	0.62	--	0.97
	225	5.51	0.50	110	0.739	0.68	0.70	0.94
	250	6.01	0.55	--	--	0.74	0.77	--
Boron-Epoxy, specimen F-7, 76 K, $\sigma_{cu} = 12.0 \times 10^8$ $\text{N/m}^2$ , $\epsilon_{cu} = 0.93\%$ , 30 Hz Compression	0	--	--	137	--	--	--	1.00
	25	1.009	0.07	132	--	0.08	0.08	0.96
	50	2.017	0.14	140	--	0.17	0.15	1.02
	75	3.026	0.22	137	--	0.25	0.24	1.00
	100	4.035	0.28	144	--	0.34	0.30	1.05
	125	5.043	0.34	148	--	0.42	0.37	1.08
	150	6.052	0.42	140	--	0.50	0.45	1.02
	175	7.061	0.54	133	--	0.59	0.68	0.97
	200	8.069	0.75	113	--	0.67	0.81	0.82
Boron-Epoxy, specimen F-18, 76 K, $\sigma_{cu} = 12.0 \times 10^8$ $\text{N/m}^2$ , $\epsilon_{cu} = 0.93\%$ , 30 Hz, Compression	0	--	--	156	--	--	--	1.00
	25	1.02	0.06	156	--	0.09	0.06	1.00
	50	2.05	0.12	148	--	0.17	0.13	0.95
	75	3.07	0.20	144	--	0.26	0.21	0.93
	100	4.10	0.28	140	--	0.34	0.30	0.90
	125	5.12	0.35	139	--	0.43	0.38	0.89
	150	6.15	0.44	139	--	0.51	0.47	0.89
	175	7.17	0.53	133	--	0.60	0.57	0.85
	185.07	8.19	--	--	--	--	--	--

Table 4. continued

	Fatigue Cycles $10^3$	Dynamic		Static		$\frac{\sigma_{\max}}{\sigma_{tu}}$	$\frac{\epsilon_{\max}}{\epsilon_{tu}}$	$\frac{E_f}{E_o}$
		$\sigma_{\max}$ $10^8 \text{ N/m}^2$	$\epsilon_{\max}$ %	E $10^9 \text{ N/m}^2$	$\nu$			
Boron-Epoxy, specimen F-15, 76 K, $\sigma^{cu} = 12.0 \times 10^8$ $\text{N/m}^2$ , $\epsilon^{cu} = 0.93\%$ , 30 Hz, Compression	0	--	--	152	--	--	--	1.00
	10	0.99	0.07	150	--	0.08	0.08	0.99
	20	1.97	0.14	151	--	0.16	0.15	0.99
	30	2.96	0.21	143	--	0.25	0.23	0.94
	40	3.94	0.30	130	--	0.33	0.32	0.85
	50	4.93	0.37	136	--	0.41	0.39	0.89
	60	5.91	0.46	132	--	0.49	0.50	0.87
Boron-Epoxy, specimen F-16, 76 K, $\sigma^{cu} = 12.0 \times 10^8$ $\text{N/m}^2$ , $\epsilon^{cu} = 0.93\%$ , 15 Hz, Compression	25	1.02	0.08	--	--	0.09	0.08	--
	50	2.03	0.15	147	--	0.17	0.16	1.00
	75	3.05	0.24	129	--	0.25	0.25	0.88
	100	4.06	0.31	131	--	0.34	0.34	0.89
	125	5.07	0.39	134	--	0.42	0.42	0.91
	150	6.09	0.48	129	--	0.51	0.52	0.88
	175	7.10	0.57	125	--	0.59	0.61	0.85
	200	8.12	0.64	157	--	0.68	0.69	1.07
Boron-Epoxy, specimen F-6, 295 K, $\sigma^{cu} = 12.4 \times 10^8$ $\text{N/m}^2$ , $\epsilon^{cu} = 1.20\%$ , 30 Hz, Compression	0	--	--	134	--	--	--	1.00
	25	1.015	0.11	145	--	0.08	0.09	1.08
	50	2.029	0.20	135	--	0.16	0.17	1.01
	75	3.044	0.24	133	--	0.25	0.20	0.99
	100	4.058	0.33	128	--	0.33	0.28	0.96
	125	5.091	0.40	128	--	0.41	0.33	0.96
	150	6.088	0.49	122	--	0.49	0.41	0.91
	175	7.102	0.57	121	--	0.57	0.48	0.96
	200	8.117	0.73	106	--	0.65	0.61	0.79
Boron-Epoxy, specimen F-10, 295 K, $\sigma^{cu} = 12.4 \times 10^8$ $\text{N/m}^2$ , $\epsilon^{cu} = 1.20\%$ , 30 Hz, Compression	0	--	--	88	--	--	--	1.00
	25	0.99	0.12	93	--	0.08	0.10	1.05
	50	1.99	0.23	91	--	0.16	0.19	1.04
	75	2.98	0.31	103	--	0.24	0.26	1.16
	100	3.97	0.41	104	--	0.32	0.34	1.17
	125	4.96	0.51	99	--	0.40	0.43	1.12
	150	5.95	0.63	94	--	0.48	0.53	1.07
	175	<b>6.95</b>	<b>0.75</b>	<b>87</b>	--	<b>0.56</b>	<b>0.62</b>	<b>0.99</b>
	186.18	7.94	0.95	--	--	0.64	0.79	--
Boron-Epoxy, specimen F-12, 295 K, $\sigma^{cu} = 12.4 \times 10^8$ $\text{N/m}^2$ , $\epsilon^{cu} = 1.20\%$ , 30 Hz, Compression	0	--	--	107	--	--	--	1.00
	10	1.00	0.08	104	--	0.08	0.07	1.02
	20	1.99	0.20	107	--	0.16	0.16	0.99
	30	2.99	0.31	112	--	0.24	0.26	1.04
	40	3.98	0.38	111	--	0.32	0.32	1.03
	50	4.98	0.45	109	--	0.40	0.37	1.01
	60	5.97	0.55	107	--	0.48	0.46	1.00
	70	6.97	0.68	106	--	0.56	0.56	0.98
	80	7.96	0.79	104	--	0.64	0.66	0.97
	90	8.91	0.88	103	--	0.72	0.73	0.96



Table 4. continued

	Fatigue Cycles $10^3$	Dynamic		Static		$\frac{\sigma_{\max}}{\sigma_{tu}}$	$\frac{\epsilon_{\max}}{\epsilon_{tu}}$	$\frac{E_f}{E_o}$
		$\sigma_{\max}$ $10^8 \text{ N/m}^2$	$\epsilon_{\max}$ %	$E$ $10^9 \text{ N/m}^2$	$\nu$			
Boron-Epoxy, Specimen E-11, 295 K, $\sigma_{cu}^{tu} = 12.4 \times 10^8$ $\text{N/m}^2$ , $\epsilon_{cu}^{tu} = 1.2\%$ , 15 Hz Compression	0 25 50 75 100 125	-- 1.00 2.00 3.00 4.00 5.01	-- 0.09 0.16 0.26 0.33 0.42	132 123 119 116 118 116	-- -- -- -- -- --	-- 0.08 0.16 0.24 0.32 0.40	-- 0.07 0.14 0.21 0.27 0.35	1.00 0.94 0.91 0.88 0.90 0.88
Boron-Aluminum, specimen 1-3, 76 K, $\sigma_{tu}^{tu} = 7.61$ $\times 10^8 \text{ N/m}^2$ , $\epsilon_{tu}^{tu} = 0.58\%$ , 30 Hz, Tension	0 25 50 75 100 125 150 175	-- 0.56 1.13 1.69 2.82 3.95 5.08 6.21	-- 0.03 0.07 0.10 0.17 0.25 0.33 0.42	199 197 193 200 199 200 196 189	-- -- -- -- -- -- -- --	-- 0.07 0.15 0.22 0.37 0.52 0.67 0.82	-- 0.06 0.11 0.18 0.30 0.44 0.58 0.72	1.00 0.99 0.97 1.01 1.00 1.01 0.98 0.95
Boron-Aluminum, specimen 1-6, 295 K, $\sigma_{tu}^{tu} = 8.14$ $\times 10^8 \text{ N/m}^2$ , $\epsilon_{tu}^{tu} = 0.68\%$ , 30 Hz, Tension	0 25 50 75 100 125 150 175	-- 0.56 1.11 1.67 2.79 3.90 4.46 5.01	-- 0.03 0.07 0.10 0.18 0.26 0.30 0.34	187 189 188 188 186 184 183 185	-- -- -- -- -- -- -- --	-- 0.07 0.14 0.21 0.34 0.48 0.55 0.62	-- 0.05 0.11 0.15 0.27 0.38 0.44 0.50	1.00 1.01 1.01 1.01 0.99 0.98 0.98 0.99

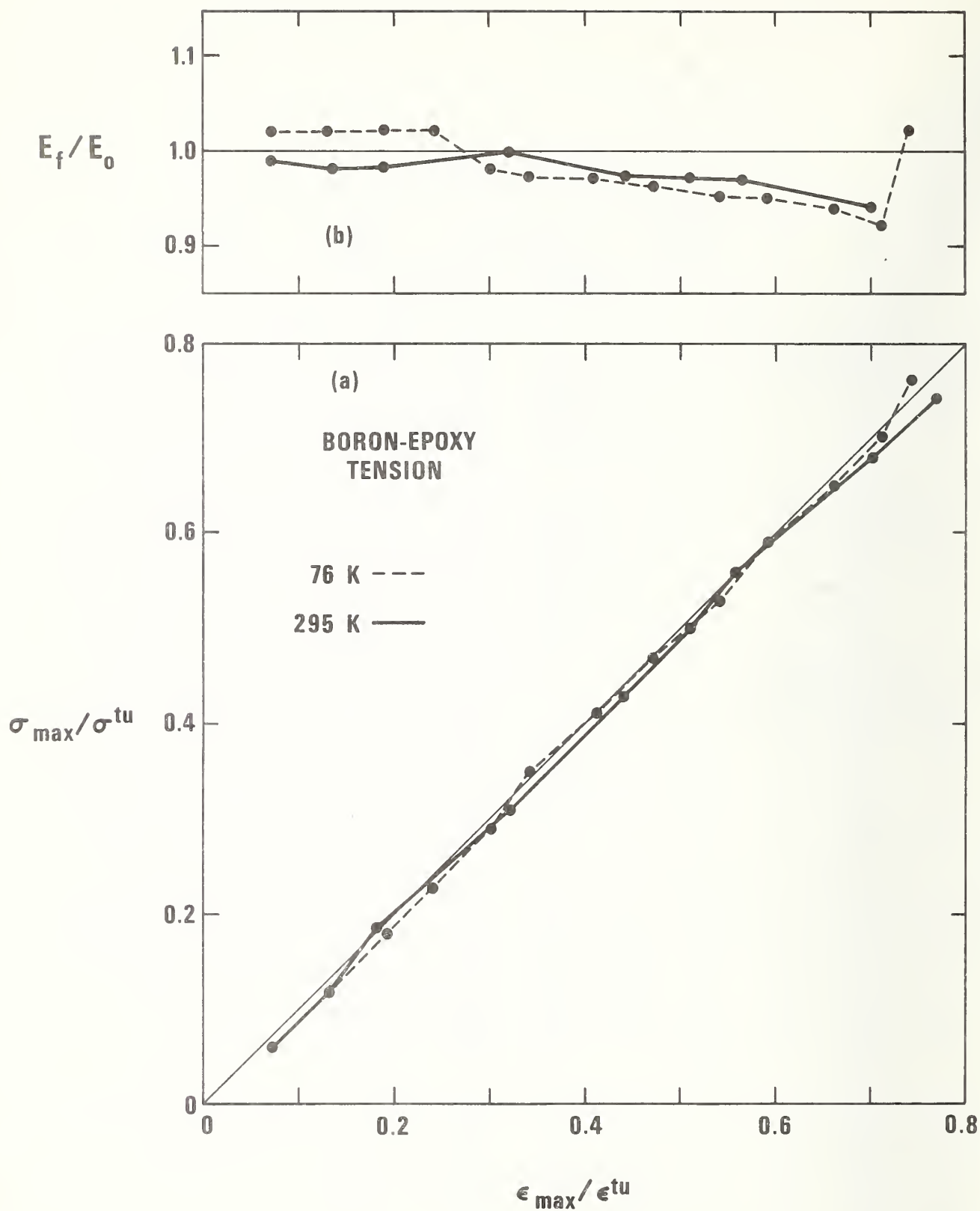


Fig. 1. Relative stress and relative modulus as a function of relative strain for boron-epoxy during tensile fatigue. Each point represents an increment of 25,000 cycles.

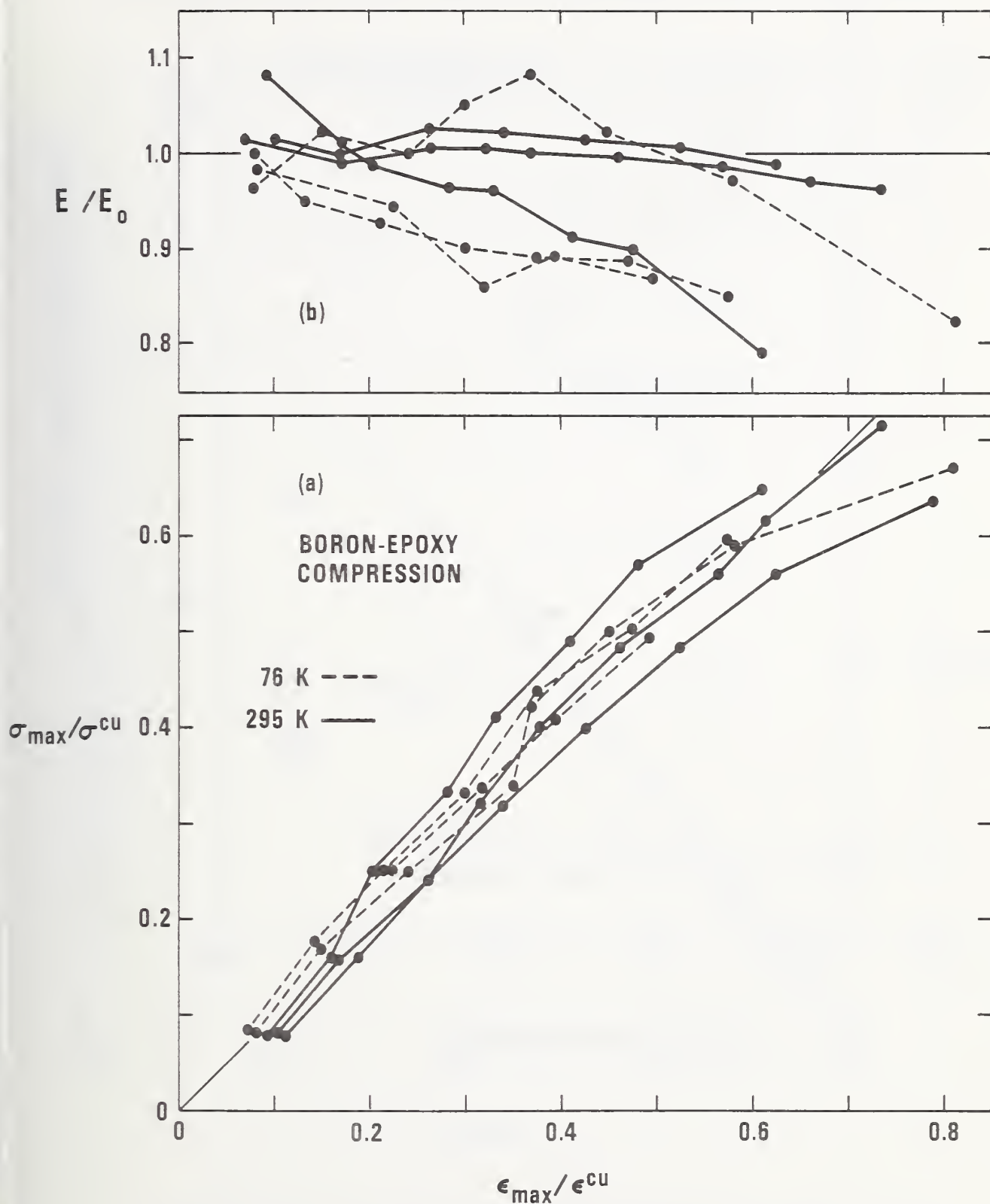


Fig. 2. Relative stress and relative modulus as a function of relative strain for boron-epoxy during compressive fatigue. Each point represents an increment of 25,000 cycles.

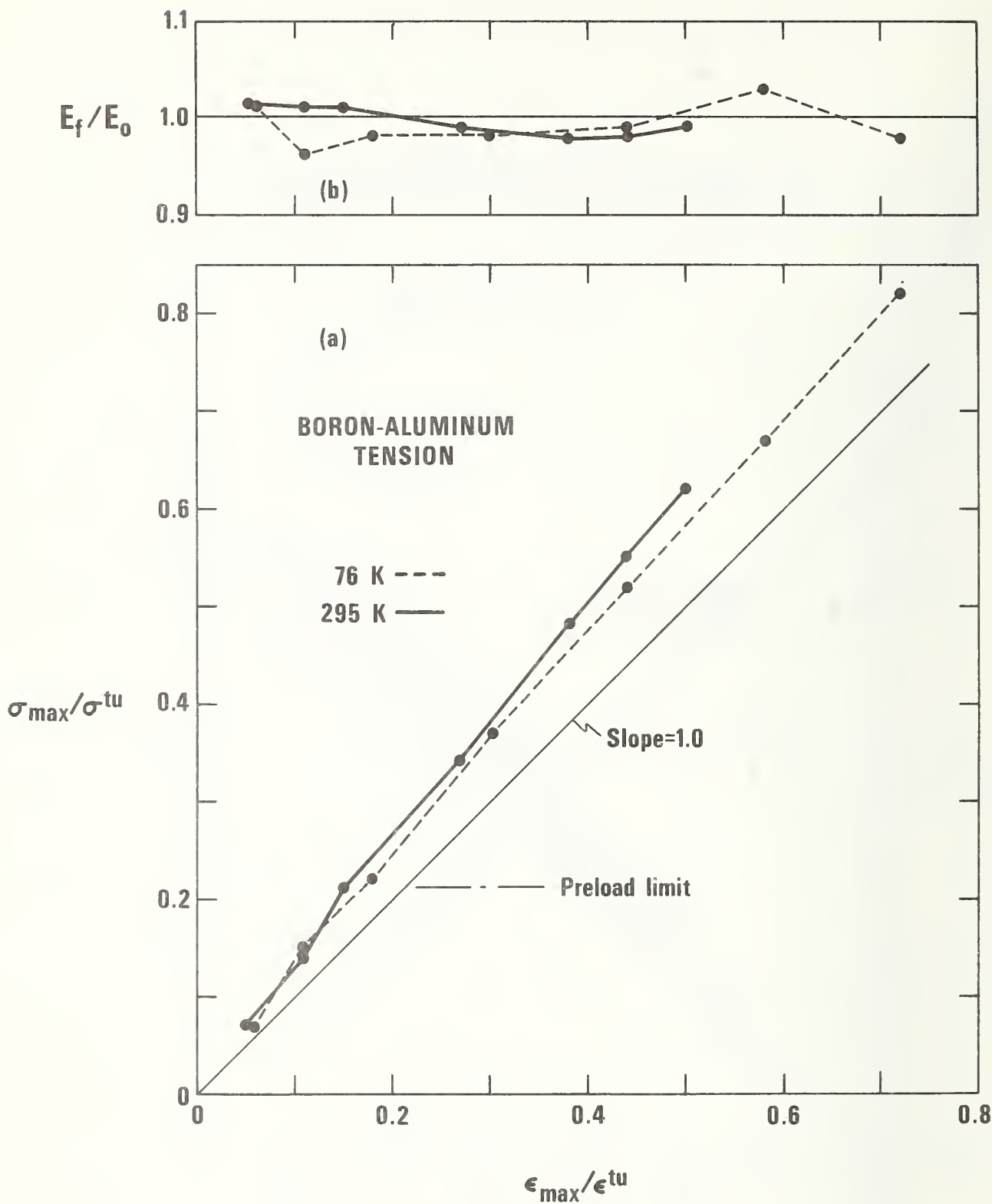


Fig. 3. Relative stress and relative modulus as a function of relative strain for boron-aluminum during tensile fatigue. Each point represents an increment of 25,000 cycles.

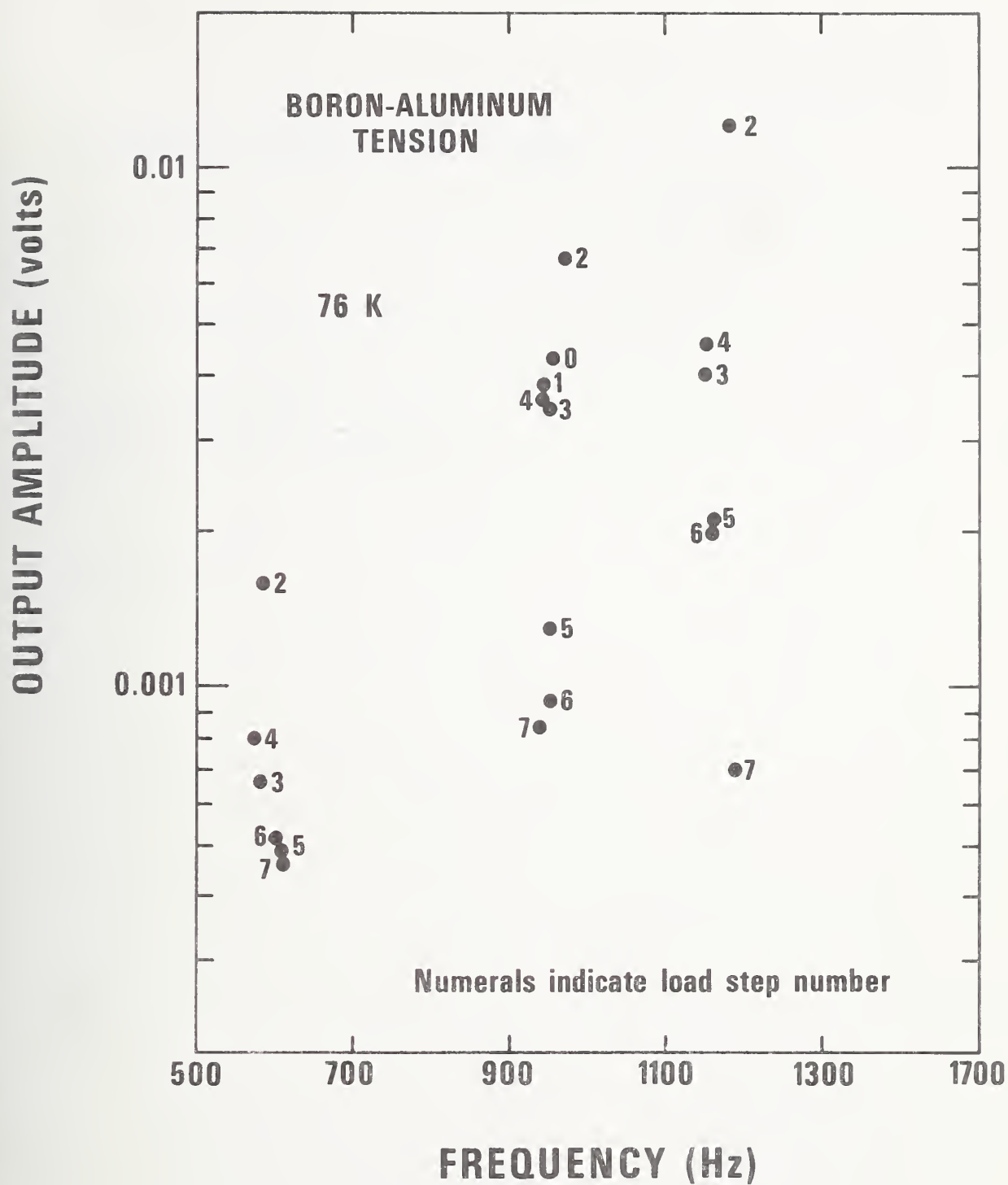


Fig. 4. Frequency and amplitude of three maxima in piezo electric transducer output after the indicated fatigue-stress steps.



SEMI-ANNUAL REPORT ON MATERIALS RESEARCH  
IN SUPPORT OF SUPERCONDUCTING MACHINERY

ELASTIC PROPERTIES

H. M. Ledbetter and D. T. Read

Cryogenics Division  
Institute for Basic Standards  
National Bureau of Standards  
Boulder, Colorado 80302

October 1976

NBS ELASTIC-PROPERTIES STUDIES DURING ARPA-SPONSORED  
PROGRAM, SEPTEMBER 1973 TO SEPTEMBER 1976.

	Material	ARPA Report No.	Experimental Method(s)
1.	Aluminum alloy 1100	2,(5)*	P**
2.	" " 2019	5	P
3.	" " 2215	5	P
4.	" " 5083	2,(5)	P
5.	" " 7005	2,(5)	P
6.	" " 7075	2,(5)	P
7.	Copper	4	R,P
8.	" -10Ni	4	R,P
9.	" -30Ni	4	R,P
10.	" -0.3Cd-0.3Cr(PD135)	4,6	R,P
11.	Inconel 600	1,(4)	P
12.	" 718	3,(5)	P
13.	" X750	1,(4)	P
14.	Iron-36Ni (Invar)	4	R,P
15.	Maraging steel	6	P
16.	Nitronic 40(21-6-9)	6	R,P
17.	Stainless steel A286	2,(4)	P
18.	" " 304	2,(4)	P
19.	" " 310	2,(4)	P
20.	" " 316	2,(4)	P
21.	Titanium-6Al-4V	1,(2)	P
22.	" -5Al-2.5Sn	1,(2)	P
	Composites:		
23.	Boron/aluminum	6	R
24.	Fiberglass/epoxy	3,(5)	R
25.	NbTi/Cu	6	P,R
26.	NbTi/Cu/epoxy	3,(5)	R

\* Numbers in parentheses refer to report numbers in which reprint versions of the manuscripts occur. Other numbers refer to preprint versions.

\*\*P = pulse, R = resonance.



## ELASTIC PROPERTIES OF ENGINEERING MATERIALS AT CRYOGENIC TEMPERATURES

H. M. Ledbetter

Six manuscripts on the elastic properties of engineering materials are included in the present report:

1. "Low temperature elastic properties of a precipitation-hardened copper alloy" by H. M. Ledbetter. This manuscript on the cryogenic elastic properties of copper alloy PD 135 complements the manuscript in the fourth semi-annual report that described the anomalous elastic properties of this alloy at room temperature.
2. "Orthorhombic elastic constants of an NbTi/Cu composite superconductor" by H. M. Ledbetter and D. T. Read. This manuscript describes the elastic symmetry of a material used in cryogenic magnets.
3. "Temperature dependence of the elastic constants of an NbTi/Cu superconducting composite" by D. T. Read and H. M. Ledbetter. This manuscript complements item (2), giving the low-temperature elastic constants.
4. "Anomalous low-temperature elastic behavior of a nitrogen-strengthened chromium-manganese stainless steel" by H. M. Ledbetter. This is the first study of the low-temperature elastic properties of this steel. It behaves anomalously because of a paramagnetic-antiferromagnetic transition.
5. "Low-temperature elastic properties of a 300-grade maraging steel" by H. M. Ledbetter.
6. "Elastic properties of a boron-aluminum composite at low temperatures" by D. T. Read and H. M. Ledbetter.

Since this is the final report of the three-year ARPA-sponsored program on materials research for superconducting machinery, it is appropriate to review briefly the entire elastic-properties effort. The table on the previous page summarizes the NBS experimental studies on low-temperature elastic properties. Twenty-six materials were studied in the temperature region 4-300 K: six aluminum alloys; four copper alloys; three inconels; an iron-nickel alloy; a maraging steel; a nitrogen-strengthened stainless steel; two titanium alloys; and four composites: boron/aluminum, fiberglass/epoxy, NbTi/Cu, and NbTi/Cu/epoxy. Some of the special properties of these materials include: precipitation hardening, low thermal expansion, high strength-density ratio, and high strength-thermal conductivity.

NBS PUBLICATIONS ON ELASTIC PROPERTIES, RESULTING FROM  
ARPA-SPONSORED PROGRAM, SEPTEMBER 1973 TO SEPTEMBER 1976

1. E. R. Naimon, H. M. Ledbetter, and W. F. Weston, Low-temperature elastic properties of four wrought and annealed aluminum alloys, J. Mater. Sci. 10 (1975) 1309-1316.
2. D. T. Read and H. M. Ledbetter, Temperature dependencies of the elastic constants of precipitation-hardened aluminum alloys 2014 and 2219, submitted for publication.
3. H. M. Ledbetter and W. F. Weston, Low-temperature elastic properties of some copper-nickel alloys, Ultrasonics Symposium Proc., Cat. No. 75 Ch 8 994-4SU (IEEE, New York, 1975) 623-627.
4. H. M. Ledbetter, Anomalous elastic properties of a precipitation-hardened copper alloy, submitted for publication.
5. H. M. Ledbetter, Low-temperature elastic properties of a precipitation-hardened copper alloy, submitted for publication.
6. W. F. Weston, H. M. Ledbetter and E. R. Naimon, Dynamic low-temperature elastic properties of two austenitic nickel-chromium-iron alloys, Mater. Sci. Engg. 20 (1975) 185-194.
7. W. F. Weston and H. M. Ledbetter, Low-temperature elastic properties of a nickel-chromium-iron-molybdenum alloy, Mater. Sci. Engg. 20 (1975) 287-290.
8. H. M. Ledbetter, E. R. Naimon, and W. F. Weston, Low-temperature elastic properties of invar, Proc. ICMC, Kingston, Ontario, July 1975 (Plenum, New York, forthcoming).
9. H. M. Ledbetter and D. T. Read, Low-temperature elastic properties of a 300-grade maraging steel, submitted for publication.
10. H. M. Ledbetter and D. T. Read, Low-temperature elastic properties of a nitrogen-strengthened chromium-manganese stainless steel, submitted for publication.
11. H. M. Ledbetter, W. F. Weston, and E. R. Naimon, Low-temperature elastic properties of four austenitic stainless steels, J. Appl. Phys. 46 (1975) 185-194.
12. E. R. Naimon, W. F. Weston, and H. M. Ledbetter, Elastic properties of two titanium alloys at low temperatures, Cryogenics 14 (1974) 246-249.
13. D. T. Read and H. M. Ledbetter, Low-temperature elastic properties of a boron/aluminum composite, submitted for publication.
14. W. F. Weston, Elastic constants of a superconducting-coil composite material, J. Appl Phys. 46 (1975) 4458-4465.
15. H. M. Ledbetter and D. T. Read, Orthorhombic elastic constants of an NbTi/Cu composite superconductor, submitted for publication.
16. D. T. Read and H. M. Ledbetter, Low-temperature elastic constants of an NbTi/Cu composite superconductor, submitted for publication.

ORTHORHOMBIC ELASTIC CONSTANTS OF AN  
NbTi/Cu COMPOSITE SUPERCONDUCTOR\*

H. M. Ledbetter and D. T. Read\*\*

Cryogenics Division  
Institute for Basic Standards  
National Bureau of Standards  
Boulder, Colorado 80302

ABSTRACT

Elastic properties of a niobium-titanium-filament, copper-matrix composite superconductor were studied experimentally. Ultrasonic pulse and resonance measurements showed the material has orthorhombic symmetry and, therefore, nine independent elastic constants. With respect to copper:  $C_{11}$ ,  $C_{22}$ , and  $C_{33}$  are about seven percent lower;  $C_{44}$ ,  $C_{55}$ , and  $C_{66}$  are about fifteen percent lower; the off-diagonal elastic constants are unchanged; and the bulk modulus is about five percent lower. Deviations from isotropic elastic behavior are small.

Key words: Bulk modulus; composite; compressibility; copper; elastic constants; niobium-titanium; Poisson's ratio; pulse method; resonance method; shear modulus; sound velocity; superconductor; Young's modulus.

\* Contribution of NBS, not subject to copyright.

\*\*NRC-NBS Postdoctoral Research Associate, 1975-6.

ORTHORHOMBIC ELASTIC CONSTANTS OF AN  
NbTi/Cu COMPOSITE SUPERCONDUCTOR\*

H. M. Ledbetter and D. T. Read\*\*

Cryogenics Division  
Institute for Basic Standards  
National Bureau of Standards  
Boulder, Colorado 80302

I. INTRODUCTION

The purpose of this paper is to report an experimental study of the elastic properties of a composite material, emphasizing elastic symmetry and the value of applying familiar single-crystal methods to composites. This composite contains unidirectional niobium-titanium (NbTi) filaments in a copper (Cu) matrix. It is designed as a superconductor for magnets. Manufacture and morphology suggest that the filament direction is an elastic symmetry axis. Thus, the macroscopic elastic symmetry is orthorhombic, tetragonal, hexagonal, or cubic. Oblique axis systems--triclinic, monoclinic, trigonal--are excluded.

The present study shows that this composite is orthorhombic. But, deviations from isotropy are small. Thus, it can be referred to other co-ordinate axes--for example, hexagonal-- without introducing large errors. Advantages of this simplification are discussed below. Nevertheless, a complete set of nine orthorhombic elastic constants was determined.

Experimentally, two dynamic methods were used: pulse and resonance. Most measurements were made by a pulse method; eighteen ultrasonic wave velocities were measured along the orthorhombic  $\langle 100 \rangle$  and  $\langle 110 \rangle$  directions. Resonance experiments were done to achieve two ancillary objectives. First, to detect dispersion, the variation of sound-velocity with frequency. Second, to confirm the off-diagonal elastic constants.

It is emphasized that the elastic constants reported here may differ from those of apparently identical composites for reasons discussed below in sections IIIC and VF.

## II. WAVE MOTION IN ORTHORHOMBIC MEDIA

Usual crystallographic notations for vectors and elastic constants are used in this report, although all components of the studied composite material are polycrystalline. Symmetries discussed here are strictly macroscopic. The filament direction of the composite is designated [001], and the principal directions perpendicular to the filaments are [100] and [010]. These directions are indicated in Fig. 1.

As stated above, the studied material has orthorhombic symmetry. Materials with orthorhombic symmetry have nine dependent elastic constants. These are displayed in Eq. (1) in the Voigt contracted notation in matrix form.

$$C_{ij} = \begin{bmatrix} C_{11} & C_{12} & C_{13} & 0 & 0 & 0 \\ & C_{22} & C_{23} & 0 & 0 & 0 \\ & & C_{33} & 0 & 0 & 0 \\ & & & C_{44} & 0 & 0 \\ & & & & C_{55} & 0 \\ & & & & & C_{66} \end{bmatrix}, \quad (1)$$

where the matrix is symmetrical about its main diagonal. The Christoffel equations, which relate the elastic constants to the plane, monochromatic phase velocities, are:<sup>1</sup>

$$(C_{ijkl} n_j n_k - \rho v^2 \delta_{il}) p_l = 0 \quad (2)$$

where  $C_{ijkl}$  is the fourth-rank elastic stiffness tensor,  $\underline{n}$  is the wave-propagation direction,  $\rho$  is the mass density,  $v$  is the wave velocity,  $\delta_{il}$



is the Kronecker delta, and  $\tilde{p}$  is the displacement vector. It is easy to show that the resulting secular equation is diagonal for the [100], [010], and [001] directions. Thus, waves traveling along  $\langle 100 \rangle$  directions are pure modes. Their velocities are determined by  $C_{11}$ ,  $C_{55}$ ,  $C_{66}$ ;  $C_{22}$ ,  $C_{44}$ ,  $C_{66}$ ; and  $C_{33}$ ,  $C_{44}$ ,  $C_{55}$ ; respectively. Thus, all diagonal elastic constants  $C_{ii}$  can be determined by propagating waves in  $\langle 100 \rangle$  directions. For each direction, there is one longitudinal wave and two shear waves; the three are polarized mutually orthogonally. Thus, checks on each of the three shear elastic constants  $C_{44}$ ,  $C_{55}$ , and  $C_{66}$  are available. The off-diagonal elastic constants  $C_{12}$ ,  $C_{13}$ , and  $C_{23}$  must be determined by measurements where the  $\tilde{n}$  vectors are oblique to the  $\langle 100 \rangle$  directions.

In general, waves traveling along lower-symmetry directions are not pure modes.<sup>2</sup> For  $\tilde{n} = \langle 110 \rangle$ , there is a single pure mode whose velocity is determined by  $\frac{1}{2} (C_{55} + C_{66})$ ,  $\frac{1}{2} (C_{44} + C_{66})$ , and  $\frac{1}{2} (C_{44} + C_{55})$  for the [011], [101], and [110] directions, respectively. These provide additional checks on the three  $C_{ii}$  shear constants measured along  $\langle 100 \rangle$  directions. The two impure modes that propagate along each  $\langle 110 \rangle$  direction can be determined from the Christoffel equations.

The  $\langle 011 \rangle$  propagation-direction case is now outlined. The Kelvin-Christoffel elastic stiffnesses

$$\Gamma_{il} = C_{ijkl} \tilde{n}_j \tilde{n}_k \quad (3)$$

are for the case  $\tilde{n} = \frac{1}{\sqrt{2}} [011]$ :

$$\Gamma_{il} = \frac{1}{2} \begin{bmatrix} C_{55} + C_{66} & 0 & 0 \\ 0 & C_{22} + C_{44} & C_{23} + C_{44} \\ 0 & C_{23} + C_{44} & C_{33} + C_{44} \end{bmatrix}. \quad (4)$$

Thus, one solution is

$$\rho v^2 = \frac{1}{2} (C_{55} + C_{66}), \quad (5)$$

a torsion mode. And the remaining two roots are

$$\rho v^2 = \frac{1}{2} \{ C_{22} + C_{33} + [(C_{22} - C_{33})^2 + 4(C_{23} + C_{44})^2]^{1/2} \} + C_{44}. \quad (6)$$

Experimentally,  $\rho v^2$  is measured and  $C_{23}$  is unknown. Thus, by rearrangement

$$C_{23} = \pm \{ [2\rho v^2 - \frac{1}{2}(C_{22} + C_{33} + 2C_{44})]^2 - \frac{1}{4}(C_{33} - C_{22})^2 \}^{1/2} - C_{44}. \quad (7)$$

The spurious second value of  $C_{23}$  from this equation can be discarded on physical grounds. Similarly, [101] and [110] planes can be used to determine  $C_{13}$  and  $C_{12}$ , respectively. For these cases

$$C_{13} = \pm \{ [2\rho v^2 - \frac{1}{2}(C_{11} + C_{33} + 2C_{55})]^2 - \frac{1}{4}(C_{33} - C_{11})^2 \}^{1/2} - C_{55} \quad (8)$$

and

$$C_{12} = \pm \{ [2\rho v^2 - \frac{1}{2}(C_{11} + C_{33} + 2C_{66})]^2 - \frac{1}{4}(C_{22} - C_{11})^2 \}^{1/2} - C_{66}. \quad (9)$$

Further details on the problem of wave propagation in orthorhombic media were given by Musgrave.<sup>3</sup>



### III. EXPERIMENTAL

#### A. Material

The samples used in this study were cut from a short section of Kryo 210\* superconductor supplied by Magnetics Corporation of America. This is a copper-matrix, niobium-titanium-filament composite material. The Cu/NbTi volume ratio is 6:1, and the bar contains 2640 filaments with a twist each 7.6 cm. The distribution of filaments is shown in Fig. 2. The sample obtained for this study was about 20 cm long, 1.0 cm wide, and 0.5 cm thick. Four samples were cut for ultrasonic pulse measurements, one with its surfaces perpendicular to the symmetry axes of the material and three with the largest surface oriented at 45° to two symmetry axes. Sample geometries are shown in Fig. 1. Samples were studied in the as-received condition, that is, optimized by the manufacturer for use as a superconductor. The thermal and mechanical treatments that optimize such superconductors were described by McInturff and Chase.<sup>4</sup> The specimen with {100} surfaces was 0.5 cm by 1.0 cm by 1.0 cm, while the three off-axis specimens had thicknesses of 5 mm, 3 mm, and 2 mm. All specimens were ground sufficiently flat and parallel for ultrasonic study.

#### B. Procedures

Eighteen different ultrasonic-wave modes could be studied in these four specimens. All eighteen were examined at room temperature using the following procedure. Quartz-crystal transducers either 9.5 mm or 6.4 mm in diameter with fundamental resonance

---

\*A trade name is used to describe the studied material; its use is not an NBS endorsement of the product.

frequencies between 5 and 10 MHz were bonded to one sample surface with phenyl salicylate (salol). Ultrasonic pulses were generated and detected in the transducer using an electronic apparatus described previously.<sup>5</sup> The time interval between the arrival of selected pulses from the ultrasonic echo train was measured using an oscilloscope with a delaying time base calibrated against a precision time-mark generator. The ultrasonic echo patterns obtained in this study were of good quality. They had three to thirty well-defined echoes.

Using the velocity  $v$  of the ultrasonic wave obtained from the transit time and the path length and the specimen mass density  $\rho$  the room-temperature elastic constants were calculated using the relationship

$$C = \rho v^2 \quad (10)$$

a simplified form of Eq. (2), where  $C$  is a combination of the  $C_{ij}$ 's depending on the mode. Results derived from Eq. (2) for the eighteen modes studied here are given in Table 1.

Resonant-bar elastic-constant measurements were performed on two other specimens at room temperature. These specimens were 4.8 mm diameter cylinders with lengths of 1.9 cm and 3.1 cm prepared with filaments along the specimen axis.

In the resonant-bar technique, the sample is excited into longitudinal or torsional resonance by an attached quartz-crystal driver of appropriate mode and frequency. Resonance is detected using a quartz gauge crystal attached to the driver. The driver, gauge, and specimen form a composite oscillator. The appropriate elastic constant of the specimen can be calculated from the resonant frequency of the composite oscillator, the

specimen density, and known properties of the driver and gauge crystals. Since the composite-oscillator resonant frequency is often tens of kilohertz, this technique is sometimes called a kilohertz technique. But, in the literature it is called a composite-oscillator technique.<sup>6</sup>

### C. Uncertainties

Experimental uncertainties of the elastic constants are discussed in two parts: imprecision and systematic error. Imprecisions affect many conclusions of the study. Systematic errors do not; they affect slightly only the  $C_{ij}$ 's themselves.

Bounds on the  $C_{ij}$ 's in Table I are imprecisions expressed as  $\pm \sigma$ , where  $\sigma$  is the standard deviation based on a normal distribution. For the diagonal  $C_{ij}$ 's, these imprecisions are based on two to five pure-mode measurements. Imprecisions of the non-diagonal  $C_{ij}$ 's depend both on these values and on an assumed imprecision of 0.005 in the quasi-transverse values of  $\rho v^2$ . Sources of imprecision include: deviations of specimens from flat and parallel, specimen-length mismeasurement, specimen-to-specimen bond variations, transit-time mismeasurement, and, for this material, specimen inhomogeneity.

There are two principal systematic errors, one arising from the mass density and one from the transducer-bond coupling to the specimen. Maximum error in the mass density is estimated

to be less than 0.15 percent. Transit-time error due to the ultrasonic wave traveling through the transducer and the coupling agent is estimated to be less than one percent; and, when corrected for, increases the  $\rho v^2$  values. Thus, the overall uncertainty in the  $C_{ij}$ 's is estimated to be less than  $\pm 1.5$  percent.

A possible source of sample-to-sample variation in the elastic constants of any composite material is its thermal-mechanical treatment, which may vary considerably for the type of material reported on here. For example, for copper, elastic-constant differences up to ten percent have been reported for annealed and deformed specimens.<sup>7</sup> Such variations can also occur in copper-base composites. Residual stresses of the order of the yield strength may occur in the composite, but simple computations show that these would change the elastic constants by less than one percent.

#### IV. RESULTS

Results of the study are displayed in the first four tables. In Table I, the observed room-temperature values of  $\rho v^2$  are given for eighteen measurement modes. This table also contains expressions for the  $\rho v^2$  in terms of the  $C_{ij}$ 's. These expressions were derived from the Christoffel equations. When a  $\pm$  sign occurs, the + sign corresponds to the longitudinal mode, and the - sign corresponds to the transverse mode. Estimated errors for the derived elastic constants are also in Table I. The basis for estimating these errors was described above.

Results of the resonance studies are in Table II.  $S_{33}$  is the reciprocal Young's modulus along the filament direction, and  $\frac{1}{2}(S_{44} + S_{55})$  is the reciprocal torsion (or shear) modulus around that direction.

The elastic compliances, the  $S_{ij}$ 's, are in Table III along with a summary of the  $C_{ij}$  data. The  $S_{ij}$ 's were determined by inverting the  $C_{ij}$  matrix displayed in Eq. (1) and substituting the  $C_{ij}$  values from Table I. Except for  $S_{44}$ ,  $S_{55}$ , and  $S_{66}$ , which are simple reciprocals of the corresponding  $C_{ij}$ 's, errors in the  $S_{ij}$ 's are larger than those in the  $C_{ij}$ 's because of error accumulation.

The practical elastic constants ( $E$  = Young's modulus,  $G$  = shear modulus, and  $\nu$  = Poisson's ratio) are given in Table IV. These parameters are related to the  $S_{ij}$ 's displayed in the matrix equation:

$$S_{ij} = \begin{bmatrix} 1/E_{11} & -\nu_{21}/E_{22} & -\nu_{31}/E_{33} & 0 & 0 & 0 \\ & 1/E_{22} & -\nu_{32}/E_{33} & 0 & 0 & 0 \\ & & 1/E_{33} & 0 & 0 & 0 \\ & & & 1/G_{44} & 0 & 0 \\ & & & & 1/G_{55} & 0 \\ & & & & & 1/G_{66} \end{bmatrix} \quad (11)$$

where the Poisson ratios are defined

$$\nu_{ij} = -S_{ij}/S_{ii} \text{ (no sum)} \quad (12)$$

and the  $S_{ij}$  matrix is symmetrical about its main diagonal.



## V. DISCUSSION

### A. Symmetry

On the basis of its internal and external geometry, the composite appears to be orthorhombic. If an object has three mutually perpendicular two-fold axes, then it belongs to the orthorhombic symmetry system. These rotation axes are labeled  $x$ ,  $y$ , and  $z$  in Figs. 1 and 2.

Other possible symmetry systems can be excluded. Triclinic has no symmetry axis. Monoclinic has a single two-fold axis. Trigonal has a single three-fold axis. Clearly, these three systems are less symmetrical than the composite.

Orthorhombic symmetry includes four other symmetry systems: tetragonal, hexagonal, cubic, and isotropic. Relationships among the  $C_{ij}$ 's for these systems are listed in Table V together with tests of the relationships. Clearly, from Table V, none of the higher-symmetry systems can be used to describe exactly the observed  $C_{ij}$ 's. But the deviations are small for any of these four symmetry choices. Tetragonal is a slightly better choice than hexagonal. The advantage of describing an object by its highest symmetry is that there are fewer independent elastic constants: six for tetragonal, five for hexagonal, three for cubic, and two for isotropic. Thus, measurements and calculations are simplified to various degrees. In Table IV, the present orthorhombic results are also expressed in higher-symmetry co-ordinates to facilitate comparisons with other studies. When necessary, elastic constants were simply averaged.

### B. Off-Diagonal Elastic Constants

The off-diagonal ( $i \neq j$ ) elastic constants are more difficult to determine and almost always have higher uncertainties than the diagonal ( $i = j$ ) elastic constants. This problem is reflected in



the present study in Table I. The problem arises because the off-diagonal elastic constants are not related simply to any pure mode of mechanical deformation. This is best shown in the  $S_{ij}$  matrix displayed in Eq. (11). All the diagonal  $S_{ij}$ 's are related reciprocally to either a Young's modulus or to a shear modulus. But all the off-diagonal terms are related to a Young's modulus and a Poisson's ratio, which is in turn determined by two other elastic constants, as shown in Eq. (12).

In the present study, another difficulty arose in determining the off-diagonal elastic constants. As shown in Table I, different values of the off-diagonal  $C_{ij}$ 's were obtained depending on whether the observed  $pv_\ell^2$  or the observed  $pv_t^2$  were substituted into the  $C_{ij}$  expressions given in the table. For example, in the [011] direction the quasi-transverse datum gave  $C_{23} = 0.715$  while the quasi-longitudinal datum gave  $C_{23} = 1.041$ . The  $C_{12}$  and  $C_{13}$  cases are similar. On the basis of small imprecisions of the measurements, and on the basis of the correctness of the value of the third (pure shear) mode, it seemed that the off-diagonal terms should be less uncertain than this and that one of the two values was perhaps correct.

To resolve this uncertainty in the off-diagonal elastic constants, an independent experiment was done. Some of the  $S_{ij}$ 's were determined by a resonance method. Dilatational and shear modes were measured on a cylindrical specimen with filaments along the cylinder axis. Results shown in Table II for the torsional mode  $\frac{1}{2}(S_{44} + S_{55})$  agree exactly with the value calculated from the  $C_{ij}$ 's. (The  $S_{ij}$ 's are computed from the  $C_{ij}$ 's by inverting the  $C_{ij}$  matrix.) Similarly, exact agreement is also obtained for the dilatational mode,  $S_{33}$ , if the  $C_{ij}$  data from quasi-transverse modes rather than quasi-longitudinal modes are used. Thus, it was concluded that the quasi-transverse velocity data are both correct and consistent with other

data. However, the quasi-longitudinal wave velocities are low by about five percent. This slowing can be interpreted as a longer path length in the specimen due to interactions between the quasi-longitudinal waves and internal boundaries due to the presence of filaments.

#### C. Comparison with Copper

It is useful to compare the elastic constants of the composite with those of the matrix material, unalloyed copper,<sup>7</sup> to determine the effects of the filaments. Comparative data are shown in Table IV. Both the Young's moduli and the shear moduli of the composite are about fifteen percent lower than those of copper. The compressibility

$$K = \frac{1}{9} \sum_{i,j=1,3} S_{ij} \quad (13)$$

of the composite is about five percent higher. The off-diagonal  $C_{ij}$ 's are identical to the value for copper, within one percent. This result is quite unexpected. And it may be accidental since it has no obvious physical interpretation.

#### D. Comparison with Previous Studies

The elastic constants of this composite were measured by Sun and Gray<sup>8</sup> using static methods, assuming hexagonal symmetry. Their results are shown in Table IV. Considering the higher inaccuracies usually associated with static methods, the agreement between the two sets of data is good. The static Young's and shear moduli are up to nine percent higher than the values reported here. The largest discrepancy is in  $\nu_{21}$  and is due probably to error accumulation in the computed static value. Possibly, the differences in the two data sets are real, but this cannot be decided without knowing the uncertainties of the static values. A real

difference is, however, unlikely because, ignoring dispersion effects, dynamic elastic moduli are almost always higher than static elastic moduli, and the opposite effect is observed in this case.

#### E. Dispersion

No dispersion effects were observed, either in the limited 5-10 MHz region that was studied or in comparing the MHz pulse data with the 60 kHz resonance data. By dispersion is meant the dependence of sound velocity on frequency. Dispersive effects have been reported in many composite materials; they are usually due to either relaxation or resonance effects. Their absence here is attributed to coherent interfaces between the filaments and the matrix and to the small difference in acoustic impedance between the filaments and the matrix. Absence of dispersion is also consistent with the well-defined echo patterns that were obtained.

#### F. Relationship to Similar Composites

Elastic-property data have not been reported for NbTi/Cu composites with different ratios of NbTi or with different thermal-mechanical treatments. The present data can be applied to other NbTi/Cu composites through predictive schemes that relate the elastic constants of a composite to those of its components. Using the values of the NbTi elastic constants given by Sun and Gray<sup>8</sup> and formulas summarized by them, it follows that the present material obeys approximately simple rules of mixtures. Thus, similar composites would also be expected to follow these rules approximately. The present study is a useful guide to the elastic properties of any NbTi/Cu composite, but it is a source of exact elastic data only for the particular material studied. Even when the filament matrix volume ratio is adjusted for, several other variables remain that can affect elastic properties. These include: the state of mechanical deformation

(the number and distribution of lattice defects), composition of the NbTi filaments, preferred orientations in either the filaments or the matrix, and degree of coherency of the filament-matrix interfaces.

#### G. Low-Temperature Elastic Constants

Since this composite is intended for use as a superconductor, its low-temperature elastic properties are important. Studies down to liquid-helium temperature are underway in our laboratory, and results will be reported subsequently. Preliminary results are that the composite behaves on cooling approximately like unalloyed copper. But the magnitudes of the elastic constant changes are slightly different, and there are some anomalous effects that are both reproducible and reversible.

## VI. CONCLUSIONS

The chief conclusions of this study are:

(1) Ultrasonic (5-10 MHz) waves, both dilatational and shear, can be propagated in an NbTi/Cu composite in directions parallel, perpendicular, and oblique to the filaments.

(2) Except as noted below, usual single-crystal elasticity techniques could be used to establish the complete set of elastic constants of the composite.

(3) Longitudinal waves propagated obliquely to  $\langle 100 \rangle$  directions had velocities about five percent lower than expected. Obliquely propagated shear waves traveled with their expected velocities.

(4) The studied composite has orthorhombic symmetry, and, therefore, nine independent elastic constants. But the deviations from isotropy are small.

(5) Compared to copper, the  $C_{ij}$  ( $i = j$ ) of the composite are lower by about seven percent for  $C_{11}$ ,  $C_{22}$ , and  $C_{33}$ , and by about fifteen percent for  $C_{44}$ ,  $C_{55}$ , and  $C_{66}$ . But the  $C_{ij}$  ( $i \neq j$ ) are about the same. The composite's compressibility is about five percent higher than copper's.

(6) The present dynamic results agree reasonably well with existing static measurements.

(7) Advantages of combining pulse-echo measurements and resonance measurements were found.

(8) No dispersion, change of velocity with frequency, was observed.

## ACKNOWLEDGMENT

This study was supported by the Advanced Research Projects Agency of the U.S. Department of Defense. G. A. Miranda of Los Alamos kindly contributed a photomicrograph of the studied material. W. H. Gray of Oak Ridge National Laboratory contributed a critical reading of the manuscript.



## REFERENCES

1. L. D. Landau and E. M. Lifshitz, Theory of Elasticity (Pergamon, London, 1959), p. 104.
2. J. R. Neighbors and G. E. Schacher, J. Appl. Phys. 38, 5366-5375 (1967).
3. M. J. P. Musgrave, Crystal Acoustics (Holden-Day, San Francisco, 1970), p. 117-123.
4. A. D. McInturff and G. G. Chase, J. Appl. Phys. 44, 2378-2384 (1973).
5. E. R. Naimon, W. F. Weston, and H. M. Ledbetter, Cryogenics 14, 246-249 (1974).
6. J. Marx, Rev. Sci. Instrum. 22, 503-509 (1951).
7. H. M. Ledbetter and E. R. Naimon, J. Phys. Chem. Ref. Data 3 897-935 (1974).
8. C. T. Sun and W. H. Gray, Sixth Symp. Engrng. Probs. Fusion Res., San Diego, CA, Nov. 1975.



Table I. Room-temperature elastic constants  $C_{ij}$  for an NbTi/Cu composite with macroscopic orthorhombic symmetry. The wave-front normal is denoted by  $\underline{n}$ , and the displacement direction by  $\underline{p}$ . Both  $\rho v^2$  and  $C_{ij}$  have units of  $10^{11}$  N/m<sup>2</sup>. Impure modes are denoted by asterisks. Daggers indicate values discarded for reasons discussed in text.

Specimen	Measurement Number	$\underline{n}$	$\underline{p}$	$\rho v_{\ell}^2$	$\rho v_t^2$	$C_{ij}$	Derived $C_{ij}$
A	1	100	100	1.834		$C_{11}$	$C_{11}=1.834\pm0.005$
	2		010		0.404	$C_{66}$	$C_{66}=0.414\pm0.007$
	3		001		0.407	$C_{55}$	$C_{55}=0.407\pm0.011$
	4	010	010	1.878		$C_{22}$	$C_{22}=1.878\pm0.015$
	5		100		0.413	$C_{66}$	
	6		001		0.413	$C_{44}$	$C_{44}=0.416\pm0.003$
	7	001	001	1.880		$C_{33}$	$C_{33}=1.880\pm0.002$
	8		100		0.414	$C_{55}$	
	9		010		0.419	$C_{44}$	
B	10	011	011*	1.713		$\left\{ \begin{array}{l} 1/2\{C_{22}+C_{33}+[(C_{22}-C_{33})^2+4(C_{23}+C_{44})^2]^{1/2}\}+C_{44} \\ 1/2\{C_{22}+C_{33}-[(C_{22}-C_{33})^2+4(C_{23}+C_{44})^2]^{1/2}\}+C_{44} \end{array} \right\}$	$(C_{23}=0.715)^{\dagger}$
	11		011*		0.419		$C_{23}=1.041\pm0.040$
	12		100		0.407	$1/2(C_{55}+C_{66})$	
C	13	101	101*	1.740		$\left\{ \begin{array}{l} 1/2\{C_{11}+C_{33}+[(C_{11}-C_{33})^2+4(C_{13}+C_{55})^2]^{1/2}\}+C_{55} \\ 1/2\{C_{11}+C_{33}-[(C_{11}-C_{33})^2+4(C_{13}+C_{55})^2]^{1/2}\}+C_{55} \end{array} \right\}$	$(C_{13}=0.809)^{\dagger}$
	14		101*		0.409		$C_{13}=1.039\pm0.040$
	15		010		0.408	$1/2(C_{44}+C_{66})$	
D	16	110	110*	1.744		$\left\{ \begin{array}{l} 1/2\{C_{11}+C_{22}+[(C_{11}-C_{22})^2+4(C_{12}+C_{66})^2]^{1/2}\}+C_{66} \\ 1/2\{C_{11}+C_{22}-[(C_{11}-C_{22})^2+4(C_{12}+C_{66})^2]^{1/2}\}+C_{66} \end{array} \right\}$	$(C_{12}=0.804)^{\dagger}$
	17		110*		0.400		$C_{12}=1.056\pm0.040$
	18		001		0.394	$1/2(C_{44}+C_{55})$	

Table II. Elastic compliances of an NbTi/Cu composite measured by a resonance method. Units are  $10^{-11} \text{ m}^2/\text{N}$ .

$S_{ij}$	Observed	Calculated from $C_{ij}$
$S_{33}$	$0.873 \pm 0.009$	$0.878 \pm 0.073$ from quasi-shear modes (0.692 from quasi-longitudinal modes)
$\frac{1}{2} (S_{44} + S_{55})$	$2.398 \pm 0.024$	$2.430 \pm 0.041$

Table III. Room-temperature elastic stiffnesses  $C_{ij}$  and elastic compliances  $S_{ij}$  of an NbTi/Cu composite and copper.  $C_{ij}$  units are  $10^{11} \text{ N/m}^2$ ;  $S_{ij}$  units are  $10^{-11} \text{ m}^2/\text{N}$ . Values in parentheses are derived from  $2C_{44} = C_{11} - C_{12}$  and  $S_{44} = 2(S_{11} - S_{12})$ .

ij	Composite		Copper <sup>a</sup>	
	$C_{ij}$	$S_{ij}$	$C_{ij}$	$S_{ij}$
11	1.834	0.924	2.006	0.780
22	1.878	0.894		
33	1.880	0.879		
44	0.416	2.404	0.477	2.096
55	0.407	2.457		
66	0.414	2.415		
12	1.056	-0.341	(1.052)	(-0.268)
13	1.039	-0.322		
23	1.041	-0.307		

<sup>a</sup> Ref. 7

Table IV. Practical elastic constants  $E$  = Young's modulus,  $G$  = shear modulus,  $\nu$  = Poisson's ratio for NbTi/Cu composite in different co-ordinate systems at room temperature. Units are  $10^{11}$  N/m<sup>2</sup>, except  $\nu$ 's, which are dimensionless.

Elastic Constant	Orthorhombic Basis	Tetragonal Basis	Hexagonal Basis	Isotropic Basis	Copper <sup>a</sup> Values	Static Results <sup>b</sup> (Hexagonal Basis)
$E_{11}$	1.082	1.100	1.100	1.112	1.282	1.22
$E_{22}$	1.119					
$E_{33}$	1.138	1.138	1.138			1.19
$G_{44}$	0.416	0.411	0.411	0.412	0.477	0.448
$G_{55}$	0.407					
$G_{66}$	0.414	0.414	(0.398) <sup>c</sup>			(0.431)
$\nu_{21}$	0.381	0.381	0.381			(0.415) <sup>c</sup>
$\nu_{31}$	0.365	0.357	0.357			0.347
$\nu_{32}$	0.349					

<sup>a</sup> Ref. 7

<sup>b</sup> Ref. 8

<sup>c</sup> Quantities in parentheses are derived from given data using  $G_{66} = E_{11}/2(1 + \nu_{12})$ .

Table V. Checks for various symmetries for NbTi/Cu composite. For hexagonal and cubic cases, relationships (1), (2), and (3) also hold. For isotropic case, all eight relationships must hold; either number (4) or (8) is redundant.

Symmetry System	Relationships	Ratio of L.H.S./R.H.S. for NbTi/Cu
Tetragonal	(1) $C_{22} = C_{11}$	$1.024 \pm 0.020$
	(2) $C_{55} = C_{44}$	$0.978 \pm 0.014$
	(3) $C_{23} = C_{13}$	$1.002 \pm 0.040$
Hexagonal	(4) $C_{66} = \frac{1}{2} (C_{11} - C_{12})$	$1.064 \pm 0.020$
Cubic	(5) $C_{33} = C_{11}$	$1.025 \pm 0.007$
	(6) $C_{12} = C_{13}$	$1.016 \pm 0.040$
	(7) $C_{66} = C_{55}$	$1.017 \pm 0.018$
Isotropic	(8) $C_{44} = \frac{1}{2} (C_{11} - C_{12})$	$1.069 \pm 0.016$

## LIST OF FIGURES

- Fig. 1. Schematic geometries of four pulse specimens. Filaments along  $[001]$  are indicated by striping. The wave-propagation directions (indicated by dashed lines) and displacement vectors are given in Table I. The  $x$ ,  $y$ , and  $z$  axes are equivalent to the  $[001]$ ,  $[010]$ , and  $[001]$  axes that are used in the text and tables.
- Fig. 2. Photomicrograph showing distribution of filaments. Plane of photo is perpendicular to filaments. Width shown corresponds to 4.3 mm in specimen. Vertical direction is  $x = [100]$  and horizontal direction is  $y = [010]$ .

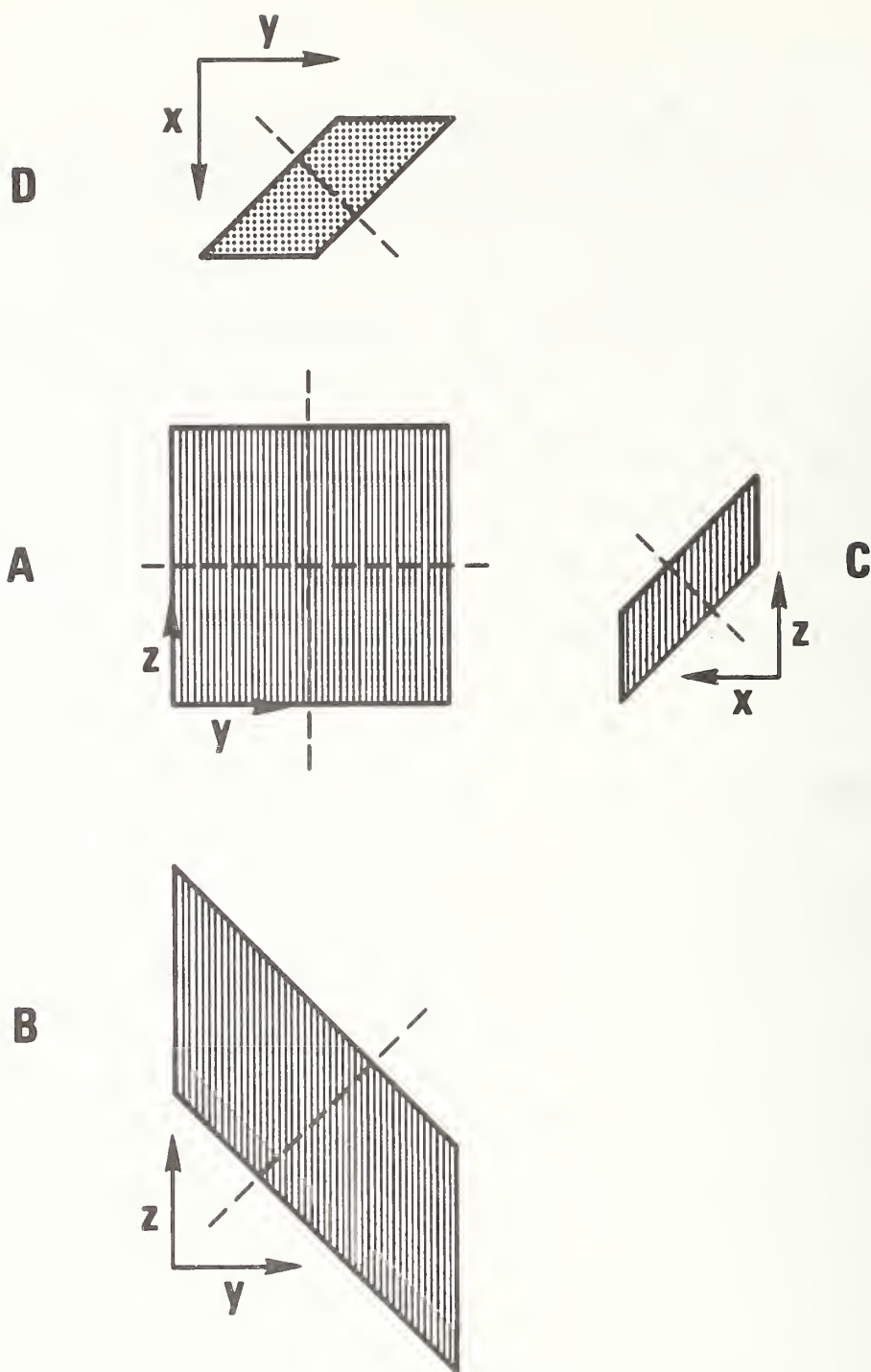


Fig. 1. Schematic geometries of four pulse specimens. Filaments along  $[001]$  are indicated by striping. The wave-propagation directions (indicated by dashed lines) and displacement vectors are given in Table I. The  $x$ ,  $y$ , and  $z$  axes are equivalent to the  $[001]$ ,  $[010]$ , and  $[001]$  axes that are used in the text and tables.



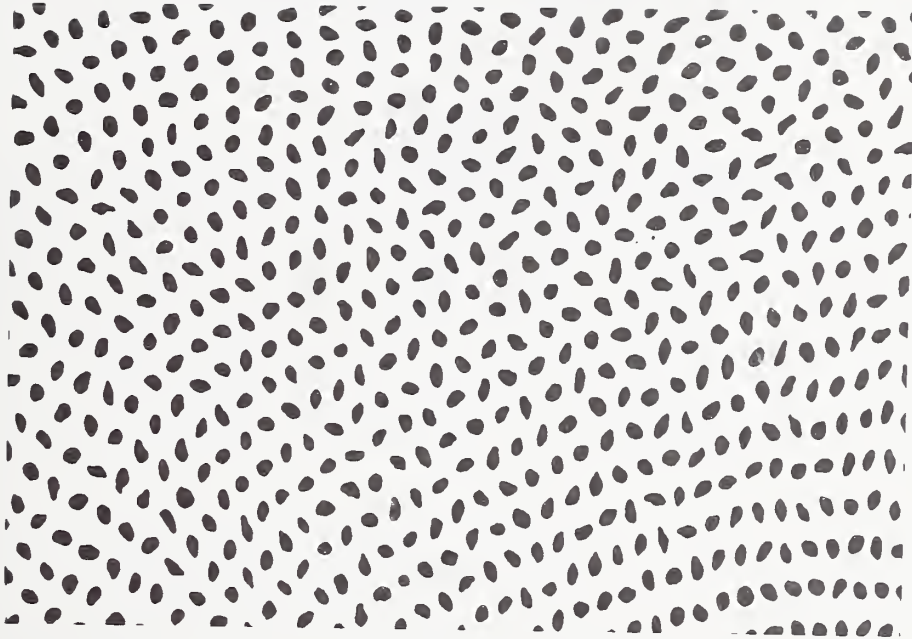


Fig. 2. Photomicrograph showing distribution of filaments. Plane of photo is perpendicular to filaments. Width shown corresponds to 4.3 mm in specimen. Vertical direction is  $x = [100]$  and horizontal direction is  $y = [010]$ .

TEMPERATURE DEPENDENCE OF THE ELASTIC CONSTANTS OF  
AN NbTi/Cu SUPERCONDUCTING COMPOSITE\*

D. T. Read\*\* and H. M. Ledbetter

Cryogenics Division  
Institute for Basic Standards  
National Bureau of Standards  
Boulder, Colorado 80302

ABSTRACT

Low-temperature elastic properties are reported for a commercial superconducting composite consisting of niobium-titanium filaments in a copper matrix. Both an ultrasonic (10 MHz) pulse-superposition technique and a composite oscillator (100 kHz) technique were used. Seven of the nine independent elastic constants of this material were determined between 76 and 300 K; and two, the Young's modulus along the filament axis and a shear modulus perpendicular to that axis, were determined between 4 and 300 K. All these elastic-stiffness constants are about ten percent lower than the corresponding values for copper. All increase about ten percent on cooling from 300 to 4 K. And all have anomalous temperature behavior.

Keywords: Bulk modulus; composite; compressibility; copper; cryogenic temperatures; elastic constants; niobium-titanium; Poisson's ratio; shear modulus; superconductor; Young's modulus.

\* Contribution of NBS, not subject to copyright.

\*\*NRC-NBS Postdoctoral Research Associate, 1975-76.

## INTRODUCTION

Superconducting composites consisting of niobium-titanium filaments in a copper matrix are now available commercially for applications in which high electrical-current density must be obtained in high magnetic fields. Components containing these conductors are designed critically. Elastic constants of such conductors are useful for two reasons: for computing the recoverable deflections due to applied loads, and for computing thermoelastic stresses due to either temperature changes or differential thermal contractions. Also, elastic constants provide a valuable characterization of a material. For composite materials, accurate elastic data provide key tests for theories that relate macroscopic elastic properties to elastic properties of constituents.

The particular NbTi/Cu composite reported on here has orthorhombic symmetry, and the room-temperature values of all nine independent elastic constants, the  $C_{ij}$ 's, were reported previously.<sup>1</sup> The temperature dependencies to 77 K of seven of these nine were determined in the present study:  $C_{11}$ ,  $C_{22}$ ,  $C_{33}$ ,  $C_{55}$ ,  $C_{66}$ ,  $E_{33}$ , and  $2/(S_{44} + S_{55})$ , where  $E_{33}$  is Young's modulus along the filament axis and  $2/(S_{44} + S_{55})$  is the torsion modulus about that axis. Two elastic constants,  $E_{33}$  and  $C_{66}$ , were determined to 4 K. The temperature dependencies of the other elastic constants, such as  $C_{12}$  and  $C_{13}$ , were not determined because they are not measured directly and they have larger errors. Symmetries discussed here are strictly macroscopic. The filament direction of the composite is designated [001], and the principal directions perpendicular to the filaments are [100] and [010]. These directions are indicated in Fig. 1.

## EXPERIMENTAL

### A. Material

Specimens were cut from a short section of Kryo 210\* superconductor supplied by Magnetics Corporation of America. This is a copper-matrix, niobium-titanium-filament composite material. The Cu/NbTi volume ratio is 6:1, and the bar contains 2640 filaments with a twist pitch of 7.6 cm. The section obtained for this study was about 20 cm long, 1.0 cm wide, and 0.5 cm thick. Four specimens were cut for ultrasonic pulse measurements, one with its surfaces perpendicular to the symmetry axes of the material and three with their largest surface oriented at 45° to two symmetry axes. Specimen geometries are shown in Fig. 1. The material was studied in the as-received condition. The thermal and mechanical treatments of such superconductors during manufacture were described by McInturff and Chase.<sup>2</sup> The specimen with {100} surfaces was 0.5 cm by 1.0 cm by 1.0 cm, while the three off-axis specimens had thicknesses of 5 mm, 3 mm, and 2 mm. All specimens were ground sufficiently flat and parallel for ultrasonic study.

Two composite-oscillator specimens were prepared. These were right-circular cylinders 4.8 mm in diameter and 3.1 and 1.9 cm long for the extensional and torsional measurements, respectively.

---

\* A trade name is used here to characterize the studied material. Its use is not an NBS endorsement of a particular product.

## B. Procedures

The room-temperature elastic constants of the specimens used in this study were reported previously.<sup>1</sup> The temperature dependence of five of these constants, the elastic stiffnesses  $C_{11}$ ,  $C_{22}$ ,  $C_{33}$ ,  $C_{55}$ , and  $C_{66}$ , were measured using a pulse-superposition technique in which the ratio of the ultrasonic velocity,  $v$ , at low temperatures to its value at room temperature was measured every five degrees between room temperature and the lowest temperature obtained during each cooling. These ratios of sound velocities were used to calculate the temperature dependence of the appropriate elastic constant,  $C$ , from  $C = \rho v^2$  where  $\rho$  is the mass density of the specimen. Each sample was cooled by enclosing it in a sample chamber and lowering it gradually into the ullage of a dewar containing either liquid nitrogen or liquid helium. The low-temperature apparatus and techniques were described previously.<sup>3</sup>

The temperature dependencies of the Young's modulus and the torsional modulus were measured using a composite-oscillator technique. Briefly, the resonant frequency is measured of a composite oscillator consisting of the specimen, a quartz-crystal driver, and a quartz-crystal gauge. This composite oscillator is also cooled by putting it in a sample holder and inserting the specimen end into the ullage of a dewar containing either liquid nitrogen or liquid helium. The resonant frequency of the specimen is calculated from the resonant frequency of the composite oscillator, the masses and geometries of the specimen and the sample, and known properties of the gauge and quartz crystals. From its resonant frequency, the elastic constant of the sample can be calculated easily. The apparatus and techniques used in such measurements were described previously.<sup>4</sup>



## RESULTS

The measured value of  $E_{33}$  (Young's modulus along the filament direction) for the NbTi/Cu composite is shown in Fig. 2. Young's modulus,  $E$ , of polycrystalline copper is shown for comparison.<sup>5</sup> Young's modulus of the composite is about ten percent lower than that of copper, and it rises with decreasing temperature to a value at 4 K about ten percent above its room-temperature value. Irregularities in the curve for the composite are not observed in copper, and they are significant deviations from the temperature dependence of Young's modulus for ordinary materials, of which copper is a good example. The upturn in the curve below 20 K is believed to be a real effect.

The value of  $2/(S_{44} + S_{55})$ , the modulus of torsion about the filament axis, is shown in Fig. 3. Shown also is the torsional or shear modulus,  $G$ , of copper. It is clear that the temperature behavior of  $2/(S_{44} + S_{55})$  is dissimilar to the of  $E_{33}$ , and that its approximate relationship to the torsional modulus of copper is nearly the same as the relationship of  $E_{33}$  to the Young's modulus of copper. The dashed part of the curve is an extrapolation based on the usual behavior of elastic constants at low temperatures and the behavior of the elastic constants of this composite that were measured to 4 K.

The Poisson ratios of this composite material that relate the strain along the filament axis (produced by a stress along that axis) to the strains perpendicular to the axis were found to be 0.366 and 0.349 along the x and y axes respectively at room temperature.<sup>1</sup> The temperature dependencies of these ratios are not easily measured by dynamic techniques, and they were not measured in this study. However, since Poisson's ratio for copper decreases by two percent on cooling



of the composite are intermediate between those of the two copper moduli. Based on simple rule-of-mixture arguments it follows from Fig. 6 that the shear modulus of NbTi must increase with temperature similar to copper, but the longitudinal modulus of NbTi must increase considerably more than that of copper.

## DISCUSSION

In a previous study,<sup>1</sup> it was shown that the room-temperature magnitudes of the elastic constants of this composite can be predicted approximately from a rule of mixtures from the known elastic constants of copper and NbTi. It was also shown that the observed values of the practical elastic constants  $E_{33}$  and  $2/(S_{44} + S_{55})$  were consistent with the measured values of the elastic stiffnesses, the  $C_{ij}$ 's.

Rules of mixtures could not be used to predict the temperature dependence of the composite material studied here because the temperature dependencies of the elastic constants of the niobium-titanium alloy have not been reported. An attempt to obtain such data failed.<sup>6</sup>

Weston<sup>7</sup> reported the temperature dependencies of the elastic constants of an NbTiCu/fiberglass-epoxy coil composite. Although that composite included fiberglass and epoxy, the temperature dependence of its elastic constants reflects that of the NbTi/Cu part, because the stiffness of the fiberglass-epoxy is low and it constitutes only about one-fourth the total volume. The sign and magnitude of the temperature dependencies observed by Weston were about the same as those observed in the present study. For most of the elastic constants, Weston reported very small deviations from the usual temperature behavior of ordinary materials. But, in the Young's modulus along the filaments, Weston found a large deviation from usual temperature behavior. However, none

of the elastic constants of the coil composite studied by Weston showed the type of anomaly observed in the present study.

The observed increase in all the elastic stiffnesses of about ten percent on cooling from 295 K to 4 K is expected for this material. Elastic constants of most metals increase between five and fifteen percent on cooling to zero temperature;<sup>8</sup> the polycrystalline longitudinal modulus  $C_\ell$  of copper increases four percent on cooling. Thus, the sign and magnitude of the observed temperature dependencies of the elastic constants of the NbTi/Cu composite studied here are not surprising.

As shown in Figs. 2-6, all the measured elastic constants reported here have irregular temperature dependencies compared to copper. Experimental evidence for these anomalies is strong: they occur in seven different measured elastic constants; they were observed on measurements made during both heating and cooling; and they occurred in repeated experiments. These anomalies are probably insignificant from the viewpoint of engineering design because they change the elastic constants only a few percent from regular behavior scaled against copper. However, they indicate unexpected behavior of the composite.

The cause of these anomalies is uncertain. Two hypotheses can be suggested. First, since elastic constants are changed by stress, the anomalies may arise from internal-stress changes due to differential thermal contraction during cooling. Second, the anomalies may arise from similar anomalies in the temperature dependencies of the elastic constants of the niobium-titanium filaments. Anomalies similar to those observed here were reported in niobium and in other transition metals, where they are ascribed to the electronic structure,<sup>9,10</sup> and in a niobium-zirconium alloy, where they are attributed to the formation of omega phase.<sup>11</sup>

from 300 to 4 K, a similar change would be expected for Poisson's ratio of the composite.

Attention is now turned from the practical elastic constants to the elastic-stiffness coefficients, the  $C_{ij}$ 's. Although  $C_{11}$ ,  $C_{22}$ , and  $C_{33}$  were all measured, the data for  $C_{22}$  practically coincide with those for  $C_{33}$ , so only  $C_{11}$  and  $C_{33}$ , normalized separately to their 300 K values (given in Table I) are shown in Fig. 4 together with the longitudinal modulus,  $C_\ell$ , of copper. The dashed curves are extrapolations. Again, these elastic constants are about seven percent lower than those of copper, and they increase about five percent on cooling. As in the previous cases of the practical elastic constants, anomalous changes in these elastic constants occur during cooling.

The temperature dependence of  $C_{66}$ , normalized to 300 K, is shown in Fig. 5.  $C_{55}$  was measured between 300 and 76 K; the resulting data nearly coincide with those for  $C_{66}$  and they are not shown.  $C_{55}$  and  $C_{66}$  for the composite material are about fourteen percent lower than the value for copper, and they increase about ten percent on cooling. They also exhibit anomalous temperature behavior. The data point shown as an open square at 4 K in Fig. 5 represents an absolute, rather than a relative, elastic-constant measurement; it confirms the overall elastic-constant change due to cooling.

$C_{33}$  and  $C_{55}$ , a longitudinal and a transverse stiffness of the composite material are shown in Fig. 6 together with  $C_\ell$  and  $C_t$ , the longitudinal and transverse moduli of polycrystalline copper. In both copper and the composite, the transverse (shear) moduli have stronger temperature dependencies than the longitudinal moduli. Surprisingly, the temperature dependencies of both the transverse and longitudinal moduli

## CONCLUSIONS

The following principal results and conclusions emerge from the present study:

(1) The Young's modulus along the filaments,  $E_{33}$ , increases twelve percent on cooling from 300 to 4 K, compared to eight percent for copper. The extrapolated torsional modulus around the filaments,  $G_{\parallel}$ , increases nine percent on cooling, the same as copper.

(2) The extrapolated elastic stiffnesses  $C_{11}$ ,  $C_{22}$ , and  $C_{33}$  increase five percent on cooling, compared to four percent for copper.

(3) The shear elastic constants  $C_{55}$  and  $C_{66}$  increase ten percent on cooling, compared to nine percent for copper.

(4) All measured elastic constants are anomalous in their temperature dependencies.

## ACKNOWLEDGMENT

This study was supported by the Advanced Research Projects Agency of the U.S. Department of Defense.

## REFERENCES

1. H. M. Ledbetter and D. T. Read, submitted for publication.
2. A. D. McInturff and G. G. Chase, J. Appl. Phys. 44, 2378-2384 (1973).
3. E. R. Naimon, W. F. Weston, and H. M. Ledbetter, Cryogenics 14, 246-249 (1974).
4. J. Marx, J. Sci. Instrum. 22, 503-509 (1951).
5. W. C. Overton and J. Gaffney, Phys. Rev. 98, 969-977 (1955).
6. C. N. Reid, J. L. Routbort, and R. A. Maynard, J. Appl. Phys. 44, 1398-1399 (1973).
7. W. F. Weston, J. Appl. Phys. 46, 4458-4465 (1975).
8. R. F. S. Hearmon, in Numerical Data and Functional Relationships in Science and Technology, Group III, Vol. I, K. H. Hellwege and A. M. Hellwege, Eds. (Springer-Verlag, Berlin, 1969).
9. K. J. Carroll, J. Appl. Phys. 36, 3689-3690 (1965).
10. F. H. Featherston and J. R. Neighbors, Phys. Rev. 130, 1324-1333 (1963).
11. C. Goasdue, P. S. Ho, and S. L. Sass, Acta Met. 20, 725-733 (1972).



Table 1. Elastic constants of an NbTi/Cu composite and polycrystalline copper at selected temperatures in units of  $10^{11}$  N/m<sup>2</sup>, except  $\nu$ , which is dimensionless; numbers in parentheses are based on extrapolated data.

	300 K	200 K	100 K	0 K
NbTi/Cu Composite:				
$E_{33}$	1.138	1.189	1.238	1.287
$G_{  }$	0.417	0.427	0.445	(0.454)
$\nu_{31}$	0.365	---	---	---
$\nu_{32}$	0.349	---	---	---
$C_{11}$	1.834	1.865	1.908	(1.915)
$C_{22}$	1.878	1.911	1.952	(1.957)
$C_{33}$	1.880	1.919	1.965	(1.983)
$C_{55}$	0.407	0.418	0.436	(0.442)
$C_{66}$	0.414	0.425	0.442	0.456
Polycrystalline Copper <sup>a</sup> :				
$E$	1.282	1.329	1.369	1.386
$G$	0.477	0.496	0.512	0.519
$\nu$	0.344	0.341	0.339	0.338
$C_{\ell}$	2.006	2.053	2.093	2.111
$C_t$	0.477	0.495	0.511	0.518

<sup>a</sup> Ref. 5, arithmetic average of Hashin-Shtrikman bounds.



## LIST OF FIGURES

- Fig. 1. Schematic geometries of four pulse specimens. Filaments along [001] are indicated by striping. In specimen A, waves were propagated along the [100], and [010] directions; in B along [011]; in C along [101]; and in D along [110].
- Fig. 2. Young's modulus of the composite along [001] compared to the Young's modulus of polycrystalline copper.
- Fig. 3. Shear, or torsional, modulus of the composite around the [001], or filament, axis compared to the shear modulus of polycrystalline copper.
- Fig. 4. Longitudinal elastic stiffnesses of the composite in the [100] and [001] directions compared to the longitudinal elastic modulus of polycrystalline copper.
- Fig. 5. A shear modulus of the composite compared to that of polycrystalline copper.  $C_{66}$  corresponds to the shear resistance on a (100) plane in a [010] direction, or vice versa.
- Fig. 6. Comparison of a longitudinal and a shear elastic constant of the composite.  $C_{33}$  is measured in the [001] direction, along the filament axis.  $C_{55}$  corresponds to the shear resistance on a (100) plane in a [001] direction or of a (001) plane in a [001] direction. Values for copper are shown for comparison.

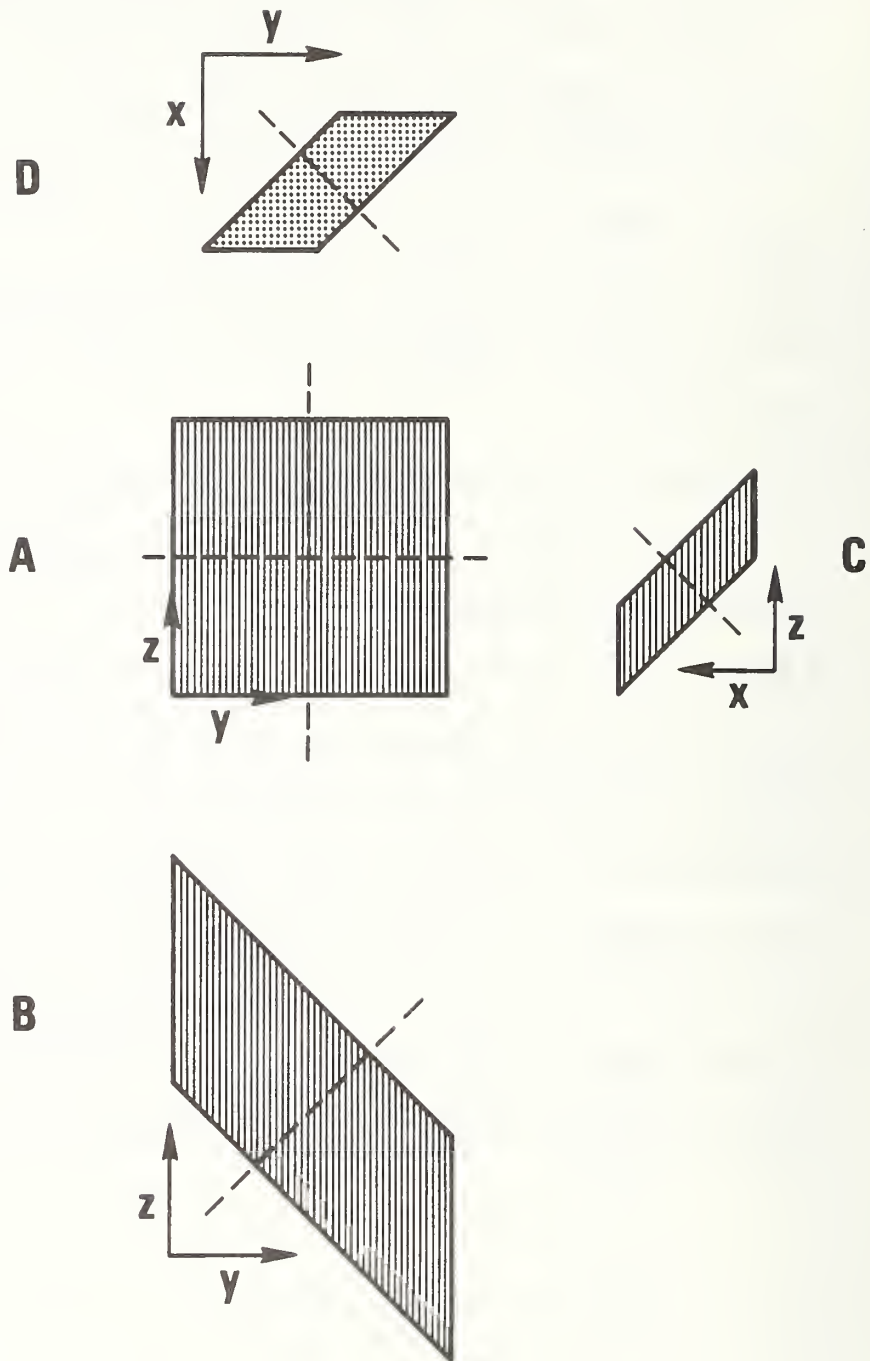


Fig. 1. Schematic geometries of four pulse specimens. Filaments along  $[001]$  are indicated by striping. In specimen A, waves were propagated along the  $[100]$ ,  $[010]$ , and  $[001]$  directions; in B along  $[001]$ ; in C along  $[101]$ ; and in D along  $[110]$ .

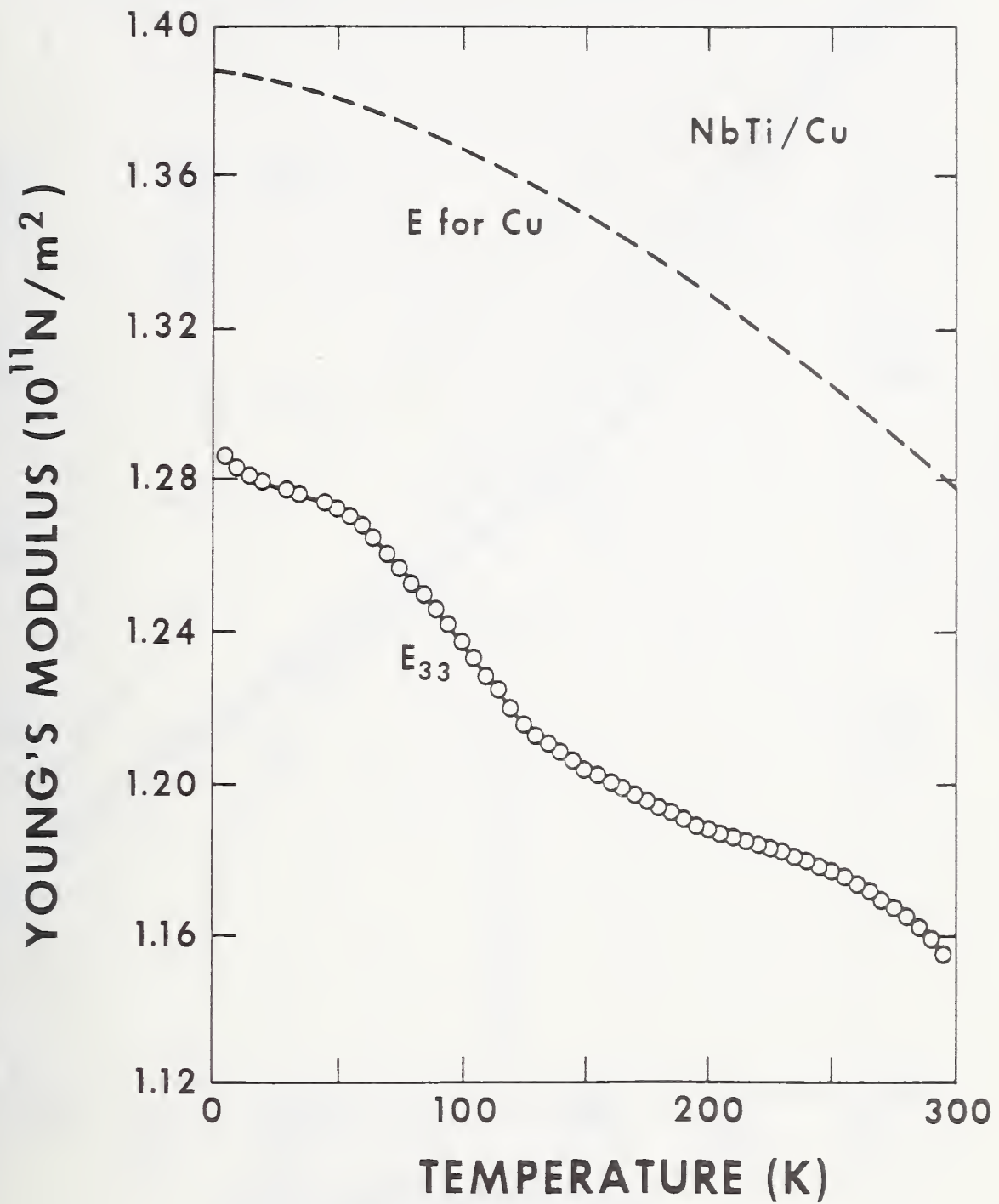


Fig. 2. Young's modulus of the composite along [001] compared to the Young's modulus of polycrystalline copper.

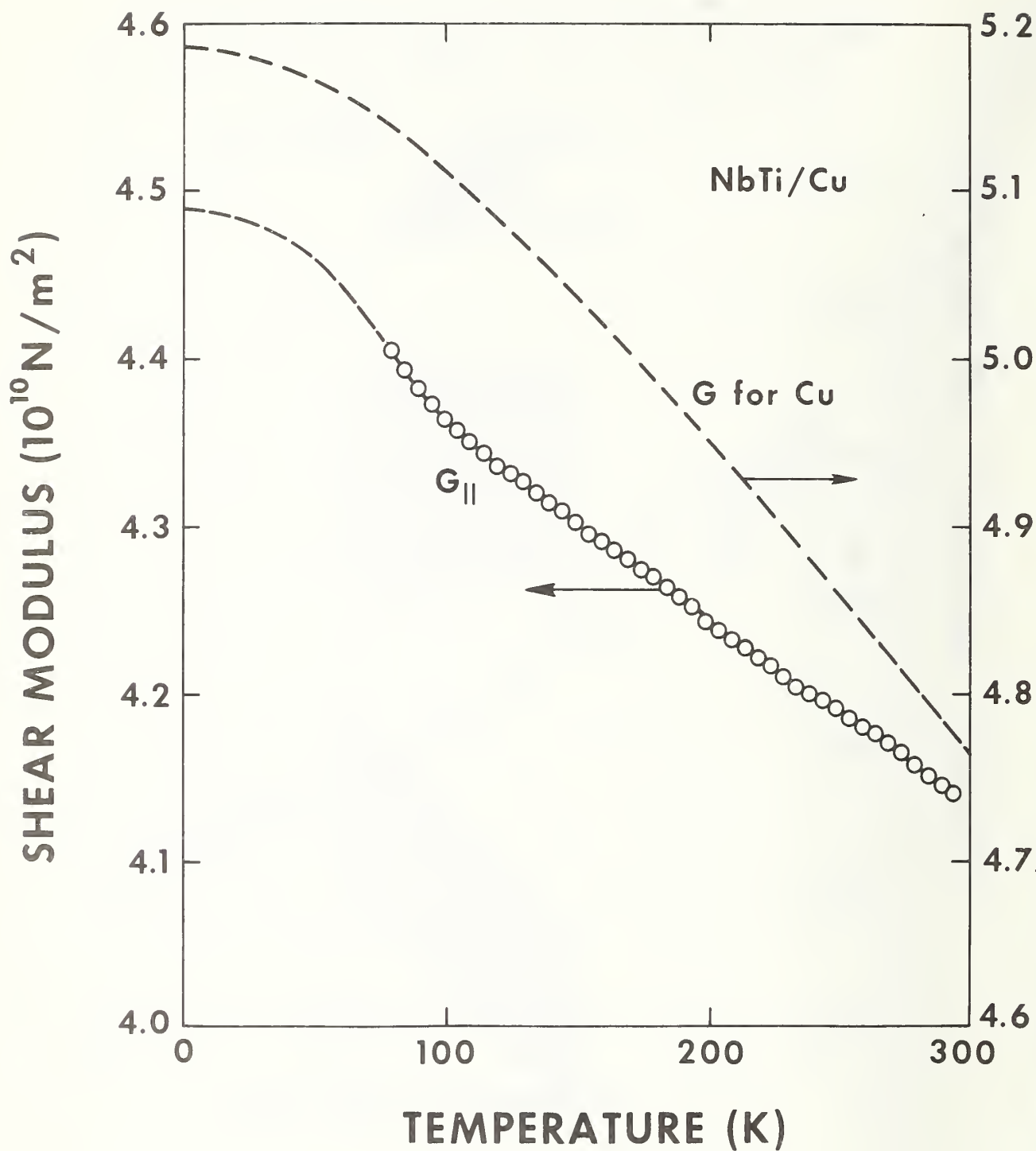


Fig. 3. Shear, or torsional, modulus of the composite around the [001], or filament, axis compared to the shear modulus of polycrystalline copper.

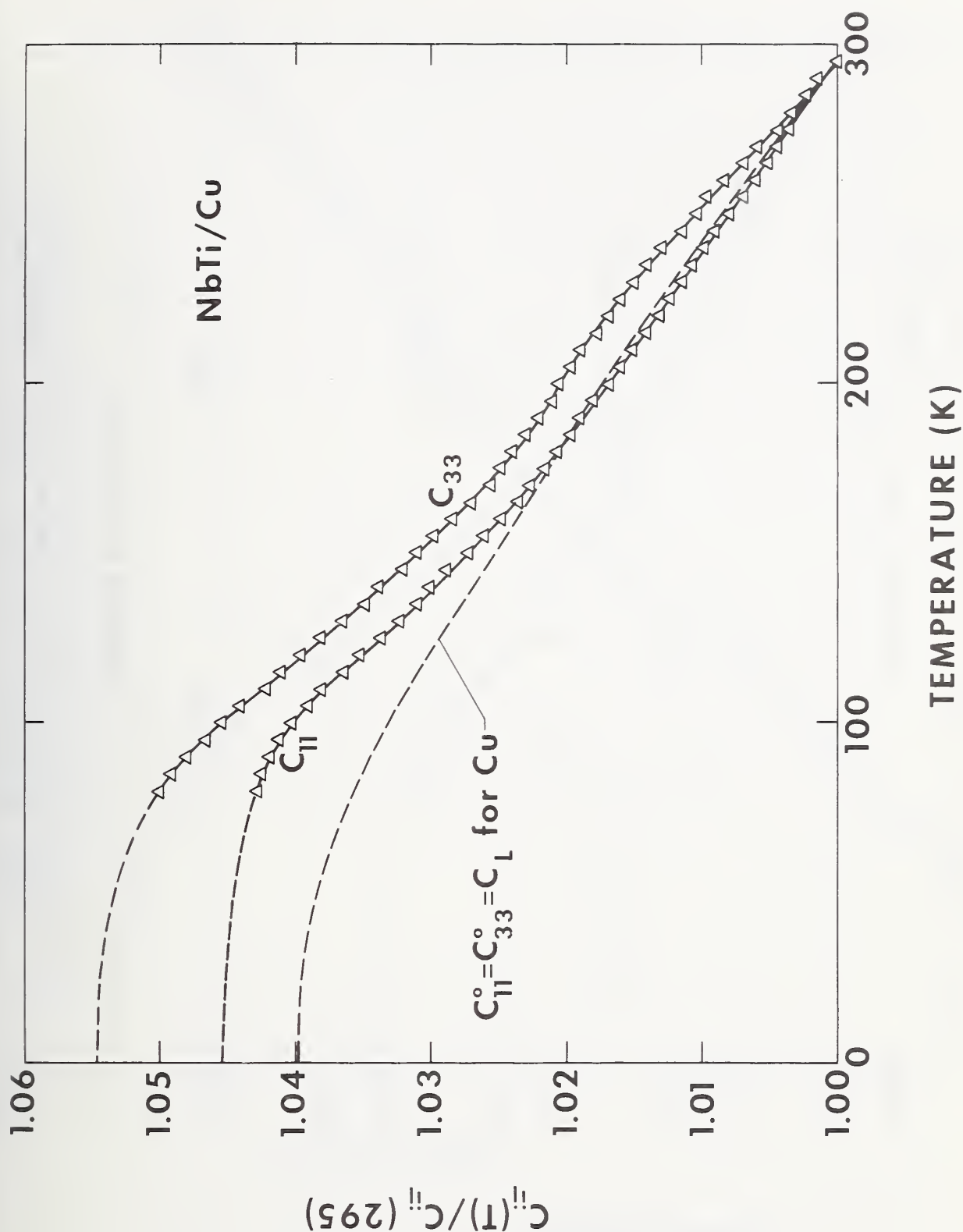


Fig. 4. Longitudinal elastic stiffnesses of the composite in the [100] and [001] directions compared to the longitudinal elastic modulus of polycrystalline copper.

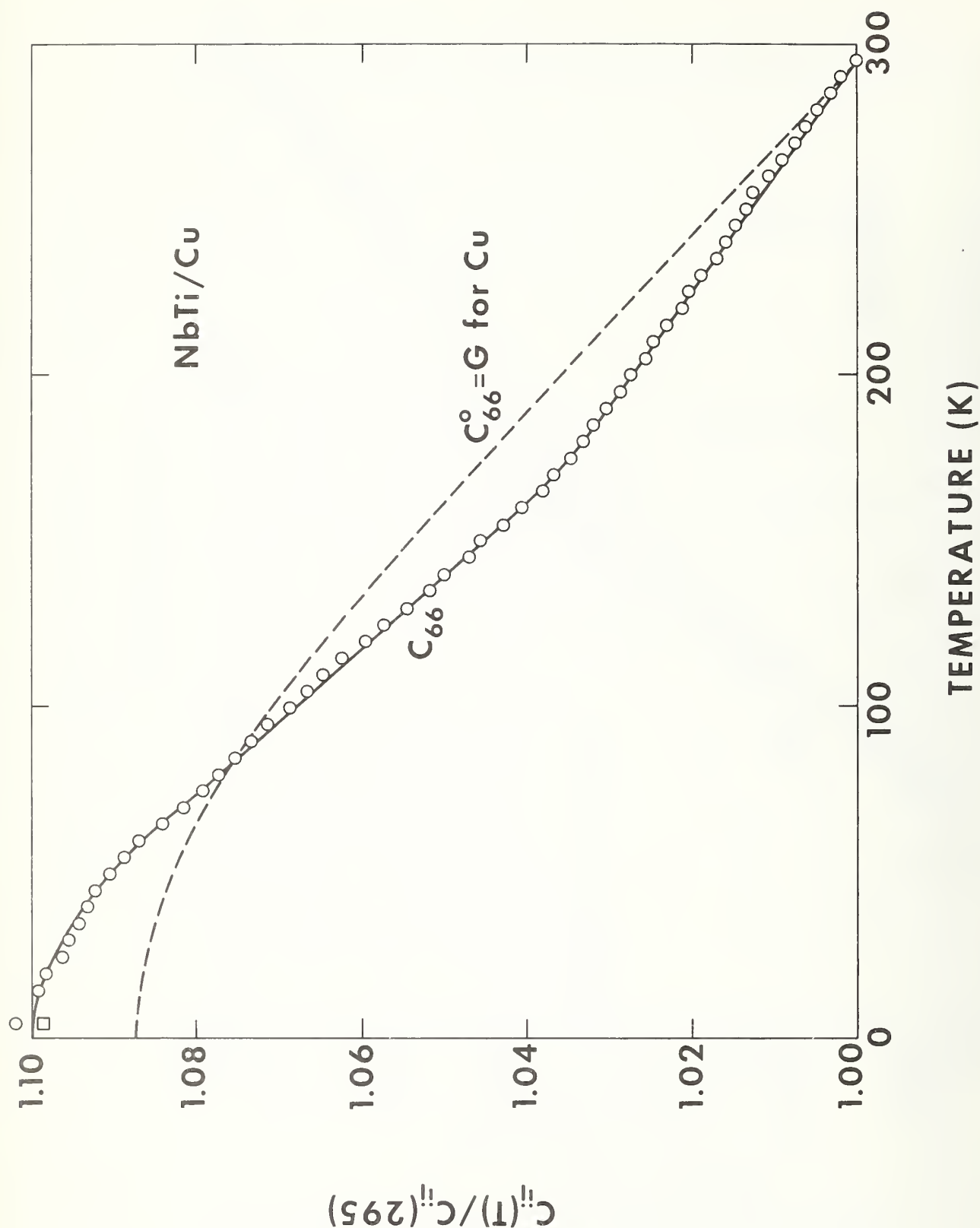


Fig. 5. A shear modulus of the composite compared to that of polycrystalline copper.  $C_{66}$  corresponds to the shear resistance on a (100) plane in a [010] direction, or on a (010) plane in a [100] direction.



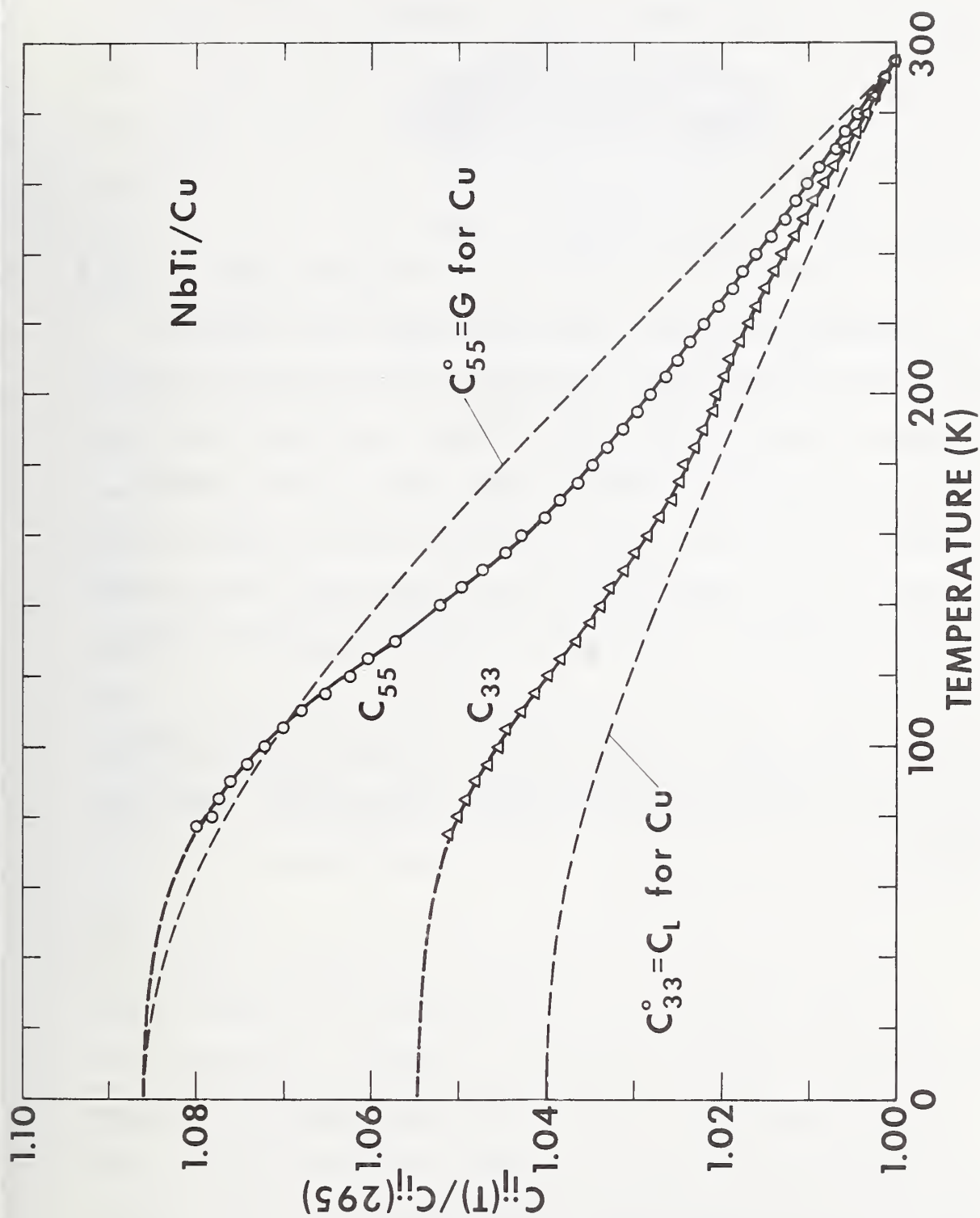


Fig. 6. Comparison of a longitudinal and a shear elastic constant of the composite  $C_{33}$  is measured in the [001] direction, along the filament axis.  $C_{55}$  corresponds to the shear resistance on a (100) plane in a [001] direction or of a (001) plane in a [100] direction. Values for copper are shown for comparison.

# Low-Temperature Elastic Properties of a 300-grade Maraging Steel†

H. M. Ledbetter and D. T. Read\*

Cryogenics Division  
Institute for Basic Standards  
National Bureau of Standards  
Boulder, Colorado 80302

## ABSTRACT

Elastic properties of an annealed 300-grade maraging steel (18 Ni, 9 Co, 5 Mo percent by weight) were studied between room temperature and liquid-helium temperature. Longitudinal and transverse ultrasonic velocities were determined by a pulse method. The reported elastic constants are: longitudinal modulus, shear modulus, Young's modulus, bulk modulus, and Poisson's ratio. Except for the bulk modulus, the room-temperature elastic constants are all lower than those of iron; and their temperature dependencies are regular in the studied temperature region.

Key words: Bulk modulus; compressibility; iron alloy; maraging steel; nickel alloy; Poisson ratio; shear modulus; sound velocity; Young's modulus.

† Contribution of NBS, not subject to copyright.

\* NRC-NBS Postdoctoral Research Associate, 1975-6.

110

## INTRODUCTION

Elastic properties of a 300-grade maraging steel (18 Ni, 9 Co, 5 Mo) were studied between room temperature and liquid-helium temperature. Elastic constants were determined by measuring the velocities of both longitudinal and transverse ultrasonic waves in a polycrystalline aggregate. The following constants are reported here:  $C_L$  = longitudinal modulus,  $G$  = shear modulus,  $B$  = bulk modulus,  $E$  = Young's modulus, and  $\nu$  = Poisson's ratio.

Maraging steels exhibit some of the best available combinations of high strength and high toughness at room temperature.<sup>1</sup> Some alloy steels with high nickel contents also have good toughness at cryogenic temperatures. However, the usual heat treatment of maraging steels would probably embrittle them at these temperatures. Thus, maraging steels would probably be used at low temperatures in their annealed conditions. An annealed 300-grade maraging steel was studied (300 indicates a yield stress of approximately  $300 \times 10^6$  psi). This alloy has a body-centered-cubic crystal structure, and it is ferromagnetic at room temperature. Other grades of annealed maraging steels are expected to be similar elastically because of their similar chemical compositions.

Elastic constants are interesting for two principal reasons. First, elastic constants are related directly to interatomic forces; thus, they are connected with a variety of solid-state phenomena, including maximum attainable strengths, phase stabilities, and lattice specific heats. Second, elastic constants are essential design parameters; the elastic constants must be known to compute deflections due to applied loads or stresses due to temperature changes of constrained components.

While some data on the temperature dependence of the Young's modulus of a 250-grade maraging steel are available<sup>2</sup>, data on the other elastic constants (shear modulus, bulk modulus, Poisson's ratio) and on other grades of maraging steel have not been reported. Furthermore, because of the many elastic-constant anomalies exhibited by iron-nickel alloys (both those with higher and lower nickel contents than maraging steels), and because of the complicated chemistry of maraging steels, their elastic behavior cannot be estimated confidently by usual predictive methods. Therefore, detailed experimental studies of the elastic behavior of these alloys are required.

## EXPERIMENTAL

### Material

The studied material was obtained from a commercial source in the form of a 10 x 23 x 108 cm ingot. The chemical (mill) analysis of the material by weight is: 18.41 Ni, 9.27 Co, 4.95 Mo, 0.002 C, 0.12 Al, 0.01 Mn, 0.006 P, 0.003 S, 0.01 Si, 0.59 Ti, balance Fe. The Rockwell B hardness is 105, and the mass density is  $8.188 \text{ g/cm}^3$  as determined by Archimedes's method using distilled water as a standard.

### Room-Temperature Sound Velocities

Room-temperature sound velocities were measured by a pulse technique.<sup>3</sup> Briefly, a quartz piezoelectric transducer with a fundamental resonance frequency of 10 MHz was cemented with phenyl salicylate (salol) to one end of a specimen having flat and parallel faces. The specimen in this case was a 1.25 x 1.25 x 1.6 cm parallelepiped with opposite faces ground flat and parallel within  $2.5 \text{ } \mu\text{m}$ . Ultrasonic pulses about one  $\mu\text{s}$  in duration were sent into the specimen by electrically exciting the transducer. The pulses propagated through the specimen, reflected from

the end, and propagated back. The echoes were detected by the transducer and displayed on an oscilloscope. The sound velocity was computed by

$$v = 2\ell/t \quad (1)$$

where  $\ell$  is the specimen length and  $t$  is the transit (round-trip) time. On the oscilloscope,  $t$  was the time between subsequent echoes. The oscilloscope was calibrated against a precision time-mark generator. An x-cut quartz transducer was used for longitudinal waves, and an ac-cut quartz transducer was used for transverse waves.

#### Low-Temperature Sound Velocities

Low-temperature measurements of the sound velocities were made by a pulse-superposition technique.<sup>4</sup> Briefly, the repetition rate of the pulse was increased so that each pulse coincided with the second echo of the preceding pulse. Since the excitation voltage was large compared with the echo voltages, the oscilloscope display consisted of alternating pulses of excitation voltages and "echo" voltages where the "echo" voltage represented the sum of all odd-numbered echoes of the non-superimposed case. Because of interference effects, the envelope of the summed odd-numbered echoes is highly sensitive to small changes in the ultrasonic velocity that are caused, in this case, by cooling.

The transducer-specimen bonding material was a stopcock grease. Temperatures were monitored with a chromel-constantan thermocouple placed near the specimen. Cooling rates were about 2 K/min. The specimen holder was described previously.<sup>5</sup> Cooling was achieved by lowering the specimen-holder assembly stepwise into the ullage of a helium dewar. No thermal contraction corrections were made. For this alloy, the maximum thermal



contraction correction to the elastic constant, which applies at  $T = 0$  K, is 0.3 percent. No correction was made for the transducer-cement-coupling phase shift; the McSkimin<sup>6</sup> analysis gives a correction of less than 0.5 percent in the velocity, assuming a maximum phase shift of  $\pi$ . The transit time was corrected to allow for the thickness of the transducer; this correction is approximately one cycle at 10 MHz; thus, the observed longitudinal-wave and transverse-wave transit times were reduced about 1.0 and 0.5 percent, respectively.

## RESULTS

Room-temperature sound velocities are given in Table 1. Velocities were measured in three orthogonal directions for three orthogonal polarizations. The experimental uncertainties in these velocities are estimated to be 0.5%.

Longitudinal and shear elastic constants were computed from the velocities according to

$$C_{\ell} = \rho v_{\ell}^2 \quad (2)$$

and

$$G = C_t = \rho v_t^2 \quad (3)$$

where  $\rho$  is the mass density. The uncertainty of these elastic constants is estimated to be 1%.

The temperature variations of  $C_{\ell}$  and  $C_t$  are shown in Figs. 1 and 2. Curves in those figures are least-squares fits of the data to the Varshni<sup>7</sup> relationship:

$$C = C^0 - \frac{S}{\exp(t/T) - 1} \quad (4)$$



where  $C$  is  $C_\ell$  or  $C_t$ ,  $C^0$ ,  $s$ , and  $t$  are adjustable parameters, and  $T$  is temperature. The value of  $C$  at  $T = 0$  K is  $C^0$ , and  $-s/t$  is the high-temperature limit of the temperature derivative  $dC/dT$ . By invoking an Einstein oscillator model, it can be shown that  $t$  is the Einstein temperature. Parameters  $C^0$ ,  $s$ , and  $t$  are given in Table II. Average differences between measured and curve values are 0.04 and 0.05 percent for the longitudinal and transverse cases, respectively.

Temperature variations of Young's modulus, the bulk modulus, and Poisson's ratio are shown in Figs. 3-5. These elastic constants were computed from Eq. (4) and the parameters in Table II using the relationships:

$$B = C_\ell - (4/3)G \quad (5)$$

$$E = 9GB/(G + 3B) \quad (6)$$

and

$$\nu = (E/2G) - 1 \quad (7)$$

The experimental uncertainties of these elastic constants are estimated to be  $\pm 1\%$ . Values of these elastic constants at selected temperatures are given in Table III, and temperature coefficients of the elastic constants are given in Table IV.

#### DISCUSSION

The present study is discussed in two parts: the room-temperature elastic constants and the changes of the elastic constants due to cooling to liquid-helium temperature.

As shown in Table III, the Young's and shear moduli of the steel are about twenty percent lower than those of unalloyed iron, the bulk modulus

is about the same, and Poisson's ratio is about ten percent higher. Usually, the elastic-stiffness constants of alloys are lower than those of their base metal. Two of the three principal alloying elements in the steel -- nickel<sup>11</sup> and molybdenum<sup>12</sup> -- lower the elastic stiffnesses of iron, while cobalt raises them. Nickel has the largest effect of the three. Thus, it is appropriate to compare the elastic constants of the steel with those of the corresponding iron-nickel alloy, and this is done in Table III. Except for the bulk modulus, the elastic constants of the steel are very close to those of an iron-18 nickel alloy. Cobalt and molybdenum seem to have very little effect on Young's modulus, the shear modulus, and Poisson's ratio, that is, on elastic constants that are determined either entirely or largely by the resistance of a material to shear deformations.

The bulk modulus is determined by the resistance of a material to dilatational deformations, and it is surprising that the bulk moduli of the steel and of unalloyed iron are the same. There appears to be no simple explanation for the unexpectedly high bulk modulus of the maraging steel. The usual effects of alloying are that the bulk modulus changes approximately in the same way as Young's modulus and the shear modulus. However, there is no a priori requirement that the bulk and shear moduli change similarly, and the present case is an interesting departure from usual behavior. Possible explanations for this effect may lie in the high bulk modulus of molybdenum, which is fifty percent higher than that of iron. Of all the elastic constants, the bulk modulus would be expected to come closest to a Vegard-law type behavior<sup>13</sup> because it is the most structure-independent elastic constant, depending much more on atomic volume than on other factors. Also, the bulk modulus is the elastic constant least affected by the usual magnetic energies that contribute to the elastic constants of iron-base alloys.<sup>14</sup>

As shown in the figures, the temperature behavior of the elastic constants of maraging steel is quite regular; that is, qualitatively the same as that exhibited by almost all simple metals and alloys. The salient features of regular behavior are: zero slope at zero temperature, as required by the third law of thermodynamics, continuous decrease with increasing temperature, consistent with the softening of interatomic bonding forces due to increased thermal vibrations; and a linear slope at high temperatures.

The regular temperature behavior of the maraging steel is unexpected. While no low-temperature elastic constants have been reported previously for body-centered-cubic iron alloys with so high a nickel content, some data exist for lower nickel content alloys. Weston, Naimon, and Ledbetter<sup>10</sup> reported the low-temperature elastic constants of iron-nickel alloys containing 3.5, 5, 6, and 9 percent nickel. These alloys show regular behavior above about 40 K, but are anomalous at lower temperatures. The anomalies are due, presumably, to magnetic transitions. But the maraging steel shows no such behavior. It is well known that iron-nickel alloys containing more than about 30 percent nickel are face-centered cubic and have very large anomalies in their elastic constants between room temperature and liquid-helium temperature. These anomalies are also due to magnetic effects.<sup>15</sup>

The maraging steel has considerably higher temperature coefficients of Young's modulus and the shear modulus than unalloyed iron, as shown in Table IV. This suggests that the steel has a considerably lower Debye temperature than iron, consistent with the Debye temperatures reported for b.c.c. iron-nickel alloys by Weston, Naimon, and Ledbetter.<sup>10</sup> Practically, this means the elastic stiffness of the steel, upon cooling, increases more than in the case of iron.

## CONCLUSIONS

In the present study, several conclusions were reached concerning the elastic properties of annealed 300-grade maraging steel:

1. The Young's modulus, shear modulus, and Poisson's ratio are all about 15 percent lower than the corresponding elastic constants of unalloyed iron. The bulk modulus is the same as that of iron.
2. Except for the bulk modulus, all the elastic constants are essentially the same as those of an iron-18 nickel alloy, implying that the effects of cobalt and molybdenum on the elastic constants are effectively canceled.
3. All the elastic constants show regular behavior over the entire studied temperature range, 4-300 K, indicating the absence of magnetic transitions that have been reported at low temperatures in other body-centered-cubic iron-nickel alloys.
4. Temperature coefficients of Young's modulus and the shear modulus are about 40 percent higher than those of unalloyed iron. This implies a lower Debye temperature for the steel.

## ACKNOWLEDGMENT

This study was supported by the Advanced Research Projects Agency of the U.S. Department of Defense.

## REFERENCES

1. A Maynée, J. M. Drapier, J. Dumont, D. Coutsouradis and L. Habraken: Cobalt - Containing High-Strength Steels, 1974, p. 50, Centre D'Information Du Cobalt, Brussels.
2. F. R. Schwartzberg, S. H. Osgood, and R. Herzog: Cryogenic Materials Data Handbook, 1968, U.S. Air Force Systems Command (Tech. Doc. Rpt. No. AFML-TDR-64-280).
3. R. T. Beyer and S. V. Letcher: Physical Ultrasonics, 1969, pp. 79-87, Academic, New York.
4. H. J. McSkimin: J. Acoust. Soc. Amer., 1961, Vol. 33, pp. 12-16.
5. E. R. Naimon, W. F. Weston, and H. M. Ledbetter: Cryogenics, 1974, Vol. 14, pp. 246-49.
6. H. J. McSkimin: IRE Trans. Ultrasonics Engr., 1957, Vol. 5, pp. 25-43.
7. Y. P. Varshni: Phys. Rev., 1970, Vol. 2, pp. 3952-3955.
8. J. A. Rayne and B. S. Chandrasekhar: Phys. Rev., 1961, Vol. 122, pp. 1714-1716.
9. H. M. Ledbetter and R. P. Reed: J. Phys. Chem. Ref. Data, 1974, Vol. 2, pp. 531-618.
10. W. F. Weston, E. R. Naimon, and H. M. Ledbetter: in Properties of Materials for Liquefied Natural Gas Tankage, ASTM STP 579, 1975, pp. 397-420, Amer. Soc. Test. Mater., Philadelphia.
11. W. C. Leslie: Metall. Trans., 1972, Vol. 3, pp. 5-26.
12. S. Takeuchi: J. Phys. Soc. Japan, 1969, Vol. 27, pp. 929-940.
13. N. F. Mott: Rep. Prog. Phys., 1962, Vol. 25, pp. 218-243.
14. W. F. Brown: Phys. Rev., 1936, Vol. 50, pp. 1165-1172.
15. G. Hausch: Phys. Status Solidi., 1973, Vol. 15, pp. 501-510.



Table I. Room-temperature acoustic-wave velocities  
in units of  $10^6$  cm/s

Propagation Direction	$v_\ell$	$v_{t_1}$	$v_{t_2}$
x	0.5673	0.2882	0.2879
y	0.5648	0.2881	0.2865
z	0.5589	0.2848	0.2841

Table II. Parameters determined from  
the Varshni equation

	Longitudinal	Transverse
$C^0, 10^{11} \text{ N/m}^2$	2.654	0.7047
$s, 10^{11} \text{ N/m}^2$	0.1036	0.05959
$t, \text{ K}$	221.9	264.4



Table III. Elastic constants of a 300-grade maraging steel at selected temperatures and those of iron and iron-18 nickel at room temperature in units of  $10^{11}$  N/m<sup>2</sup> except  $\nu$ , which is dimensionless.

Material	Temp. (K)	E	G	B	$\nu$
Maraging steel, 300-grade	300	1.756	0.663	1.676	0.325
	200	1.806	0.683	1.692	0.322
	100	1.848	0.700	1.708	0.320
	0	1.859	0.705	1.714	0.319
Iron <sup>a</sup>	300	2.140	0.831	1.680	0.288
Iron-18 Ni <sup>b</sup>	300	1.710	0.653	1.463	0.309

a. Ref. 8

b. Ref. 9, 10

Table IV. Temperature coefficients  $(1/C)(dC/dT)$  at room temperature in units of  $10^{-4}$  K<sup>-1</sup>.

Material	E	G	B	$\nu$
Maraging steel	-2.92	-3.18	-0.98	1.04
Unalloyed iron <sup>2</sup>	-2.11	-2.31	-0.90	0.95

a. Computed from data in Ref. 8 using a Voigt-Reuss-Hill arithmetic average.

## LIST OF FIGURES

- Fig. 1. Longitudinal modulus  $C_{\ell} = \rho v_{\ell}^2$  for 300-grade maraging steel as a function of temperature.
- Fig. 2. Shear modulus  $G = C_t = \rho v_t^2$  for 300-grade maraging steel.
- Fig. 3. Young's modulus for 300-grade maraging steel.
- Fig. 4. Bulk modulus for 300-grade maraging steel.
- Fig. 5. Poisson's ratio for 300-grade maraging steel.

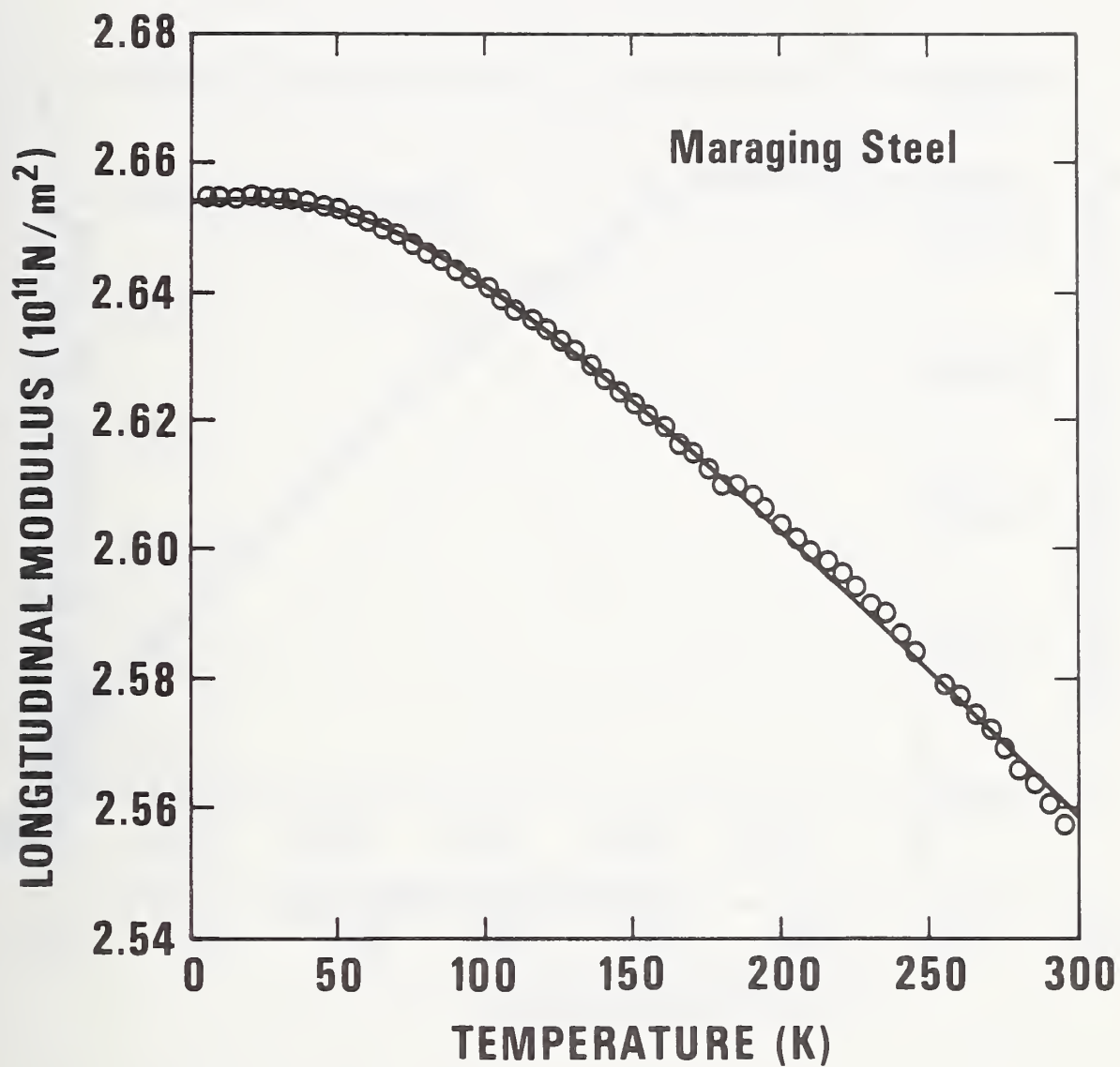


Fig. 1. Longitudinal modulus  $C_\ell = \rho v_\ell^2$  for 300-grade maraging steel as a function of temperature.

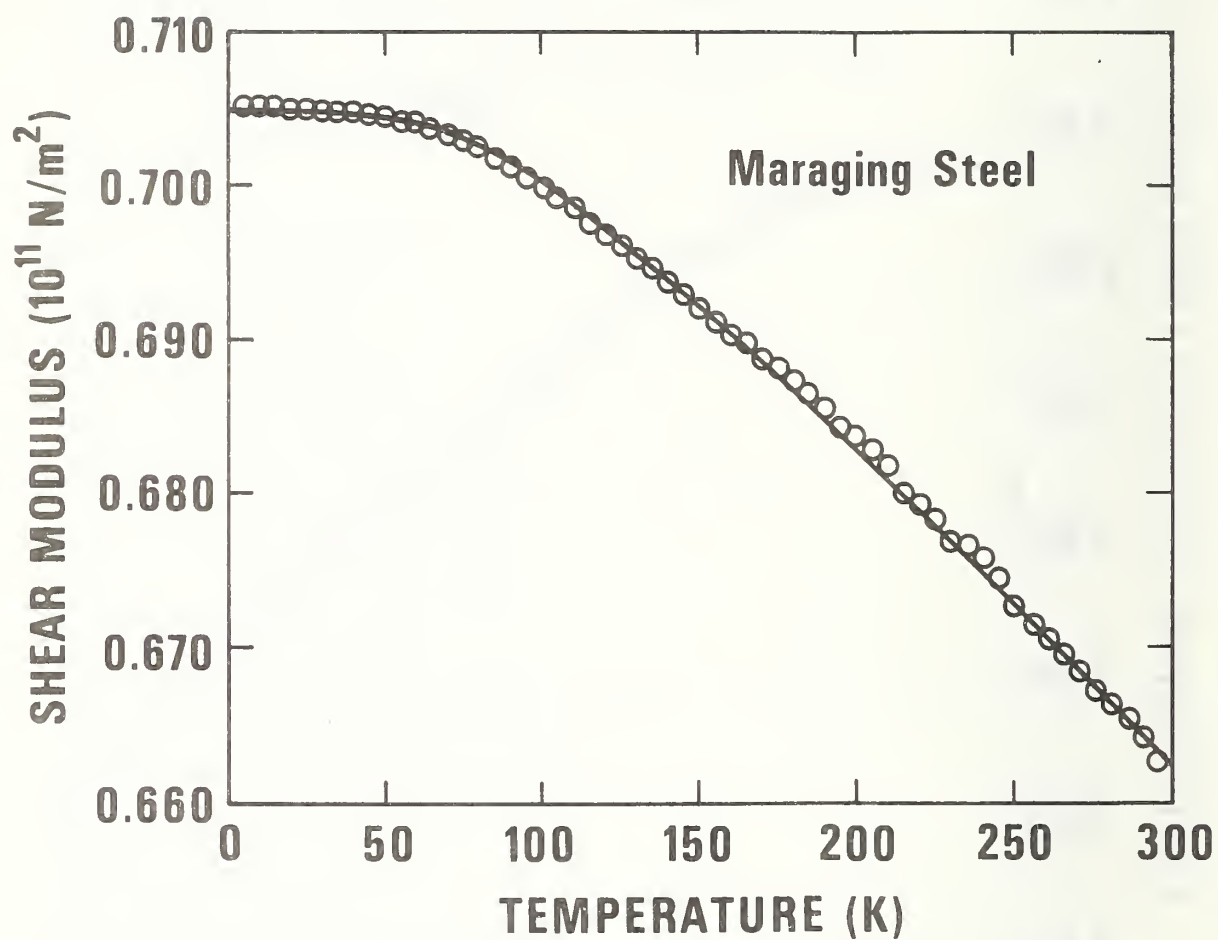


Fig. 2. Shear modulus  $G = C_t = \rho v_t^2$  for 300-grade maraging steel.

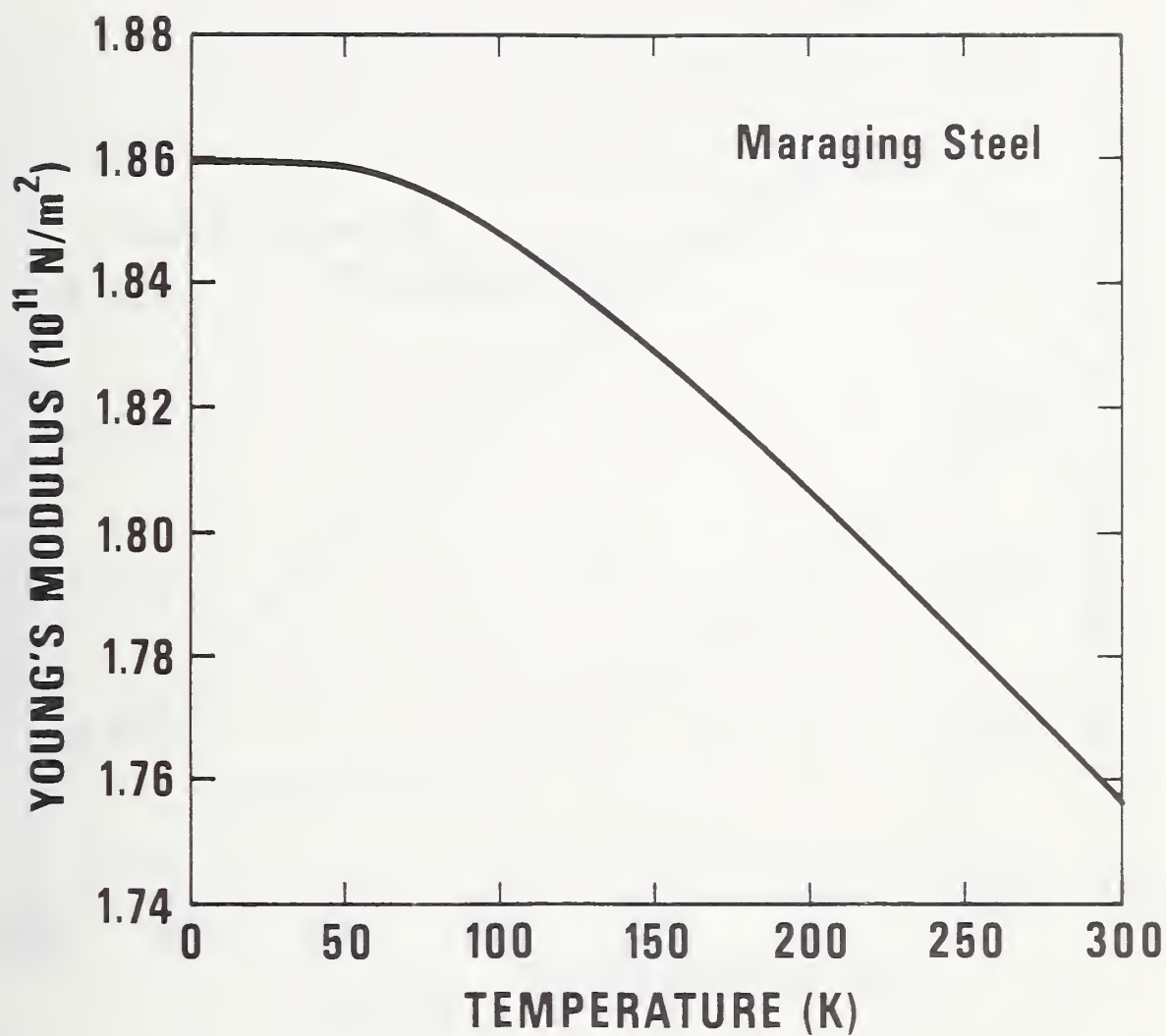


Fig. 3. Young's modulus for 300-grade maraging steel.

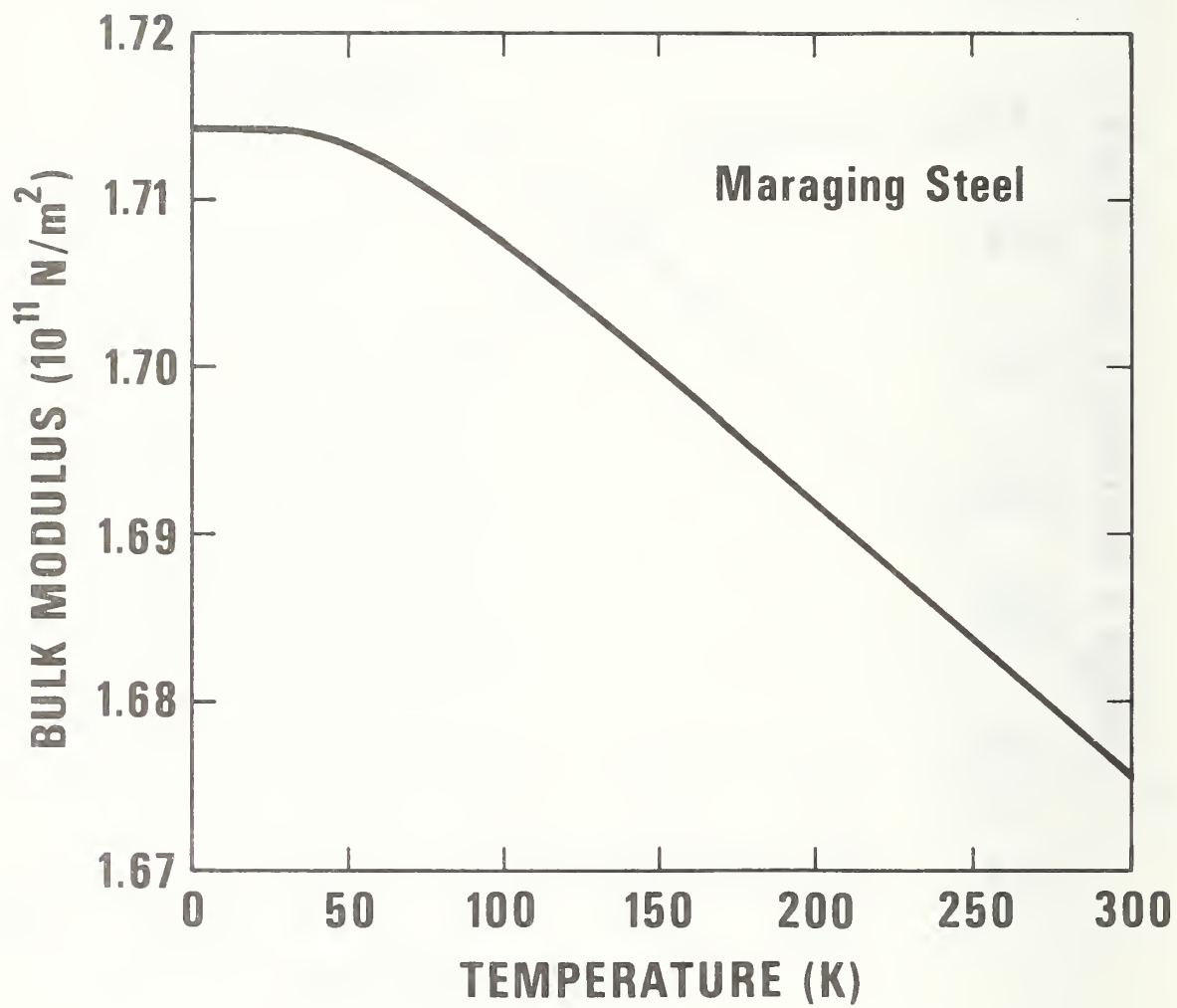


Fig. 4. Bulk modulus for 300-grade maraging steel.



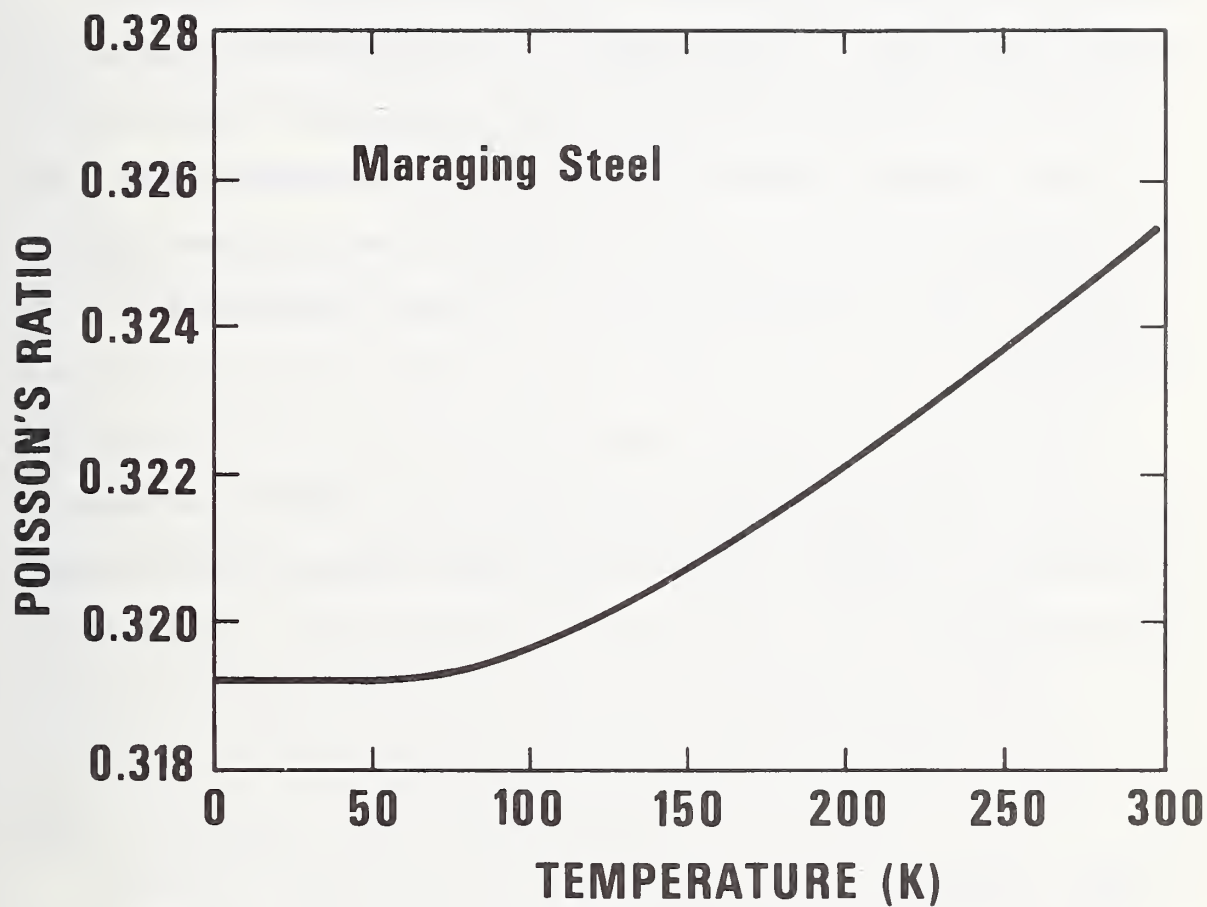


Fig. 5. Poisson's ratio for 300-grade maraging steel.

Low-Temperature Elastic Properties of a  
Precipitation-Hardened Copper Alloy\*

H. M. Ledbetter

Cryogenics Div., Institute for Basic Standards, NBS, Boulder, CO 80302

ABSTRACT

Elastic properties of a copper-cadmium-chromium precipitation-hardened alloy differ considerably from those of copper. The shear modulus of the alloy is higher than copper's while the bulk modulus is lower. The temperature behavior of the alloy's elastic constants is regular. Despite different second-order elastic constants, the temperature derivatives of the elastic constants are similar to those of copper. The alloy's Debye temperature is seven percent higher than copper's.

Key words: Bulk modulus; compressibility; copper alloy; Debye temperature; elastic constants; Poisson's ratio; shear modulus; sound velocity; Young's modulus.

\* Contribution of NBS, not subject to copyright.

## INTRODUCTION

Precipitation is a principal hardening-and-strengthening mechanism in metals and alloys. Precipitates can significantly raise a material's yield strength by pinning the dislocations that initiate plastic flow. Because precipitates occupy a small volume fraction, they usually have little effect on most physical properties, including the elastic constants.

Ledbetter<sup>1</sup> reported recently that a precipitation-hardened copper-0.3 cadmium-0.3 chromium alloy has elastic constants that differ about fifteen percent from copper's. Such large elastic-constant changes in such a dilute alloy are unusual, but not necessarily anomalous. The alloy is anomalous because its shear modulus is higher than copper's while its bulk modulus is lower. Most elastic-constant models predict that the shear and bulk moduli always change in the same direction when affected by metallurgical variables such as composition, temperature, or pressure. Usually, only variables that introduce anisotropies -- mechanical deformation or structural phase transformation, for example -- are expected to change the shear and bulk moduli oppositely. But there are no such anisotropies in a precipitation-hardened alloy; precipitates are usually equiaxed, and no macroscopic elastic anisotropy was detected in the studied alloy.

Deviation of the Cu-Cd-Cr alloy's Poisson ratio from that of copper also represents a significant departure from usual behavior. Köster and Franz<sup>2</sup> pointed out that Poisson's ratio is quite insensitive to most metallurgical variables, including alloying. The reason for this is simple. Poisson's ratio,  $\nu$ , is given by

$$\nu = \frac{1}{2} \frac{3B - 2G}{3B + G} \quad (1)$$

where B and G denote the bulk and shear moduli, respectively. By differentiation

$$\frac{d\nu}{\nu} = \frac{9GB}{(G + 3B)(3B - 2G)} \left( \frac{dB}{B} - \frac{dG}{G} \right) \quad (2)$$

which gives for  $\nu \approx 1/3$ , a typical value for metals, including copper,

$$\frac{d\nu}{\nu} \approx \frac{4}{9} \left( \frac{dB}{B} - \frac{dG}{G} \right) \quad (3)$$

Thus, the usually parallel changes in B and G tend to cancel and leave  $\nu$  unaffected. But opposite changes in B and G affect  $\nu$  additively. Thus, the precipitation-hardened Cu-Cd-Cr alloy is an exceptional case where a large change in  $\nu$  can occur in a macroscopically isotropic material.

The low-temperature elastic constants of this alloy are of interest for two reasons. First, how do the alloy's temperature coefficients compare with copper's? Second, what are the alloy's low-temperature elastic constants, which are needed for the cryogenic engineering applications of this material. Because the room-temperature elastic constants are anomalous, no basis exists for scaling the alloy's temperature dependence against copper's temperature dependence. And there is neither a model nor a data base for estimating the alloy's low-temperature elastic constants. In fact, very few low-temperature elastic-property studies have been reported for precipitation-hardened materials.

The main purpose here is to report the elastic constants of a precipitation-hardened Cu-Cd-Cr alloy between room temperature and liquid-helium temperature. Two experimental methods were used: resonance (60 kHz) and pulse (10 MHz). For most purposes, the differences between the dynamic elastic constants reported here and the more familiar static elastic constants determined by stress-strain methods are small; for the shear modulus they are zero at all temperatures; for dilatation-type elastic constants such as the bulk modulus, they are zero at zero temperature, and they increase to a few percent at room temperature.

## EXPERIMENTAL

### A. Material

The studied material is the same as that reported on previously<sup>1</sup>, and it is characterized as follows: The weight-percent chemical composition is: 0.31 Cd, 0.33 Cr, < 0.01 Pb, < 0.01 Fe, < 0.01 Ni, < 0.01 Mn, balance Cu. Mass density determined by hydrostatic weighing is 8.94 g/cm<sup>3</sup>. Hardness is 57.5 on a Rockwell 30-T scale. ASTM grain size number is five. The material was produced by the Phelps Dodge Corporation in the form of a flat extrusion 2.5 cm x 10.8 cm in cross-section. The extrusion temperature was 1227 K and the subsequent aging temperature was 866 K for 1 h. The commercial designation of this material is alloy PD 135. (This trade name is used here to identify the material; it is not an NBS endorsement of a particular product).

### B. Specimens

For ultrasonic-pulse measurements, a "cube" was prepared measuring 0.9 x 1.3 x 1.3 cm. Opposite faces were ground flat and parallel within 3  $\mu$ m. For torsional resonance measurements, cylindrical specimens were prepared 0.4 cm in diameter and 2.1 cm long.

### C. Methods

Experimental methods used in the present study were described previously<sup>3,4</sup>. Thus, only a brief outline is given here.

Room-temperature pulse measurements were made using McSkimin's<sup>5</sup> method. A quartz transducer with a fundamental frequency between 6 and 10 MHz was bonded to a specimen with salol. X-cut transducers were used for longitudinal waves and ac-cut transducers were used for shear waves. The pulse length was about one  $\mu$ s. The ultra-sound velocity was computed from

$$v = 2\ell / t \quad (4)$$

where  $\ell$  = specimen length and  $t$  = transit (round-trip) time. On an oscilloscope,  $t$  was the time between subsequent echoes. The oscilloscope was calibrated with a precision time-mark generator. Elastic constants are computed from the velocities by

$$C = \rho v^2 \quad (5)$$

where  $\rho$  = mass density.

Low-temperature pulse measurements were made with a superposition method<sup>5</sup> where the envelope of the sum of the odd-numbered echoes is maximized by tuning the carrier frequency,  $f$ . Neglecting thermal contraction, the change in ultrasonic velocity is

$$\Delta v / v = \Delta f / f \quad (6)$$



Details of the specimen holder, cooling procedures, and temperature measurements were given previously.<sup>3</sup> Measurements were made at intervals of 5 K with a cooling rate of about 2 K/min.

The torsional (shear) modulus was also measured with a composite-oscillator method<sup>6</sup> during cooling. The oscillator has three components: a quartz-crystal driver, a quartz-crystal gage, and a specimen. The resonant frequency of the specimen is

$$f_s^2 = f_o^2 + (f_o^2 - f_q^2)(m_q/m_s)(r_q/r_s)^2 \quad (7)$$

where  $m$  = mass,  $r$  = radius of cylindrical specimen, and the subscripts  $s$ ,  $o$ , and  $q$  denote specimen, oscillator, and quartz. For torsional resonance, the shear modulus is then

$$G = 4\pi \ell_s^2 f_s^2 \quad (8)$$

where  $\ell$  = length. During cooling, the frequency  $f_o$  is tuned to the resonance condition, which is determined by a maximum output voltage across a gage crystal.

## RESULTS

Results of the present study are shown in Table 1 and in Figs. 1-5. Both the  $C_l$  and the  $G = C_t$  data were least-squares fitted to a relationship due to Varshni<sup>7</sup>:

$$C(T) = C^\circ - s/[\exp(t/T) - 1] \quad (9)$$

where  $C^\circ$ ,  $s$ , and  $t$  are adjustable parameters and  $T$  is temperature.

The fitting-parameter values are given in Table 2. Average differences between measured and curve values are 0.07 and 0.06 percent for the longitudinal and transverse cases, respectively. The elastic constants  $B$ ,  $E$ , and  $\nu$  were computed from the smoothed results of Eq. (9) and the relationships

$$B = C_1 - (4/3)G \quad (10)$$

$$E = 9GB/(G + 3B) \quad (11)$$

and

$$\nu = (E/2G) - 1 \quad (12)$$

Temperature coefficients of the elastic constants are given in Table 3. Point-to-point  $2\sigma$  imprecisions in the modulus-temperature data are estimated to be less than 0.1 percent. Uncertainties in the room-temperature experimental moduli are given in Table 1. No significant elastic-constant anisotropy was detected. Resonance results for the shear modulus agreed exactly with pulse results, and they are not reported here.

#### DISCUSSION

The temperature dependencies of the elastic constants of PD 135 resemble closely those of unalloyed copper,<sup>8</sup> as shown in Figs. 1-5. Both materials exhibit regular behavior: linearity at high temperatures, continuously decreasing slope due to cooling, relative flatness at low

temperatures, and zero slope at zero temperature in accordance with the third law of thermodynamics. Hiki, Thomas, and Granato<sup>9</sup> showed that the temperature derivatives  $dC/dT$  depend on elastic constants of second, third, and fourth order. Thus, second-order elastic constants (which are reported here) of two materials can differ considerably, but their temperature derivatives  $dC/dT$  can be similar.

The Debye temperature  $\Theta$  is of considerable interest in a variety of applications, especially at cryogenic temperatures. It can be computed from the elastic constants by

$$\Theta = \frac{h}{k} \left( \frac{3N}{4\pi V_a} \right)^{1/3} v_m \quad (13)$$

where  $h$  = Planck's constant,  $k$  = Boltzmann's constant,  $N$  = Avogadro's number,  $V_a$  = atomic volume, and the mean acoustic-wave velocity is

$$v_m^{-3} = \frac{1}{3} (v_\ell^{-3} + 2\bar{v}_t^{-3}) \quad (14)$$

Using elastic data extrapolated to  $T = 0$  K, the Debye  $\Theta$  of the Cu-Cd-Cr alloy is 369 K; for copper,  $\Theta = 344$  K. The higher Debye  $\Theta$  of the alloy follows directly from its higher shear modulus.

#### CONCLUSIONS

The following principal results and conclusions emerge from the

present study:

(1) All the elastic constants of the studied Cu-Cd-Cr precipitation-hardened alloy behave regularly during cooling from room temperature to liquid-helium temperature.

(2) Despite the differences in the elastic constants of Cu-Cd-Cr and Cu, the constants change similarly during cooling. This would be expected if the third-order and fourth-order elastic constants of the two materials were similar.

(3) The Debye temperature of the Cu-Cd-Cr alloy is seven percent higher than that of copper, reflecting the higher elastic shear modulus of the alloy.

#### ACKNOWLEDGMENTS

This work was supported by the Advanced Research Projects Agency of the U.S. Department of Defense. The PD 135 alloy was originally supplied by B. H. Wilson of the Phelps Dodge Copper Products Co. to Dr. J. M. Wells of the Westinghouse Research Laboratories who provided the material and its characterization to NBS.

#### REFERENCES

1. H. M. Ledbetter, submitted for publication.
2. W. Köster and H. Franz, *Met. Rev.* 6, 1-55 (1961).
3. E. R. Naimon, W. F. Weston, and H. M. Ledbetter, *Cryogenics* 14, 246-249 (1974).
4. W. F. Weston, *J. Appl. Phys.* 46, 4458-4465 (1975).
5. H. J. McSkimin, *IRE Trans. Ultrasonics Engr.* 5, 25-43 (1957).
6. J. Marx, *Rev. Sci. Instrum.* 22, 503-509 (1951).
7. Y. P. Varshni, *Phys. Rev.* 2, 3952-3955 (1970).
8. W. C. Overton and J. Gaffney, *Phys. Rev.* 98, 969-977 (1955).
9. Y. Hiki, J. F. Thomas, and A. V. Granato, *Phys. Rev.* 153, 764-771 (1967).

Table 1. Elastic constants of a precipitation-hardened copper-chromium-cadmium alloy (PD 135) at selected temperatures.  $C_l$  = longitudinal modulus,  $C_t$  = transverse modulus,  $G$  = shear modulus,  $E$  = Young's modulus,  $B$  = bulk modulus, and  $\nu$  = Poisson's ratio. Units are  $10^{11}$  N/m<sup>2</sup>, except  $\nu$ , which is dimensionless.  $C_l$  and  $C_t$  are the measured quantities, and their standard deviations are 0.009 and 0.014 based on 12 and 10 measurements, respectively.

T, K	$C_l$	$G=C_t$	E	B	$\nu$
300	1.876	0.540	1.402	1.154	0.298
250	1.894	0.550	1.424	1.161	0.296
200	1.913	0.558	1.445	1.169	0.294
150	1.931	0.566	1.464	1.176	0.293
100	1.948	0.573	1.479	1.184	0.292
76	1.953	0.575	1.484	1.188	0.292
4	1.960	0.576	1.487	1.192	0.292

Table 2. Fitting parameters for the Varshni relationship, Eq. (9).

	Longitudinal	Transverse
$C^\circ, 10^{11}$ N/m <sup>2</sup>	1.960	0.576
$s, 10^{11}$ N/m <sup>2</sup>	0.0873	0.0652
$t, K$	211.1	313.0

Table 3. Temperature derivatives ( $1/C$ ) ( $dC/dT$ ) of the elastic constants  $C$  at room temperature, in units of  $10^{-4} \text{ K}^{-1}$ .

	B	E	G	$\nu$
Cu-Cd-Cr (PD 135)	-1.24	-3.20	-3.51	1.34
Copper <sup>a</sup>	-1.02	-3.31	-3.70	0.85

a. Reference 8

#### LIST OF FIGURES

- Fig. 1. Temperature dependence of the longitudinal modulus of a copper-based, cadmium-chromium, precipitation-hardened alloy (PD 135) compared to that of copper. The longitudinal modulus is defined in terms of the bulk and shear modulus in Eq. (10). The copper values are higher. Copper values were obtained from Overton and Gaffney<sup>8</sup> using a Voigt-Reuss-Hill averaging method.
- Fig. 2. Temperature dependence of the shear, or transverse modulus of copper alloy PD 135. The copper values are lower.
- Fig. 3. Temperature dependence of the Young's modulus of copper alloy PD 135.
- Fig. 4. Temperature dependence of the bulk modulus, or reciprocal compressibility of copper alloy PD 135. Note that copper values are higher. Compare with the shear modulus shown in Fig. 2 where they are lower.
- Fig. 5. Temperature dependence of the Poisson's ratio of copper alloy PD 135. The relatively large difference between this alloy and copper results because  $B$  and  $G$  are affected oppositely by precipitation-hardening.



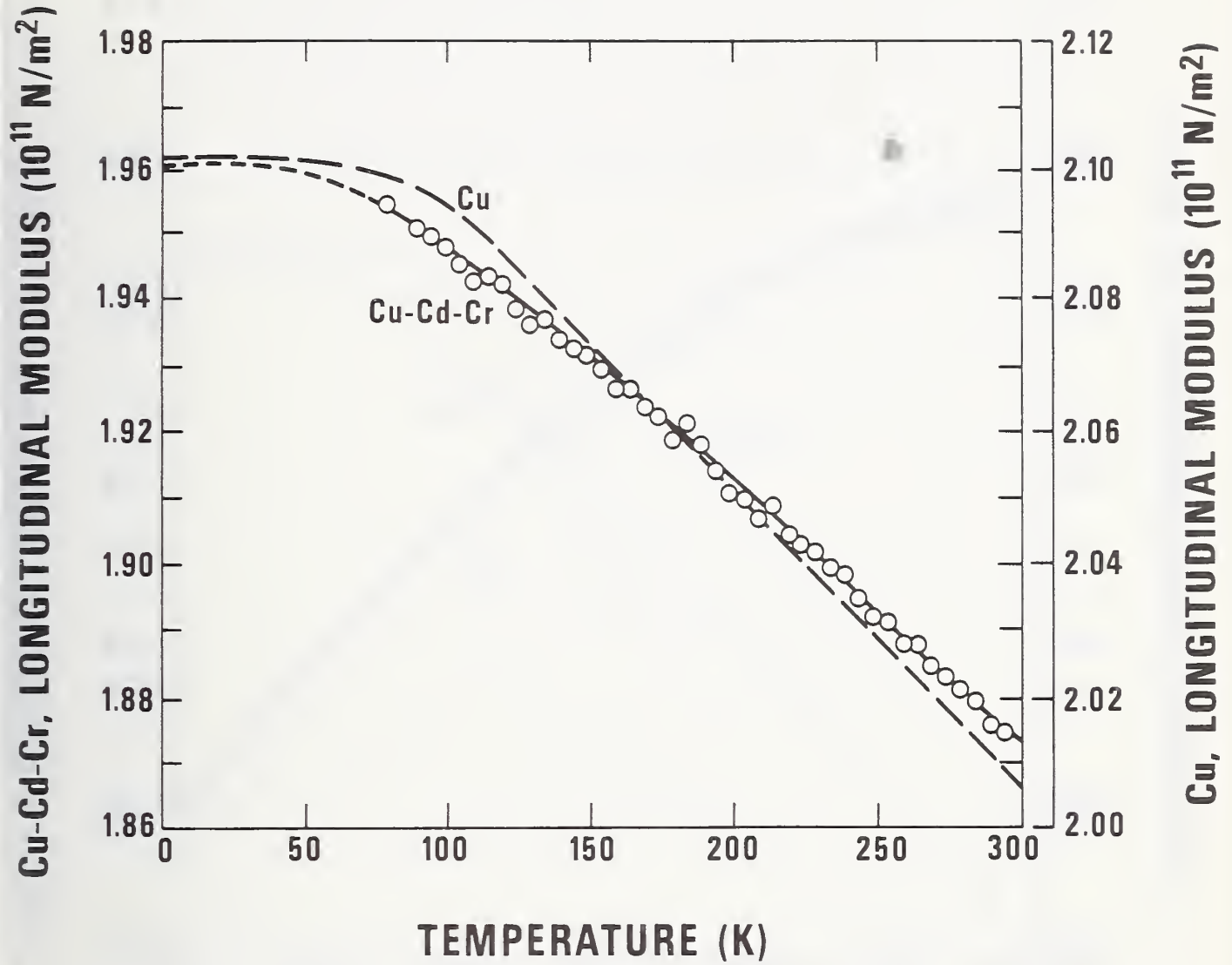


Fig. 1. Temperature dependence of the longitudinal modulus of a copper-based, cadmium-chromium, precipitation-hardened alloy (PD 135) compared to that of copper. The longitudinal modulus is defined in terms of the bulk and shear modulus in Eq. (10). Note copper values are higher.

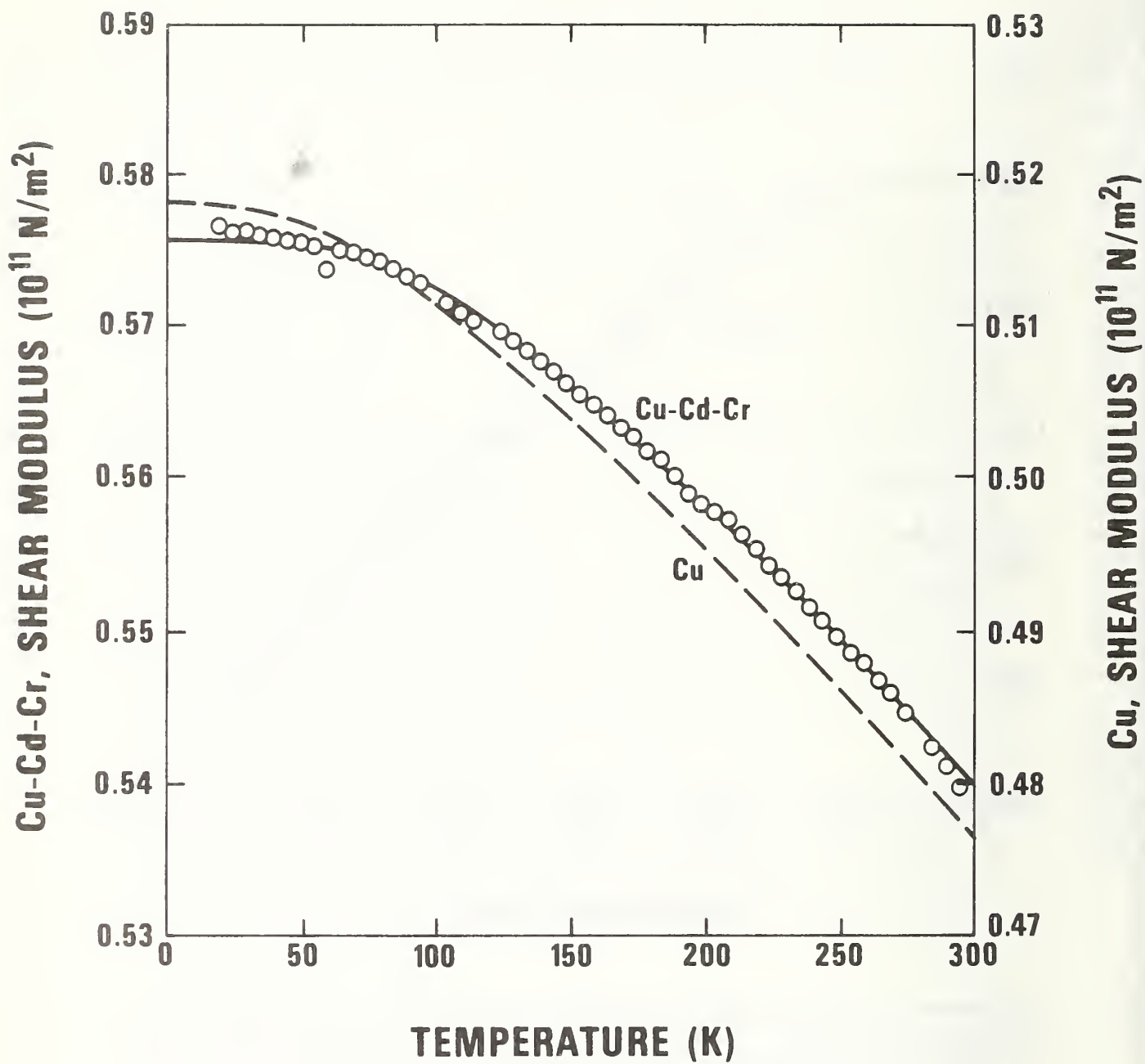


Fig. 2. Temperature dependence of the shear, or transverse, modulus of copper alloy PD 135. Note that copper values are lower.

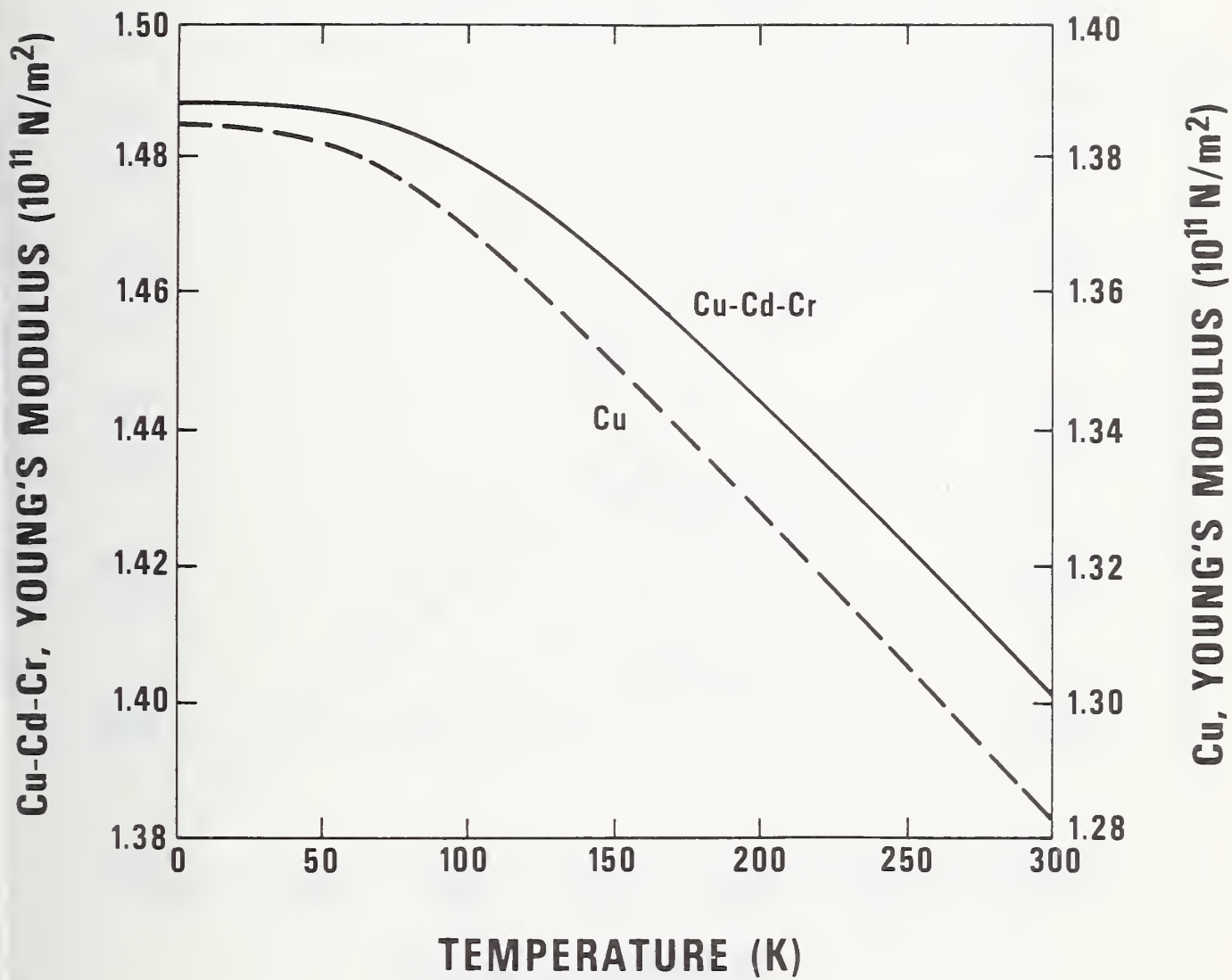


Fig. 3. Temperature dependence of the Young's modulus of copper alloy PD 135.

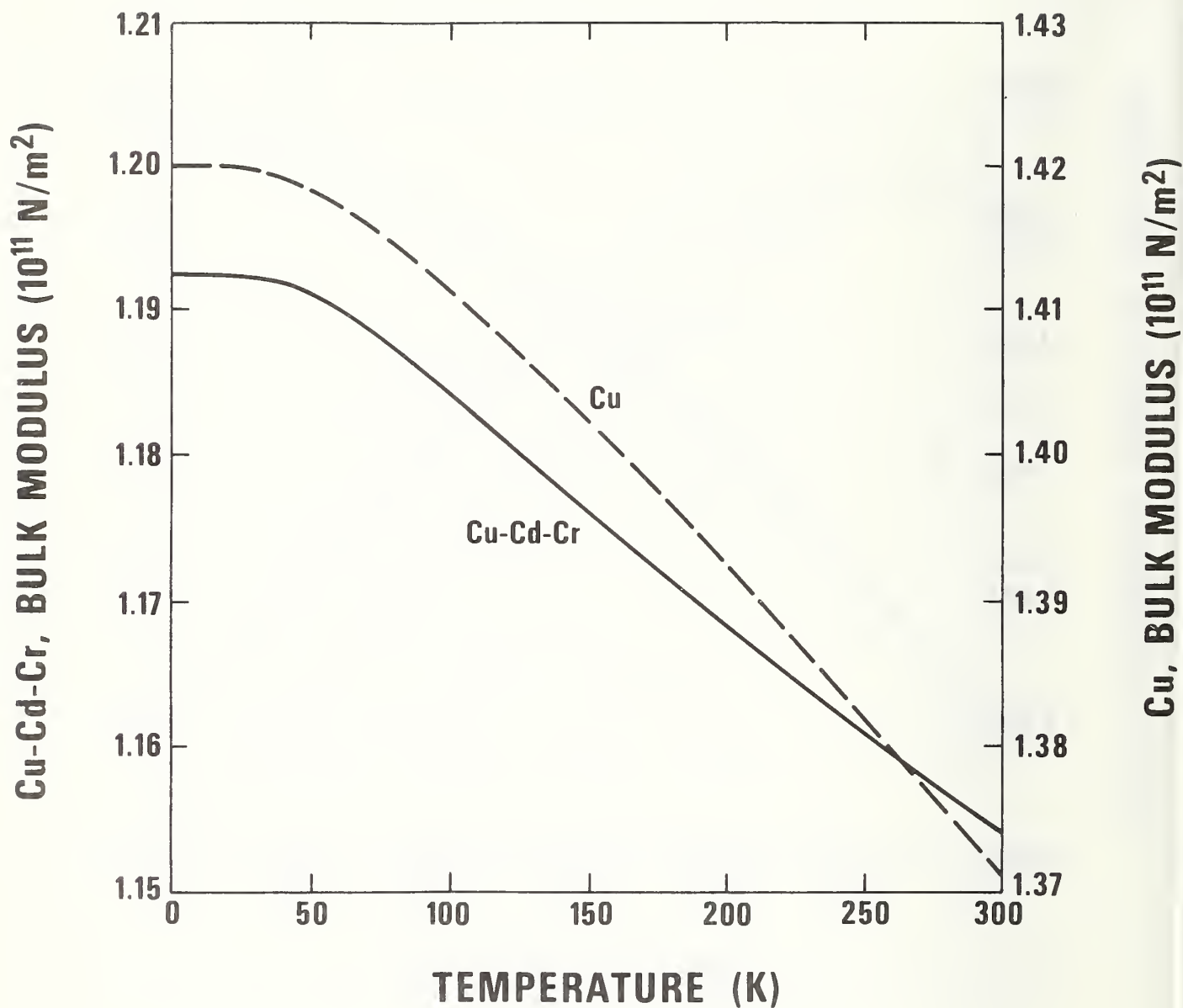
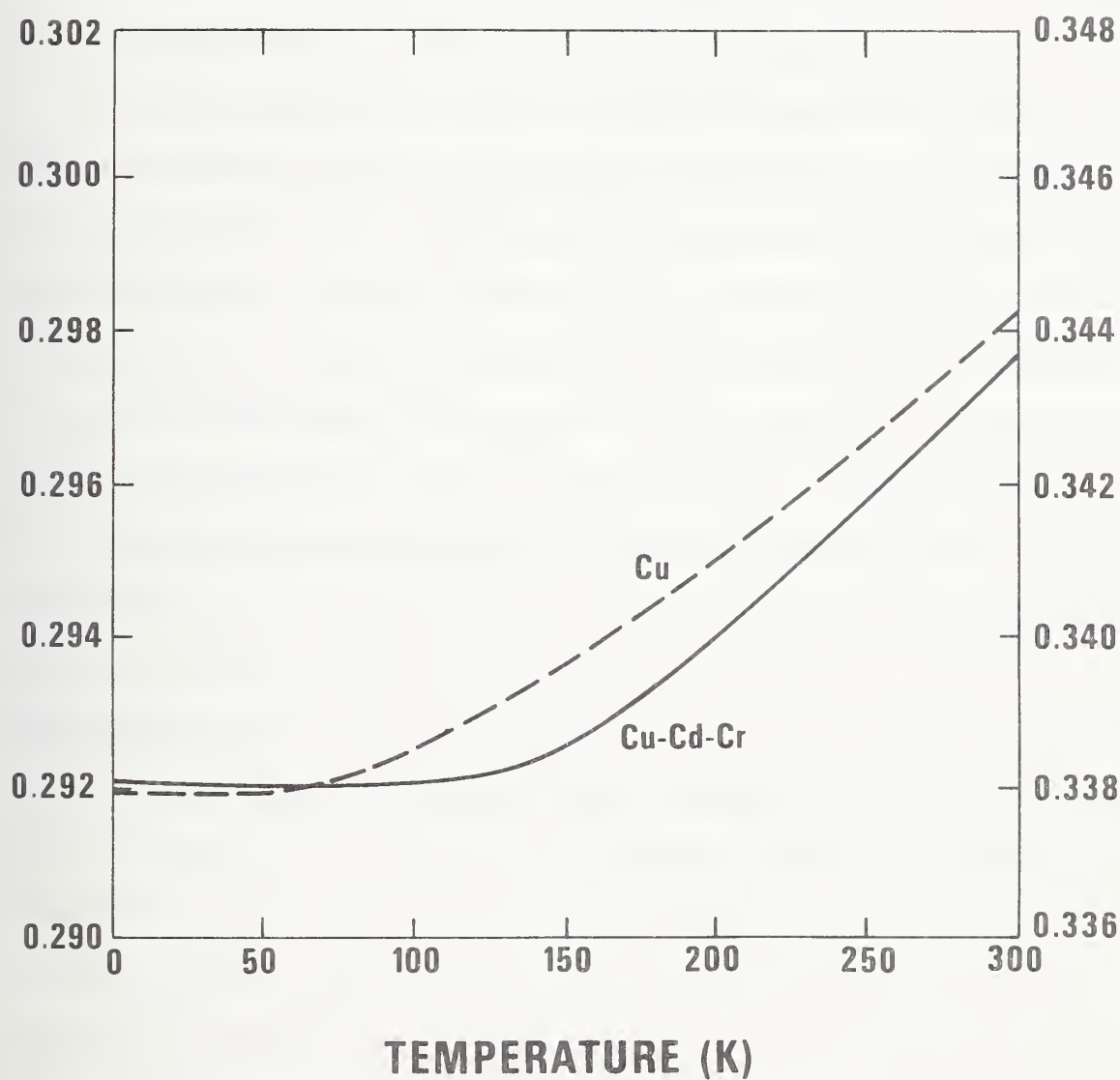


Fig. 4. Temperature dependence of the bulk modulus, or reciprocal compressibility, of copper alloy PD 135. Note that copper values are higher. Compare with the shear modulus shown in Fig. 2 where they are lower.

Cu-Cd-Cr, POISSON'S RATIO



Cu, POISSON'S RATIO

Fig. 5. Temperature dependence of the Poisson's ratio of copper alloy PD 135. The relatively large difference between the alloy and copper is due to B and G being affected oppositely by precipitation-hardening.

Elastic Properties of a Boron-Aluminum  
Composite at Low Temperatures†

D. T. Read\* and H. M. Ledbetter

Cryogenics Division  
Institute for Basic Standards  
National Bureau of Standards  
Boulder, Colorado 80302

ABSTRACT

Elastic properties of a boron-filament-reinforced, aluminum-matrix composite were studied experimentally. Assuming transverse-isotropic elastic symmetry, five independent elastic constants were measured using a piezoelectric composite-oscillator method. Two constants -- Young's modulus along the filament axis and the torsional modulus perpendicular to the filament axis -- were determined between 300 and 4 K. The composite's elastic constants are between boron's and aluminum's, and closer to aluminum's. Along the filament axis, Young's modulus is  $2.30 \times 10^{11}$  N/m<sup>2</sup>. Cooling from 300 to 4 K increases all the elastic stiffnesses up to eleven percent.

Key words: Aluminum; boron; boron-aluminum; bulk modulus; composite; compressibility; elastic constants; resonance method; shear modulus; torsional modulus; Young's modulus.

† Contribution of NBS, not subject to copyright.

\* NRC-NBS Postdoctoral Research Associate, 1975-76.



## INTRODUCTION

Boron-aluminum composites are useful because they have high elastic-modulus/density ratios (specific modulus) and high strength/density ratios (specific strength). These properties, together with comparatively high electrical conductivity, make boron-aluminum a candidate material for various structural applications: aerospace components; leisure products such as tennis rackets, bicycle frames, and golf shafts; orthotic and prosthetic devices; truck bodies; etc.

Elastic constants are important parameters in designing such components because they relate the mechanical load on a component to its resulting deflection. Elastic constants are also related to the basic structure of a material, to ultimate strengths, to melting points, and to phase stabilities. In a composite, elastic constants are due to both constituent properties and constituent interactions. Thus, besides describing the average stress-strain response of the composite, elastic constants provide tests of the mechanical and geometrical relationships between composite properties and constituent properties and a basis for improved material development.

## EXPERIMENTAL

The studied boron-aluminum composite consisted of 0.14 mm ( $5.6 \times 10^{-3}$  in)-diameter, uniaxial boron filaments in a matrix of aluminum alloy 6061. The aluminum alloy was in the F-tempered condition (as diffusion bonded). The composite, containing 48 percent filaments by volume, was fabricated as a plate measuring about 10 x 10 x 1.1 cm. The plate contained about 70 plies (as computed from an average ply thickness of 0.165 mm found by Kasen and Schramm<sup>1</sup> for a fifteen-ply sheet of the same material). This unusually thick composite was required for the elastic-constant measurements described below.

Elastic constants were measured by dynamic techniques. Such techniques have been used in our laboratory to obtain accurate values of complete sets of elastic constants of many polycrystalline materials, and to measure elastic-constant temperature dependencies between 300 and 4 K. There are two main dynamic techniques: pulse and resonance; each has many variations.

In the present study, a three-component composite-oscillator resonance technique<sup>2</sup> was used principally. A composite oscillator (consisting of a quartz-crystal driver, an identical quartz gage-crystal, and a specimen) was resonated by applying a sinusoidal voltage to electrodes plated on the drive crystal. The resulting oscillation amplitude was monitored by observing the voltage developed between electrodes plated on the gage crystal. The drive-signal frequency was varied until a sharp maximum indicating resonance was observed in the gage-voltage amplitude. The elastic constant was computed from the composite-oscillator resonant frequency, the specimen mass, the quartz-crystals' mass, the quartz-crystals' resonant frequency with no specimen attached, and the specimen's mass density and length. By using quartz crystals with orientations and electrode configurations appropriate for extensional oscillation, the Young's modulus,  $E$ , of the specimen was measured. Quartz crystals driven in torsional oscillation were used to measure the torsional (or shear) modulus,  $G$ .

Elastic constants at low temperatures were measured by enclosing the composite oscillator in a vacuum-tight container and lowering it gradually into a dewar containing liquid helium. As the composite oscillator cooled (about 2 K/min), its resonant frequency was measured. The oscillator temperature was monitored with a thermocouple. Data were obtained between 300 and 4 K using this technique, which was

described previously in more detail.<sup>3</sup>

#### ANISOTROPIC ELASTICITY

A boron-aluminum composite is macroscopically elastically anisotropic because the filaments affect the elastic modulus more strongly along the filament direction than in other directions. Using the notation indicated in Fig. 1, the Young's modulus along the filament direction,  $E_{33}$ , is expected to be larger than either  $E_{11}$  or  $E_{22}$ . Values of  $E_{11}$ ,  $E_{22}$  and the Young's modulus along other directions in the 1-2 plane may be different. However, if the filaments are oriented randomly in the 1-2 plane, and if the matrix is elastically isotropic, then Young's modulus is invariant in the 1-2 plane (transversely isotropic). A hexagonal packing of filaments produces the same effect. The aluminum matrix in this composite is almost elastically isotropic. Based on the filament arrangement shown in Fig. 2, transverse isotropy was assumed. This assumption is often made for composites of this type, and it is not expected to introduce significant errors.

Elastic anisotropies of single crystals have been studied extensively; the theory<sup>4</sup> of materials with complete rotational symmetry about an axis and translational symmetry along that axis is used for hexagonal single crystals. This formalism also applies to macroscopic treatments of filament-reinforced composites that are transversely isotropic. In this theory, such a material has five independent elastic constants; all other elastic constants can be computed from these. At least five independent measurements are required to determine these five values. Four can be obtained by measuring Young's modulus along the filament direction ( $E_{33}$ ), the torsional modulus about the filament direction ( $G_{44} = G_{55}$ ), Young's modulus perpendicular to the filament direction ( $E_{11}$ ), and the torsional modulus about an axis perpendicular

to the filament direction  $2(G_{44}^{-1} + G_{66}^{-1})^{-1}$ . The fifth elastic constant must be obtained from specimens oriented obliquely to the filament axis. Such off-axis specimens often exhibit coupling between the desired resonance mode and unwanted modes. This problem is analogous to pure and non-pure modes in transmitting ultrasonic pulses. This coupling can sometimes be avoided by appropriately choosing the angle between the filament axis and the specimen axis. Even if this coupling occurs, however, its effects can often be alleviated by allowing the specimen to vibrate unconstrained.

Six specimens were used. Four of these were cut either parallel or perpendicular to the filament axis. Two oblique specimens were prepared with filament-axis/specimen-axis angles of  $78^\circ$  and  $45^\circ$ . The specimen orientations are illustrated in Fig. 1. The  $78^\circ$  specimen was computed to have zero coupling between the desired resonance mode and other modes; zero coupling occurs when the elastic compliance  $S_{15}$  is zero in the coordinate system of the specimen. The  $78^\circ$  specimen had the disadvantage that its Young's modulus was quite insensitive to the fifth elastic constant,  $S_{13}$ . Therefore, a  $45^\circ$  specimen was prepared. For this orientation, Young's modulus is quite sensitive to  $S_{13}$ . Mode coupling in this specimen was minimized by allowing the sample to hang almost freely in resonance.

## RESULTS

The six measured modulus values are given in Table 1. The subscripts indicate that the modulus was measured using specimens with filaments parallel, perpendicular, or at an angle  $\theta$  to the specimen axis. The elastic-compliance matrix  $S_{ij}$  was computed from these data by the relationships:

$$S_{33} = 1/E_{\parallel} \quad (1)$$

$$S_{11} = S_{22} = 1/E_{\perp} \quad (2)$$

$$S_{44} = S_{55} = 1/G_{\parallel} \quad (3)$$

$$S_{66} = 2/G_{\perp} - 1/G_{\parallel} \quad (4)$$

$$S_{13} = \frac{(1/E_{\theta}) - S_{33}\cos^4\theta - S_{11}\sin^4\theta}{2\cos^2\theta \sin^2\theta} - \frac{1}{2} S_{55} \quad (5)$$

$$S_{12} = S_{11} - \frac{1}{2} S_{66} \quad (6)$$

The two off-axis specimens gave slightly different  $S_{13}$  values. The value chosen was that producing the smallest total deviation of the two calculated and measured  $E_{\theta}$  values. Room-temperature elastic compliances are given in Table 2.

The practical elastic constants can be calculated from the compliances using the relationships shown in Eq. (7), which reflects either transverse-isotropic or hexagonal symmetry:



$$\begin{array}{cccccc}
S_{11}=1/E_{11} & S_{12}=-\nu_{12}/E_{11} & S_{13}=-\nu_{31}/E_{33} & 0 & 0 & 0 \\
& S_{11}=1/E_{11} & S_{13}=-\nu_{31}/E_{33} & 0 & 0 & 0 \\
S_{ij}= & & S_{33}=1/E_{33} & 0 & 0 & 0 \quad (7) \\
& & & & S_{44}=1/G_{44} & 0 \\
& & & & & S_{44}=1/G_{44} & 0 \\
& & & & & & S_{66}=1/G_{66}
\end{array}$$

Some other useful relationships are:

$$S_{ij} = S_{ji} \quad (8)$$

$$\nu_{ij} = S_{ij}/S_{ii} \quad (9)$$

$$\nu_{21}/E_{22} = \nu_{12}/E_{11} \quad (10)$$

$$S_{66} = 2(S_{11} - S_{12}) = (1 + \nu_{12})/E_{11} \quad (11)$$

The practical elastic constants measured in the present study are given in Table 3 together with data of Gieske and Allred<sup>5</sup> and of Schramm and Kasen.<sup>1</sup> The measured room-temperature Young's and shear moduli listed in Table 1 are estimated to have inaccuracies of less than one percent. The values listed in Tables 2 and 3 include additional uncertainties due to propagation of errors and to the assumption of transverse isotropy.



The Poisson's ratios  $\nu_{13}$  and  $\nu_{31}$  were obtained by indirectly measuring  $S_{13}$  using two off-axis specimens. The Young's moduli in these specimens are insensitive to  $S_{13}$ , and the values of  $\nu_{13}$  and  $\nu_{31}$  may have inaccuracies as high as twenty percent.

The  $E_{\parallel}$  and  $G_{\perp}$  temperature dependencies were measured between 300 and 4 K; and the results are given in Figs. 2 and 3 and, for selected temperatures, in Table 4. In these figures, most of the data-point deviations from the dashed curves are believed to be measurement artifacts and not real material behavior. However, the deviations in the region 0-30 K are believed to be real. The dashed curve is a three-parameter fit to the data using Varshni's<sup>6</sup> equation; it represents typical elastic-stiffness behavior of typical metals. The measured elastic-constant changes with temperature are believed to be inaccurate to less than 0.05 percent of the elastic constant.

#### DISCUSSION

As expected, the composite's room-temperature elastic stiffnesses are between aluminum's and boron's. Also as expected, the boron-filament contribution to Young's modulus is largest along the filament axis. But, two of the composite's Poisson's ratios are outside the boron and aluminum bounds. No reason for this is obvious.

The room-temperature elastic constants measured in the present study are compared with previously reported values, both dynamic and static, in Table 3. The two dynamic-study sets of results differ by five to fourteen percent. This disagreement is not surprising because different filament volume fractions and different measurement methods were used in these studies. Poisson's ratios disagree between the two sets of dynamic measurements; reasons for this are unclear, but they

are probably due to Poisson's ratio being measured indirectly, and less accurately. The two static elastic-stiffness values disagree about fourteen percent with the dynamic values, and in opposite senses. The static Poisson's ratios disagree considerably more. Reasons for this disagreement are unclear.

The composites elastic-constant temperature dependencies are expected to be between those of boron and aluminum. Aluminum's values are well known.<sup>7</sup> Boron's values have not been reported, but they are expected to be much lower than aluminum's because boron has a much higher Debye temperature (1362 K)<sup>8</sup> than aluminum (430 K).<sup>7</sup> The measured  $E_{||}$  and  $G_{\perp}$ , temperature dependencies shown in Table 4, are lower than the temperature dependencies of aluminum, as expected.

The measured stiffness-constant temperature dependencies of boron-aluminum shown in Figs. 2 and 3 show regular behavior; that is, the stiffnesses increase approximately linearly with decreasing temperature near room temperature, and increase less steeply with decreasing temperature. This regular behavior resembles aluminum's, and it shows that nothing exceptional occurs during cooling to the stiffnesses, except for a small rise below about 30 K.

The composite's geometry suggests that  $E_{||}$  is the elastic modulus that behaves most like boron's and least like aluminum's. The high value of  $E_{||}$  compared to the composite's other moduli shows this is so. Because  $E_{||}$  is most like boron's modulus, it must be the Young's moduli of boron-aluminum with the weakest temperature dependence because boron's temperature dependence is probably small. This explains why the change in  $E_{||}$  on cooling from 300 to 4 K is only four percent,

significantly less than the changes observed in aluminum during cooling and less than the temperature dependencies of boron-aluminum's other moduli. Similar considerations indicate that  $E_{\parallel}$  and  $G_{\perp}$  must have the strongest temperature dependencies of boron-aluminum's moduli, and that  $G_{\parallel}$  should have a slightly weaker temperature dependence than  $G_{\perp}$ . Also,  $E_{\perp}$  is expected to increase by ten percent or less upon cooling from 300 to 4 K. This increase must exceed four percent and is probably close to ten. Similarly,  $G_{\parallel}$  should increase by up to, and probably close to, ten percent or less during cooling from 300 to 4 K. Thus, all the practical stiffness moduli of boron-aluminum increase eleven percent or less on cooling from 300 to 0 K, and Young's modulus along the fiber axis increases four percent on cooling.

## CONCLUSIONS

The following principal findings and conclusions emerge from the present study:

1. Single-crystal methods can be used to study the anisotropic elastic properties of a composite such as boron-aluminum.
2. For dynamic studies of a composite's elastic constants, resonance methods have some distinct advantages over pulse methods. For example, the composite reported on here gave very poor, virtually unusable, pulse-echo patterns in the 6-10 MHz region. However, the resonance peaks were well defined over a broad frequency range.
3. The elastic constants of a uniaxial boron-aluminum composite (48 percent volume fraction of filaments) are between those of boron and aluminum, and closer to aluminum's.
4. The composite's elastic stiffnesses increase by eleven percent or less during cooling from 300 to 4 K; Young's modulus along the

filaments increases four percent during this cooling.

5. Except for a non-zero slope at temperatures below 30 K, the composite's elastic constants show essentially regular behavior during cooling.

#### ACKNOWLEDGMENTS

This study was supported by the Advanced Research Projects Agency of the U.S. Department of Defense.

#### REFERENCES

1. R. A. Schramm and M. B. Kasen, in National Bureau of Standards Report No. NBSIR 75-828, 1975.
2. J. Marx, Rev. Sci. Instrum. 22, 503-509 (1951).
3. W. F. Weston, J. Appl. Phys. 46, 4458-4465 (1975).
4. J. F. Nye, Physical Properties of Crystals (Oxford U. P., Oxford, 1960), p. 141.
5. J. G. Gieske and R. E. Allred, Exper. Mech. 14, 158-165 (1974).
6. Y. P. Varshni, Phys. Rev. 2, 3952-3955 (1970).
7. E. R. Naimon, H. M. Ledbetter, and W. F. Weston, J. Mater. Sci. 10, 1309-1316 (1975).
8. K. A. Gschneider, in Solid State Physics, edited by F. Seitz and D. Turnbull (Academic, New York, 1964), Vol. 16, p. 370.

Table 1. Direct experimental elastic stiffnesses of a boron-aluminum composite containing 0.48 volume fraction of filaments, in units of  $10^{11} \text{N/m}^2$ .

Constant	Value
$E_{\parallel}$	2.30
$E_{\perp}$	1.39
$G_{\parallel}$	0.568
$G_{\perp}$	0.515
$E_{78^\circ}$	1.41
$E_{45^\circ}$	1.45

Table 2. Elastic-compliance matrix of boron-aluminum composite at 300 K as displayed in Eq. (7); matrix is symmetrical about main diagonal; derived from results in Table 1; units are  $10^{-11} \text{m}^2/\text{N}$ .

0.719	-0.343	-0.074	0	0	0
	0.719	-0.074	0	0	0
		0.435	0	0	0
			1.755	0	0
				1.755	0
					2.123

Table 3. Practical elastic constants of boron-aluminum (0.48 volume fraction boron) at T = 295 K.

	Present	Gieske, Allred <sup>a</sup>	Schramm, Kasen <sup>b</sup>	Boron <sup>c</sup>	Aluminum <sup>d</sup>
$E_{11}$ ( $10^{11}$ N/m <sup>2</sup> )	1.39	1.34	--	4.41	0.703
$E_{22}$ "	1.39	1.19	1.61	4.41	0.703
$E_{33}$ "	2.30	2.11	2.00	4.41	0.703
$G_{44}$ "	0.569	0.539	0.397	2.03	0.259
$G_{55}$ "	0.569	0.542	--	2.03	0.259
$G_{66}$ "	0.471	0.455	--	2.03	0.259
$\nu_{12}$ (dimensionless)	0.48	0.41	--	0.086	0.357
$\nu_{31}$ "	0.17	0.25	--	0.086	0.357
$\nu_{32}$ "	0.17	0.23	0.299	0.086	0.357

- a. Linear interpolation of data between 0.34 and 0.54 volume fractions of boron.  
b. Static test results, Ref. 1.  
c. Ref. 8, polycrystalline,  $\nu = (E/2G) - 1$ .  
d. Ref. 7, polycrystalline.



Table 4. Elastic stiffnesses of boron-aluminum at selected temperatures; in units of  $10^{11} \text{ N/m}^2$ .

	300 K	200 K	100 K	0 K
$E_{\parallel}$	2.30	2.33	2.37	2.38
$G_{\perp}$	0.515	0.543	0.569	0.578

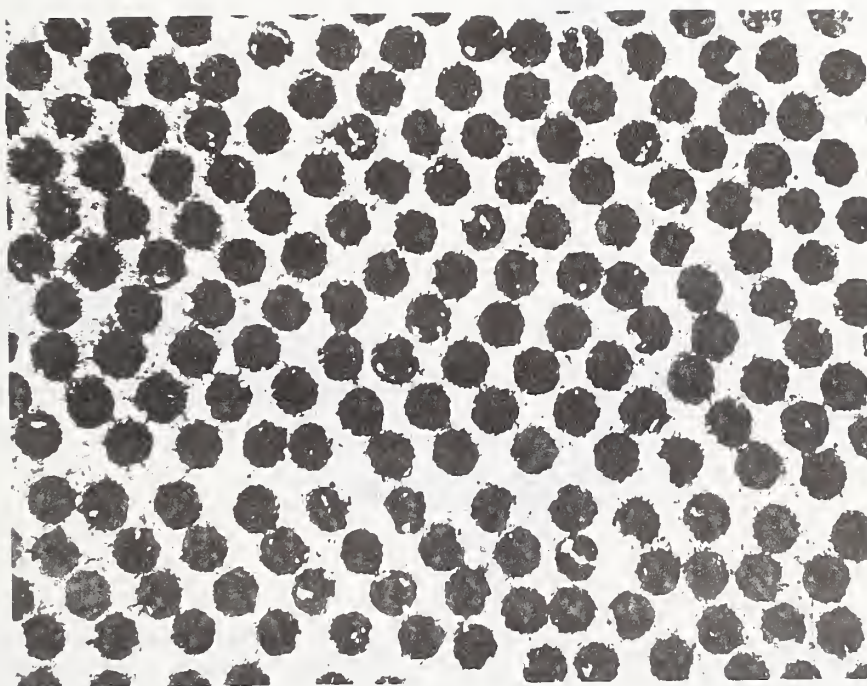


Fig. 2. Photomicrograph showing distribution of 0.14-mm-diameter boron filaments in aluminum matrix. Plane of photo is perpendicular to filaments.

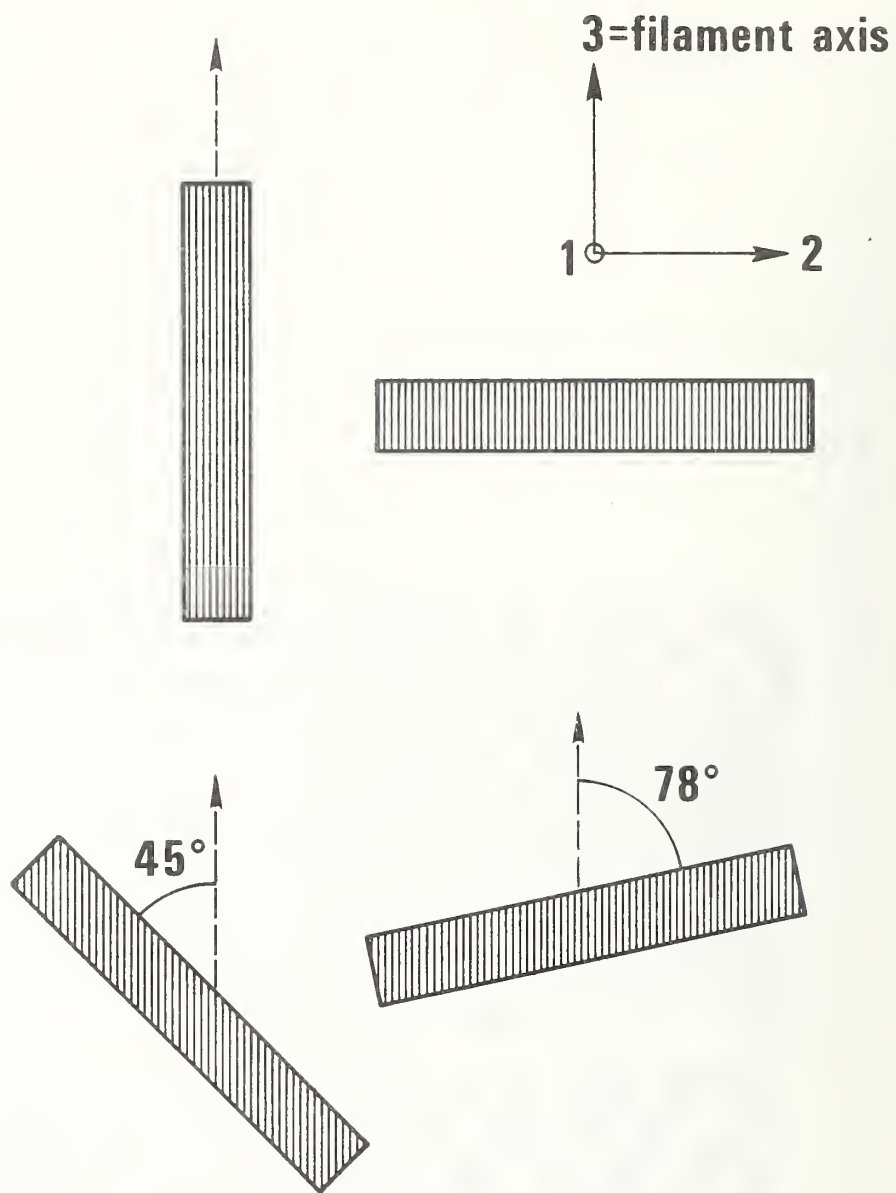


Fig. 1. Co-ordinate system, specimen geometries, and specimen orientations. Striping indicates filaments.

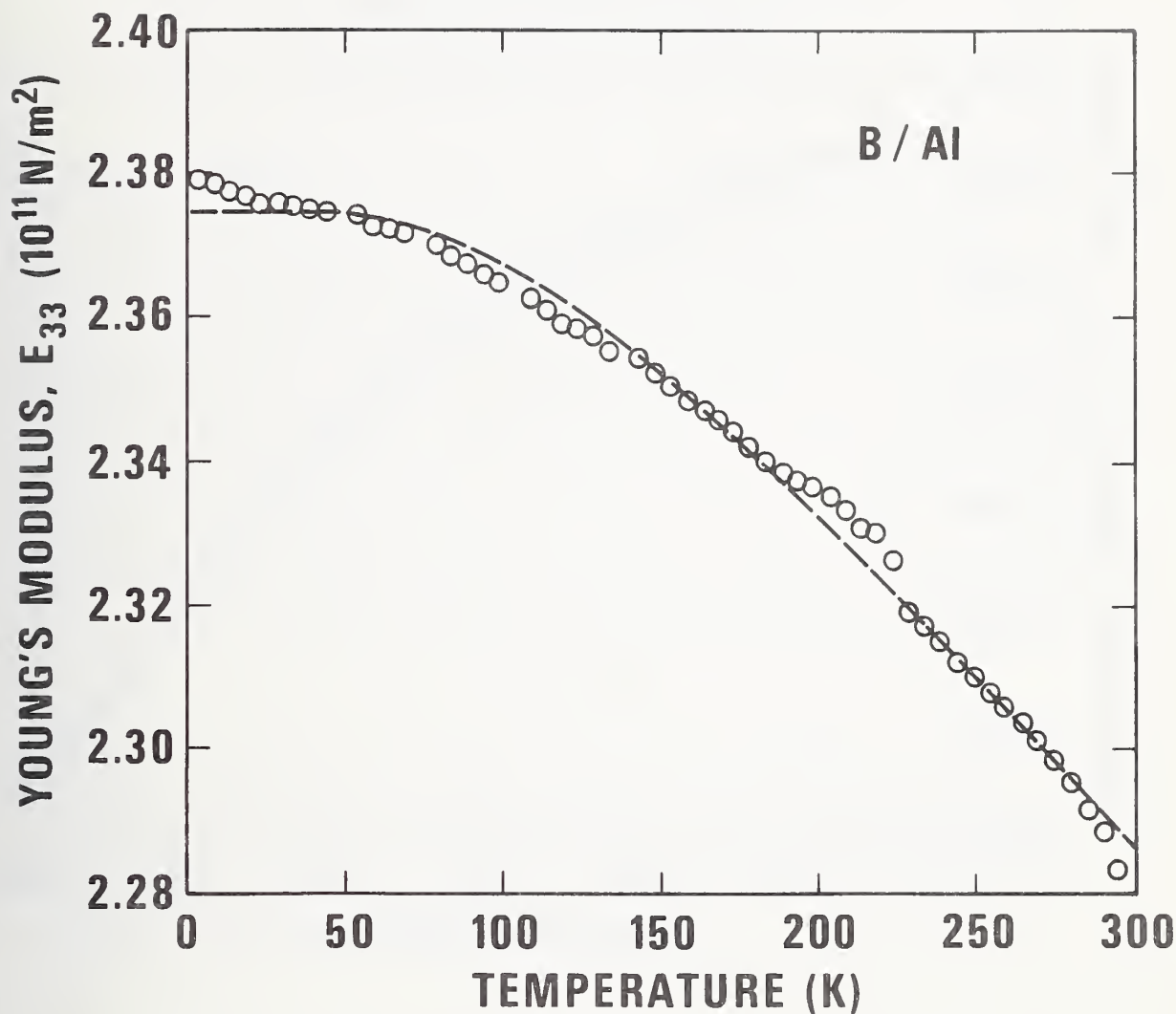


Fig. 3. Temperature dependence of Young's modulus  $E_{\parallel} = E_{33}$  along the filament axis. Dashed curve is a semi-empirical three-parameter equation that is typical for most materials. Except for the rise below 30 K, data scatter are experimental artifacts.

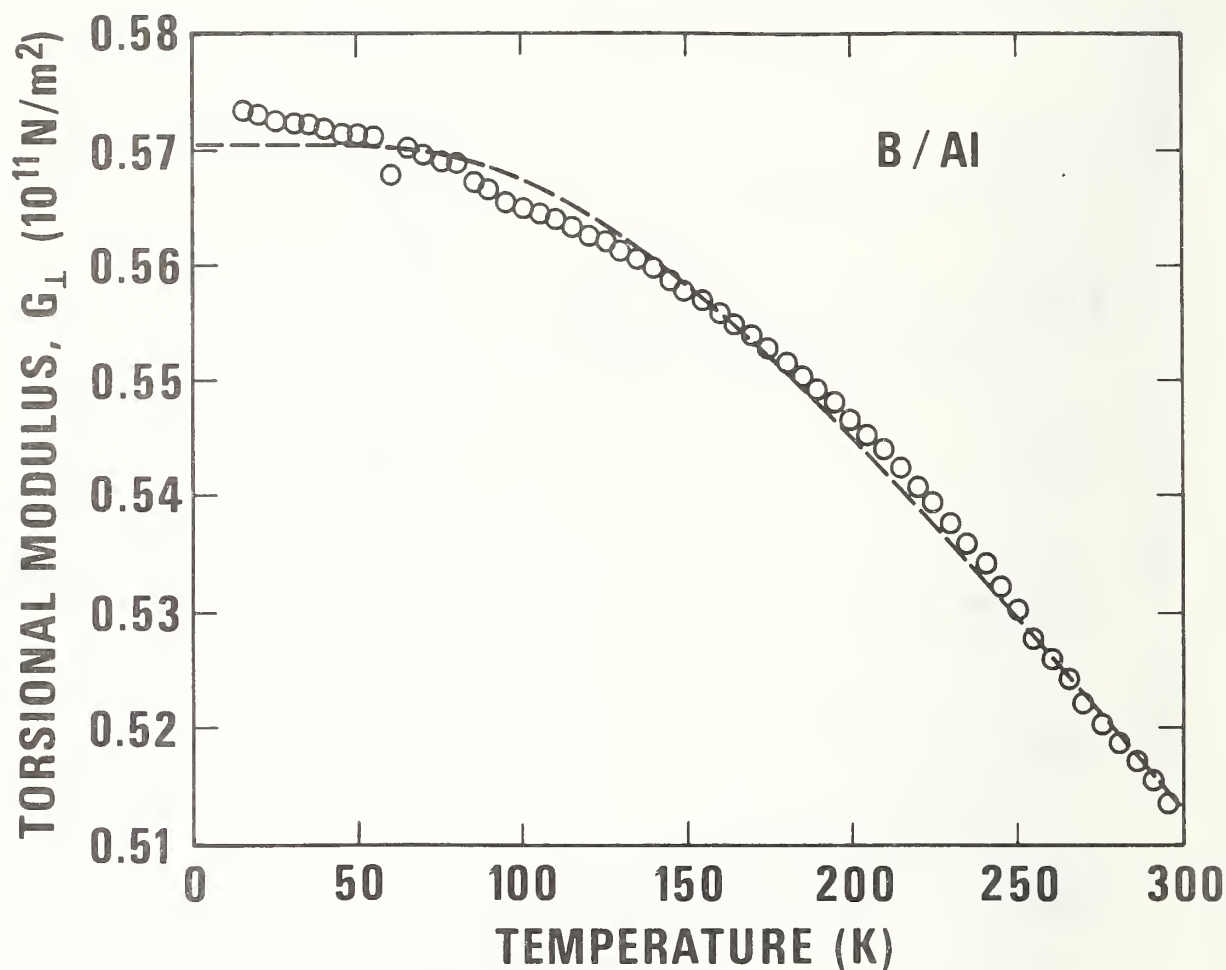


Fig. 4. Temperature dependence of the torsional (or shear) modulus about an axis perpendicular to the filament axis. See caption of Fig. 3.

ANOMALOUS LOW-TEMPERATURE ELASTIC BEHAVIOR OF A  
NITROGEN-STRENGTHENED CHROMIUM-MANGANESE STAINLESS STEEL<sup>+</sup>

H. M. Ledbetter  
Institute for Basic Standards  
National Bureau of Standards  
Boulder, Colorado 80302

ABSTRACT

Elastic constants of an Fe-21Cr-6Ni-9Mn stainless steel were studied experimentally by both pulse and resonance methods. The room-temperature elastic constants are similar to those of AISI 304. During cooling to liquid-nitrogen temperature (76 K), all the elastic constants behave anomalously below 130 K. As in Fe-Mn alloys, these anomalies are probably due to a Néel transition. A further anomaly in the compressibility at 190 K suggests a second transition of unknown nature.

Key words: Bulk modulus; compressibility; elastic constants; Poisson's ratio; pulse method; resonance method; shear modulus; stainless steel; sound velocity; Young's modulus.

<sup>+</sup> Contribution of NBS, not subject to copyright.

ANOMALOUS LOW-TEMPERATURE ELASTIC BEHAVIOR OF A  
NITROGEN-STRENGTHENED CHROMIUM-MANGANESE STAINLESS STEEL

H. M. Ledbetter  
Institute for Basic Standards  
National Bureau of Standards  
Boulder, Colorado 80302

Nitrogen-strengthened chromium-manganese stainless steels containing other alloying elements such as nickel and molybdenum are promising alloys for low-temperature applications.<sup>1</sup> They have high strength and toughness at cryogenic temperatures, and they resist stress-induced martensitic transitions that are often accompanied by undesirable property changes. Some low-temperature mechanical and physical properties of these materials have been reported.<sup>1</sup> And other low-temperature studies are in progress, including fatigue-crack growth rate and fracture toughness<sup>2</sup> and tensile and strength properties of weldments.<sup>3</sup>

The purpose of the study reported here was to determine the low-temperature elastic properties of a nitrogen-strengthened steel containing 21 chromium, 6 nickel, and 9 manganese, percent by weight. This steel is commonly called 21-6-9. The applicable elastic properties are: Young's modulus, the shear modulus, the bulk modulus (reciprocal compressibility), and Poisson's ratio. Besides characterizing a material, the elastic constants are also essential for computing either stress-induced deflections or thermo-elastic stresses. Elastic constants are inherent in fracture mechanics; for example, the plane-strain stress-intensity factor,  $K_{IC}$ , is computed from the elastic-plastic fracture criterion,  $J_{IC}$ , by using Young's modulus and Poisson's ratio.



In the presently reported study, the elastic constants were determined by measuring the velocities,  $v$ , of longitudinal waves and shear waves in a thin-rod resonance experiment near 60 kHz and in an infinite-plate pulse experiment with a carrier frequency near 10 MHz. Elastic-stiffness constants,  $C$ , are computed by

$$C = \rho v^2 \quad (1)$$

where  $\rho$  is the mass density. Depending on the velocity mode -- longitudinal, shear, extensional, torsional, etc. -- different types of elastic-stiffness constants are determined. The dynamic elastic constants were obtained because the measurements were made at high frequencies. These differ very little from the more-familiar static elastic constants that result from stress-strain-type experiments. For the bulk modulus, the difference is zero at zero temperature, and it increases to a few percent at room temperature. For the shear modulus, the difference is zero at all temperatures. Depending on their relative shear and dilational parts, all other elastic constants fall between these two behavior bounds. For example, Young's modulus behaves nearly like the shear modulus because volume is nearly unaffected by uniaxial elastic deformation.

## EXPERIMENTAL

### A. Material

The steel was provided by Lawrence Livermore Laboratories in the form of a 50 x 50 x 3.6 cm plate that was hot-rolled (1366-1089 K) from a 30.5 x 30.5 x 10 cm slab in twelve steps with 90° rotations of the slab between rollings. The plate was annealed 1.5 h at 1283 K,

air cooled, annealed 1.5 h at 1366 K, and water quenched. This material has a hardness of  $R_B = 92$ , an average grain diameter of 0.16 mm, and a mass density of  $7.838 \text{ g/cm}^3$  (determined by hydrostatic weighing). Its chemical composition in weight percent is: 19.75 Cr, 7.16 Ni; 9.46 Mn, 0.019 C, 0.15 Si, 0.004 P, 0.003 S, 0.28 N, balance Fe.

#### B. Specimens

For ultrasonic-pulse measurements, cylindrical specimens were prepared 1.7 cm in diameter and 0.5 to 1.0 cm long. Opposite faces were ground flat and parallel within  $3 \mu\text{m}$ .

For resonance measurements, cylindrical specimens were prepared 0.4 cm in diameter and 4.2 and 2.6 cm long for the extensional and torsional modes, respectively.

#### C. Methods

Experimental methods used in the present study were described previously<sup>4,5</sup>. Thus, only a brief outline is given here.

Room-temperature pulse measurements were made with a McSkimin<sup>6</sup> method. A quartz transducer with a fundamental frequency between 6 and 10 MHz was bonded to a specimen with phenyl salicylate. X-cut transducers were used for longitudinal waves and ac-cut transducers were used for shear waves. The pulse length was about one  $\mu\text{s}$ . The ultra-sound velocity was computed from

$$v = 2\ell/t \quad (2)$$

where  $\ell$  = specimen length and  $t$  = transit (round-trip) time. On an oscilloscope,  $t$  was the time between subsequent echoes. The oscilloscope was calibrated with a precision time-mark generator.

Low-temperature pulse measurements were made with a superposition method<sup>6</sup> where the envelope of the sum of the odd-numbered echoes is maximized by tuning the carrier frequency,  $f$ . Neglecting thermal contraction, the ultrasonic-velocity change is

$$\Delta v/v = \Delta f/f \quad (3)$$

Details of the specimen holder, cooling procedures, and temperature measurements were given previously.<sup>4</sup> Measurements were made at intervals of 5 K with a cooling rate of about 2 K/min.

Young's modulus and the shear (torsional) modulus were also measured with a composite-oscillator method<sup>5</sup> during cooling. The resonance frequency of the specimen is computed from

$$f_s^2 = f_o^2 + (f_o^2 - f_q^2)m_q/m_s \quad (4)$$

where  $m$  = mass and the subscripts  $s$ ,  $o$ , and  $q$  denote specimen, oscillator, and quartz. For an extensional resonance, Young's modulus is

$$E = 4\rho(\ell_s f_s)^2 \quad (5)$$

where  $\rho$  = mass density and  $\ell$  = length.

## RESULTS

Room-temperature elastic constants are given in Table I for both pulse and resonance cases. Resonance values of many of the elastic constants are not shown because they are much more inaccurate than those obtained by a pulse method.

Temperature variations of the two experimentally determined elastic constants -- the longitudinal and shear moduli -- are shown in Fig. 1. The temperature variations of the derived elastic constants -- Young's modulus, the bulk modulus, and Poisson's ratio -- are shown in Fig. 2. Resonance-method temperature data are not reported here because they contain higher inaccuracies than the pulse-method data. The two sets of data were consistent within a few percent.

Based on several measurements, the  $2\sigma$  uncertainties in the room-temperature elastic constants are estimated to be  $\pm 3\%$ . The point-to-point imprecision in the temperature-dependence measurements is estimated to be  $\pm 0.1\%$ .

## DISCUSSION

Results shown in Figs. 1 and 2 are surprising; all the elastic constants of Fe-21Cr-6Ni-9Mn behave anomalously during cooling. The primary purpose of this section, then, is to explain this alloy's anomalous temperature behavior. Any fundamental model-explanation is precluded by the alloy's complexity -- four major components, all transition metals with incomplete d shells that exhibit either ferromagnetism, antiferromagnetism, or both. But several alternative types of "explanation" are possible. The problem is -- why doesn't 21-6-9 show regular temperature behavior (indicated by the dashed curves in Fig. 1): zero slope at zero temperature, a  $T^4$  dependence at low temperatures; and a decreasing linear behavior at higher, increasing temperatures? In the simplest models of solids, Debye or harmonic, elastic constants are temperature independent. But, regular temperature behavior is predicted by a quasi-harmonic approximation,<sup>7</sup> in which the vibrational energy is volume dependent.

Changes of crystal structure cannot explain the present results. Both  $\alpha$  and  $\epsilon$  phases can be produced from the  $\gamma$  phase in 21-6-9 at low

temperatures by mechanical stress. However, the stress used in the present study was infinitesimal (the strain is typically  $10^{-6}$ ), and no stress-induced phases are possible. Athermal martensitic transition can also be excluded because such transitions in ferrous alloys are always accompanied by large temperature hysteresis.<sup>8</sup> No hysteresis was observed in the present studies; within experimental error, elastic-constant/temperature curves were identical in heating, in cooling and in successive runs. Available data<sup>9</sup> indicate that the  $\gamma$ - $\epsilon$  martensitic transition increases Young's modulus, contrary to present observations. Thus, the anomalous temperature behavior has no structural origin.

Neither can present results be explained by the familiar  $\Delta E$  effect due to linear magnetostriction, arising from either ferromagnetism or antiferromagnetism. Such effects are not observed in a saturating magnetic field because domain-wall motions are prevented. While no magnetic field was used in the present study, the high frequencies (10 MHz) that were used are equivalent in suppressing the  $\Delta E$  effect because the domain-wall displacements cannot follow the oscillating stress.<sup>10</sup>

It is useful to compare the present results with studies on more-familiar stainless steels, Fe-Cr-Ni alloys, which have low-temperature elastic anomalies due to paramagnetic-antiferromagnetic transitions. For present purposes, 21-6-9 is an AISI-304-grade stainless steel containing an additional nine percent Mn. The elastic constants of these two alloys are quite similar, with the Young's and shear moduli of 21-6-9 being about three percent higher than those of AISI 304. The elastic properties of AISI 304 were reported between room temperature and liquid-helium temperature by Ledbetter, Weston, and Naimon<sup>11</sup> together with similar data for AISI 310, AISI 316, and A286. All these stainless



steels have elastic-constant anomalies below about 80 K. These anomalies were interpreted by invoking the Döring effect. Döring<sup>10</sup> showed thermodynamically that either a paramagnetic-ferromagnetic (Curie) transition or a paramagnetic-antiferromagnetic (Néel) transition must be accompanied by a Young's-modulus anomaly due to volume magnetostriction, which is manifested as the difference between Young's modulus at constant magnetic field and at constant magnetization. However, Döring's analysis does not account for an anomalous change in the shear modulus, and it is inapplicable to 21-6-9. Thus, an important difference exists between the low-temperature elastic anomalies in Fe-Cr-Ni and Fe-Cr-Ni-Mn alloys. Fe-Cr-Ni alloys are anomalous in every elastic constant except the shear modulus. Fe-Cr-Ni-Mn alloys are anomalous in every elastic constant. This difference is important for developing models of elastic behavior, and it can be identified only when continuous, complete sets of elastic constants are available over a wide temperature region.

Since Fe-21Cr-6Ni-9Mn behaves differently from Fe-Cr-Ni alloys, it is appropriate to compare it with Fe-Mn alloys. Several authors<sup>9,12-15</sup> have reported low-temperature elastic constants of these alloys, which are often called manganese steels. The present alloy compares closely with Fe-Mn alloys in several respects: (1) all elastic constants are anomalous; (2) the anomaly consists of a lowering of the elastic stiffnesses during cooling; (3) little or no hysteresis; (4) a wide temperature range of transition; (5) frequency independence; and (6) a maximum-minimum-maximum behavior exhibited during cooling. Antiferromagnetism in Fe-Mn alloys was demonstrated first by Sedov,<sup>16</sup> who measured the



temperature dependence of the magnetic susceptibility of alloys containing 13.0 to 43.9 wt. pct. Mn. Elastic anomalies associated with the Néel transition in Fe-Mn alloys were reported first by Sokolov and Melker,<sup>12</sup> who measured the temperature dependence of Young's modulus of alloys containing 11.1 to 52.4 wt. pct. Mn. Young's modulus anomalies were also reported by Bogachev et al.<sup>13,14</sup> (13-44 and 14-38 wt. pct. Mn). Tanji<sup>15</sup> reported anomalies in both Young's modulus and the shear modulus of alloys containing 30 to 48 wt. pct. Mn. Tanji also reported very peculiar behavior of the bulk modulus in the vicinity of the Néel transition. Young's modulus anomalies were also reported by Lysek et al.<sup>9</sup>, although they were complicated by the  $\gamma$ - $\epsilon$  structural transition. These previous studies can be summarized as follows: Fe-Mn alloys containing 13-48 pct. Mn undergo a Néel transition during cooling; both Young's modulus and the shear modulus decrease anomalously because of the transition; the bulk-modulus behavior during the transition may be peculiar, and further study is appropriate; no results have been reported for changes in Poisson's ratio. Thus, it is concluded that in Fe-21Cr-6Ni-9Mn the basic magnetic mechanism causing the elastic anomaly is the same as in Fe-Mn alloys.

Two additional results of the present study deserve mention. First, as shown in Fig. 2, Poisson's ratio is the most sensitive elastic-constant indicator of the transition, that is, a locator of the Néel temperature. Within the paramagnetic region, Poisson's ratio is almost linear over a wide temperature range. Since Poisson's ratio is not related simply to interatomic forces in solids, the physical implications of this behavior are unclear. Second, as also shown in Fig. 2, the bulk modulus has a maximum at 190 K, about 60 K above the suggested Néel transition. This

implies a second transition. The nature of this transition is unknown; but it also is probably magnetic, and magnetic-susceptibility measurements might elucidate its nature.

Several further studies are suggested by the present results: (1) Thermal expansion. Elastic-constant/temperature anomalies are often accompanied by anomalous thermal expansion, particularly in magnetic materials where they have a common cause -- magnetostriction. A weaker interatomic bond usually means a higher specific volume and lower elastic stiffnesses. Regions of negative thermal expansion are possible in this alloy since the magnetic effects may overcompensate for the usual thermal expansion. Alloys with both low thermal expansion and low temperature coefficients of the elastic constants are of considerable technological interest.<sup>17</sup> Also, thermal-expansion data would be useful for distinguishing among possible magnetic mechanisms. (2) Damping. Changes in elastic constants are always accompanied by increases in damping. The possibility of high damping over a temperature region (determined by Mn content) in a non-ferromagnetic material is an interesting possibility. (3) Compressibility. The variation of the compressibility in the vicinity of the Néel transition needs further, detailed study. Tanji's<sup>15</sup> results suggest that the compressibility is discontinuous at the Néel temperature, implying a first-order phase transition. But, Néel transitions are known to be second-order. (4) Additional alloys. It would be useful to study other 21-6-9-type alloys to determine the more general validity and utility of the present results. In particular, effects of manganese content should be determined. (5) Magnetic susceptibility. Such measurements made continuously versus temperature would verify the occurrence of a Néel transition and possibly elucidate the nature of the transition that lowers the bulk modulus at 190 K.

## CONCLUSIONS

The following principal results and conclusions emerge from the present study:

(1) At room temperature, an Fe-21Cr-6Ni-9Mn alloy has elastic properties similar to those of AISI 304; all the elastic constants except Poisson's ratio are slightly higher in 21-6-9.

(2) Upon cooling, all the elastic constants show anomalous behavior, which is reproducible and reversible, showing no hysteresis.

(3) These anomalies are believed to result from a paramagnetic-antiferromagnetic (Néel) transition, with a transition temperature near 130 K, as evidenced by drops in the shear modulus and in Young's modulus.

(4) Poisson's ratio is especially sensitive to the Néel transition. It is almost linear in the paramagnetic region, and the slope  $dv/dT$  reverses sharply at the transition.

(5) This alloy's behavior resembles the Fe-Mn case rather than the Fe-Cr-Ni case, emphasizing the role of manganese in affecting properties.

(6) There may be a second transition in this alloy, evidenced by the drop in the bulk modulus upon cooling below 190 K.

(7) Such alloys may offer exceptional physical properties for non-ferromagnets, for example: high damping, low thermal expansion, and a small elastic-modulus change with temperature.

## ACKNOWLEDGMENT

This work was supported by the Advanced Research Projects Agency of the U.S. Department of Defense.

## REFERENCES

1. Handbook on Materials for Superconducting Machinery (Metals and Ceramics Information Center, Battelle, Columbus, Ohio, Nov. 1975).
2. R. L. Tobler, in National Bureau of Standards Rep. No. NBSIR 76-848 (1976).
3. J. M. Wells, R. Kossowsky, W. A. Logsdon, and M. R. Daniel, Westinghouse Research Rep. No. 76-9D4-CRYMT-R1 (1976).
4. E. R. Naimon, W. F. Weston, and H. M. Ledbetter, Cryogenics 14, 246-249 (1974).
5. W. F. Weston, J. Appl. Phys. 46, 4458-4465 (1975).
6. H. J. McSkimin, IRE Trans. Ultrasonics Engr. 5, 25-43 (1957).
7. G. Leibfried and W. Ludwig, in Solid State Physics, edited by F. Seitz and D. Turnbull (Academic, New York, 1961), Vol. 12, p. 383.
8. R. P. Reed and J. F. Breedis, in Behavior of Materials at Cryogenic Temperatures, ASTM STP 387 (Amer. Soc. Test. Mater., Philadelphia, 1966).
9. L. I. Lysek, S. P. Kondratev, Yu. N. Makogon, and B. I. Nikolin, Soviet Phys.-Doklady 18, 428-429 (1973).
10. R. M. Bozorth, W. P. Mason, and H. J. McSkimin, Bell Syst. Tech. J. 30, 970-989 (1951).
11. H. M. Ledbetter, W. F. Weston, and E. R. Naimon, J. Appl. Phys. 46, 3855-3860 (1975).
12. O. G. Sokolov and A. I. Melker, Soviet Phys.-Doklady 9, 1019-1021 (1965).
13. I. N. Bogachev, V. F. Egolaev, and B. A. Potekhin, Soviet Phys.-Doklady 12, 377-379 (1967).
14. I. N. Bogachev, V. F. Yegolayev, and T. L. Frolova, Fiz. Metal. Metalloved 29, 358-363 (1970).
15. Y. Tanji, J. Japan Inst. Met. 35, 1-5 (1971).
16. V. L. Sedov, Soviet Phys. JETP 15, 88-89 (1962).
17. G. Hausch and W. Warlimont, Z. Metallkd. 64, 152 (1973).

Table I. Elastic constants of an Fe-21Cr-6Ni-9Mn alloy at room temperature, compared to those of AISI 304.

	Fe-21Cr-6Ni-9Mn Pulse	Resonance	AISI 304 Pulse
$\rho, \text{g/cm}^3$	7.838		7.864
$v_l, 10^6 \text{cm/s}$	0.571		0.563
$v_t, 10^6 \text{cm/s}$	0.310		0.306
$C_l, 10^{11} \text{N/m}^2$	2.534		2.491
$G=C_t, 10^{11} \text{N/m}^2$	0.755	0.779	0.735
$B, 10^{11} \text{N/m}^2$	1.527		1.506
$E, 10^{11} \text{N/m}^2$	1.945	1.957	1.897
$\nu$	0.288		0.290

#### LIST OF FIGURES

- Fig. 1. Longitudinal and shear moduli variations with temperatures, as determined by an ultrasonic pulse-superposition method. Data are shown for a single cooling. Subsequent heatings and coolings reproduced these data within  $\pm 0.1$  percent. Dashed curves represent behavior expected for a typical material.
- Fig. 2. Shear modulus (G), Young's modulus (E), Poisson's ratio ( $\nu$ ), and bulk modulus (B) computed from data in Fig. 1 by using standard formulas. Note that the bulk-modulus anomaly begins about 60 K higher than the shear-modulus anomaly.



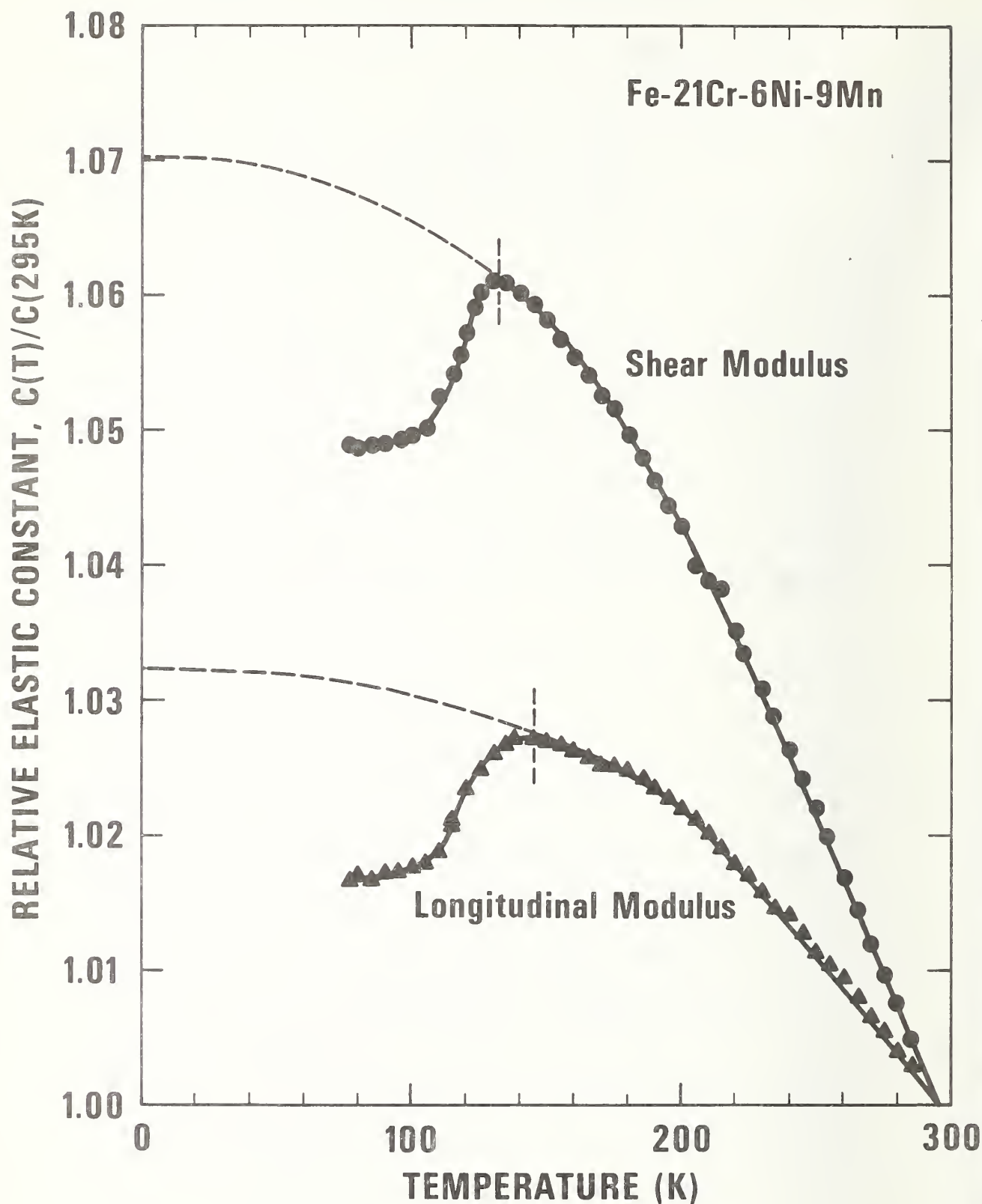


Fig. 1. Longitudinal and shear moduli variations with temperature, as determined by an ultrasonic pulse-superposition method. Data are shown for a single cooling. Subsequent heatings and coolings reproduced these data within  $\pm 0.1$  percent. Dashed curves represent behavior expected for a typical material.



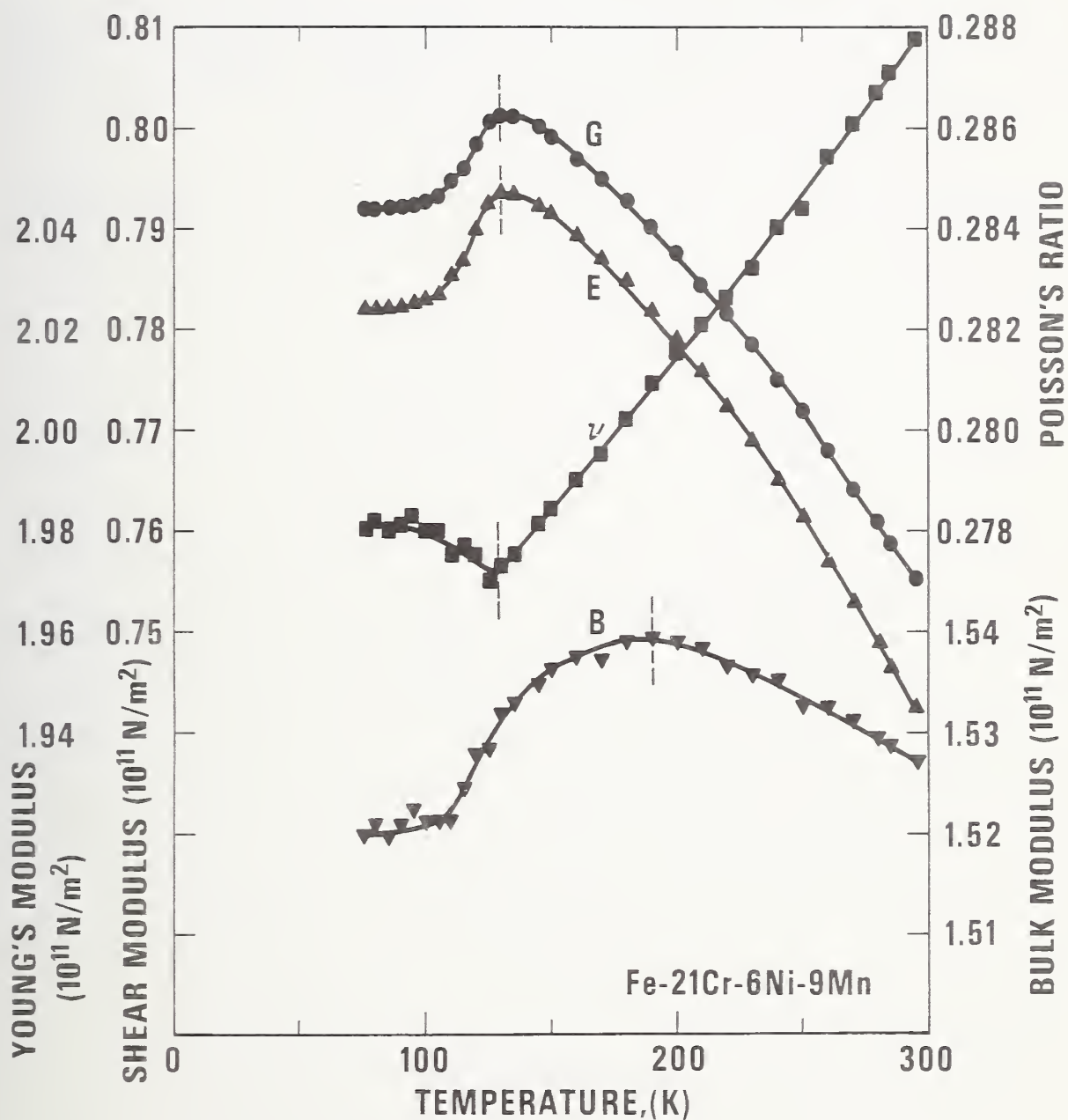


Fig. 2. Shear modulus ( $G$ ), Young's modulus ( $E$ ), Poisson's ratio ( $\nu$ ), and bulk modulus ( $B$ ) computed from data in Fig. 1 by using standard formulas. Note that the bulk-modulus anomaly begins about 60 K higher than the shear-modulus anomaly.



SEMI-ANNUAL REPORT ON MATERIALS RESEARCH  
IN SUPPORT OF SUPERCONDUCTING MACHINERY

FRACTURE MECHANICS PARAMETERS

R. L. Tobler, H. I. McHenry, R. P. Reed, and R. E. Schramm

Cryogenics Division  
Institute for Basic Standards  
National Bureau of Standards  
Boulder, Colorado 80302

October 1976

NBS FRACTURE MECHANICS PROPERTIES STUDIES DURING ARPA  
SPONSORED PROGRAM, SEPTEMBER 1973 TO SEPTEMBER 1976.

Material			Fracture Toughness	Fatigue Crack Growth
1.	Aluminum alloy	2014-T652	5,6	NA
2.	"	" 2219-T87	5	NA
3.	"	" 5083-0	6	6
4.	Inconel alloy	718	5	5
5.	Inconel alloy	750	2	2
6.	Maraging steel,	18Ni, 300 grade	6	6
7.	Iron-49% Ni		6	6
8.	Stainless steel	Nitronic 40 (21-6-9)	5,6	6
9.	"	" A 286	3	3,6
10.	"	" AISI 304	1	1,6
11.	"	" AISI 304L	NA	6
12.	"	" AISI 310	2	2,6
13.	"	" AISI 316	1	1,6
14.	Titanium alloy	Ti-6Al-4V, Normal	1,3	1,3
15.	"	" Ti-6Al-4V, ELI	3	3
16.	"	" i-5Al-2.5Sn, Normal	2	2
17.	"	" Ti-5Al-2.5Sn, ELI	NA	6

## ALUMINUM ALLOY AT LOW TEMPERATURES†

R. L. Tobler and R. P. Reed

Cryogenics Division  
Institute for Basic Standards  
National Bureau of Standards  
Boulder, Colorado 80302

## ABSTRACT

The fatigue crack growth and fracture resistance of a 5083-0 aluminum alloy plate were investigated at four temperatures in the ambient-to-cryogenic range -- 295, 111, 76, and 4 K. J-integral test methods were applied using compact specimens 3.17 cm thick, and the value of J required to initiate crack extension ( $J_{IC}$ ) is reported as an index of fracture toughness. The fracture toughness was orientation dependent, with anisotropy accounting for  $J_{IC}$  variations of up to a factor of 2. For specimens having fracture planes parallel to the rolling direction,  $J_{IC}$  increases progressively from 9 to 25  $\text{kJm}^{-2}$  as temperature decreases between 295 and 4 K. In contrast, the fatigue crack growth rates ( $da/dN$ ) are insensitive to specimen orientation. The fatigue crack growth rates at cryogenic temperatures are up to 10 times lower than in air at room temperature, but are virtually constant between 111 and 4 K. These results should be useful in fracture mechanics analyses of cryogenic structures, including liquified natural gas tankers.

Key words: Aluminum alloys; cryogenics; crack propagation; fatigue; fracture; low temperature tests; mechanical properties.

†Contribution of NBS, not subject to copyright.

## INTRODUCTION

The aluminum alloy designated 5083-0 is strengthened by solid solution additions of magnesium and used in the annealed condition. Excellent formability, weldability, toughness, and relatively low cost are some advantages that make this alloy an attractive low temperature structural material. Applications include storage and transport tanks for cryogenic fluids. Currently, thousands of tons of 5083-0 alloy are destined for use in liquefied natural gas (LNG) tankers at service temperatures as low as 111 K. Emerging applications may include structural components for superconducting machinery. These structures are costly, and in the case of LNG tankers, the transported cryogen is flammable. Design engineers and regulatory agencies therefore require efficient and fail-safe design.

Extensive mechanical property data exist for 5083-0 aluminum [1-7]. Between room and liquid helium temperatures (295 to 4 K), the yield and ultimate strengths increase by 25% and 70%, respectively, with most of the improvement occurring at lower temperatures [2]. Ductility also improves at low temperatures, and precracked specimens retain the ability to deform prior to fracture. Nevertheless, quantitative fracture toughness data for this alloy are lacking. Several attempts to measure the critical stress intensity factor,  $K_{IC}$ , have been unsuccessful. As defined by the ASTM testing method for plane strain fracture toughness of metallic materials (ASTM E 399-74), the parameter  $K_{IC}$  applies to linear-elastic loading behavior. Kaufman, Nelson, and Wygonik [3] showed that 5083-0 alloys in section thicknesses up to 20 cm remain sufficiently plastic to invalidate direct  $K_{IC}$  measurements.



This study employs an alternative approach to fracture toughness characterization. The method is based on Rice's formulation of the J-integral [8], which is the rate of change of potential energy with respect to crack area. In applications of the J-integral, Begley and Landes identify a parameter denoted  $J_{IC}$  which, unlike  $K_{IC}$ , can be measured under nonlinear-elastic conditions [9,10]. Since experimental results for aluminum alloys support the hypothesis that  $J_{IC}$  is a material constant [11,12], the J-resistance curve test method [10] was applied here to a 5083-0 aluminum plate. The  $J_{IC}$  values and fatigue crack growth rates reported in this study should assist fracture mechanics analyses of 5083-0 structures at temperatures in the ambient-to-cryogenic range.

## PROCEDURES

### Material and Specimens

A 4.32 cm thick 5083-0 aluminum alloy plate was obtained from a commercial source and tested in the as-received condition. The microstructure is shown in Figure 1. The ASTM specification B 209-66 gives the chemical composition of this alloy in wt% as: 4.0-4.9 Mg, 0.3-1.0 Mn, 0.05-0.25 Cr, 0.4 max. Si, 0.4 max. Fe, 0.10 max. Cu, 0.25 max. Zn, 0.15 max. Ti, and 0.15 max. of other impurities.

After machining 0.44 cm of metal from each surface of the stock plate, 3.17 cm thick compact specimens were fabricated with the geometry shown in Figure 2. The specimen width,  $W$ , was 7.62 cm. The width-to-thickness ratio,  $W/B$ , was 2.4. Knife edges were machined integral to the notch to enable clip gage attachment and deflection measurements at the loadline. Most of the specimens were machined in the TL orientation (fracture plane normal to the long transverse direction), but

several specimens of the LT orientation (fracture plane normal to the longitudinal or rolling direction) were also tested.

Tensile tests of unnotched, longitudinally-oriented specimens were performed at room and liquid nitrogen temperatures, following ASTM Method E 8-69. Two tests were performed at each temperature. The yield and ultimate strengths, elongation, and reduction of area results, shown in Table 1, agree with other data for similar 5083-0 products [13].

#### Fatigue Crack Growth

A 100 kN servo-hydraulic test machine adaptable for cryogenic service was used in all fatigue and fracture tests. Room temperature tests were conducted in unconditioned air at a relative humidity,  $H$ , of approximately 30%. Low temperatures were achieved by enclosing the load frame, specimen, and clip gage in a dewar of liquid helium (4 K), liquid nitrogen (76 K), or nitrogen gas ( $111 \pm 4$  K). The low temperature apparatus and techniques were previously described [14,15]. The clip gage satisfied ASTM Method E 399-74 linearity requirements, and its sensitivity changed by no more than 5% over the temperature range investigated.

The compact specimens were precracked at their test temperatures using maximum fatigue stress intensity factors of from 10 to 22  $\text{MPa}\cdot\text{m}^{1/2}$ . The minimum-to-maximum load ratio,  $R$ , was 0.1. Some fatigue crack growth rates were measured during precracking, but additional rates at relatively high stress intensity factors or  $R$  values were measured using specimens not intended for J-tests. All precracking and fatigue crack growth tests used sinusoidally-varying loads at a frequency of 20 Hz.

A correlation between crack length ( $a$ ) and specimen compliance

(deflection per unit load,  $\delta/P$ ) was established using measurements from fractured specimens. Crack length was defined as the average of three measurements at the middle and quarter points of specimen thickness. The fatigue tests were then interrupted periodically to record compliance, and the inferred crack length was plotted as a function of load cycles,  $N$ . The fatigue crack growth rates,  $da/dN$ , were calculated by graphical differentiation of  $a$ -versus- $N$  curves, while the corresponding stress intensity factor ranges,  $\Delta K$ , were calculated from the maximum and minimum fatigue loads:

$$\Delta K = (P_{\max} - P_{\min})B^{-1}W^{-1/2}[f(a/W)], \quad (1)$$

According to ASTM Method E 399-74,

$$f(a/W) = 29.6(a/W)^{1/2} - 185.5(a/W)^{3/2} + 655.7(a/W)^{5/2} - 1017.0(a/W)^{7/2} + 638.9(a/W)^{9/2}. \quad (2)$$

The uncertainty in crack growth rates is estimated at less than  $\pm 25\%$ .

#### Fracture Toughness

At each test temperature, a series of specimens having similar pre-crack lengths were loaded to selected deflections at the stroke rate of  $0.05 \text{ mms}^{-1}$ . These loadings were sufficient to cause stable crack extensions of up to 0.25 cm. Each specimen was then unloaded and refatigued using cyclic loads no greater than 70% of the maximum static load. After the refatigue crack was propagated several millimeters, the specimens were fractured into halves by a single loading.

The fracture surfaces showed, in succession: (1) a precrack zone, (2) a crack extension increment due to static loading, and (3) a refatigue

crack zone. The relatively coarse and less reflective increment of static crack extension was measured to the nearest 0.003 cm with a traveling microscope at the center and quarter points of specimen thickness, the three-point average being defined as  $\Delta a$ . The corresponding values of  $J$  were calculated for each test, using the approximate solution for deeply cracked compact specimens [16]:

$$J = 2A/Bb. \quad (3)$$

Here,  $A$  is the total area (energy) under the test record up to the point of unloading, and  $b$  is the original ligament depth ( $b = W - a$ ). The uncertainty in  $J$  measurements was not greater than  $\pm 2\%$ .

To obtain critical  $J$  values, the resistance curves of  $J$ -versus- $\Delta a$  were back-extrapolated to  $\Delta a = 0.005$  cm. In tests of a 2219-T6 aluminum alloy, Read and Reed [12] suggested that defining  $J_{IC}$  at 0.005 cm crack extension leads to reproducible results. The uncertainty in the  $J_{IC}$  values obtained in this way for 5083-0 aluminum is estimated at  $\pm 15\%$ .

## RESULTS AND DISCUSSION

### Fatigue Crack Growth

Fatigue crack growth data at 4, 76, 111, and 295 K for 5083-0 aluminum specimens of the TL orientation at  $R = 0.1$  are shown in Figure 3. The results span two orders of magnitude from  $5 \times 10^{-6}$  mm/cycle to  $2.5 \times 10^{-3}$  mm/cycle. For a given  $\Delta K$  value, the rates of crack growth at 111, 76, and 4 K are equivalent within the degree of scatter among replicate tests. However, the rates at room temperature are up to 10 times faster than the rates at cryogenic temperatures.

As plotted on logarithmic coordinates, the low temperature fatigue crack growth data describe an approximately linear trend over the entire  $\Delta K$  range, whereas the room temperature data do not. The linear approximation to the data at 111, 76 and 4 K, shown in Figure 3, is consistent with a Paris equation of the form:

$$\frac{da}{dN} = C(\Delta K)^n. \quad (4)$$

Here  $da/dN$  (mm/cycle) is a power law function of  $\Delta K$  ( $\text{MPa}\cdot\text{m}^{1/2}$ ). The constants  $C$  and  $n$  correspond to the ordinate intercept at  $\Delta K = 1$ , and the slope, respectively. A graphical solution for the equation of the line drawn through the 111, 76 and 4 K data yields:

$$\frac{da}{dN} = 1.3 \times 10^{-10} (\Delta K)^{5.2}. \quad (5)$$

The room temperature data fail to conform to a single power-law equation, due to the appearance of a "shoulder" on the  $da/dN$ -versus- $\Delta K$  plot at  $\Delta K$  values between 10 and 15  $\text{MPa}\cdot\text{m}^{1/2}$ . This shoulder brings the room and low temperature crack growth rates into closer agreement at higher  $\Delta K$  values. Consequently, the room temperature fatigue crack growth resistance is only slightly inferior at stress intensity factor ranges greater than 15  $\text{MPa}\cdot\text{m}^{1/2}$ .

Figure 4 shows additional crack growth data for the TL orientation at 295 and 111 K ( $R = 0.3$ ), as well as data on specimens of the LT orientation at 111 K ( $R = 0.1$ ). Scatterbands representing the data of Figure 3 are superimposed on Figure 4 for comparison. This comparison indicates that the change in  $R$  from 0.1 to 0.3 had no effect on the



room temperature fatigue crack growth rates, whereas, at 111 K, this change increased the rates by nearly a factor of 2. Also the data obtained for specimens of the LT orientation at 111 K fall within the band for TL orientations for the same stress ratio,  $R = 0.1$ . Thus, specimen orientation has no measureable effect on fatigue crack growth rates. Kaufman and Kelsey [17] also noted relatively isotropic fatigue crack growth in their tests of a 5083-0 aluminum alloy.

Comparisons of fatigue crack growth data reported in the literature for compact specimens of 5083-0 aluminum are shown in Figures 5 and 6. Although these data show considerable variance, most results can be rationalized in terms of the different test variables and procedures. Usually, higher  $R$  values lead to increased fatigue crack growth rates. Other significant factors to be considered include the procedure used to obtain  $a$ -versus- $N$  data, and the relative humidity at room temperature.

In reference to Figures 5 and 6 note first that the present study yielded somewhat lower rates at a given  $\Delta K$  value as compared with other investigations [4,17-19]. In our study, the crack length was defined as an average of measurements at the center and quarter points of thickness. Other studies used measurements of the crack at specimen edges. In our study the edge crack lengths were typically 5 to 8% shorter than the average crack lengths. If edge crack lengths had been used, the  $f(a/W)$  values of Eq. (1) would have been reduced, and the  $\Delta K$  value for a given growth rate would have been 10 to 17% lower than actually reported. This would shift the bands of Figures 5 and 6 into good agreement with the bulk of previously published results.

As shown in Figure 5, at least three other laboratories report a shoulder in room temperature fatigue crack growth rates [17-19]. This



shoulder occurs at rates near  $3 \times 10^{-4}$  mm/cycle, for tests conducted in air with appreciable moisture contents. Kelsey, Nordmark and Clark's [4] room temperature results at 90% relative humidity and  $R = 0.33$  are nearly in agreement with Argy, Paris, and Shaw's [18] results at  $\sim 50\%$  relative humidity and  $R = 0.4$ . However, as the relative humidity is decreased to less than 10%, the shoulder is eliminated and fatigue crack propagation resistance at low  $\Delta K$  is improved. Note in Figure 5 that the overall agreement of data is better at high  $\Delta K$  values where differences in relative humidity are less influential.

Deleterious effects on the fatigue crack growth resistance of this alloy due to moisture are not surprising in view of the trends exhibited by other aluminum alloys [20]. Hartman and Schijve's [21] data for a 7075-T6 alloy demonstrate trends analogous to the behavior indicated in Figure 5. In dry air, their logarithmic plots of  $da/dN$ -versus- $\Delta K$  display a linear trend for growth rates in the range  $10^{-5}$  to  $10^{-3}$  mm/cycle; in moist air (relative humidity = 45%), a shoulder appears in the data at  $\Delta K \approx 15 \text{ MPa}\cdot\text{m}^{1/2}$ , and the rates at lower  $\Delta K$  are accelerated by up to a factor of 10. Again, the rates at high  $\Delta K$  are not sensitive to moisture.

Thus, the effects of moisture on the room temperature fatigue crack growth behavior of 5083-0 and 7075-T6 alloys are remarkably similar. The trend of the Kelsey et al. [4] data for 5083-0 aluminum in a dry air environment probably represents the true trend of room temperature results when moisture effects are practically eliminated. Note from Figures 5 and 6 that the rates reported by Kelsey et al. [18] for tests in dry air at 295 K are nearly equivalent to but slightly faster than their rates at 76 K. Based on these observations, it may be concluded

that moisture effects at 295 K are predominant, and temperature variations between 295 K and 4 K intrinsically have little effect on the fatigue crack propagation resistance of 5083-0 aluminum. This is consistent with results for other face-centered cubic alloys which show only modest improvements of fatigue crack growth resistance at low temperatures [22].

### Fracture Toughness

Plasticity and stable crack extension caused nonlinearity in the fracture test records at all temperatures, and unstable cracking was never observed. As expected, the linearity requirements of sections 9.1.2 and 9.1.5 of ASTM Method E 399-74 could not be satisfied using our specimens of aluminum alloy 5083-0, so it was appropriate to conduct J-integral tests. Table 2 lists the J-integral test results for both the LT and TL specimen orientations.

Resistance curves (J-versus- $\Delta a$  graphs) for the TL orientation are shown in Figure 7. The results at 295, 111, 76, and 4 K show that higher J values are required for a given crack extension as temperature decreases. The  $J_{IC}$  values obtained at  $\Delta a = 0.005$  cm progressively increase from 9 to 25  $\text{kJm}^{-2}$  between 295 and 4 K. Moreover, the rate of increase of J with respect to  $\Delta a$  is greater at 111, 76, and 4 K than at room temperature. Thus, greater energy is expended in fracture initiation and propagation at cryogenic temperatures. Kahn-type tear and dynamic tear tests render a similar conclusion [5-7, 23].

Figure 8 compares the J-resistance curves for the TL and LT orientations at 111 K, demonstrating the anisotropy of fracture toughness for this alloy. Based on these curves,  $J_{IC}$  for the LT orientation is approximately 39  $\text{kJm}^{-2}$  at 111 K, or twice the value for the TL orientation. The superiority of the LT orientation in comparison with the TL

orientation is typical of many alloys, and the tear test results and projected  $K_{IC}$  values reported by Kaufman et al. [3,5,6] indicate a similar orientation dependence for 5083-0 aluminum.

The fracture anisotropy is also evident in Figure 9, which shows TL and LT specimens that were tested at 111 K. The LT specimen was fatigue cracked and fractured in a single loading. The TL specimen was used in a J-test, and it shows an increment of crack extension,  $\Delta a$ , located between two fatigue cracks. The LT specimen displays shear fracture portions amounting to 30% of specimen thickness; delaminations are also visible at mid-thickness. In comparison, the TL specimen exhibits a flat fracture mode requiring less energy for crack extension. The fracture surface appearance of the TL orientation was not significantly influenced by test temperature.

The  $J_{IC}$  data listed in Table 2 can be used to estimate  $K_{IC}$  values by using the equation:

$$K_{IC}^2 = \frac{E J_{IC}}{1 - \nu^2} \quad (6)$$

In this equation,  $E$  is Young's modulus of elasticity and  $\nu$  is Poisson's ratio. The values of  $E$  and  $\nu$  at temperatures between 295 and 4 K are known from Naimon, Weston, and Ledbetter's study [24]. The  $K_{IC}$  estimates based on these data at 295, 111, 76 and 4 K are plotted in Figure 10, along with the corresponding  $J_{IC}$  values.

As shown in Figure 10, the  $K_{IC}$  estimates converted from  $J_{IC}$  data range from 27.0 to 60.2  $\text{MPa}\cdot\text{m}^{1/2}$ , depending on temperature and specimen orientation. For the TL orientation, the  $K_{IC}$  estimates at 295 and 76 K are 27.0 and 43.4  $\text{MPa}\cdot\text{m}^{1/2}$ , respectively. These are lower than Kaufman

and Kelsey's [17] projected  $K_{IC}$  estimates of  $49.5 \text{ MPa}\cdot\text{m}^{1/2}$  at 295 K and  $55 \text{ MPa}\cdot\text{m}^{1/2}$  at 77 K. Kaufman and Kelsey's  $K_{IC}$  estimates also pertain to specimens of the TL orientation, but their K calculations are based on the maximum load observed in fracture tests. Their procedure does not account for the fact that crack extension occurs prior to maximum load.

Finally, it should be noted that Merkle and Corten's method [25] of J calculation could have been used in this study. When applied to the 5083-0 aluminum experiments described in the text, that method amounts to replacing the coefficient 2 in Eq. (3) by higher factors from 2.2 to 2.3. The  $J_{IC}$  values would have been increased by about 10%; the  $K_{IC}$  estimates, by 5%. Read and Reed [12] found from measuring both  $K_{IC}$  and  $J_{IC}$  at 76 K for the aluminum alloy 2219-T87 that  $J_{IC}$  as calculated from the measured  $K_{IC}$  was about 40% greater than the measured  $J_{IC}$ . Thus, the  $J_{IC}$  data and  $K_{IC}$  estimates reported here for 5083-0 may be considered conservative.

#### SUMMARY AND CONCLUSIONS

The fatigue crack growth behavior and J-integral fracture toughness of a 5083-0 aluminum alloy have been investigated at 295, 111, 76 and 4 K, a wider range of temperatures than previously studied. Specifically:

1. Fatigue crack growth resistance at 111 K was insensitive to specimen orientation, but improves at decreasing R ratios.
2. Although the fatigue crack growth rates in ambient air at room temperature exceed the rates at cryogenic temperatures by up to a factor of 10, the rates between 111 and 4 K are nearly equivalent. The high rates in ambient air can be attributed to the presence of moisture, rather than temperature effects per se.

3. Results for the TL orientation at decreasing temperatures between 295 K and 4 K indicate nearly a three-fold increase of  $J_{IC}$  from 9 to 25  $\text{kJm}^{-2}$ .

4. Anisotropy in rolled plate caused a  $J_{IC}$  variation of a least 2:1 at the LNG temperature of 111 K.

5. In view of the favorable low temperature effects on tensile, fatigue, and fracture properties, it is apparent that the structural reliability of flawed or unflawed 5083-0 alloy components will not be decreased by cryogenic temperatures.

#### ACKNOWLEDGMENTS

This work was sponsored by the Maritime Administration and the Advanced Research Projects Agency of the U.S. Department of Defense. The authors gratefully acknowledge the assistance of R. L. Durcholz and Dr. R. P. Mikesell in conducting the tensile tests. We also wish to thank Dr. R. A. Kelsey of the Alcoa Technical Center for reviewing the manuscript.



## REFERENCES

1. Properties of Materials for Liquefied Natural Gas Tankage, ASTM STP 579, Amer. Soc. Test. Mater., Philadelphia, 1975, pp. 1-204.
2. Rice, L. P., Campbell, J. E., and Simmons, W. F., in Advances in Cryogenic Engineering, Vol. 8, 1963, pp. 671-677.
3. Kaufman, J. G., Nelson, F. G., and Wygonik, R. H., in Fatigue and Fracture Toughness -- Cryogenic Behavior, ASTM STP 556, Amer. Soc. Test. Mater., 1974, pp. 125-158.
4. Kelsey, R. A., Nordmark, G. E., and Clark, J. W., in Fatigue and Fracture Toughness -- Cryogenic Behavior, ASTM STP 556, Amer. Soc. Test. Mater., 1974, pp. 159-185.
5. Kaufman, J. G., Nelson, F. G., and Wanderer, E. T., Mechanical Properties and Fracture Characteristics of 5083-0 Products and 5183 Welds in 5083 Products, Proceedings of the International Congress of Refrigeration, Washington, D.C., Vol. 1, 1971, pp. 651-658.
6. Nelson, F. G., Kaufman, J. G., and Wanderer, E. T., Tear Tests of 5083 Plate and of 5183 Welds in 5083 Plate and Extrusions, Paper D-1 in Adv. in Cryo. Eng., K. D. Timmerhaus, Ed., pp. 91-101.
7. Judy, R. J., Jr., and Goode, R. J., Fracture Resistance of Thick Plate 5083-0 Alloy, Report of NRL Progress, December 1974, pp. 36-38.
8. Rice, J. R., J. Appl. Mechs., Trans. ASME, Vol. 35, 1968, pp. 379-386.
9. Begley, J. A. and Landes, J. D., in Fracture Toughness, ASTM STP 514, Amer. Soc. Test. Mater., 1972, pp. 1-39.
10. Landes, J. D. and Begley, J. A., in Fracture Analysis, ASTM STP 560, Amer. Soc. Test. Mater., 1975, pp. 170-186.



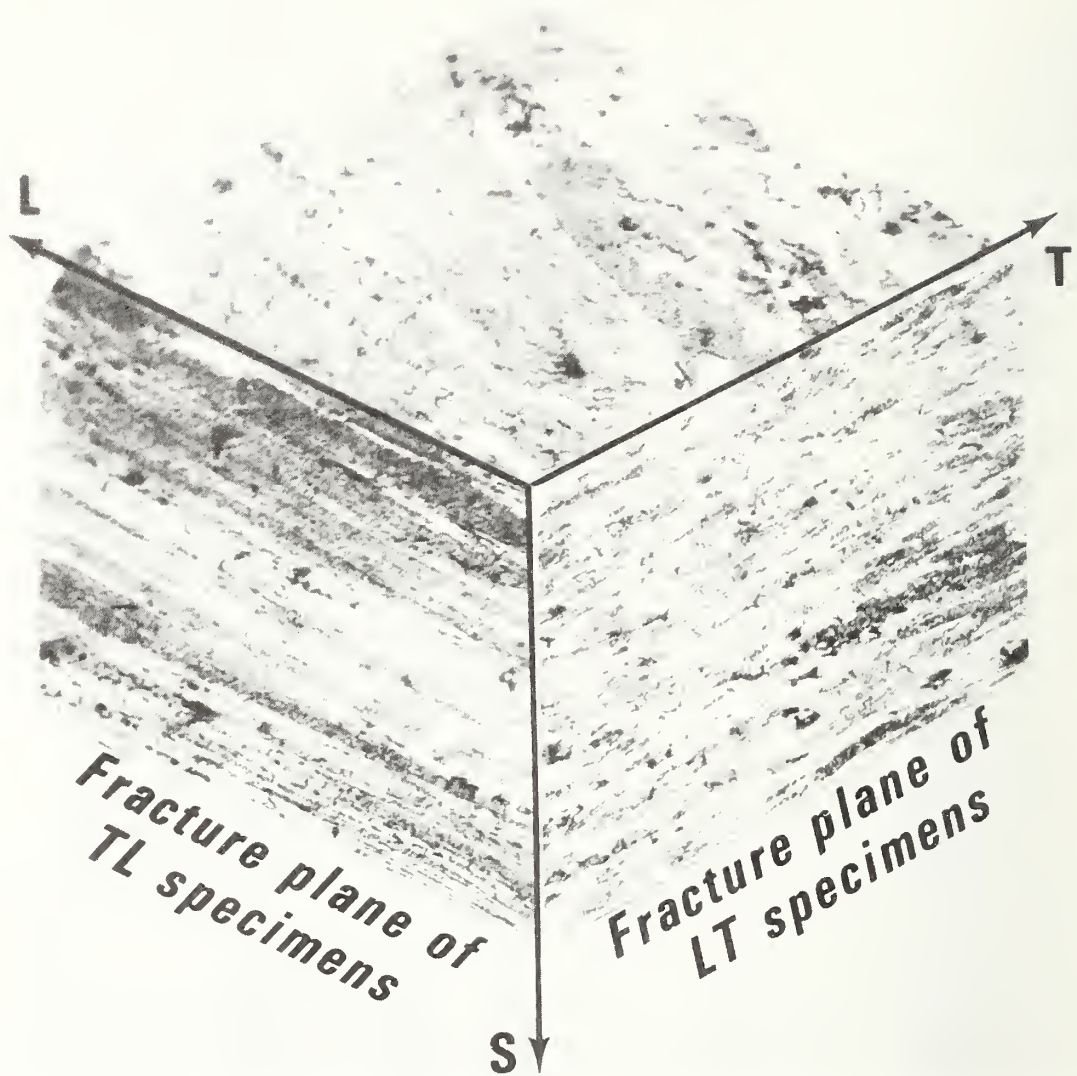
11. Griffis, C. A. and Yoder, G. R., Application of the J-Integral to Crack Initiation in a 2024-T351 Aluminum Alloy, Naval Research Report 7676, 1974, pp. 1-25.
12. Read, D. T. and Reed, R. P., Effects of Specimen Thickness on Fracture Toughness of Some Aluminum Alloys, submitted to Int. J. Fract. (1976).
13. Bogardus, K. O. and Malcolm, R. C., in Ref. 1, pp. 190-204.
14. Fowlkes, C. W. and Tobler, R. L., Fracture Testing and Results for a Ti-6Al-4V Alloy, Eng. Fract. Mechs., to be published.
15. Tobler, R. L., Mikesell, R. P., Durholz, R. L., and Reed, R. P., in Ref. 1, pp. 261-287.
16. Rice, J. R., Paris, P. C., and Merkle, J. G., in Progress in Flaw Growth and Fracture Toughness Testing, ASTM STP 536, Amer. Soc. Test. Mater., 1973, pp. 231-244.
17. Kaufman, J. G. and Kelsey, R. A., in Ref. 1, pp. 138-158.
18. Argy, R., Paris, P. C., and Shaw, F., in Ref. 1, pp. 96-137.
19. Person, N. L. and Wolfer, G. C., in Ref. 1, pp. 80-95.
20. Wei, R. P., Eng. Fract. Mechs., Vol. 4, 1970, pp. 633-651.
21. Hartman, A. and Schijve, NLR Tech Note No. MP 68001 U, 1968; see also Fig. 11 of Reference 17.
22. Materials Research in Support of Superconducting Machinery, Vols. III, IV, and V, Reed, R. P., Clark, A. F., and van Reuth, E. C., Eds., National Bureau of Standards, Boulder, CO.
23. Zinkham, R. E. and Ashton, R. F., in ASTM STP 579, Ref. 1, pp. 159-175.
24. Weston, W. F., Naimon, E. R., and Ledbetter, H. M., in Ref. 1, pp. 397-420.
25. Merkle, J. G. and Corten, H. T., "A J-Integral Analysis for the Compact Specimen, Considering Axial Force as Well as Bending Effects," presented at the Pressure Vessels and Piping Conference with Nuclear Engineering and Mechanical Divisions, American Society of Mechanical Engineers, Paper No. 74-PVP-33, 1974.

Table 1. Tensile property results for 5083-0 aluminum alloy specimens in the longitudinal orientation (average values for two tests per temperature).

Temperature K	(°F)	0.2% Yield Strength MPa	Strength (ksi)	Ultimate Strength MPa	Strength (ksi)	Elongation (2.54 cm gage) %	Reduction of Area %
295	(70)	142	(20.6)	305	(44.2)	23.4	36.9
76	(-323)	150	(21.7)	404	(58.6)	34.1	36.7
4	(-452)	186	(27.0)	472	(68.5)	23.2	11.6

Table 2. J-integral test results.

Temperature K	Specimen	Orientation	$K_{fmax}$ $MPa \cdot m^{1/2}$	a/W cm	$\Delta a$ cm	J $kJm^{-2}$	$J_K$ $kJm^{-2}$
295	13	TL	14	.642	.010	10.3	9
	28	TL	21	.647	.020	15.8	
	9	TL	15	.647	.029	20.1	
	8	TL	21	.620	.036	22.9	
	31	TL	13	.641	.059	27.5	
	7	TL	15	.644	.070	30.5	
	14	TL	22	.611	.109	41.6	
111	2	LT	16	.622	.033	65.6	41
	3	LT	18	.612	.019	54.2	
	4	LT	18	.622	.033	60.8	
	5	LT	18	.619	.053	76.0	
111	30	TL	19	.622	.010	23.6	19
	20	TL	13	.630	.023	36.4	
	22	TL	14	.617	.056	59.1	
	10	TL	20	.629	.103	78.5	
	11	TL	20	.617	.253	122.4	
76	20	TL	15	.629	.010	27.9	21
	17	TL	14	.623	.019	31.2	
	19	TL	16	.631	.026	40.5	
	16	TL	14	.633	.039	54.7	
	14	TL	17	.628	.083	72.5	
	9	TL	21	.632	.093	77.3	
4	15	TL	19	.602	.003	13.7	25
	11	TL	18	.597	.003	17.6	
	10	TL	20	.608	.010	30.2	
	17	TL	19	.602	.019	38.3	
	16	TL	18	.602	.030	47.3	
	18	TL	18	.597	.056	61.4	



**L—longitudinal or rolling direction**

**T—long transverse direction**

**S—short transverse or plate thickness direction**

Figure 1. Microstructure of 5083-O after rolling and annealing, 100X.

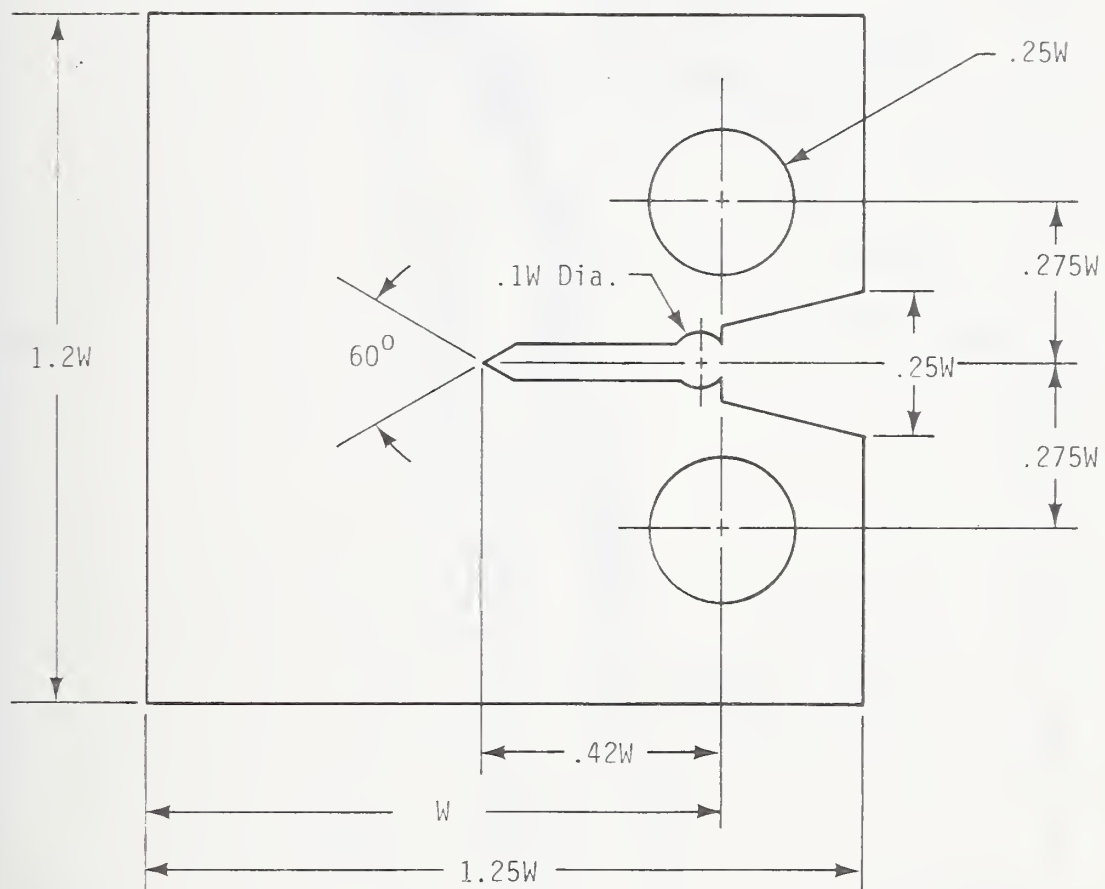


Figure 2. Compact specimen used in fatigue and fracture tests (thickness,  $B = 3.17$  cm; dimensions are in cm).

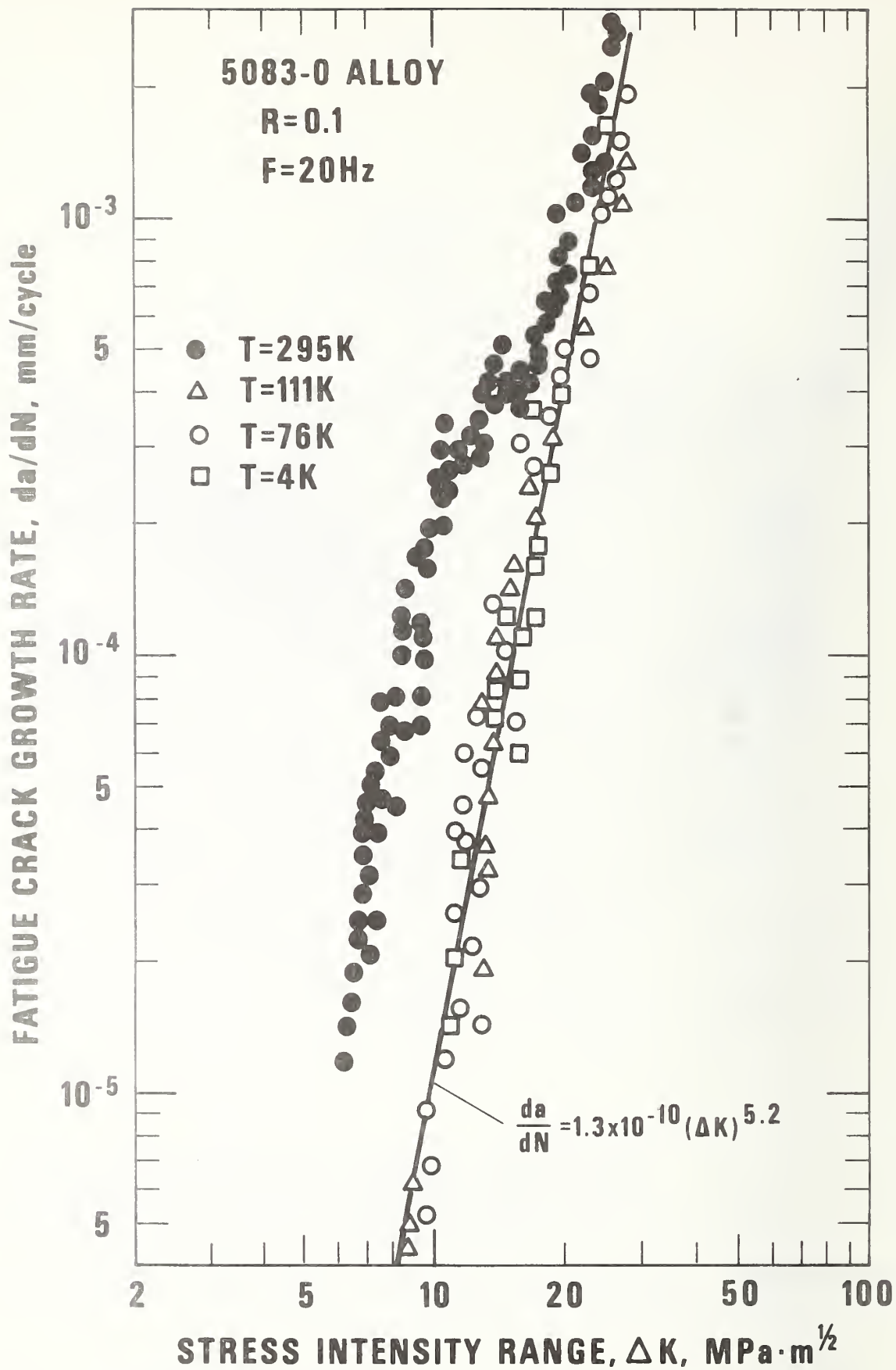


Figure 3. Fatigue crack growth rate results for TL orientations at 295, 111, 76 and 4 K.



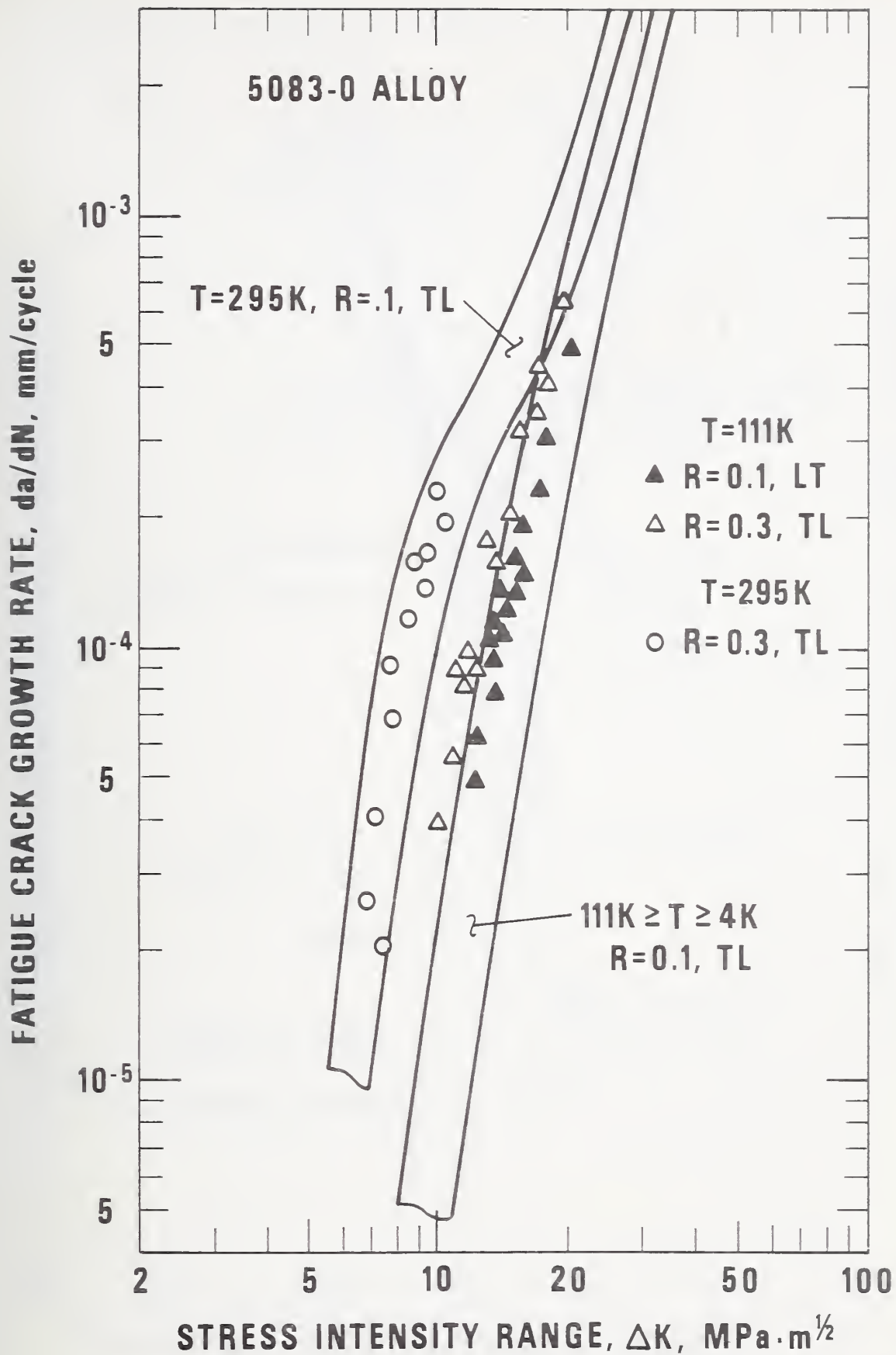


Figure 4. Fatigue crack growth rate results at 295 and 111 K, showing the effects of orientation and R ratio variations.

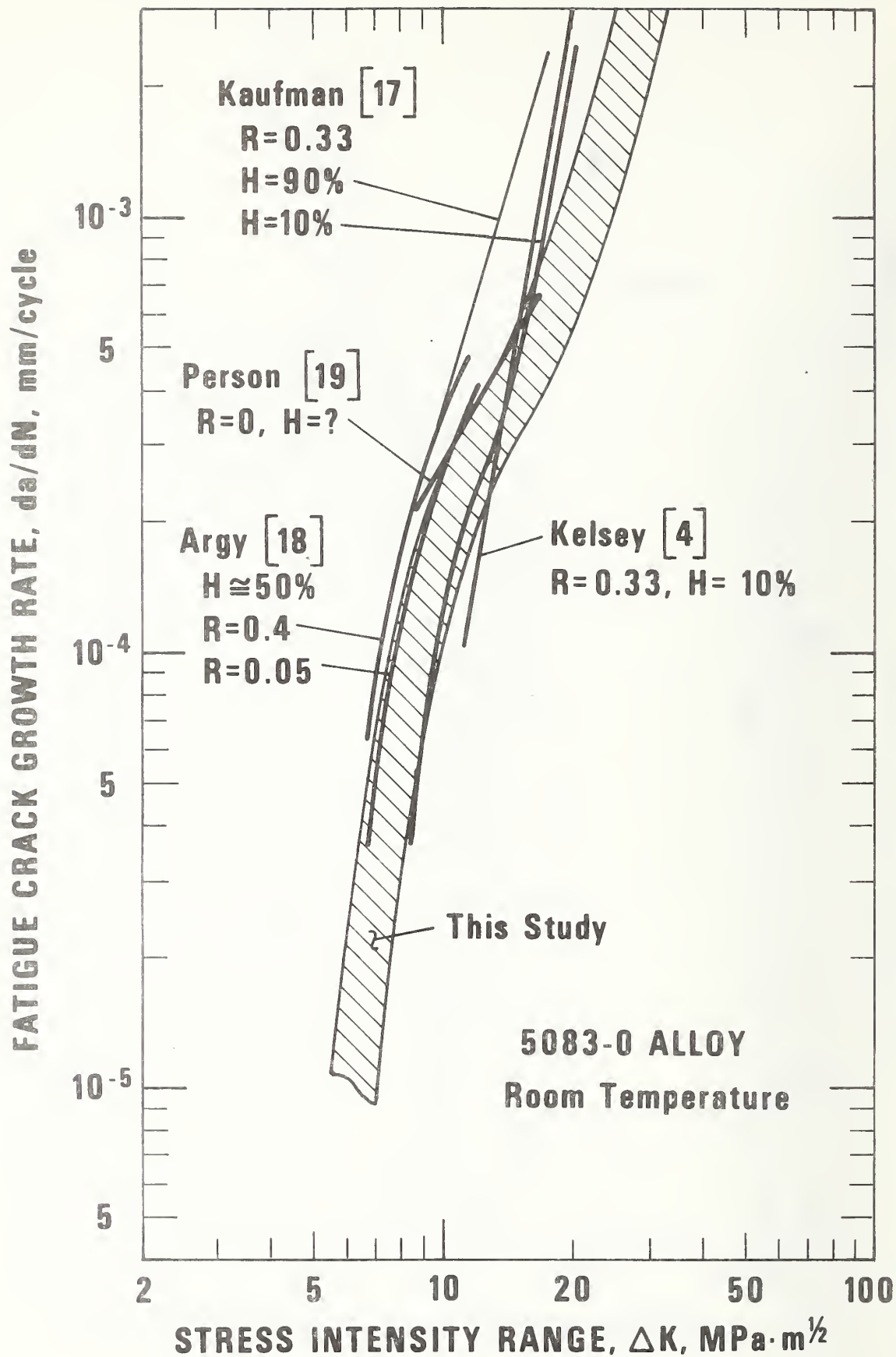


Figure 5. Comparison of fatigue crack growth data at 295 K.

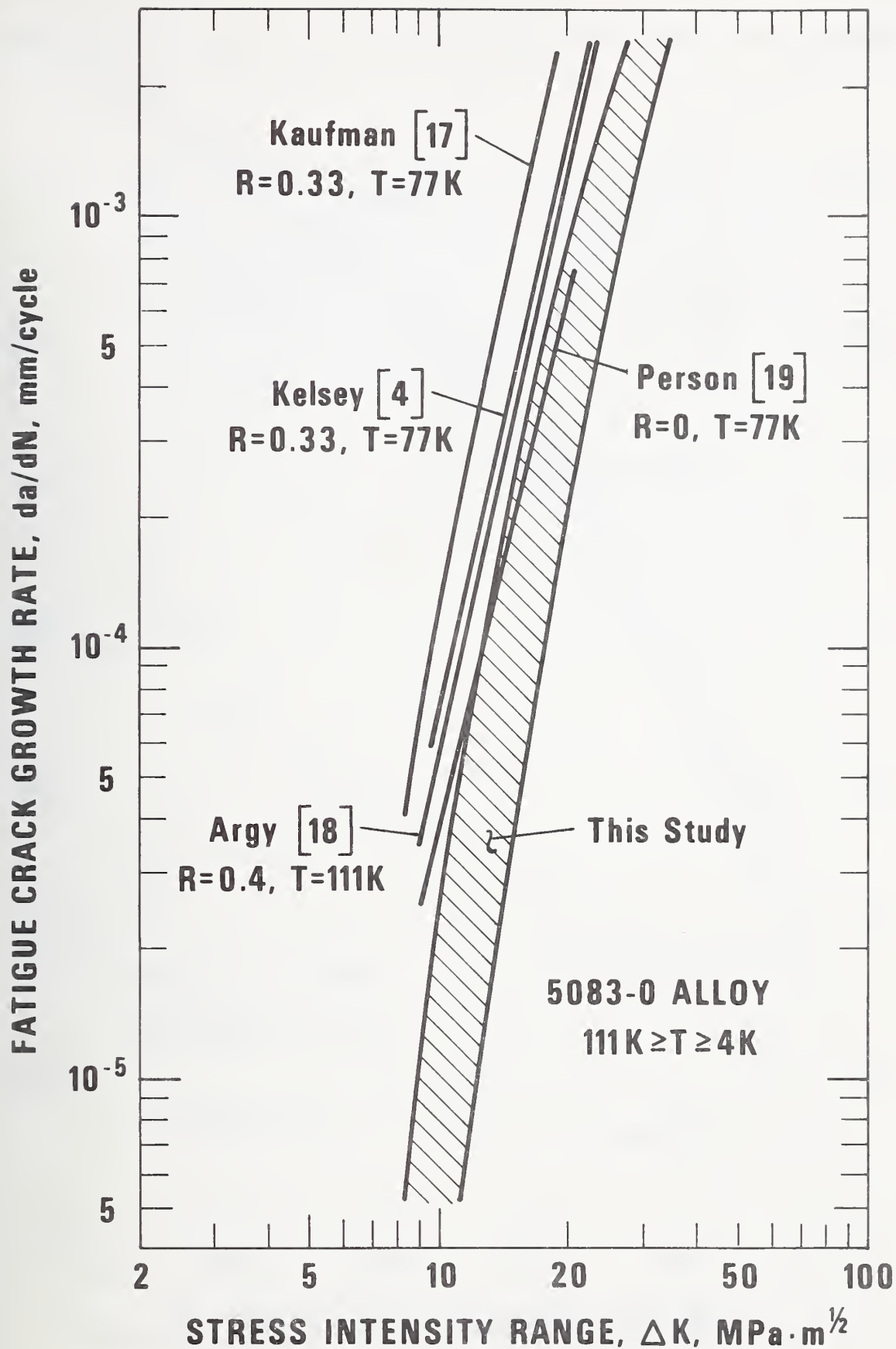


Figure 6. Comparison of fatigue crack growth data at low temperatures.

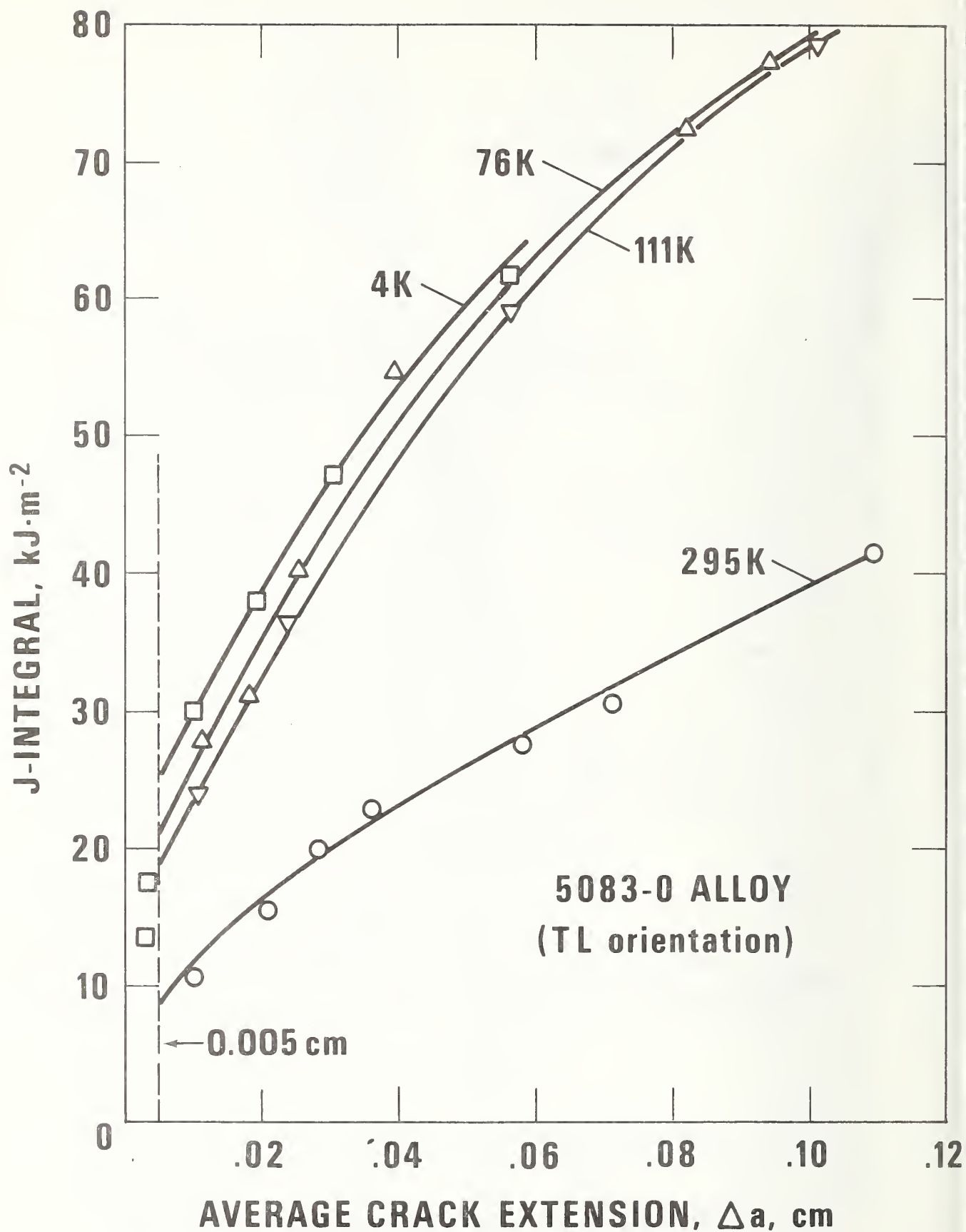


Figure 7. J-integral resistance curves for 5083-0 aluminum, showing the effect of temperature.

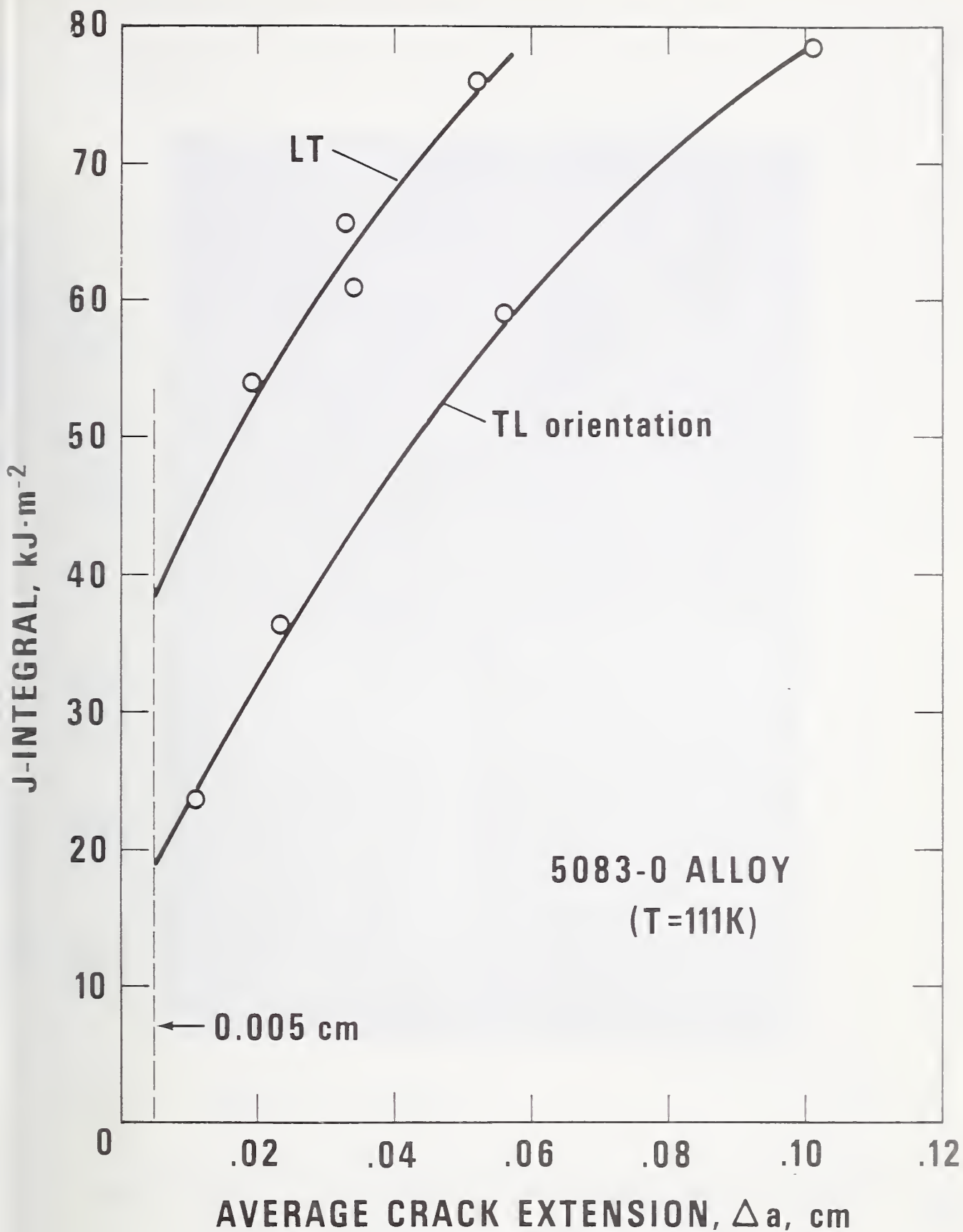


Figure 8. J-integral resistance curves for 5083-0 aluminum at 111 K, showing the effect of orientation.



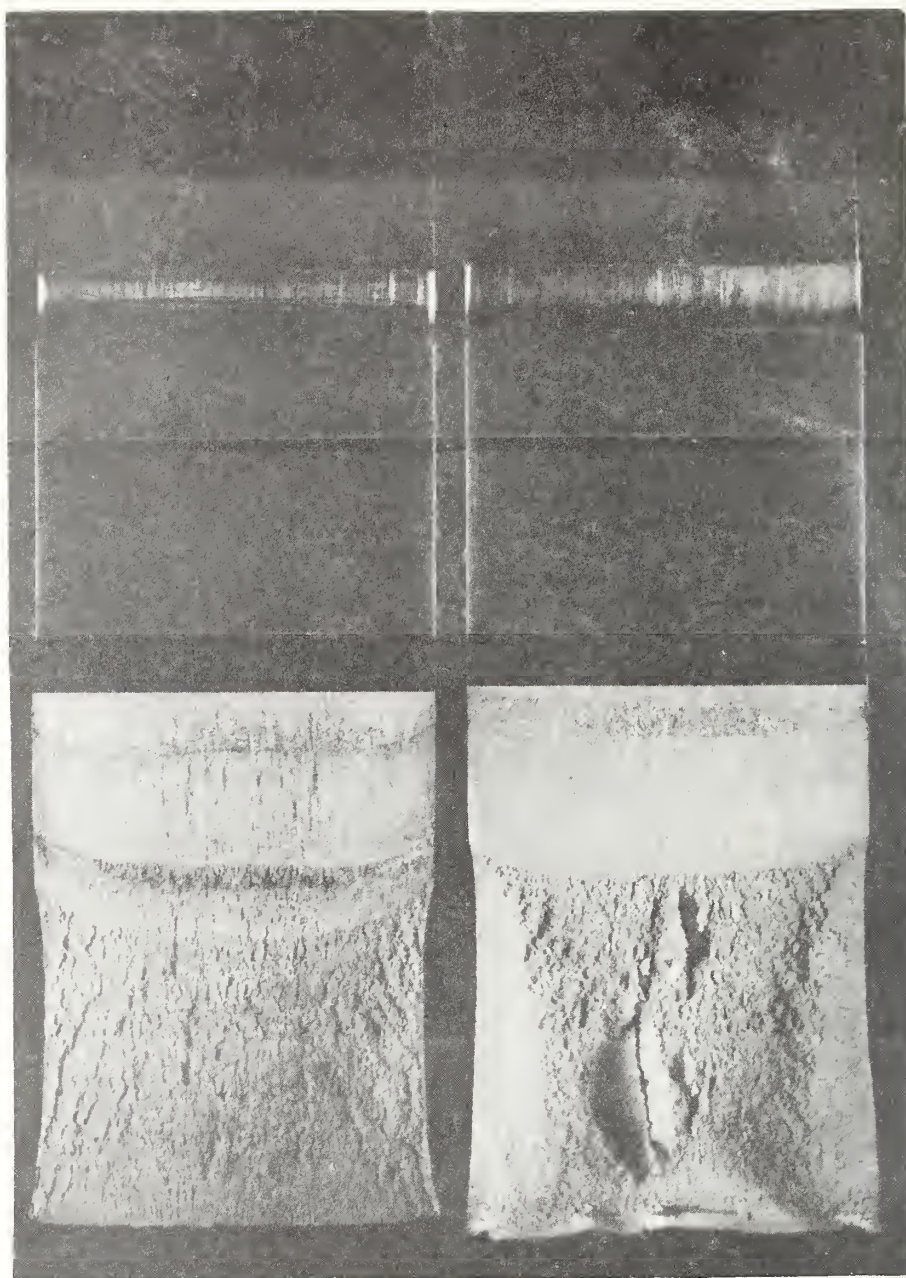


Figure 9. Fracture appearance of LT (left) and TL (right) specimens tested at 111 K.



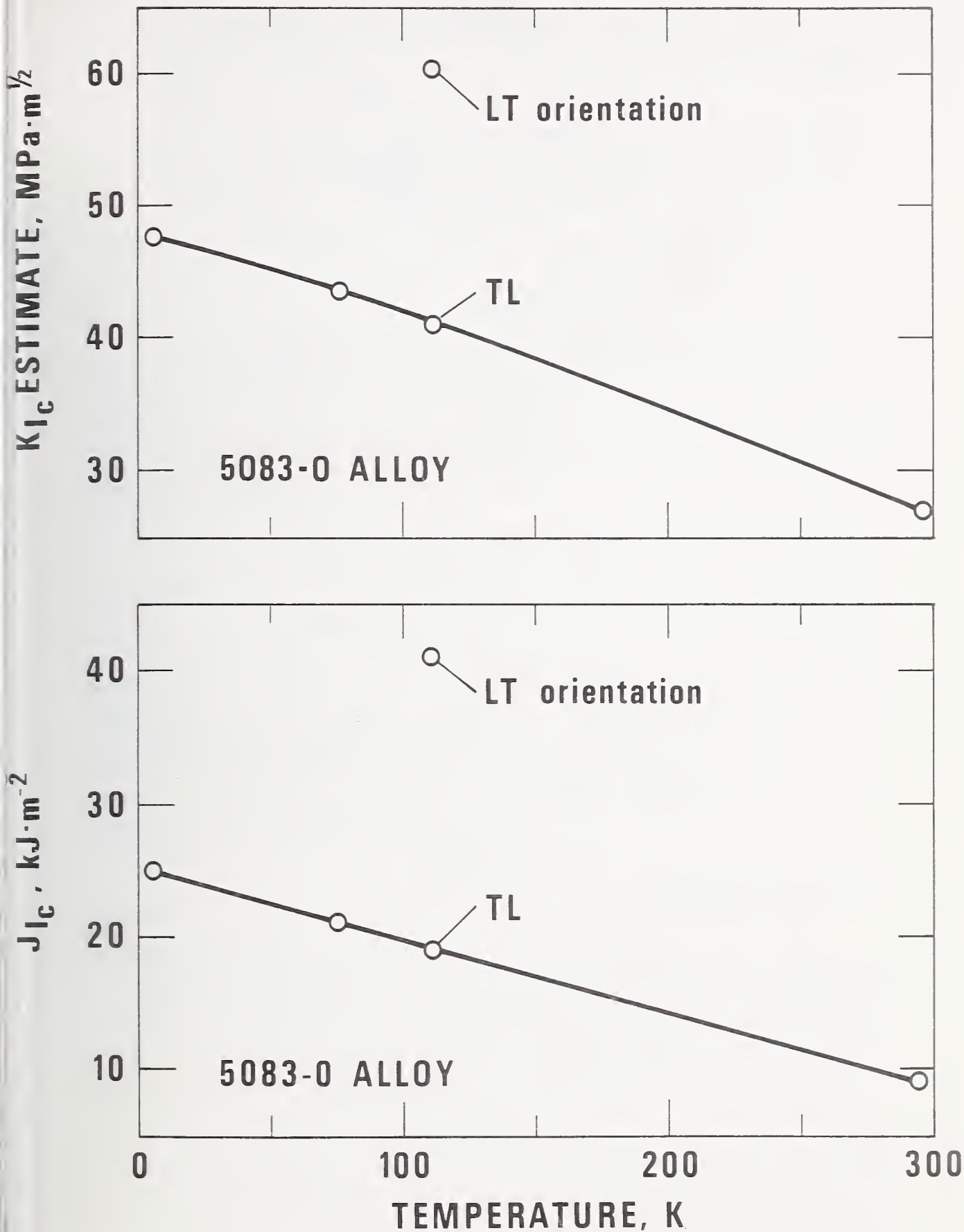


Figure 10. Temperature dependences of  $J_{Ic}$  data and  $K_{Ic}$  estimates.

TENSILE AND FRACTURE BEHAVIOR OF A NITROGEN-STRENGTHENED,  
CHROMIUM-NICKEL-MANGANESE STAINLESS STEEL AT CRYOGENIC TEMPERATURES\*

R. L. Tobler and R. P. Reed

Cryogenics Division  
Institute for Basic Standards  
National Bureau of Standards  
Boulder, Colorado 80302

ABSTRACT

J-integral-fracture and conventional tensile properties are reported for an Fe-21Cr-6Ni-9Mn austenitic stainless steel that contains 0.28% N as an interstitial strengthening element. Results at room (295 K), liquid-nitrogen (76 K), and liquid-helium (4 K) temperatures demonstrated that the yield strength and fracture toughness of this alloy are very temperature dependent. Over the investigated temperature range, the yield strength tripled to 1.24 GPa (180 ksi) at 4 K. The fracture toughness, as measured using 3.8-cm-thick compact specimens, decreased considerably between 295 and 4 K. During plastic deformation at 295 K the alloy undergoes slight martensitic transformation, but at 76 and 4 K it transforms extensively to hcp and bcc martensites. The amount of bcc martensite formed during tensile tests was measured as a function of elongation.

Key words: Cryogenics; fracture; low temperature tests; martensitic transformations; mechanical properties; stainless steel alloys.

\*NBS contribution, not subject to copyright.

## Introduction

Recently, austenitic stainless steel strengths have been increased considerably by the substitution of nitrogen and manganese for nickel. In addition to providing interstitial and solid solution strengthening, these elements serve to increase austenite stability with respect to martensitic transformations. Compared to nickel, these elements are more abundant and less expensive. The alloy studied in this report, Fe-21Cr-6Ni-9Mn-0.3N (21-6-9), has a room temperature yield strength nearly twice that of AISI 304. Available tensile and impact data<sup>(1-4)</sup> suggest that 21-6-9 retains good toughness at low temperatures, leading to consideration of its use for applications benefiting from high strength and toughness.

Accordingly, 21-6-9 is currently being considered for such critical components as the coil form for the prototype controlled thermonuclear reaction superconducting magnets and the torque tube for rotating superconducting machinery. To insure satisfactory service life and to compare with other candidate materials it is necessary to evaluate the fracture resistance of the alloy. This study presents the first fracture toughness data for this alloy.

## Material

The 21-6-9 austenitic stainless steel plate was processed and donated by Lawrence Livermore Laboratories, Livermore, California. The chemical composition (in weight percent) of this heat is: 19.75 Cr, 7.16 Ni, 9.46 Mn, 0.019 C, 0.15 Si, 0.004 P, 0.003 S, and 0.28 N. This steel was hot rolled from 30.5 x 30.5 x 10 cm slabs to 50 x 50 x 3.6 cm plate using the following schedule:

soak for 4 hours at 1366 K;

roll from 10 cm to 9.4 cm, screw down (compress) to 9.3 cm;

roll from 9.3 cm to 8.7 cm, screw down to 8.6 cm, rotate 90°;

roll from 8.6 cm to 8.0 cm, screw down to 7.9 cm;

roll from 7.9 cm to 7.4 cm, screw down to 7.3 cm, rotate 90°;

roll from 7.3 cm to 6.9 cm, screw down to 6.7 cm;

roll from 6.7 cm to 6.3 cm, screw down to 6.2 cm, rotate 90°;

roll from 6.2 cm to 5.9 cm, screw down to 5.7 cm;

roll from 5.7 cm to 5.4 cm, screw down to 5.3 cm, rotate 90°;

roll from 5.3 cm to 5.0 cm, screw down to 4.8 cm;

roll from 4.8 cm to 4.5 cm, screw down to 4.3 cm, rotate 90°;

roll from 4.3 cm to 4.2 cm, screw down to 4.0 cm;

roll from 4.0 cm to 3.8 cm, screw down to 3.6 cm.

The final plate temperature after this hot rolling was 1089 K. Each plate was then annealed at 1283 K for 1-1/2 hours and air cooled, followed by an anneal at 1366 K for 1-1/2 hours and a water quench. The resultant hardness was Rockwell B92 and the average grain diameter was 0.16 mm.

### Procedure

#### Tensile

Tensile specimens were machined following ASTM specification E8-69<sup>(5)</sup>; the reduced section diameter was 0.5 cm and gage length was 2.54 cm. The tensile axis was oriented transverse to the final rolling direction. Tests were performed at a cross-head rate of  $8.3 \times 10^{-4}$  cm/s, using a 44.5 kN screw-driven machine that was equipped with the cryostat assembly designed by Reed.<sup>(6)</sup> The tests at 295 K were conducted in laboratory air, whereas tests at 76 K and 4 K used liquid nitrogen

and liquid helium environments, respectively. Load was monitored with a 44.5 kN commercial load cell while specimen strain was measured with a clip-on, double beam, strain gage extensometer. Yield strength was determined as the stress at 0.2% offset plastic strain.

#### Magnetic

To detect the amount of ferromagnetic, body-centered cubic (bcc) martensitic phase in the paramagnetic, fcc austenitic matrix a simple bar-magnet torsion balance was used.<sup>(7)</sup> Previous measurements on Fe-Cr-Ni austenitic steels established a correlation between the force required to detach the magnet from the specimen and the percent bcc martensite.<sup>(7)</sup> The same correlation was used for this study to estimate the amount of bcc martensite in the Fe-Cr-Ni-Mn alloy.

#### Fracture

The J-integral specimens were 3.78 cm thick compact specimens of a geometry described in ASTM E 399-74.<sup>(8)</sup> The specimen width,  $W$ , and width-to-thickness ratio,  $W/B$ , were 7.6 cm and 2.0, respectively. Other dimensions are shown in Figure 1. The notch, machined parallel to the final rolling direction of the plate, was modified to enable clip gage attachment in the loadline.

The J-integral specimens were precracked at their test temperatures, using a 100 kN fatigue testing machine and cryostat<sup>(9)</sup>. All fatigue operations were conducted using load control and a sinusoidal load cycle at 20 Hz. Maximum fatigue precracking loads ( $P_f$ ) were well below the maximum load of J tests ( $P_{max}$ ), as indicated in Table 1. The maximum stress intensities during precracking ( $K_f$ ), the final relative crack lengths ( $a/W$ ), and the edge-crack-to-average-crack-length ratios ( $a_e/a$ ) at each temperature are also listed in Table 1. After precracking,



the specimens were transferred to a 267 kN (60,000 lb) hydraulic tensile machine for fracture testing. Thus, the 76 and 4 K fracture specimens were warmed to room temperature between precracking and J testing at 76 and 4 K. This was necessary since the load limitations of the 20 kN fatigue machine precluded loading this alloy to fracture at low temperatures.

The J-integral tests followed a resistance curve technique similar to that described originally by Landes and Begley.<sup>(10,11)</sup> A series of nearly identical specimens was tested at each temperature. Each specimen was loaded to produce a given amount of crack extension. The specimens were then unloaded and heat tinted to mark the amount of crack extension associated with a particular value of J. The oxidized zone of crack extension could be identified and measured after fracturing the specimen into halves.

Using the approximation for deeply cracked compact specimens,<sup>(12)</sup>

$$J = 2A/B(W-a), \quad (1)$$

the value of J for each test was calculated from the total area, A, under the load-versus-record. The values of J obtained at each temperature were plotted versus crack extension,  $\Delta a$ , which was measured at five locations equidistant across the specimen thickness, and averaged.

The critical value of the J integral,  $J_{IC}$ , defined as the J value at the initiation of crack extension, was obtained by extrapolating the best fit J- $\Delta a$  curve to the point of actual material separation.

Conversion to the plane-strain fracture toughness parameter,  $K_{IC}$ , is made using:<sup>(10-12)</sup>



$$K_{IC}^2 = \frac{E}{1-\nu} (J_{IC}) \quad (2)$$

where E is Young's modulus and  $\nu$  is Poisson's ratio. At room temperature,  $E \approx 195$  GPa and  $\nu \approx 0.287$ ; at 76 K and 4 K,  $E \approx 203$  GPa and  $\nu \approx 0.278$ , according to Ledbetter's measurements.<sup>(13)</sup>

## Results and Discussion

### Tensile

The yield and tensile strengths, elongation, and reduction of area were obtained for the 21-6-9 alloy at 295, 76, and 4 K. These data are summarized in Table 2. The results from this study are combined in Figures 2-4 with the unpublished results of Landon<sup>(1)</sup> for the same heat, also hot rolled and annealed, and with the results of Scardigno,<sup>(2)</sup> Malin,<sup>(3)</sup> and Masteller<sup>(4)</sup> for annealed bar stock. The spread of the Malin data represent results from both the longitudinal and transverse specimen orientations. Agreement is very good, except that the ultimate strength data of Masteller are consistently higher than the average of the other data.

Typical stress-strain curves at each temperature are presented in Figure 5. The pronounced discontinuous yield behavior at 4 K probably is associated with adiabatic specimen heating. Significant local heating is indicated, as the flow stress drops to stress levels less than sustained at 76 K. Another indication of significant local heating is the rise of the reduction of area to values higher than obtained during 76 K tests. Specimens tested at 4 K developed very local areas of increased plastic deformation, which resulted in sizable specimen necking prior to fracture. These load drops should not be attributed to martensitic phase transformations for three reasons: (1) more

extensive transformation was detected in this alloy at 76 K than at 4 K (see later discussion) and no discontinuities in the stress-strain mode at 76 K were observed, (2) load drops have been observed in both meta-stable (e.g., AISI/304) and stable (e.g., AISI 310) austenitic stainless steels at 4 K and no distinction is apparent between the two alloy groups,<sup>(14)</sup> and (3) in austenitic steels the amplitude and frequency of the load drops at 4K are a function of the strain rate<sup>(14)</sup> which would be expected if local heating were responsible.

From the tensile data it is clear that the alloy 21-6-9 has a significant decrease of ductility below 195 K, and tensile elongation decreases progressively between 195 and 4 K.

A primary advantage offered by this alloy is its high yield strength compared to other austenitic alloys. At room temperature the yield strength of the 21-6-9 alloy is about 0.38 GPa (55 ksi), compared to AISI 300 series (Fe-Cr-Ni) steel values of 0.21 to 0.25 GPa (30-35 ksi). The yield strength of the 21-6-9 steel approximately triples to a value of 1.24 GPa (180 ksi) as the temperature is decreased to 4 K. The Fe-Cr-Ni austenitic alloys achieve values about double or triple their room temperature values (60-110 ksi) at 4 K. Thus, the strength advantage offered by the 21-6-9 alloy is greatest at low temperatures. Fracture:

The load-versus-loadline deflection curves for compact specimens at 295, 76 and 4 K are shown in Figure 6. The curves at 295 K extended to larger deflections than indicated on the axis of the diagram. The fracture test data are tabulated in Table 3. There are no ASTM E 399-74 valid  $K_{IC}$  data. The 5% secant offset data are denoted  $K_Q$  because the ASTM E 399-74 thickness and crack front curvature criteria are not

satisfied. Using  $B \geq 2.5 (K_Q/\sigma_y)^2$ , a specimen thickness of 4.2 cm at 4 K is required, slightly larger than the 3.8 cm thickness tested. The crack front curvatures shown in Figure 7, are slightly larger than allowed by ASTM E 399-74. The surface crack lengths are 88 to 89% of the average of internal crack lengths, while 90% is specified in the ASTM E 399-74 Method as the minimum deviation.

The J-versus- $\Delta a$  results at room temperature are plotted in Figure 8. Ductile tearing or slow, stable crack extension occurred at this temperature. Large apparent crack extensions were observed due to plastic deformation at the crack tip; only in two specimens at the highest values of  $\Delta a$  was actual material separation noted. These two values fall on the same trend line as the specimen data that did not exhibit material separation. Therefore the response of this extremely ductile material to J-integral tests at room temperature is inconclusive, with no well-defined break from the linear portion of the plastic deformation curve observable.

According to the tentative size criterion suggested by Landes and Begley<sup>(11)</sup>, the specimen thickness for valid  $J_{IC}$  measurements should satisfy the relationship:

$$B \geq \alpha(J/\sigma_f) \quad (3)$$

where  $\alpha$  is 25 and  $\sigma_f$  is the average of the yield and tensile strengths. In the tests at 295 K, the conditional critical J values are in the range 925 to 1350 kJm<sup>-2</sup>. Using the flow stress value of 0.527 GPa (76.5 ksi), the J-integral results at room temperature are invalid for the specimen thickness tested here. A specimen thickness of 6.3 cm (2.5 inches) may be needed to insure valid data, according to Eq. (3).

The J-resistance curve at 76 K is also shown in Figure 8. The data fit a regular trend, with the exception of the point representing the largest observed crack extension (not shown). The curve drawn through the remaining data indicates that crack extension initiates at a  $J_{IC}$  value of about  $340 \text{ kJm}^{-2}$ . The corresponding value of  $K_{IC}(J)$ , estimated using Equation 2, is  $275 \text{ MPa}\cdot\text{m}^{1/2}$  ( $250 \text{ ksi in}^{1/2}$ ),  $\pm 5\%$ .

At 4 K, the alloy approached linear-elastic behavior, but the results of the first three tests failed to satisfy the ASTM validity criteria<sup>(8)</sup> for direct  $K_{IC}$  measurements. Eight additional J tests were conducted and these results are included in Figure 8. The J- $\Delta a$  curve at 4 K is nearly horizontal, indicating a  $J_{IC}$  value of about  $150 \text{ kJm}^{-2} \pm 10$ ; the  $K_{IC}$  estimate from Eq. (2) is  $182 \text{ MPa}\cdot\text{m}^{1/2}$  ( $165 \text{ ksi}\cdot\text{in}^{1/2}$ ).

#### Phase Transformations

After tensile tests at 76 and 4 K, the deformed specimens were magnetic. Therefore, these specimens were measured, using bar-magnet torsion balance equipment,<sup>(6)</sup> to correlate magnetic attraction with specimen reduction of area. The magnetic readings were converted to percent bcc martensite and the reduction of area converted to elongation, assuming constant volume. These data are plotted in Figure 9 and typical microstructures are shown in Figure 10.

Although not positively identified, it is probable that hcp martensite was also formed in the 21-6-9 alloy during low temperature deformation. The microphotographs after deformation at 4 K (Figure 10) identify transformed regions which are parallel to the (111) slip band traces. These appear identical to the hcp areas identified in earlier research on AISI 304, an Fe-Cr-Ni alloy.<sup>(7,14)</sup>



The amount of bcc martensite formed is large and only slightly less than that which is formed in AISI 304 at the same temperatures<sup>(7,14)</sup>. Permeability values of the order of 10 were measured in heavily deformed specimen portions at 76 K, but it is difficult to identify bcc martensite in the Figure 10 photo-micrographs. Normally, in austenitic stainless steels the bcc martensitic product has an acicular, plate-like morphology with the habit plane of the plate not {111}. Examination of specimen microstructures, typified by Figure 10 indicate that only at {111} band intersections are the distinctive plate-like microstructures observed.

There is clear evidence that the amount of the transformation is suppressed, as a function of either stress or strain, as temperature is lowered from 76 K to 4 K. This is similar to the Fe-Cr-Ni (AISI 304) alloy martensitic transformation behavior<sup>(7,14)</sup>, where formation of the hcp martensitic phase was suppressed at temperatures between 20 and 4 K. Apparently, in the complicated energy balance affecting martensitic transformation for these alloy systems at low temperatures, the increase of flow stress and the decrease of dislocation mobility more than offset the gradually increasing free energy difference between the structures.

Finally, it is not clear that martensitic transformations are deleterious to material application. Normally, the stress levels used in service are less than the yield strength, and no martensitic transformations should occur. The complexities and concern usually are discussed when one considers welds and weld techniques. Chemical segregation and stress concentrations are then more likely, rendering particular sections less stable and, locally, stressed above the yield

strength. In these situations martensitic products will form.

AISI 304 behaves in a similar manner; it is stable on cooling to low temperatures but transforms to hcp and bcc martensitic products during plastic deformation. But, unlike 21-6-9, the fracture toughness of AISI 304 remains extremely high at 4 K<sup>(15)</sup>, implying that martensitic transformations are not harmful to the fracture toughness of the Fe-Cr-Ni stainless steel. This is not clear in the case of the Fe-Cr-Ni-Mn-N alloy, however, as the toughness is rapidly decreasing between 76 and 4 K. For appropriate safety of operation at 4 K, additional research is necessary to understand the effect of martensitic transformations on fracture toughness.

### Conclusions

1. The fracture toughness of the 21-6-9 austenitic stainless steel exhibits a decided temperature dependence between 300 and 4 K, but retains a toughness of  $150 \text{ kJ/m}^2$  ( $136 \text{ ksi}\cdot\text{in}^{1/2}$ ) at 4 K. Linear-elastic behavior was approached at 4 K.

2. The yield strength of the 21-6-9 alloy is also very temperature dependent, tripling from room temperature to 4 K, and reaching a value of 1.24 GPa (180 ksi) at 4 K.

3. During plastic deformation at 76 and 4 K, bcc martensite was identified and correlated with strain. Suppression at 4 K, compared to 76 K, of the amount of bcc martensite was found.

### Acknowledgements

The authors thank D. P. Landon, Lawrence Livermore Laboratories for supplying the test material. Dr. R. P. Mikesell conducted the tensile tests, R. L. Durcholz contributed technical assistance to tensile, fracture, and metallographic preparation, and Dr. M. B. Kasen provided the photomicrographs.



## References

1. P. R. Landon, Unpublished data, Lawrence Livermore Laboratories, Livermore, CA (1975).
2. P. F. Scardigno, Masters Thesis, Naval Postgraduate School, Monterey, CA, AD/A-004555 (1974).
3. C. O. Malin, NASA SP-5921(01), Technology Utilization Office, NASA, Washington, D.C. (1970).
4. R. D. Masteller, NASA CR-72638(N70-27114), Martin Marietta Corp., Denver, CO (1970).
5. Standard Methods of Tension Testing of Metallic Materials, ASTM E8-69, 1976 Annual Book of ASTM Standards, Part 10 (ASTM, Philadelphia, PA, 1976) p. 120.
6. R. P. Reed, Advances in Cryogenic Engineering, Vol. 7 (Plenum Press, New York, 1962) p. 448.
7. R. P. Reed and C. J. Guntner, Trans. AIME, 230, (1964) p. 1713.
8. Standard Method of Test for Plane-Strain Fracture Toughness of Metallic Materials, ASTM E 399-74, 1976 Annual Book of ASTM Standards, Part 10 (ASTM, Philadelphia, PA 1976) p. 471.
9. R. P. Reed, R. L. Tobler, and R. P. Mikesell, "Advances in Cryogenic Engineering - ICMC", Vol. 22 (Plenum Press, New York, 1976), to be published.
10. J. D. Landes and J. A. Begley, Westinghouse Research Laboratory Scientific Paper 73-1E7-FMPWR-P3, Pittsburgh, PA (1973).
11. J. D. Landes and J. A. Begley, "Fracture Analyses", ASTM STP 560, (American Society for Testing and Materials, Philadelphia, PA 1974) p. 170.
12. J. R. Rice, P. C. Paris, and J. G. Merkle, ASTM STP 536 (ASTM, Philadelphia, PA 1973) p. 231.
13. H. M. Ledbetter, personal communication.
14. C. J. Guntner and R. P. Reed, ASM Trans. 55, (1962) p. 399.
15. R. P. Reed, A. F. Clark and E. C. van Reuth, Eds. "Materials Research for Superconducting Machinery III", AD-A012365/3WM, National Technical Information Service, Springfield, VA (1975).

### List of Figures

- Figure 1. Compact specimen for fracture testing of Fe-19Cr-6Ni-9Mn alloy.
- Figure 2. Summary of tensile and yield strength data as a function of temperature for the Fe-21Cr-6Ni-9Mn alloy.
- Figure 3. Summary of tensile elongation as a function of temperature for the Fe-21Cr-6Ni-9Mn alloy.
- Figure 4. Summary of tensile reduction of area as a function of temperature for the Fe-21Cr-6Ni-9Mn alloy.
- Figure 5. Stress-strain curves for the Fe-21Cr-6Ni-9Mn alloy at 295, 76 and 4 K.
- Figure 6. Typical load-deflection curves for compact specimens at 295, 76 and 4 K for annealed Fe-21Cr-6Ni-9Mn alloy.
- Figure 7. Fracture characteristics of Fe-21Cr-6Ni-9Mn alloy at 295, 76 and 4 K.
- Figure 8. The J-integral as a function of crack extension at 295, 76 and 4 K for annealed alloy Fe-21Cr-6Ni-9Mn.
- Figure 9. Estimated percent bcc martensite that forms during tensile tests as a function of tensile elongation.
- Figure 10. Microstructures of alloy 21-6-9 after deformation at 4 K. Bands lie on {111} austenite planes and probably represent hcp and bcc martensite, (a) 800X, (b) 1200X.

### List of Tables

- Table 1. Precracking parameters for J-integral specimens.
- Table 2. Tensile properties of Fe-21Cr-6Ni-9Mn alloy.
- Table 3. Fracture results for 3.8 cm thick compact specimens of alloy Fe-21Cr-6Ni-9Mn.

Table 1. Precracking parameters for J-integral test specimens.

Test Temperature (k)	$P_f/P_{max} \times 100$ (percent)	$K_f$ (MPa·m <sup>1/2</sup> )	Relative Crack Length, a/W	$a_e/a$
295	40-45	48-54	0.638	0.90-0.91
76	22-27	52-63	0.640	0.87-0.90
4	30-35	52-63	0.64 to 0.795	0.88-0.89

Table 2. Tensile properties of Fe-21Cr-6Ni-9Mn alloy.

Temperature (K)	Yield Strength 0.2% offset GPa	Tensile Strength GPa	Elongation 2.5 cm gage length (%)	Reduction of Area (%)
295 K	0.350	0.696	61	79
	<u>0.357</u>	<u>0.705</u>	<u>61</u>	<u>78</u>
Average	0.353 (51 ksi)	0.701 (102 ksi)	<u>61</u>	<u>78</u>
76 K	0.913	1.462	42	32
	<u>0.886</u>	<u>1.485</u>	<u>43</u>	<u>41</u>
Average	0.899	1.474 (214 ksi)	<u>43</u>	<u>37</u>
4 K	1.258	1.633	16	40
	<u>1.224</u>	<u>1.634</u>	<u>16</u>	<u>40</u>
Average	1.241 (180 ksi)	1.634 (237 ksi)	<u>16</u>	<u>40</u>

Table 3. Fracture results for 3.8 cm thick compact specimens of alloy Fe-21Cr-6Ni-9Mn.

Temperature (k)	a/W	$K_Q^1$ (MPa·m <sup>1/2</sup> )	J (kJm <sup>-2</sup> )	Δa (cm)	$J_{IC}^2$ (kJm <sup>-2</sup> )
295	0.638	58	177	0.013 <sup>2</sup>	1130±20%
	0.636	61	744	0.051 <sup>2</sup>	
	0.640	55	905	0.069 <sup>3</sup>	
	0.635	63	1355	0.097 <sup>3</sup>	
	0.642	50	1423	0.112 <sup>3</sup>	
76	0.612	134	261	0.0	337±10%
	0.634	153	413	0.028	
	0.640	131	499	0.053	
	0.637	137	674	0.079	
	0.645	130	788	0.091	
	0.643	130	698	0.198	
4	0.645	164	NA	NA	150±10%
	0.648	162	NA	NA	
	0.643	159	NA	NA	
	0.670	NA	100	0.0	
	0.655	167	147	0.020	
	0.670	158	149	0.080	
	0.656	160	162	0.076	
	0.750	NA	89	0.0	
	0.725	NA	191	0.0313	
	0.725	NA	274	0.105	
	0.755	NA	141	0.033	

1. Calculated from ASTM E 399-74 Method.

2. Apparent crack extension due to crack tip deformation only.

3. Crack extension due to deformation and material separation.

NOTES: 1 in·lb·in<sup>-2</sup>=0.175 kJm<sup>-2</sup>; 1 inch=2.54 cm; 1 ksi·in<sup>1/2</sup>=1.099 MPa·m<sup>1/2</sup>

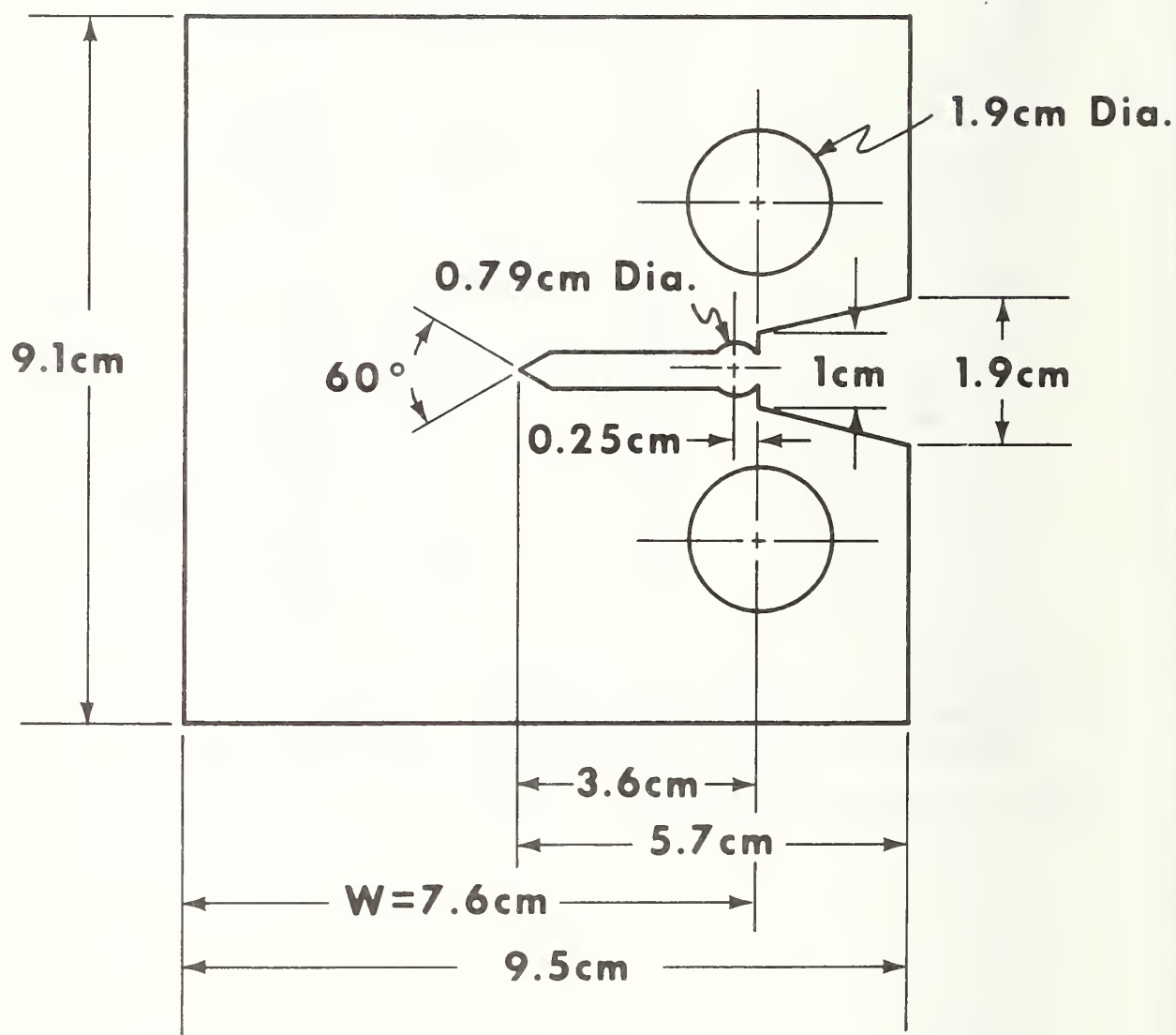


Figure 1. Compact specimen for fracture testing of Fe-19Cr-6Ni-9Mn alloy.



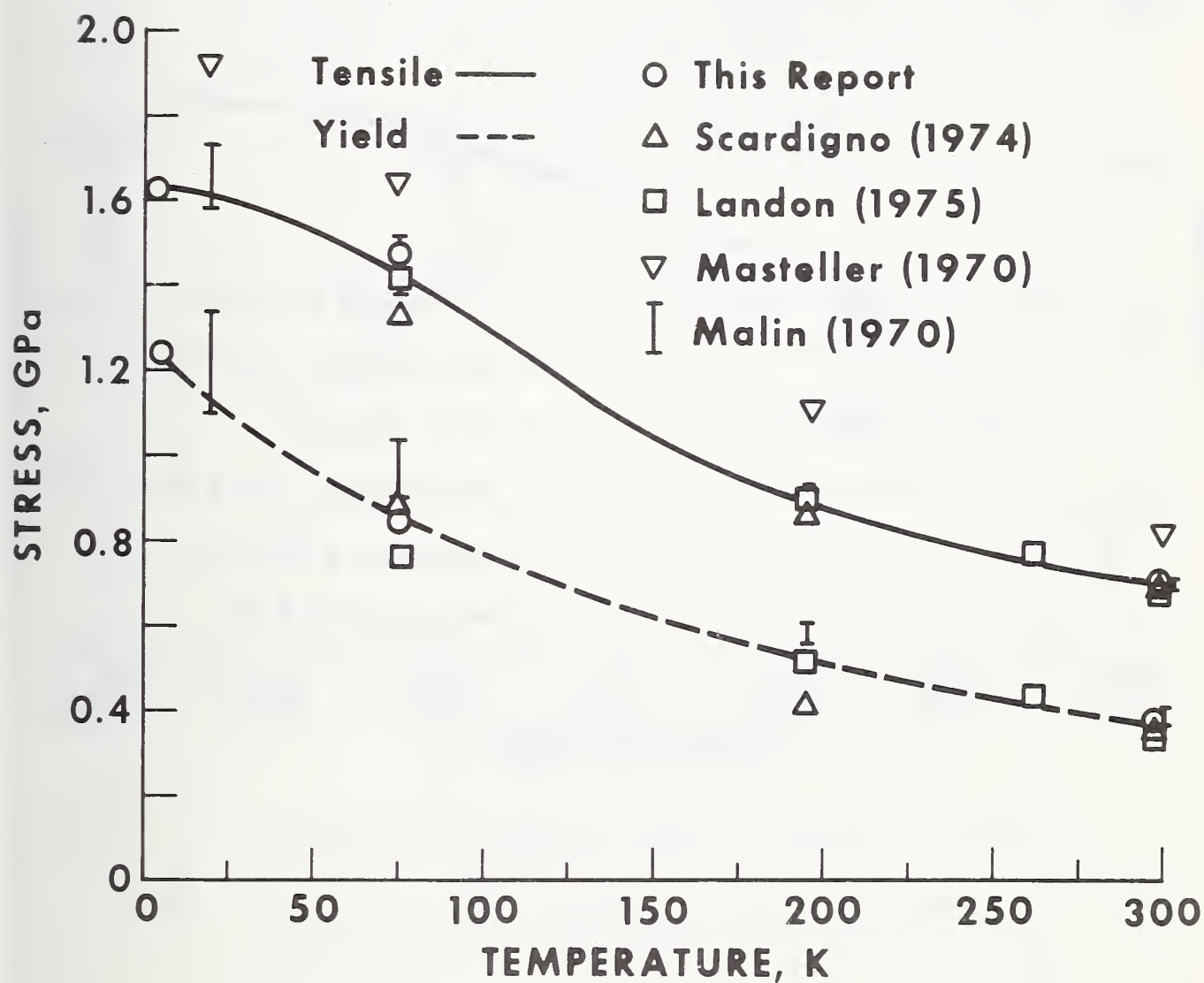


Figure 2. Summary of tensile and yield strength data as a function of temperature for the Fe-21Cr-6Ni-9Mn alloy.

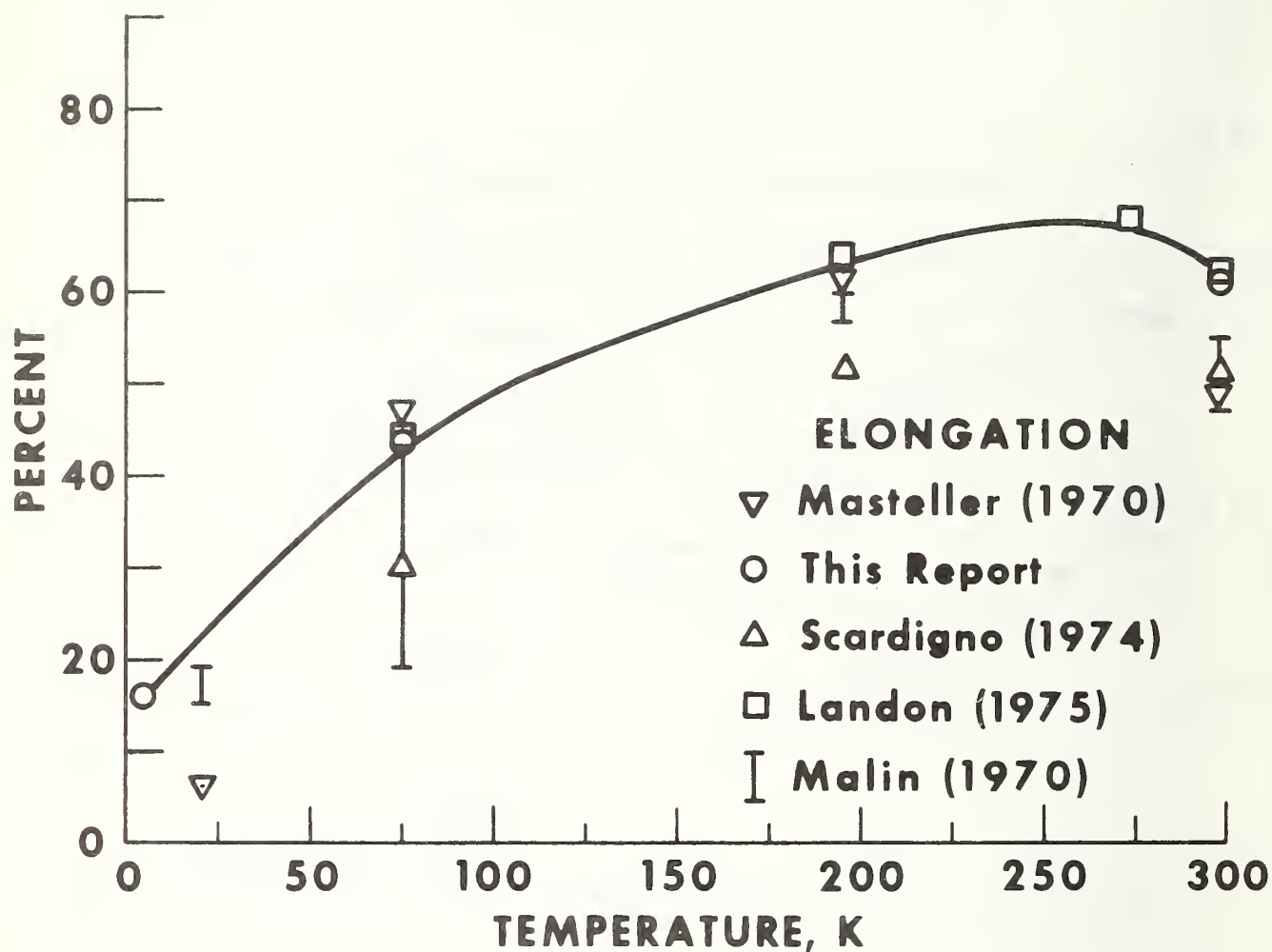


Figure 3. Summary of tensile elongation as a function of temperature for the Fe-21Cr-6Ni-9Mn alloy.

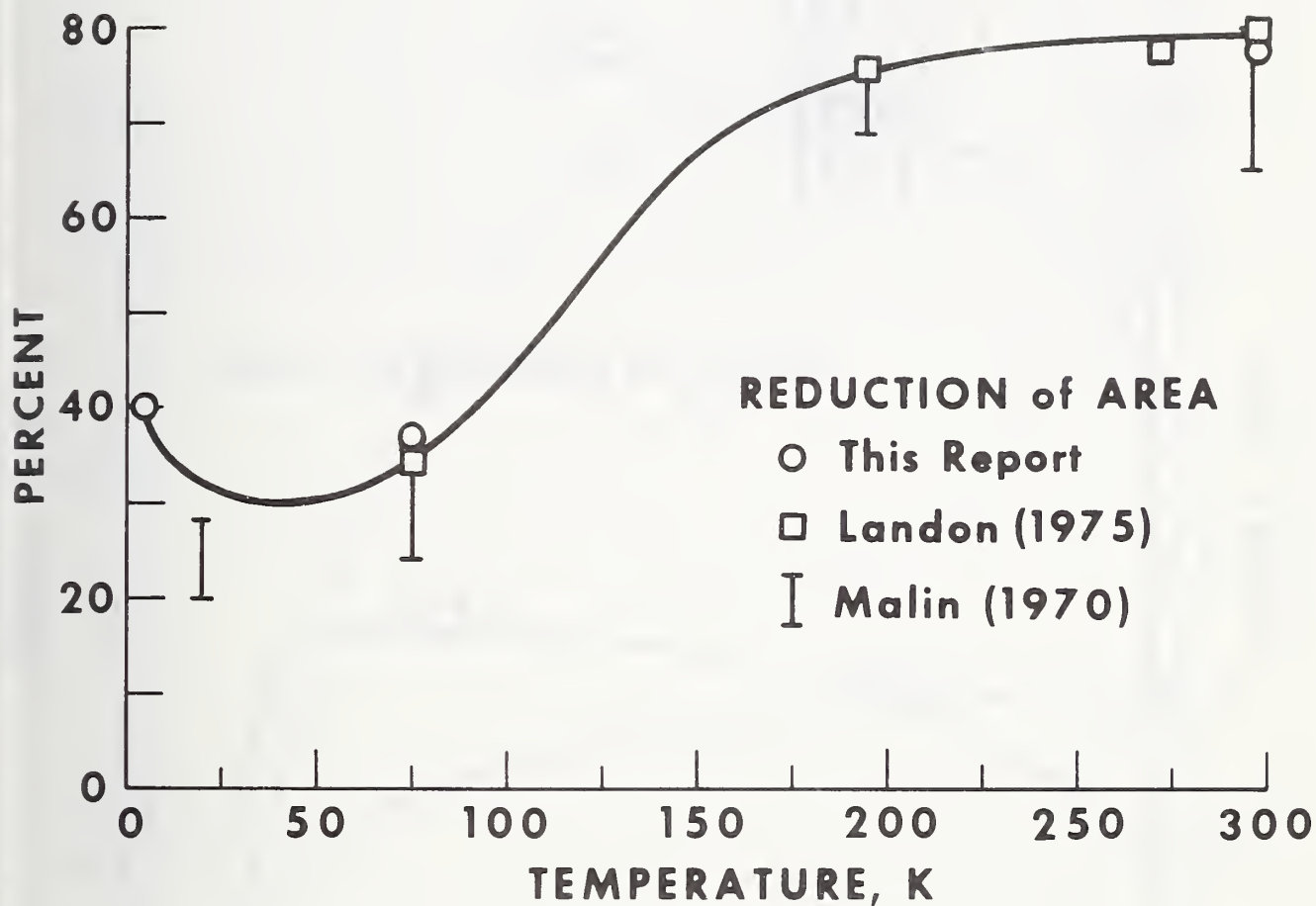


Figure 4. Summary of tensile reduction of area as a function of temperature for the Fe-21Cr-6Ni-9Mn alloy.

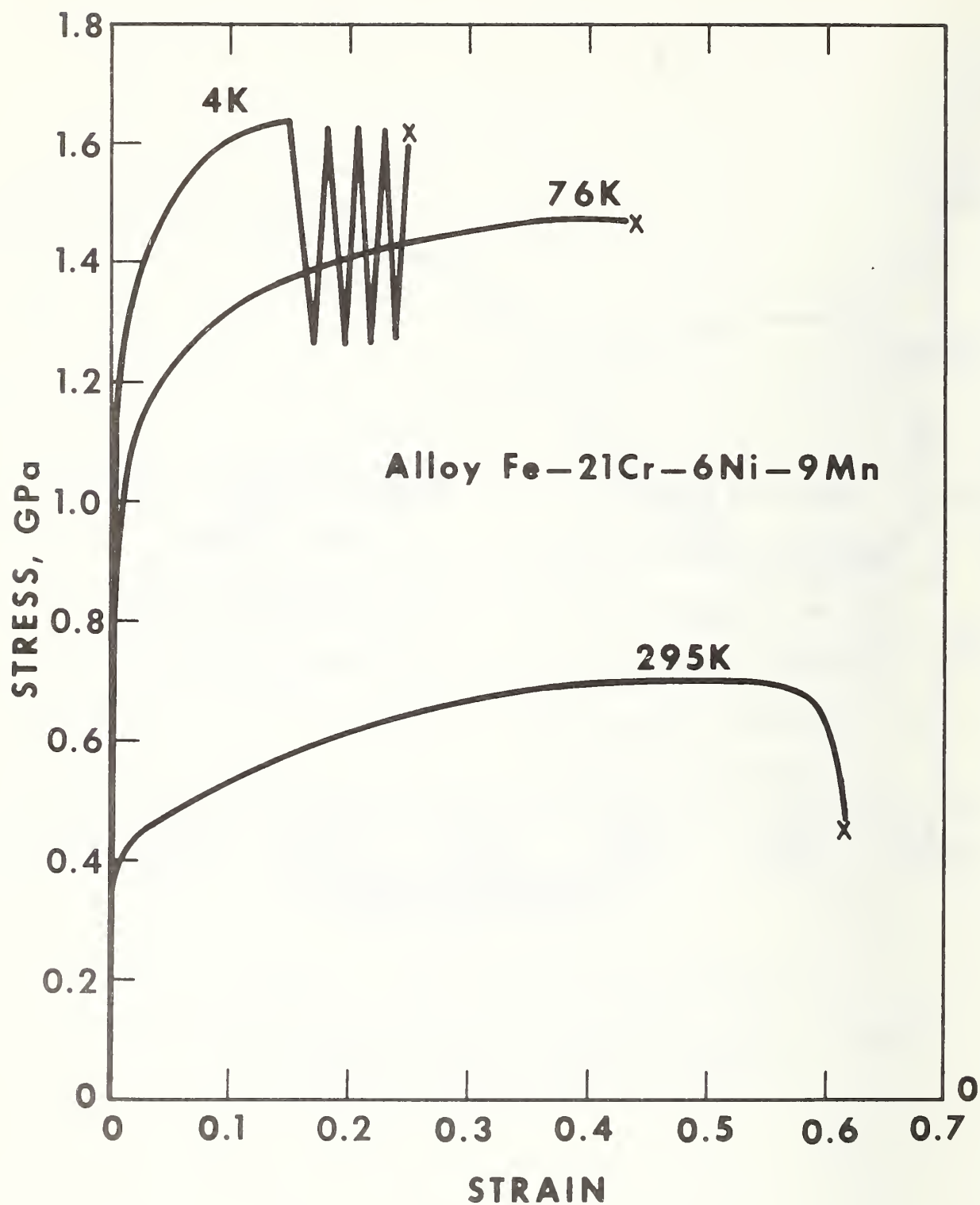


Figure 5. Stress-strain curves for the Fe-21Cr-6Ni-9Mn alloy at 295, 76, and 4 K.

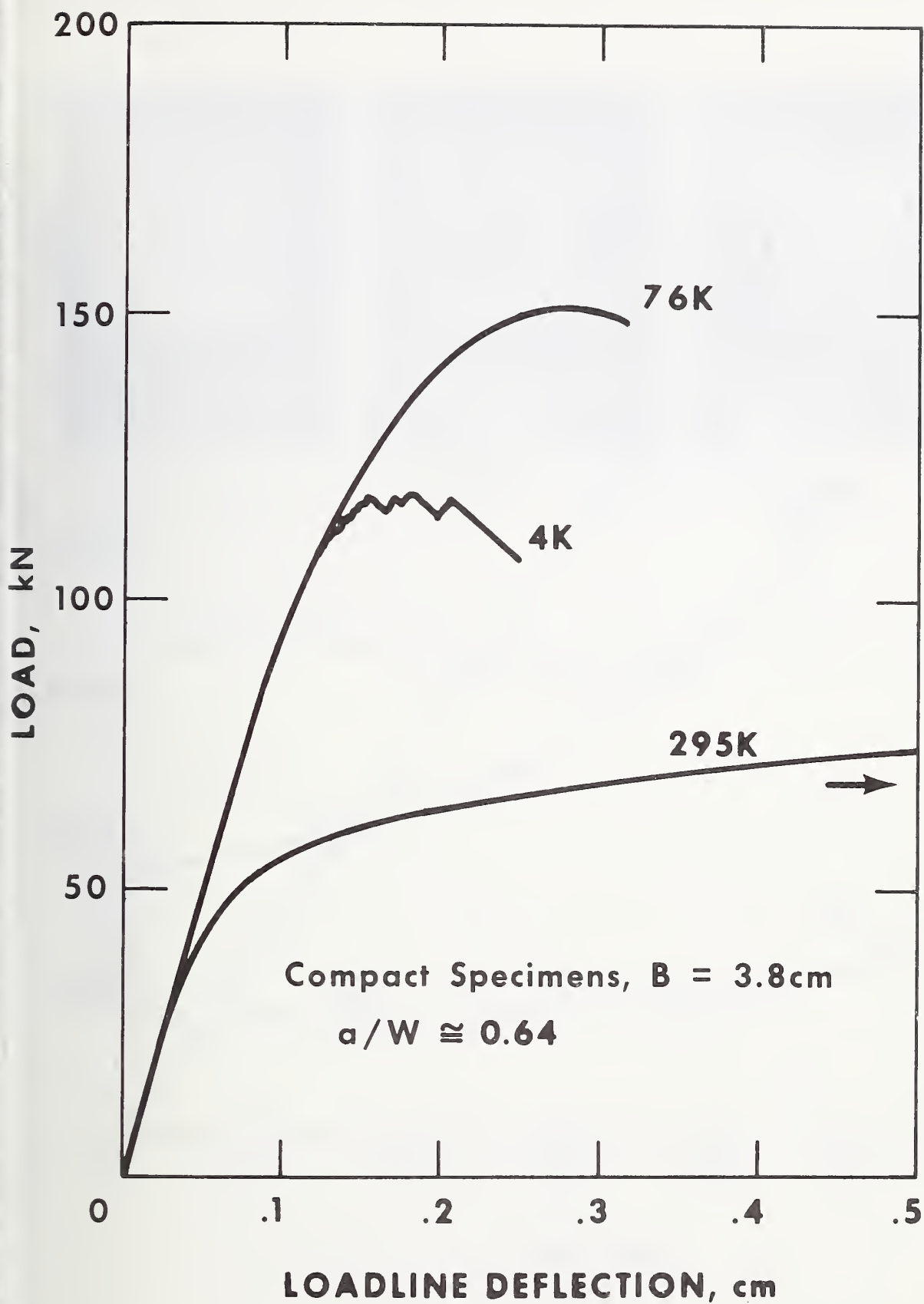


Figure 6. Typical load-deflection curves at 295, 76, and 4 K for annealed Fe-21Cr-6Ni-9Mn alloy.

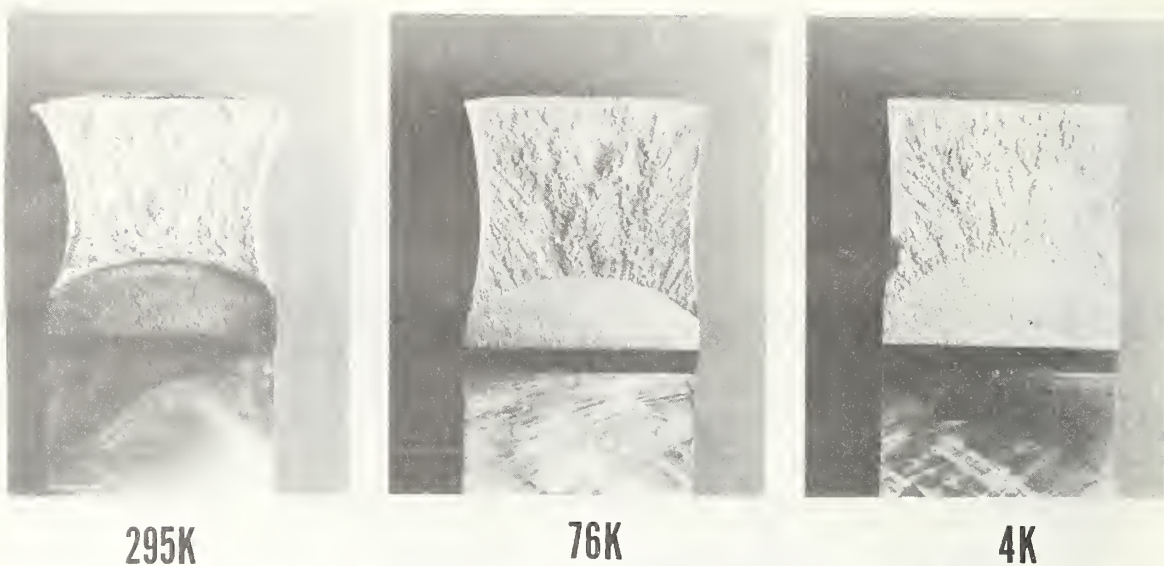


Figure 7. Fracture characteristics of Fe-21Cr-6Ni-9Mn alloy at 295, 76, and 4 K.



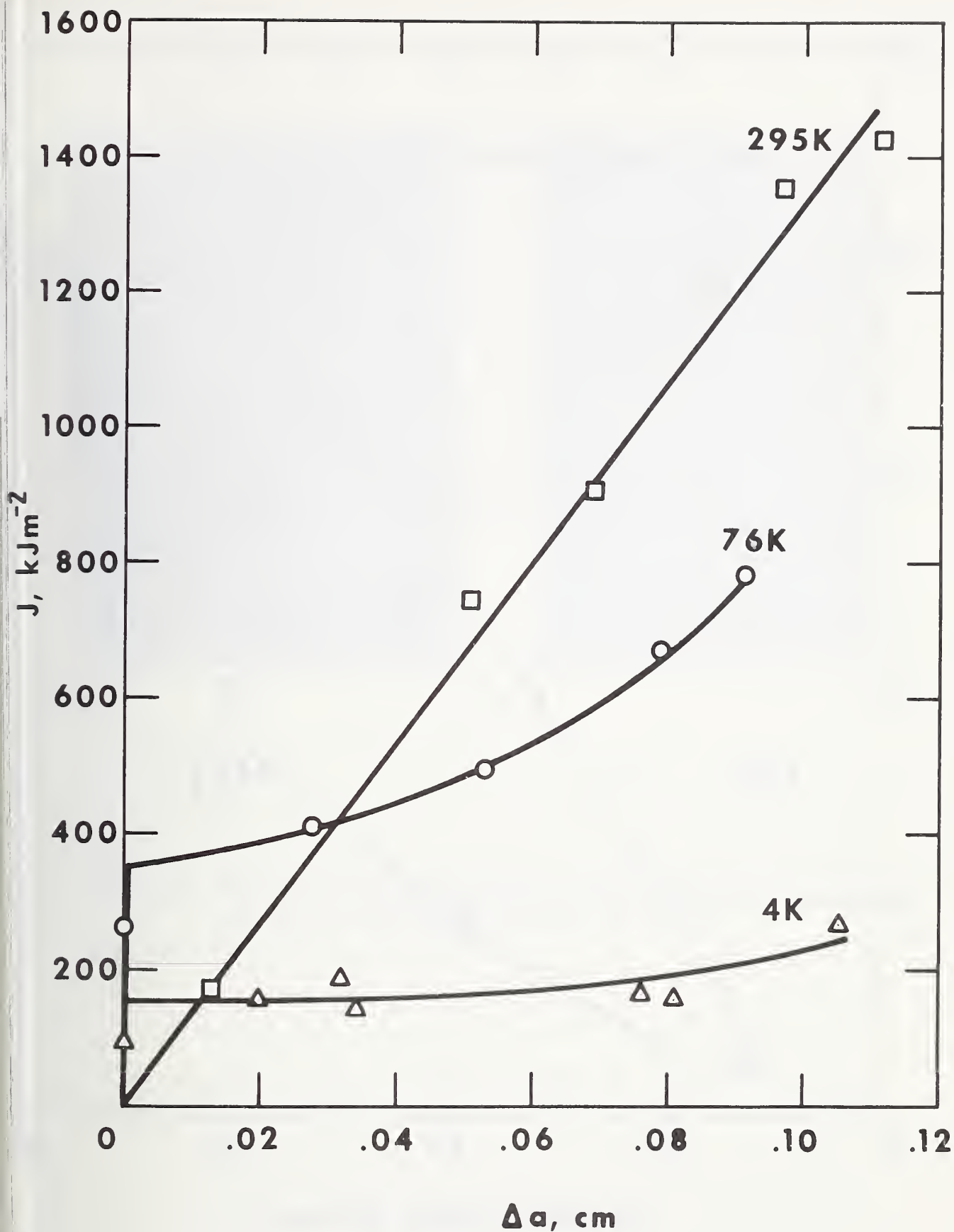


Figure 8. The J-integral as a function of crack extension at 295, 76, and 4 K for annealed alloy Fe-21Cr-6Ni-9Mn.

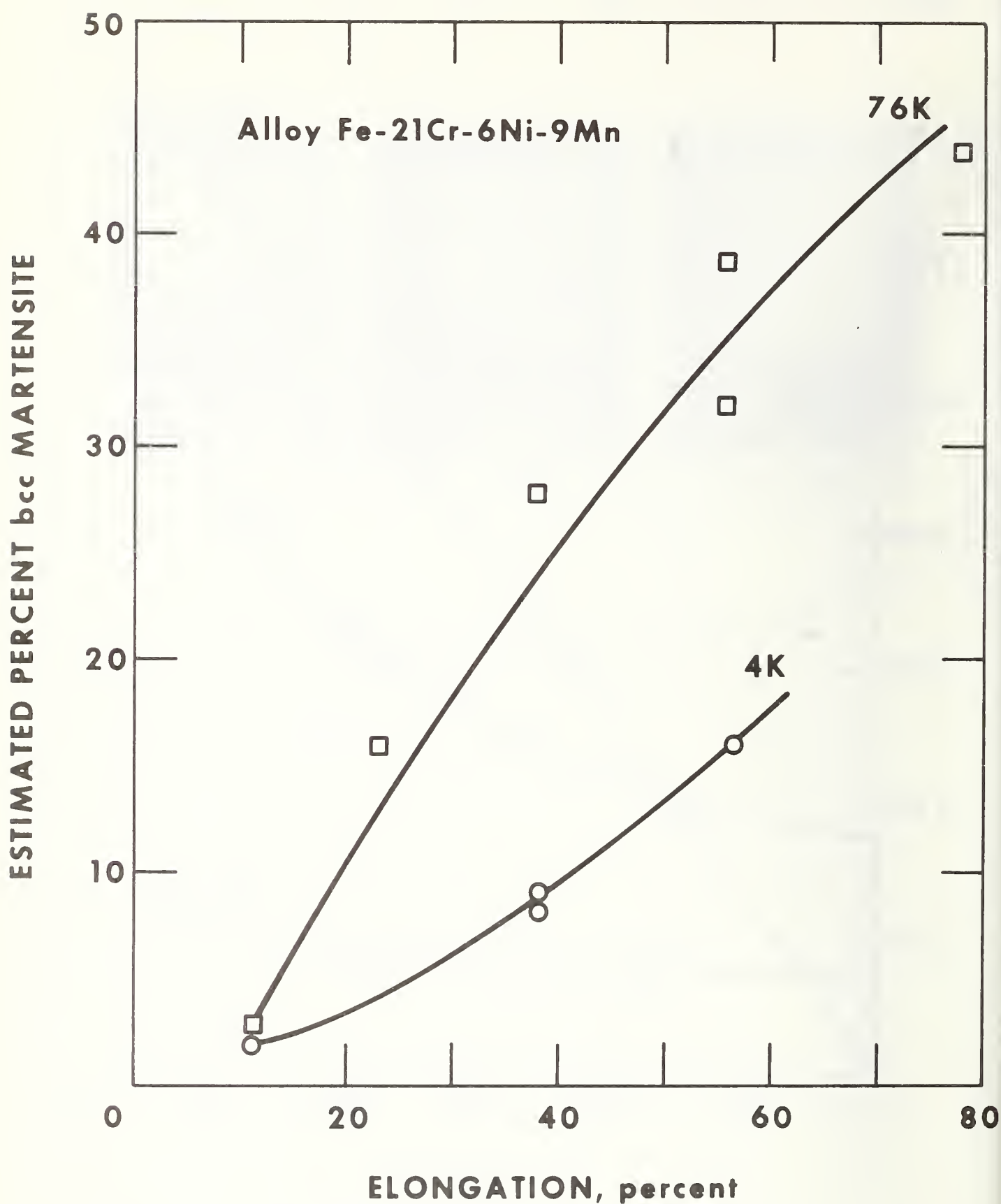


Figure 9. Estimated percent bcc martensite that forms during tensile tests as a function of tensile elongation.



**(a)**



**(b)**

Figure 10. Microstructures of alloy 21-6-9 after deformation at 4 K. Bands lie on  $\{111\}$  austenite planes and probably represent hcp and bcc martensite, (a) 800X, (b) 1200X.

CRYOGENIC TENSILE, FATIGUE, AND FRACTURE PARAMETERS  
FOR A SOLUTION-ANNEALED MARAGING STEEL<sup>+</sup>

R. L. Tobler, R. P. Reed, and R. E. Schramm

Cryogenics Division  
Institute for Basic Standards  
National Bureau of Standards  
Boulder, Colorado 80302

<sup>+</sup> Contribution of NBS, not subject to copyright.

## ABSTRACT

The mechanical properties of an eighteen percent nickel, solution-annealed 300-grade maraging steel were measured to assist in the evaluation of this material for low-temperature structural applications. Tensile, fatigue-crack growth rate, and fracture toughness tests were performed in ambient air (295 K), liquid nitrogen (76 K), and liquid helium (4 K), with the following results: (1) the yield strength of this material increases from 848 MPa at room temperature to 1596 MPa at 4 K; (2) the tensile ductility is moderate, with elongation decreasing from 15.5 to 6.7% for this temperature region; (3) the plane strain fracture toughness ( $K_{IC}$ ) decreases from  $165 \text{ MPa}\cdot\text{m}^{1/2}$  at room temperature to  $83 \text{ MPa}\cdot\text{m}^{1/2}$  at 4 K; and (4) the fatigue-crack propagation resistance at intermediate stress intensity ranges is relatively insensitive to temperature. These results are compared with similar data for other cryogenic materials.

Key words: Fatigue; fracture; low temperature tests; maraging steels; mechanical properties; nickel alloys.

## INTRODUCTION

The beneficial effect of nickel on the low temperature fracture resistance of steels is well known [1-2]. Concentrations of from 2 1/4 to 9% Ni are used in the 0.1 to 0.2% carbon ferritic steels that were specially developed for low temperature service [2]. For these steels, increasing nickel content correlates with reduced ductile-to-brittle transition temperatures. For the grade having the highest nickel content, ASTM A533-72a (9% Ni steel), the transition to low fracture toughness occurs at temperatures between 76 and 4 K. Emerging applications in the relatively new field of superconducting machinery would benefit from a commercially-available ferritic steel that retains high toughness at 4 K.

With this goal in mind, the 18% Ni maraging steels must be considered. Maraging steels are easily processed and are weldable. High nickel and low carbon contents ( $\sim 0.003\%$  C, max.) account for the relatively soft, platelet-like martensite that forms on cooling from the austenite field. Cobalt, molybdenum, titanium, and aluminum alloying contributes significantly to strengthening, and the ultra-high strengths obtained with fully aged 300 grade maraging steels represent an outstanding technological achievement [3,4]. However, low fracture toughness is often associated with high yield strength [5-8]. Therefore the fracture toughness of this material should be investigated before considering it a candidate for cryogenic structural applications. The literature contains numerous plain strain fracture toughness ( $K_{IC}$ ) and fatigue crack growth rate parameters for maraging steels [9-15], but low temperature studies are less common [10,13-15].



This paper describes the mechanical behavior of a solution-annealed 18% Ni, 300 grade maraging steel at temperatures in the ambient-to-extreme cryogenic range. The conventional tensile properties, fatigue crack growth rates, and fracture toughness values were measured at 295, 76, and 4 K, using state-of-the-art techniques. This alloy was tested in the solution-annealed condition, to maximize the fracture toughness.

### Material

The 300 grade maraging steel tested in this study was supplied by the Morris Steel and Aluminum Corporation. The material was a 5.3 x 15.4 x 58 cm forged bar that had been solution-annealed at 1088 K and air cooled. The chemical analysis quoted by the supplier is, in weight percent: 18.41 Ni, 0.002 C, 0.01 Mn, 0.006 P, 0.003 S, 0.01 Si, 9.27 Co, 4.95 Mo, 0.59 Ti, 0.12 Al, and balance, Fe. This alloy was tested in the as-received condition which is a lath martensite having the body-centered cubic crystal structure and virtually no retained austenite [9].

### Procedures

#### Tensile

Cylindrical tensile specimens having a reduced section 3.8 cm long and 0.51 cm in diameter were machined in the transverse orientation, such that the loading-axis/fracture-plane orientation matched that of the compact specimens described below. The tensile tests were conducted at a crosshead velocity of  $0.008 \text{ mm s}^{-1}$ , using the 44.5 kN screw-driven machine and cryostat previously described [16]. The commercial load cell and clip-on strain gage extensometer outputs were autographically recorded, and the resultant load-versus-deflection curves were analyzed following the standard ASTM E8-69 Method [17].

## Fracture

Compact specimens of the TL orientation [18] (notch plane normal to the long transverse forging direction) were used in all fatigue and fracture tests. The specimens were 2.3 cm thick (B) and 5.08 cm wide (W). The planar dimensions are shown in Figure 1. Knife edges were machined integral to the notch, permitting clip-gage placement and deflection measurements at the loadline.

Room temperature (295 K) tests were conducted in unconditioned air, using a 100 kN servo-hydraulic test machine and cryostat. Low temperature tests were performed with the specimen and clip gage completely submerged in liquid nitrogen (76 K) or liquid helium (4 K) environments. At each temperature, the clip-gage satisfied the ASTM E-399-74 Method linearity requirements [18]. The apparatus and low temperature techniques are described elsewhere in greater detail [19].

The test procedure involved precracking the specimens at their test temperatures and subsequently loading them to fracture by increasing the stress intensity at a rate of approximately  $1 \text{ MPa} \cdot \text{m}^{1/2} \text{ s}^{-1}$ . At 76 K and 4 K, the ASTM E 399-74 requirements for valid, linear-elastic fracture toughness tests were fulfilled. Therefore,  $K_{IC}$  was calculated directly using the solution for compact specimens [18]:

$$K_{IC} = P_Q \bar{B}^{1/2} \bar{W}^{1/2} [f(a/W)] \quad (1)$$

The calibration factor,  $f(a/W)$ , is a function of relative crack length [18]:

$$f(a/W) = 29.6(a/W)^{1/2} - 185.5(a/W)^{3/2} + 655.7(a/W)^{5/2} - 1017.0(a/W)^{7/2} + 638.9(a/W)^{9/2}$$

The load  $P_Q$  is derived from the test record using the secant offset procedure, and crack length is the average value of measurements at 25, 50, and 75% of specimen thickness. The uncertainty in  $K_{IC}$  values obtained by this method is estimated at less than 5% [20].

Nonlinearity in the test records at room temperature precluded using the ASTM E-399-74 method. Therefore,  $K_{IC}$  was estimated using the J-integral concept. J is the rate of change of potential energy with respect to crack area for nonlinear elastic materials, and it is a measure of the crack-tip strain field intensity for elastic-plastic fractures. The critical value,  $J_{IC}$ , is the value of J at the onset of crack extension [21].

Since stable crack extension occurred in the solution-annealed maraging steel at room temperature, the resistance curve technique [21] was used to measure  $J_{IC}$ . Seven nearly identical specimens ( $a/W \approx 0.6$ ) were loaded to cause crack extension increments of up to 0.4 cm. The specimens were then unloaded and heat-treated to oxidize the crack surfaces. The specimens were then cooled to 76 K (to avoid subsequent plastic deformation) and fractured into halves. The straw/blue crack extension increments ( $\Delta a$ ) created during the initial loading were measured to the nearest 0.001 cm with a travelling microscope at three points equidistant across the specimen thickness, and averaged. The J values at points of unloading were calculated using the approximation [22]:

$$J = 2AB^{-1}(W - a)^{-1} \quad (3)$$

The pairs of J and  $\Delta a$  measurements were plotted and extrapolated to obtain  $J_{IC}$  with an uncertainty of  $\pm 10\%$ . The room temperature  $K_{IC}$  was then estimated from:

$$K_{IC}^2 = EJ_{IC}(1 - \nu^2)^{-1} \quad (4)$$

where E, Young's modulus for the material is 175.6 GPa ( $25.5 \times 10^6$  psi) and  $\nu$ , Poisson's ratio is 0.325 [23].

#### Fatigue Crack Growth

Fatigue crack growth rates were measured during the precracking of fracture toughness specimens, but the maximum stress intensity factor was restricted to less than  $50 \text{ MPa}\cdot\text{m}^{1/2}$ , to insure that the precracking loads did not influence the fracture toughness test results. To obtain  $da/dN$  data at stress intensity factors greater than  $50 \text{ MPa}\cdot\text{m}^{1/2}$ , one additional specimen was tested at each temperature. The fatigue tests were conducted using controlled loads, a sinusoidal load cycle, a test frequency (F) of 20 Hz, and a minimum/maximum load ratio, R, of 0.1.

Crack length was inferred by elastic compliance or deflection-per-unit-load ( $\delta/P$ ) measurements. Following techniques previously described [24], correlations between average crack length and  $\delta/P$  were obtained experimentally using data from fractured specimens. The a-versus-N curves were constructed from compliance readings taken periodically during the fatigue tests. Using a computer program, the a-versus-N curves were fitted with a third order polynomial and differentiated, yielding  $da/dN$  with an uncertainty of less than  $\pm 20\%$ . The stress intensity factor ranges were calculated based on Eqs. (1-2) and the fatigue load range:

$$\Delta K = K_{\max} - K_{\min} = (P_{\max} - P_{\min})B^{-1}W^{-1/2}[f(a/W)] \quad (5)$$

### Tensile

The uniaxial tensile property measurements for the solution-annealed 300 grade maraging steel are itemized in Table 1, and the average values of yield strength, ultimate strength, elongation, and reduction of area are shown in Figures 2 and 3. The results show that the strength and ductility parameters exhibit opposite temperature dependences. Between 295 and 4 K, the yield strength increases from 848 MPa to 1596 MPa, while reduction of area decreases from 70% to 47%. The room temperature yield strength is significantly lower than the 1790 to 2060 MPa range for aged 300 grade maraging steels [9], but ductility is higher. On the other hand, this solution-annealed 300 grade maraging steel offers a modest improvement over the yield and ultimate strengths and reduction of area values for a commercial 9% Ni steel in the quenched and tempered condition [25]. The yield strengths of several nickel alloy steels are compared in Figure 4.

### Fracture Toughness

The fracture surfaces of compact specimens showed sizable shear-lip regions at room temperature, whereas the fractures at 76 and 4 K were relatively flat. "Type I" test records [18] having only slight nonlinear segments near the maximum load were obtained at these low temperatures. The fracture measurements at each temperature are summarized in Table 2.

Consider the room temperature results. The  $J$ -versus- $\Delta a$  curve at room temperature, Figure 5, reveals a linear trend for  $\Delta a$  greater than 0.5 mm. At smaller  $\Delta a$ , apparent crack extension is caused by crack-tip geometry changes due to blunting instead of actual material



separation. The  $J = 2\Delta\sigma_{\text{flow}}$  line was constructed to account for this blunting, as recommended [21]. The  $J_{\text{IC}}$  value taken at the intersection of the resistance curve and the flow line is  $140 \text{ kJm}^{-2}$ , and the corresponding  $K_{\text{IC}}$  estimate from Eq. (4) is  $165 \text{ MPa}\cdot\text{m}^{1/2}$ .

The 76 K and 4 K results from the ASTM E 399-74 method satisfy the linear-elastic size criterion which requires:

$$a, W-a, B \geq 2.5 \frac{K_{\text{IC}}^2}{\sigma_y} \quad (6)$$

The edge-crack-to-average-crack-length ratios were uniform, with values ranging from 0.96 to 0.98. The  $P_{\text{max}}/P_Q$  ratios were also acceptable, with values below 1.10. The data listed in Table 2 are therefore valid, and the average  $K_{\text{IC}}$  at each temperature is shown in Figure 6.

As expected, there is a substantial improvement in fracture toughness over the values reported for aged 300 grade maraging steels. The room temperature  $K_{\text{IC}}$  value for our solution-annealed material,  $165 \text{ MPa}\cdot\text{m}^{1/2}$ , is nearly threefold greater than values reported for the aged condition [3,9]. Low temperature data are scarce, but Antolovich [13] reports  $K_{\text{IC}}$  values of 115 and  $66 \text{ MPa}\cdot\text{m}^{1/2}$  for an aged 300 grade maraging steel at 295 and 77 K, respectively. Thus, the difference in  $K_{\text{IC}}$  for the solution-annealed and aged conditions may be as large as a factor of 2 at liquid nitrogen temperature.

While it is true that low temperature effects on  $K_{\text{IC}}$  for the maraging steels are adverse, our data indicate no abrupt fracture transitions such as usually observed for body-centered cubic materials, as shown in Figure 6. Nevertheless, there is a 48% reduction of  $K_{\text{IC}}$  for the solution-annealed maraging steel between 295 and 4 K. At 4 K, the fracture toughness is



$83 \text{ MPa}\cdot\text{m}^{1/2}$ , slightly higher than the  $75 \text{ MPa}\cdot\text{m}^{1/2}$  value reported [25] for quenched and tempered 9% Ni steel. The absence of transitional behavior in the maraging steel undoubtedly is related to the favorable influences of high nickel and low carbon contents on the deformation characteristics and cleavage resistance of steel [1].

The present results reinforce the view that plastic deformation and fracture processes are competitive, and that factors which tend to increase a material's resistance to slip also tend to enhance the probability of brittle fracture. In their studies of maraging steels at room temperature, Fischer and Repko [7], Jones and Brown [6], and Srawley [5] demonstrated decreases in toughness at higher yield strengths. They illustrated the inverse relationship by varying yield strength through metallurgical changes in alloying and heat treatment. In the present study, similar trends are noted on lowering the test temperature.

#### Fatigue Crack Growth Rates

Fatigue crack growth rates for the solution-annealed 18% Ni maraging steel are shown in Figure 7. The  $da/dN$  data define a scatterband approximately  $10 \text{ MPa}\cdot\text{m}^{1/2}$  wide. Within this range, the data at 76 K and 4 K are virtually equivalent, tending to be slightly lower than rates at room temperature. Since the improvement in rates at cryogenic temperatures never amounts to more than a factor of 2, all of the results at stress intensity factors between 20 and  $55 \text{ MPa}\cdot\text{m}^{1/2}$  can be specified by an upper bound equation:

$$\frac{da}{dN} = 6.6 \times 10^{-9} (\Delta K)^{3.0} \quad (7)$$

Here  $da/dN$  and  $\Delta K$  are given in SI units, mm/cycle and  $\text{MPa}\cdot\text{m}^{1/2}$ , respectively.

At  $\Delta K$  values greater than  $55 \text{ MPa}\cdot\text{m}^{1/2}$ , the rates at 295 K and 76 K remain conservative with respect to Eq. (7), at least for the range of  $\Delta K$  investigated. However, the rates at 4 K are accelerated and the fatigue crack propagation resistance becomes inferior as  $\Delta K$  exceeds 75% of the reported  $K_{IC}$  value at this temperature. The 4 K rates at stress intensity factors greater than  $55 \text{ MPa}\cdot\text{m}^{1/2}$  are not specified by the upper bound equation, Eq. (7). Rather, the behavior at 4 K can be described as resulting from a transition in the power-law dependence on  $\Delta K$ , i.e. a transition from an exponent of  $n = 3$  to an exponent of  $n = 7.6$  occurs at  $\Delta K = 55 \text{ MPa}\cdot\text{m}^{1/2}$ . Similar transitions to high values of  $n$  are known to occur in other steels as  $\Delta K$  approaches  $K_{IC}$ , due to the influence of static fracture modes on microcracking [25].

Figure 8 compares Eq. (7) for the solution-annealed 300 grade maraging steel with a band representing typical results for other steels at room temperature. Included in the band are: (1) Barsom's data [26] for non-nickel ferritic steels of various strengths, (2) our previously reported data [25] for 3.5, 5, and 9% Ni ferritic steels, and (3) some data for the 300 grade maraging steels tested by Bathias and Pelloux [11], and Antolovich, Saxena, and Chanai [12]. All of these sources report power-law equation exponents in the range 2.5 to 3.5. Evidently, the present results are typical for steels at room temperature. Bathias and Pelloux reported that their rates for a solution-annealed 300 grade maraging steel were indistinguishable from rates for the same alloy in the aged condition, for  $30 \leq \Delta K \leq 50 \text{ MPa}\cdot\text{m}^{1/2}$ . However, it would be speculative to assume that this would be true at extreme cryogenic temperatures, and data at 4 K for the aged condition are unavailable.

In Figure 9, the upper bound representation of Eq. (7) is used again in comparing the behavior of this maraging steel with bands representing rates for austenitic nickel-base superalloys and austenitic stainless steels tested at temperatures in the range 295 to 4 K. Included in the band for austenitic stainless steels are results for AISI types 304, 304L, 310, 310S, and 316 as well as Kromarc 58, A-286, and an Fe-21Cr-6Ni-9Mn alloy [27,28]. Included in the band for nickel base superalloys are data for Inconel alloys 750, 718, 706 and a low expansion alloy, LEA [29]. The fatigue-crack growth resistance of the solution-annealed maraging steel is intermediate when compared with these potential competitor alloys, suggesting that yield strength and fracture toughness comparisons should be the primary considerations governing alloy selection for cryogenic purposes.

#### CONCLUSIONS

Relatively few mechanical properties relevant to the problem of fracture-resistant design have been measured for maraging steels at low temperatures. In this study, conventional tensile properties and fracture mechanics parameters were measured for an 18% Ni, 300 grade maraging steel in the solution-annealed condition, since the toughness of aged alloys at low temperatures is marginal. The fracture toughness of the solution-annealed alloy is an inverse function of yield strength between 295 K and 4 K, with  $K_{IC}$  decreasing from  $165 \text{ MPa}\cdot\text{m}^{1/2}$  to  $83 \text{ MPa}\cdot\text{m}^{1/2}$ , and yield strength increasing from 848 MPa to 1596 MPa. These strengths compare favorably with some alloys frequently used in cryogenic environments, such as the austenitic stainless steels. The solution-annealed maraging steel can be considered for cryogenic uses, although the fracture toughness at 4 K is only about 8% greater than that of a commercially available and less expensive 9% Ni alloy steel (ASTM A 553).

## ACKNOWLEDGMENTS

This study was sponsored by the Advanced Research Projects Agency of the U.S. Department of Defense. The contributions of Dr. R. P. Mikesell and R. L. Durcholz in conducting the tensile tests are gratefully acknowledged.

## REFERENCES

1. Johnson, R. J., Metals Eng. Quart. 15 (1975) 1.
2. Pense, A. W. and Stout, R. D., in Fracture Toughness and Related Characteristics of the Cryogenic Nickel Steels, WRC Bulletin 205 reprint (Int. Nickel Co., New York, 1976) 1.
3. Zackay, V. F., in Alloy Design for Fatigue and Fracture Resistance, Conference Proceedings No. 185, AGARD-CP-185 (North Atlantic Treaty Organization, 1976) AD A021486.
4. Floreen, S., Metallurgical Reviews 126 (1968) 115.
5. Srawley, J. E., in Fracture, 1969 (Chapman and Hall, London, 1969) 131.
6. Jones, M. H. and Brown, W. F., in Review of Developments in Plane Strain Fracture Toughness Testing, ASTM STP 463 (Amer. Soc. Test. Mater., Philadelphia, 1970) 63.
7. Fischer, D. M. and Repko, A. J., J. Materials, JMLSA 7 (1972) 167.
8. Psioda, J. A. and Low, J. R., NASA Tech. Report No. 7 (Dept. Mater. Science, Carnegie-Mellon University, 1975) NASA-CR-143501. 9.
9. 18% Nickel Maraging Steels, Data Bulletin (International Nickel Co., 1969).
10. Cryogenic Materials Data Handbook, AFML-TDR-64-280 (Martin Marietta Co., 1964).

11. Bathias, C. and Pelloux, R. M., Met. Trans. 4 (1973) 1265.
12. Antolovich, S. D., Saxena, A., and Chanai, G. R., Met. Trans. 5 (1974) 623.
13. Antolovich, S. D., private communication.
14. Vishnevsky, C. and Steigerwald, E. A., in Fracture Toughness Testing at Cryogenic Temperatures, ASTM STP 496 (Amer. Soc. Test. Mater., Philadelphia, 1970) 3.
15. Shoemaker, A. K. and Rolfe, S. T., J. Basic Eng. Trans. ASME, 91 (1969) 512.
16. Reed, R. P., in Advances in Cryogenic Engineering 7 (1962) 448.
17. Standard Methods of Tension Testing of Metallic Materials, designation E8-69, in 1974 Annual Book of ASTM Standards, Part 10 (Amer. Soc. Test. Mater., Philadelphia, 1974) 90.
18. Standard Method of Test for Plane Strain Fracture Toughness of Metallic Materials, designation E 399-74, in 1974 Annual Book of ASTM Standards, Part 10 (Amer. Soc. Test. Mater., Philadelphia, 1974) 432.
19. Fowlkes, C. W. and Tobler, R. L., Eng. Fract. Mechs. 8 (1976) 487.
20. Antolovich, S. D. and Chanai, G. R., in Third International Conference on Fracture (Vereiu Deutscher Eisenhüttenleute, Dusseldorf, 1975) II-242.
21. Landes, J. D. and Begley, J. A., in Fracture Analysis, ASTM STP 560 (Amer. Soc. Test. Mater., Philadelphia, 1974) 170.
22. Rice, J. R., Paris, P. C., and Merkle, J. G., in Progress in Flaw Growth and Fracture Toughness Testing, ASTM STP 536 (Amer. Soc. Test. Mater., Philadelphia, 1973) 231.
23. Ledbetter, H. M., private communication.



24. Tobler, R. L., Mikesell, R. P., Durcholz, R. L., and Reed, R. P., in Properties of Materials for Liquified Natural Gas Tankage, ASTM STP 579 (Amer. Soc. Test. Mater., Philadelphia, 1975) 261.
25. Tobler, R. L. and Reed, R. P., to be published.
26. Barsom, J. M., J. Eng. Industry, Trans. ASME (1971) 1190.
27. Logsdon, W. A., Wells, J. M., and Kossowsky, R., in Proceedings of the Second International Conference on Mechanical Behavior of Materials (Amer. Soc. Metals, Ohio, 1976) 1283.
28. Tobler, R. L., in Proceedings of the Second International Conference on Mechanical Behavior of Materials (Amer. Soc. Metals, Ohio, 1976) 573.
29. Logsdon, W. A., Wells, J. M., and Kossowsky, R., in Materials Research for Superconducting Machinery; Reed, R. P., Ledbetter, H. M., and van Reuth, E. C., Eds. (National Bureau of Standards, Boulder, CO, 1976).

#### LIST OF FIGURES

- Figure 1. Planar dimensions of compact specimens for fatigue and fracture tests.
- Figure 2. Yield and ultimate strengths for solution-annealed 300 grade maraging steel, showing 88% and 64% increases for the temperature range 295 to 4 K.
- Figure 3. Reduction of area and elongation values for solution-annealed 300 grade maraging steel, showing gradually decreasing tensile ductility at low temperatures.
- Figure 4. A yield strength comparison of solution-annealed maraging steel and some ferritic nickel alloy steels.



- Figure 5. The J resistance curve for solution-annealed maraging steel at room temperature, showing a typical data trend.
- Figure 6. The effect of temperature on  $K_{IC}$  for solution-annealed maraging steel, which does not show the transitional behavior exhibited by other nickel-alloy steels. (Data for the 3.5, 5, and 9% Ni steels are published elsewhere [24,25]).
- Figure 7. Fatigue crack growth rates for the solution-annealed 300 grade maraging steel at 295, 76, and 4 K.
- Figure 8. The fatigue crack growth data [Eq. (7)] for solution-annealed 300 grade maraging steel versus room temperature data for other steels [11,12,25,26].
- Figure 9. The fatigue crack growth data [Eq. (7)] for solution-annealed 300 grade maraging steel versus data for austenitic superalloys and stainless steels tested at 295 and 4 K [27-29].

Table 1. Tensile property results for solution-annealed 18% Ni 300 grade maraging steel.

Temperature (K)	0.2% Yield Strength MPa (ksi)	Ultimate Strength MPa (ksi)	Elongation <sup>a</sup> (%)	Reduction in Area (%)
295	904	1069	15	71.3
	791	1068	16	70.3
	848 (123.0)	1068 (155.0)	15.5	70.8
76	1295	1569	12.6	60.4
	1302	1552	13.0	59.7
	1299 (188.4)	1560 (226.2)	12.8	60.1
4	1609	1759	5.6	44.7
	1583	1756	7.8	49.5
	1596 (231.5)	1758 (255.0)	6.7	47.1

a. 2.54 cm gage length

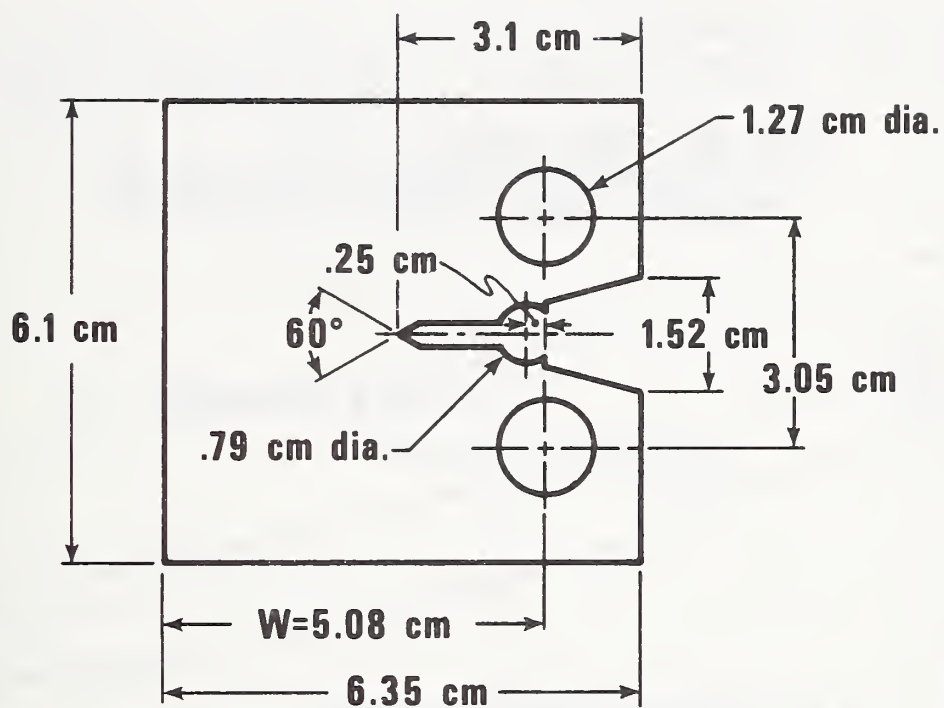
Table 2. Fracture toughness results for solution-annealed 18% Ni 300 grade maraging steel (2.3 cm thick compact specimens).

Temperature (K)	Specimen	a/W	J (kJm <sup>-2</sup> )	Δa (cm)	J <sub>IC</sub> <sup>a</sup> (kJm <sup>-2</sup> )	K <sub>IC</sub> (J) <sup>b</sup> (MPa·m <sup>1/2</sup> )	K <sub>IC</sub> <sup>c</sup> (MPa·m <sup>1/2</sup> )
295	4	0.612	199	0.166			
	5	0.599	68	0.001			
	6	0.597	183	0.105			
	15	0.660	206	0.126	140±10%	165±5%	NA
	16	0.595	272	0.392			
	17	0.598	129	0.001			
	19	0.606	159	0.006			
76	2	0.471	NA	NA	NA	NA	125.5
	3	0.498					131.0
	14	0.542					107.0
	18	0.548					117.5
							Avg = 120.2
4	7	0.466	NA	NA	NA	NA	94.1
	11	0.514					78.8
	20	0.483					79.1
	21	0.507					80.1
							Avg = 83.0

a. obtained from extrapolation, see Fig. 4

b. Calculated using Eq. (3)

c. Obtained using the ASTM E 399-74 Method



**THICKNESS,  $B = 2.3$  cm;  $W/B = 2$**

Figure 1. Planar dimensions of compact specimens for fatigue and fracture tests.

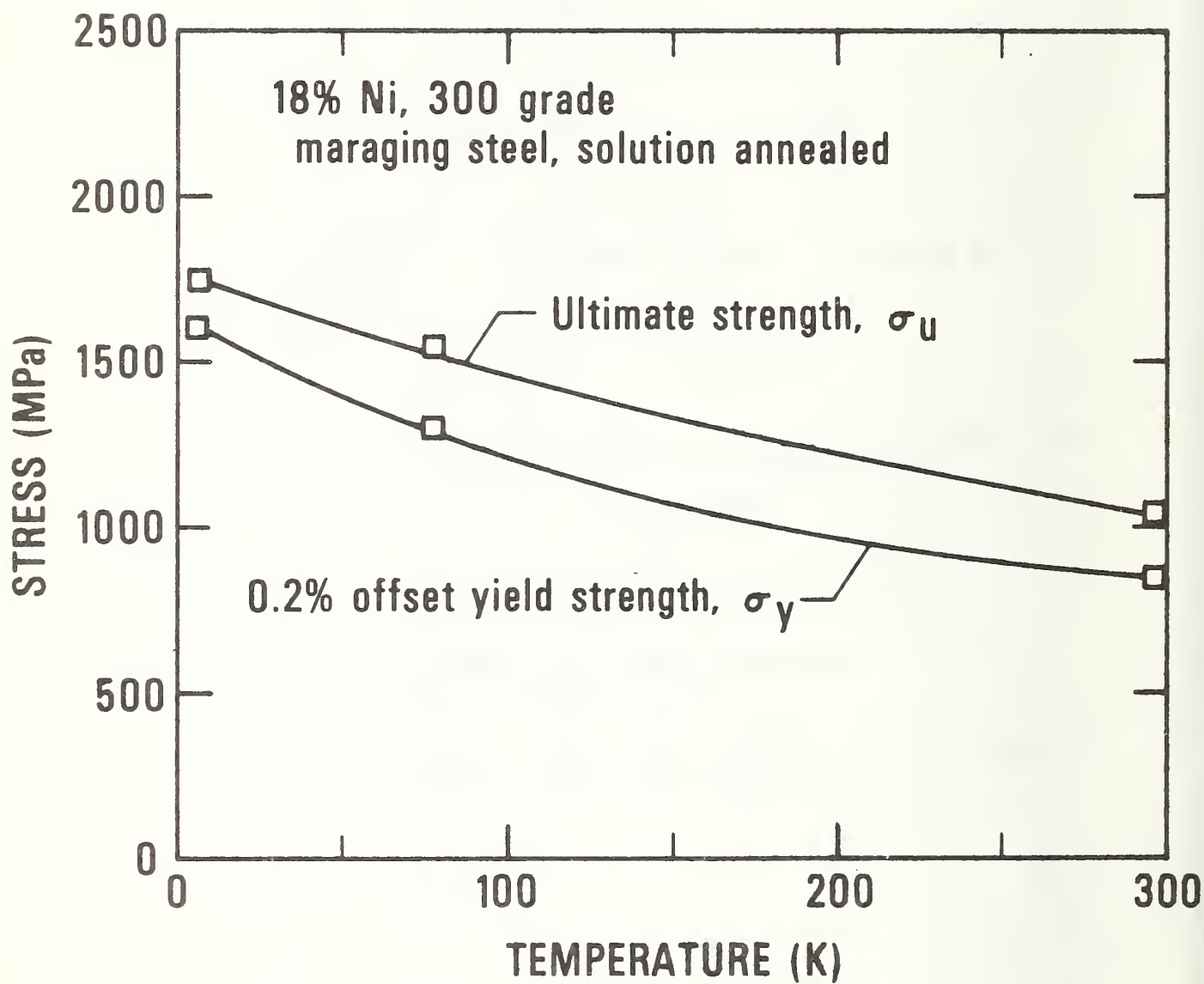


Figure 2. Yield and ultimate strengths for solution-annealed 300 grade maraging steel, showing 88% and 64% increases for the temperature range 295 to 4 K.

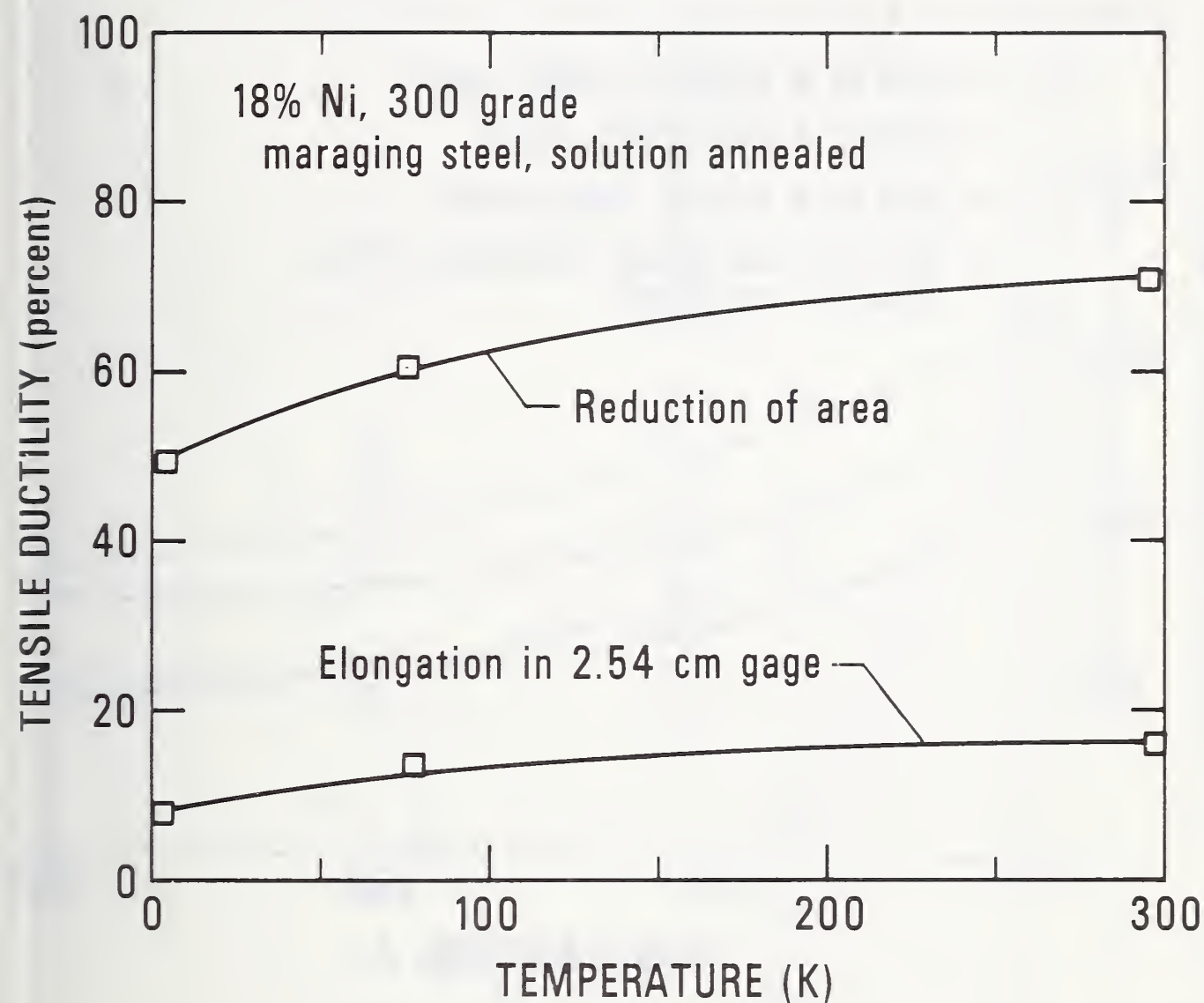


Figure 3. Reduction of area and elongation values for solution-annealed 300 grade maraging steel, showing gradually decreasing tensile ductility at low temperature.

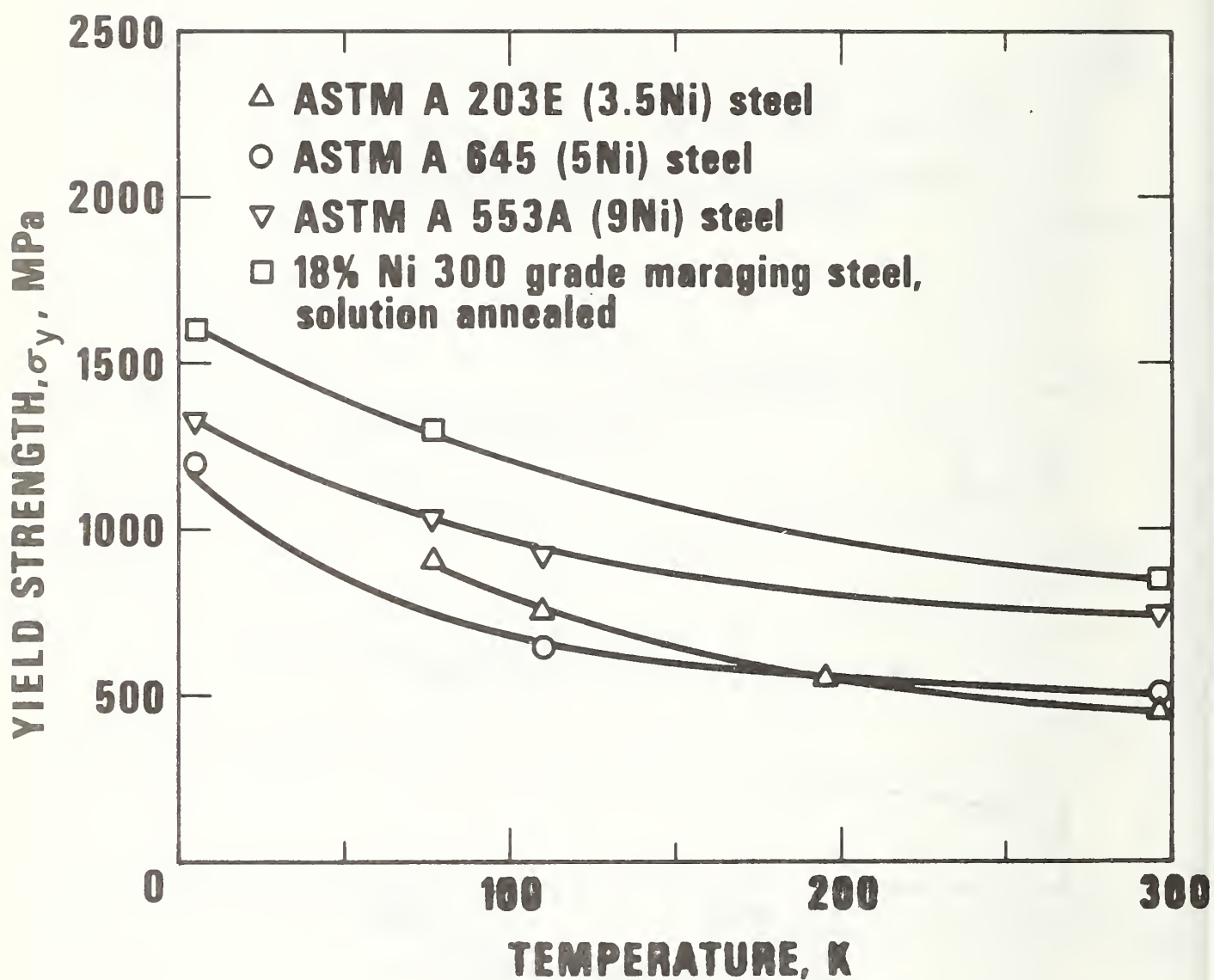


Figure 4. A yield strength comparison of solution-annealed maraging steel and some ferritic nickel alloy steels.



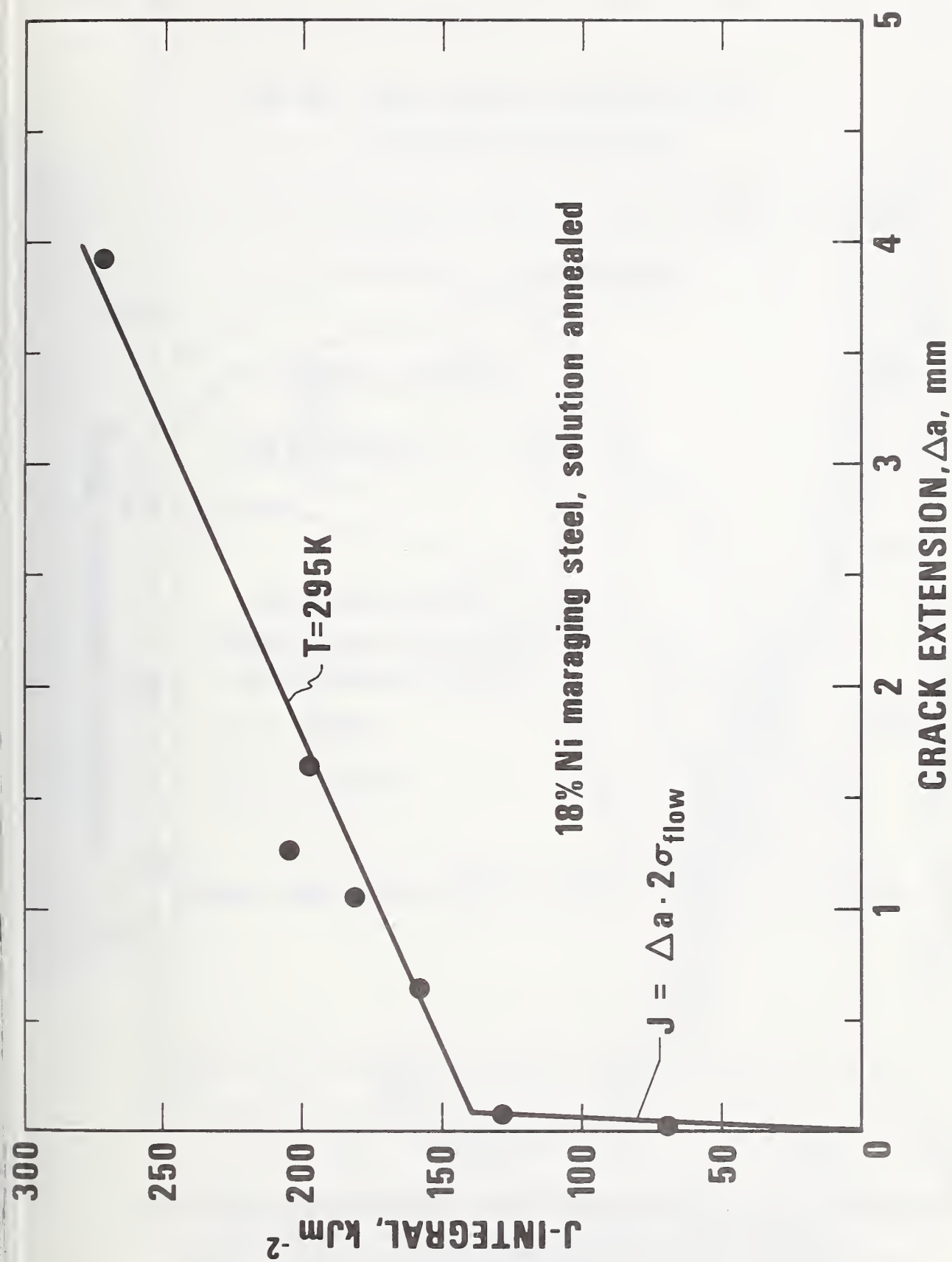


Figure 5. The J resistance curve for solution-annealed maraging steel at room temperature, showing a typical data trend.

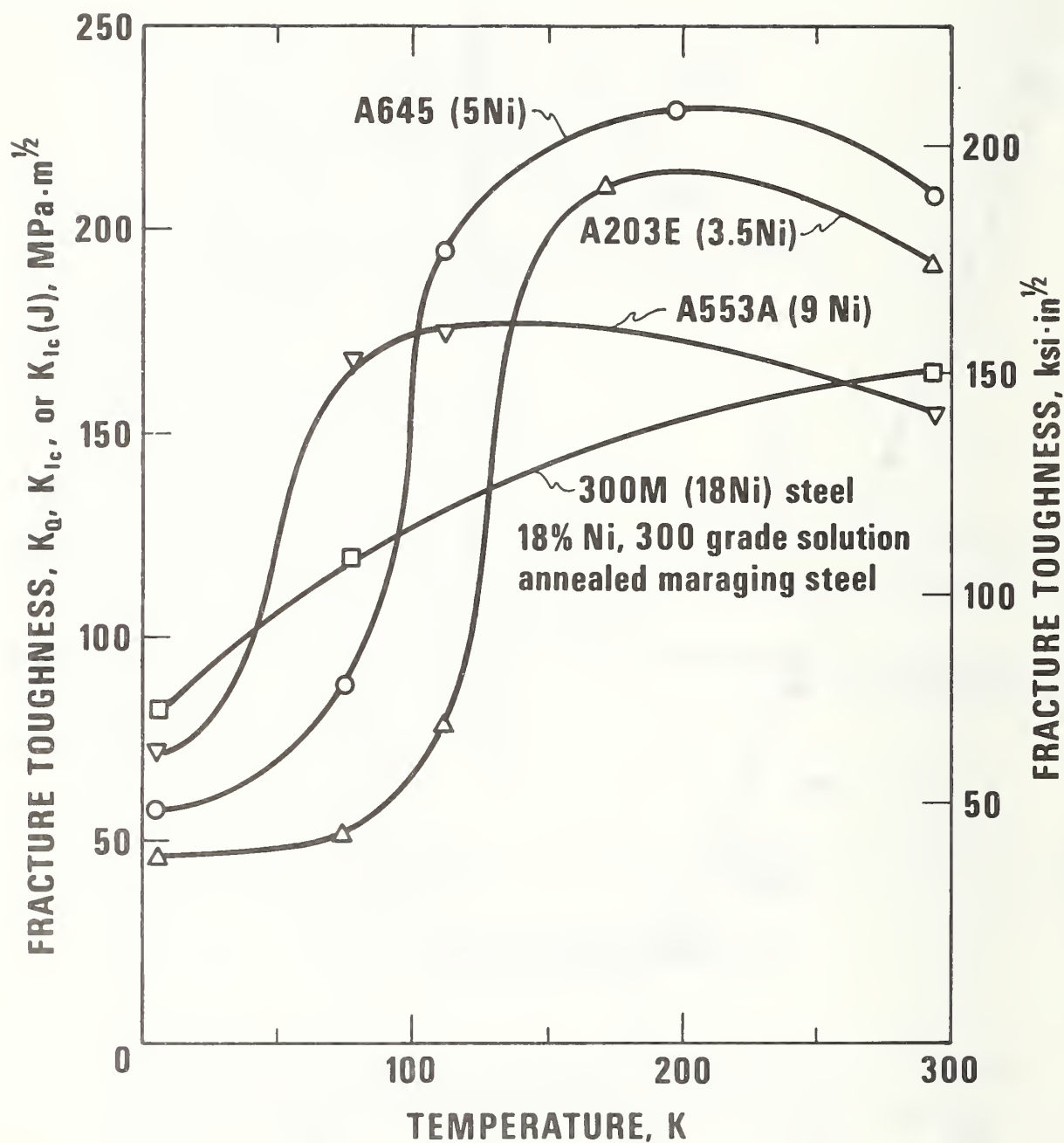


Figure 6. The effect of temperature on  $K_{IC}$  for solution-annealed maraging steel, which does not show the transitional behavior exhibited by other nickel-alloy steels. (Data for the 3.5, 5, and 9% Ni steels are published elsewhere [24,25].)

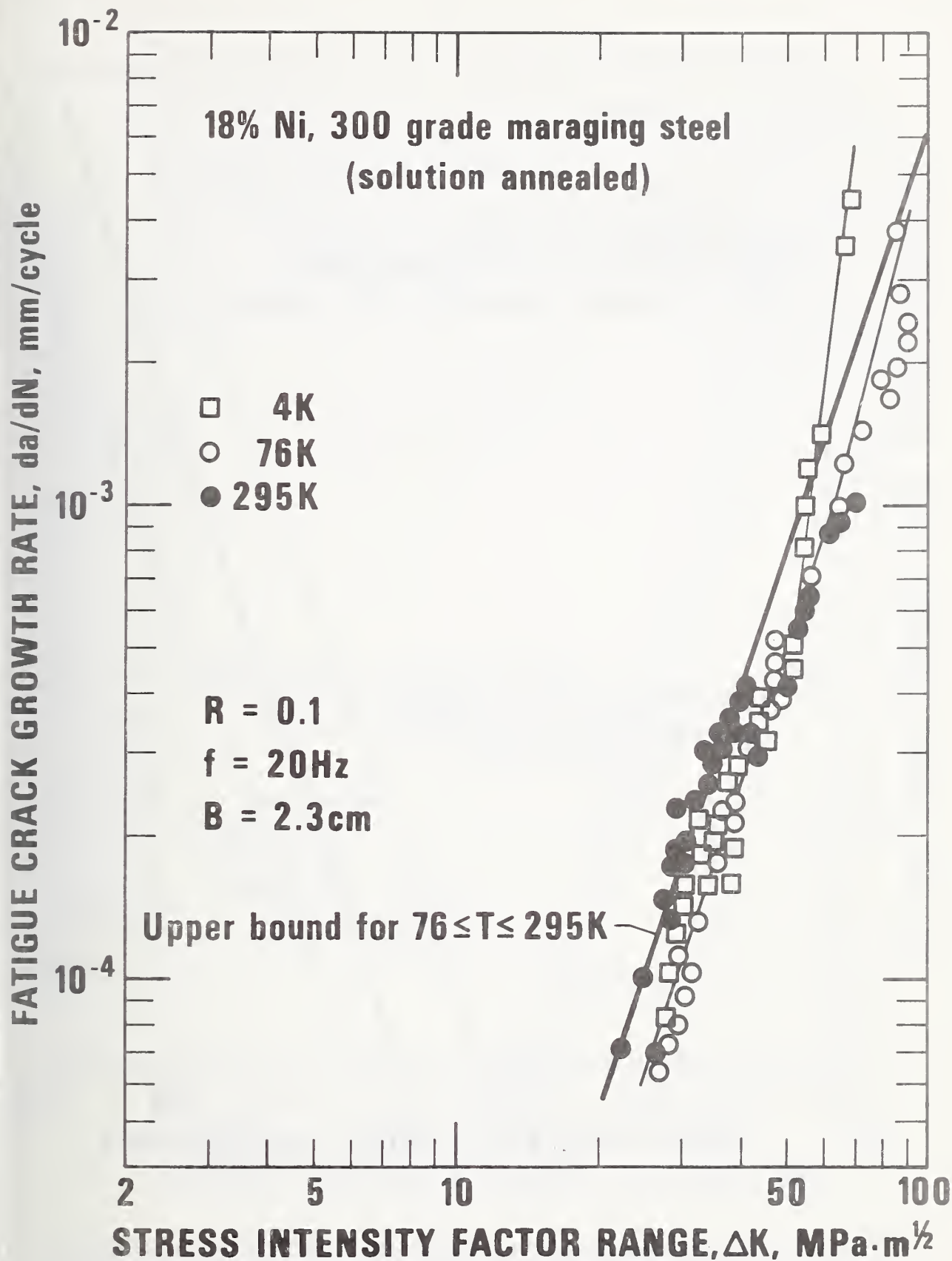


Figure 7. Fatigue crack growth rates for the solution-annealed 300 grade maraging steel at 295, 76 and 4 K.

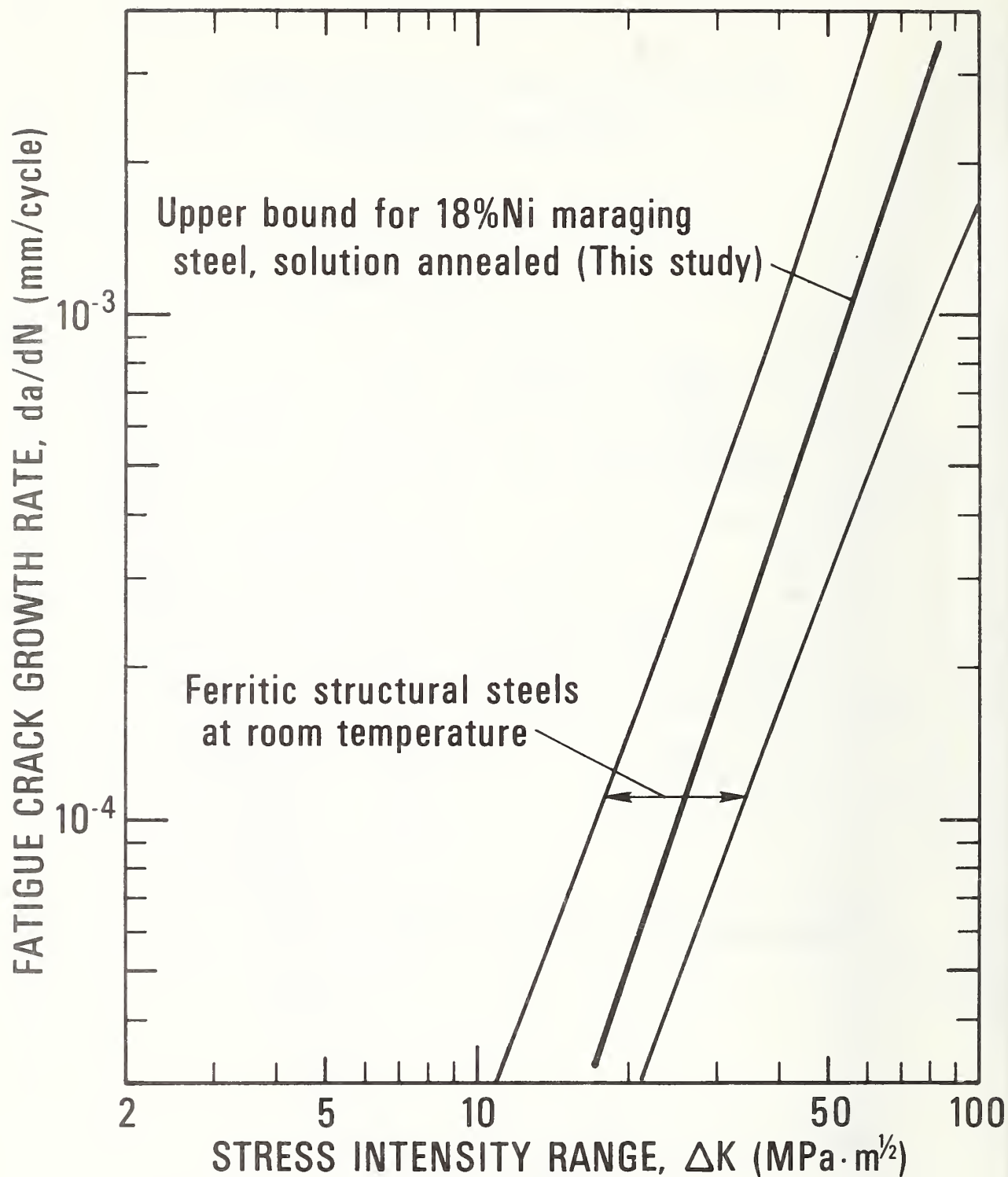


Figure 8. The fatigue crack growth data [Eq. (7)] for solution-annealed 300 grade maraging steel versus room temperature data for other steels [11, 12, 25, 26].

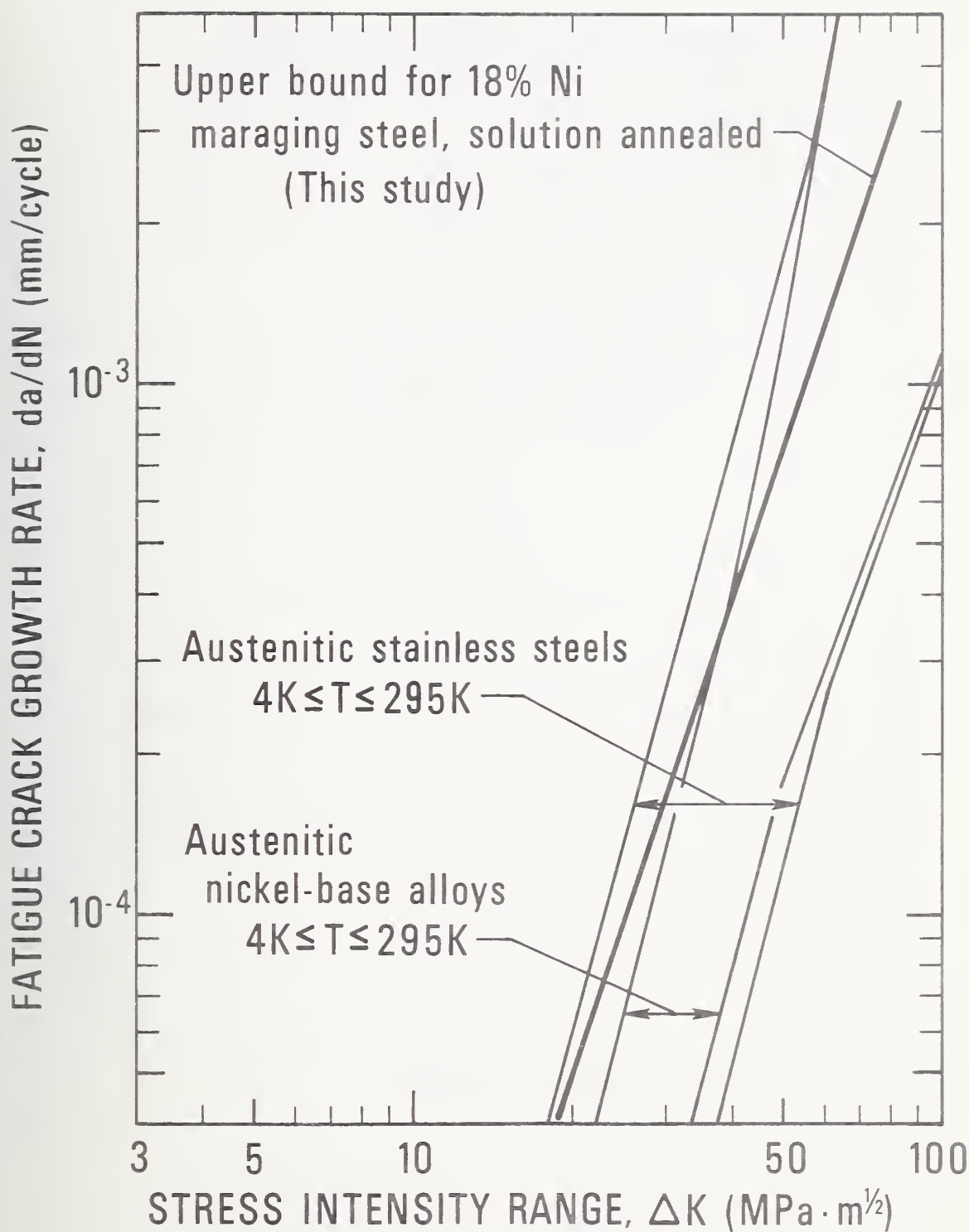


Figure 9. The fatigue crack growth data [Eq. (7)] for solution-annealed 300 grade maraging steel versus data for austenitic superalloys and stainless steels tested at 295 and 4 K [27-29].

CRYOGENIC EFFECTS ON THE FRACTURE MECHANICS  
PARAMETERS OF FERRITIC NICKEL ALLOY STEELS+

R.L. Tobler

Cryogenics Division  
Institute for Basic Standards  
National Bureau of Standards  
Boulder, Colorado 80302

+ NBS contribution, not subject to copyright.



## ABSTRACT

Fracture toughness data ( $K_{IC}$ ,  $J_{IC}$ ) and fatigue-crack growth rates ( $da/dN$ ) are reported here for quenched and tempered low carbon ferritic 3.5 Ni and 9 Ni steels at temperatures between 295 K and 4 K. Such data are needed for cryogenic fluid containment and superconducting machinery design. The tests were performed using 25 and 31 mm thick compact specimens having fracture planes normal to the long transverse plate dimension. The fracture toughness results for both steels showed qualitatively similar trends: at decreasing temperatures below 295 K,  $J_{IC}$  increased by about 20%, prior to the onset of classical ductile-to-brittle transitions involving cleavage. The transitions occurred between 172 K and 100 K for 3.5 Ni steel, and between 76 K and 4 K for 9 Ni steel. The transitional behavior was also evident in fatigue-crack growth resistance. At room temperature, the fatigue crack growth rates for these nickel steels are typical of many other ferritic materials; however the rates at sub-transition temperatures are drastically accelerated, due to cleavage. Data comparisons between 3.5 and 9 Ni steels tested here and other nickel alloy steels are included in discussion.

Key words: Fatigue; fracture; low temperature tests; mechanical properties; nickel alloys; steels.

## INTRODUCTION

Low-carbon ferritic 2 1/4 to 9% nickel alloy steels were developed to provide low-cost alternatives to the more heavily-alloyed austenitic stainless steels which are too expensive for use in many large-tonnage cryogenic structural applications. Since 1947, the effects of nickel on the mechanical properties of the ferritic steels have been studied and reviewed [1-9], one major finding being that increased nickel content leads to progressively lower ductile-to-brittle transition temperatures. Construction costs are minimized by selecting the appropriate nickel content for the intended service temperature range. For example, 3.5 Ni steel (ASTM A 203 grade E) has a minimum use temperature of 172 K (-150°F), and is used for liquid acetylene, ethylene, and propane tankage. On the other hand, 9 Ni steel (ASTM A 553 grade A) is used for liquified natural gas and nitrogen tankage at temperatures as low as 76 K (-321°F).

The tensile and impact properties of these steels are well-researched, but such data are insufficient to insure fail-safe design according to modern techniques of fracture mechanics analyses. The fracture parameters currently needed for more accurate material selection and design efficiency are:  $K_{IC}$ , the critical plane-strain stress intensity factor;  $J_{IC}$ , the critical value of the J-integral; and  $da/dN$ , the fatigue-crack growth rate where  $a$  is crack length and  $N$  is fatigue cycles. The parameters  $K_{IC}$  and  $J_{IC}$  characterize the magnitude of crack-tip elastic stresses or plastic strains, during monotonic loading, respectively, while  $da/dN$  governs sub-critical flaw growth cyclic loading. This paper investigates the temperature dependence of these parameters for quenched and tempered 3.5 Ni and 9 Ni steels tested at room temperature and reduced temperatures approaching absolute zero.

## Materials and Specimens

A 2.54 cm thick plate of ASTM A 203 grade E steel (3.5 Ni), and a 3.2 cm thick plate of ASTM A 553 grade A Type I steel (9 Ni) were obtained from commercial sources. Both steels were received and tested in the quenched and tempered conditions. The 3.5 Ni steel had been tested at 1172 K for 1 h, and water quenched, followed by tempering at 896 K 1 h, and water quenched. The 9 Ni steel was heated at 1064 K for 1.5 h, and water quenched, followed by tempering at 877 K for 1.25 h and air-cooled. The mill chemical analyses for both steels are listed in Table 1, and the uniaxial tensile properties at selected test temperatures are listed in Table 2.

Compact specimens for fatigue and fracture tests were machined in the TL orientation, having planar dimensions proportional to specimen width,  $W$ , according to the ASTM E 399-74 method [10]. The 3.5 Ni steel specimens were 2.5 cm thick, and the width-to-thickness ratio,  $W/B$ , was 2.0. The 9 Ni steel specimens were (diagrammed elsewhere [11]) were 3.1 cm thick, with  $W/B = 2.4$ . Attached to knife edges at the loadline was a double-cantilever beam-type clip gage that satisfied the ASTM E 399-74 Method linearity requirements at each test temperature.

## PROCEDURES

The environments studied here were room temperature air at 295 K, nitrogen vapor at 111 K or 172 K, liquid nitrogen at 76 K, and liquid helium at 4 K. Two 3.5 Ni steel fatigue tests were also performed in an alcohol/dry ice bath at 195 K. The low temperature apparatus included a 100 kN servo-hydraulic test machine and cryostat previously described [11,12].

## Fracture Toughness

Direct  $K_{IC}$  measurements for nickel alloy steels are seldom

reported because the ASTM E 399-74 thickness criterion for valid linear-elastic tests is difficult to satisfy. The specimen thickness criterion requires that:

$$B \geq 2.5 \left( \frac{K_{IC}}{\sigma_y} \right)^2 \quad (1)$$

where  $\sigma_y$  is the yield strength of the material. In this study J-integral and ASTM E 399-74 test methods were used alternatively, depending on the type of load-deflection (P- $\delta$ ) behavior encountered. Examples of P- $\delta$  records for 9 Ni steel specimens are shown in Fig. 1.

#### Nonlinear, Plastic Fractures

Where ductile fractures by stable tearing occurred (9 Ni steel at 295 and 111 K; 3.5 Ni steel at 295 and 172 K), J-resistance curves were determined using Landes and Begley's method [13]. J as a function of crack extension was determined by heat-tinting experiments in which a series of precracked specimens at each material/temperature combination were loaded to cause crack extensions of between zero and 0.49 cm. After unloading, tinting, and complete fracturing, crack extension was measured to the nearest 0.001 cm at three thickness locations, and averaged. J values were calculated from the approximation:

$$J = \frac{2A}{B(W - a)} \quad (2)$$

where A is the total area (energy) under the P- $\delta$  curve.  $J_{IC}$  was then obtained by extrapolating the J-versus- $\Delta a$  plots back to the critical point of material separation,  $\Delta a_c$ . (Crack extensions less than  $\Delta a_c$  are

apparent crack extensions due only to plastic deformation or blunting.) Several reasonable extrapolations were examined to account for scatter. Finally, estimates of  $K_{IC}$  denoted  $K_{IC}(J)$  were derived from the relation:

$$K_{IC}(J) = \frac{EJ_{IC}}{(1-\nu^2)}^{1/2} \quad (3)$$

Young's modulus ( $E$ ) and Poisson's ratio ( $\nu$ ) for these steels at low temperatures are known from the work of Weston, Naimon, and Ledbetter [14].

#### Linear-Elastic or Unstable Fractures

Where fast fracture occurred (9 Ni steel at 76 and 4 K; 3.5 Ni steel at 111, 76 and 4 K), conditional fracture toughness values denoted  $K_Q$  were calculated according to ASTM E 399-74. Some of the  $K_Q$  results approached nearly accurate  $K_{IC}$  determinations, but none were valid according to a strict interpretation of ASTM E 399-74.

In the case of 3.5 Ni steel at 76 K and 4 K, excessive crack front curvature proved unavoidable in combination with the restriction that the precracking stress intensity factor had to remain below  $0.6 K_{IC}$ . For 3.5 Ni steel at 111 K, Eq. (1) was not satisfied, and the  $K_Q$  data decidedly invalid. For 9 Ni steel at 76 K, Eq. (1) was not satisfied, but the  $P$ - $\delta$  curve was sufficiently linear that  $J_{IC}$  could be calculated at maximum load, assuming sub-critical crack growth was negligible. At 4 K, the 9 Ni steel test records exhibit a unique saw-toothed appearance, as shown in Fig. 1, due to multiple pop-ins (unstable crack extensions) and arrests. The  $P_{max}/P_Q$  ratios at 4 K exceeded 1.10, but heat-tinting experiments confirmed that the nonlinearity was due to cracking, not plasticity.

#### Fatigue-Crack Growth Rates

Fatigue-crack growth was monitored using the compliance method



previously described [11,12]. Rates at stress intensity factors,  $K_f$ , as high as  $50 \text{ MPa}\cdot\text{m}^{1/2}$  were measured during the precracking stages of fracture specimen preparation, while rates at higher stress intensities were measured with specimens not used for fracture toughness tests. At least two specimens were tested per temperature.

All tests used a sinusoidal load cycle at 20 Hz, and a R ratio ( $P_{\min}/P_{\max}$ ) of 0.1. The a-versus-N curves were fitted to a third-order polynomial and differentiated by computer, leading to an uncertainty in da/dN results of less than  $\pm 25\%$ . The da/dN data were plotted as a function of the stress intensity factor ranges which were calculated using the ASTM E 399-74 solutions for K and f(a/W):

$$\Delta K = K_{\max} - K_{\min} = \frac{(P_{\max} - P_{\min})}{BW^{1/2}} [f(a/W)] \quad (4)$$

## RESULTS

### Fracture Toughness

Table 3 lists the fracture toughness results for 3.5 Ni steel at 295, 172, 111, 76, and 4 K. The J-resistance curves at 295 K and 172 K, shown in Figure 2, yield  $J_{IC}$  values of  $163 \text{ kJm}^{-2}$  and  $193 \text{ kJm}^{-2}$ , respectively. The corresponding  $K_{IC}$  estimates from Eq. (1) are  $190 \text{ MPa}\cdot\text{m}^{1/2}$  at 295 K and  $219 \text{ MPa}\cdot\text{m}^{1/2}$  at 172 K. Although the ASTM E 399-74 results for this steel at lower temperatures are invalid, due primarily to excessive crack-front curvature, it appears that  $K_{IC}$  approaches 30 to  $50 \text{ MPa}\cdot\text{m}^{1/2}$  near absolute zero.

The fracture toughness results for 9 Ni steel at 295, 111, 76, and 4 K are listed in Table 4. The J-resistance curves for this steel at 295 K and 111 K (Fig. 3) yielded  $J_{IC}$  values of  $117 \text{ kJm}^{-2}$  and  $140 \text{ kJm}^{-2}$ ,



respectively, and the  $K_{IC}$  estimates are  $156 \text{ MPa}\cdot\text{m}^{1/2}$  at 295 K and  $174 \text{ MPa}\cdot\text{m}^{1/2}$  at 111 K. Between 111 K and 76 K,  $K_{IC}(J)$  is reduced slightly to  $167 \text{ MPa}\cdot\text{m}^{1/2}$ , and it appears that the ductile-to-brittle fracture transition is just beginning at 76 K. Below 76 K the fracture toughness rapidly decreases, and at 4 K nearly all of the ASTM E 399-74 criteria for  $K_{IC}$  measurements are satisfied. The sole criticism that can be levelled against the 4 K results for 9 Ni steel is that the  $a/W$  ratios of about 0.6 slightly exceed the preferred range of 0.45 to 0.55. The statement " $K_Q \approx K_{IC}$ " in Table 4 indicates that these 4 K data are believed to be nearly accurate  $K_{IC}$  results.

The temperature effects on  $K_{IC}$  estimates for the 3.5 Ni and 9 Ni steels are shown in Fig. 4, along with results for a 5 Ni steel [11] that was tested using compact specimens (3.1 cm thick) and similar procedures. The 5 Ni steel was in the austenitized, tempered, and reversion annealed condition, which tends to decrease the transition temperature slightly compared to the quenched and tempered condition. In the range 295 to 4 K, all three steels exhibit: (1) an "upper shelf" temperature region showing an initial enhancement of fracture resistance at decreasing temperatures, (2) a transition range of abruptly decreasing toughness, and (3) a temperature-insensitive sub-transition range. For each steel, absolute zero is a sub-transition temperature. Within the transition range,  $K_{IC}$  increases by factors from 2.2 to 3. An interesting point seldom noted is that each steel exhibits a maximum fracture resistance within the upper shelf range, just prior to undergoing the fracture transition. The 6 Ni steel tested in a previous study also showed this type of behavior between 295 K and 76 K [11]. For these materials, the peak  $K_{IC}(J)$  value is about 10 to 15% higher than the value at room temperature.

Nickel's beneficial effects on fracture resistance in the transition and sub-transition regions are attributed to favorable effects on the deformation characteristics and cleavage resistance of iron, combined with a tendency to promote the formation of retained austenite [3,7-9]. As indicated in Figure 4, the transition temperature intervals correlate with nickel content, lying approximately in the ranges:

1.  $4\text{ K} < T < 76\text{ K}$  for 9 Ni steel
2.  $\sim 60\text{ K} < T < 111\text{ K}$  for 5 Ni steel, and
3.  $\sim 100\text{ K} < T < 172\text{ K}$  for 3.5 Ni steel.

The fracture toughness at sub-transition temperatures also increases with nickel content, with the  $K_{IC}$  values at 4 K ranging from  $30\text{ MPa}\cdot\text{m}^{1/2}$  for 3.5 Ni steel to  $80\text{ MPa}\cdot\text{m}^{1/2}$  for 9 Ni steel. On the otherhand, the upper shelf toughness is apparently more sensitive to heat treatment and metallurgical factors other than nickel content; 5 Ni steel exhibits the highest upper shelf fracture toughness, perhaps due to the uniform distribution of carbides and other benefits [7] associated with austenitizing, temperizing, and reversion annealing [7].

#### Fatigue-Crack Growth Rates

Over the range of stress intensity factors investigated (20 to  $80\text{ MPa}\cdot\text{m}^{1/2}$ ) the fatigue-crack growth rates for the 3.5 and 9 Ni steels conform to equations of the type proposed by Paris and Erdogan [15]:

$$\frac{da}{dN} = C(\Delta K)^n \quad (5)$$

where  $n$  and  $C$  are material and temperature dependent empirical constants. Log-log plots of the  $da/dN$ -versus- $\Delta K$  were constructed to reveal linear trends from which the  $n$  and  $C$  values were determined as

the slopes and ordinate intercepts at  $\Delta K = 1$ , respectively. Table 5 lists the  $n$  and  $C$  values for each material/temperature combination.

Consider the room temperature results, shown in Fig. 5. Here, "Paris equation" equivalents representing the 3.5 Ni and 9 Ni steels of this study and the 5, 6, and 9 Ni steels of a previous study [11] are superimposed on a scatterband for commercially available construction steels where nickel is not a major alloying element [16-20]. The data spread for the nickel alloy steels is nearly equivalent to that for the non-nickel steels, with fatigue-crack growth rate variations approaching a factor of 4. However, the data for two 9 Ni steel alloys, show that heat-to-heat differences can account for fatigue-crack growth rate variations of at least a factor of 2 or three. It appears that the fatigue-crack growth resistances of nickel alloy steels at room temperature are typical of ferritic steels in general, and there seems to be no simple correlation between fatigue-crack growth rates and yield strength or nickel content.

The results in Fig. 6 reveal no dramatic temperature effects on the fatigue crack growth resistance of 3.5 Ni steel, as long as the temperature remains within the upper shelf region identified by the  $J_{IC}$  tests. The fatigue crack growth rates at 195 K and 172 K are nearly equivalent or slightly improved compared to the rates for this steel at room temperature. On the otherhand, further temperature reductions to 76 K greatly accelerate the rates to values well above those at room temperature. As indicated earlier, 76 K is a sub-transition temperature for this steel; inferior fatigue-crack growth resistance at this temperature is associated with the appearance of cleavage-type cracking modes, and a single increase of the Paris equation exponent from  $n = 3.2$  at 295 K to  $n = 7.6$  at 76 K.

The fatigue-crack growth behavior of 9 Ni steel is analogous to that of 3.5 Ni steel in that low temperature effects are moderate until the sub-transition range is approached. Data for the 9 Ni steel at 295, 111, 76, and 4 K are shown in Fig. 7. The rates decrease as temperature is lowered from 295 K to 111 K, but between 111 K and 76 K the trend is reversed. Thus, for  $\Delta K$  greater than  $40 \text{ MPa}\cdot\text{m}^{1/2}$ , the rates at 76 K exceed those at 295 K. Previous tests of a second heat of 9 Ni steel also revealed higher rates at 76 K than at 295 K [11]. At more extreme cryogenic temperatures, the present data at 4 K confirm that the fatigue crack propagation resistance continues to deteriorate. Thus, for the  $\Delta K$  range investigated, the fatigue crack growth resistance of 9 Ni steel is at a maximum near 111 K, the same temperature at which a peak in the static fracture toughness was observed.

#### DISCUSSION

Strain-rate, section thickness, and notch severity are three factors that usually influence the transition temperatures. Nevertheless, recent reports indicated the fracture toughness of 5 and 9 Ni steels to be unimpaired by dynamic loading [9]. Therefore the relatively thick and sharply-cracked compact specimens used for static fracture tests may provide a more severe test of crack tolerance than traditional tests based on Charpy impact energies.

Any comparison between the data of this report and the literature must carefully take into account the differences in measurement procedures. Standard  $K_{IC}$  determinations from the ASTM E 399-74 Method provide the most reliable comparisons, but valid  $K_{IC}$  data are rare. Pense and Stout [9] indicated that most authors reported " $K_C$ " or " $K_{max}$ "



values. The wide variety of test variables and data reduction schemes makes " $K_C$ " data comparisons difficult. In the present study, the J-integral at initiation of crack extension is reported, rather than a  $K$  value calculated at the maximum load point. Huettich, Pense and Stout [4] report a  $K_{IC}$  measurement of  $43 \text{ MPa}\cdot\text{m}^{1/2}$  for a quenched and tempered 3.5 Ni steel tested at 89 K ( $-300^\circ\text{F}$ ). Based on the data trend of Fig. 4, our 3.5 Ni steel indicates 30% higher toughness. This difference could be due to test procedures, since Huettich et al. precracked their specimens at room temperature.

In reference to 9 Ni steel, Syn, Jin, and Morris [5] reported a  $K_{IC}$  value of  $78 \text{ MPa}\cdot\text{m}^{1/2}$  for a double-normalized and tempered grade at 6 K, nearly agreeing with the present result of  $75 \text{ MPa}\cdot\text{m}^{1/2}$  for a quenched and tempered grade tested at 4 K. Our  $K_{IC}(J)$  results for 9 Ni steel are up to 16% lower than results for a second heat tested at 295 K and 76 K [11]. The difference in fracture toughness for these two heats may be attributed to material variability since: (1) the J-integral test procedures were equivalent, and (2) the fracture surface topographies reveal distinctly different features, especially at room temperature, as shown in Fig. 8.

The 9 Ni steel of this study displayed highly uniform crack fronts, as compared to results from other studies. As listed in Tables 3 and 4, the edge crack lengths for the 9 Ni steel were typically 97% as long as the average crack lengths at central thickness. Similar values for 5, 6, and 9 Ni steels (see Fig. 8) ranged from 88 to 90% [11]. These crack-front curvature effects should not greatly influence the  $da/dN$  comparisons, since the compliance method of crack growth measurement is sensitive to through-the-thickness variations.

As indicated in Table 5, the Paris equation exponents for most nickel steels are nearly 3.0 at room temperature, which is expected for ferritic steels, based on Barsom's findings [16]. The Paris equation exponents tend to increase, depending on the severity of the temperature reduction. For example, the 9 Ni steel, shows a progressively increasing exponent from  $n = 2.7$  at room temperature to  $n = 5.3$  at 4 K. As long as the temperature remains in the upper shelf range, fatigue crack growth resistance is satisfactory. The rates for 9 Ni steel at 111 K and 76 K, and for 3.5 Ni steel at 195 K and 172 K deviate from their 295 K trends by margins not greater than observed in the scatter-band shown in Fig. 5. Thus, variations in fatigue crack growth resistance due to temperature variations in the upper shelf ranges are of the same magnitude as variations induced by metallurgical effects in other ferritic steels at room temperature. It appears that the trend of decreasing fatigue crack growth resistance with decreasing temperatures is caused by the incidence of brittle cleavage modes which become predominant as the maximum fatigue stress intensity factor approaches  $K_{IC}$  at low test temperatures. Knott and Ritchie correlated high  $n$  values with steels of low fracture toughness, indicating that  $n$  is likely to exceed 4.0 if  $K_{IC}$  is  $80 \text{ MPa}\cdot\text{m}^{1/2}$  or lower [21]. Lindley and Richards also associate high  $n$  values with brittle crack propagation modes such as occur in static fracture tests [22].

#### SUMMARY

The onset of cleavage fracture modes which account for transitions to low fracture toughness in ferritic steels also lead to a deterioration of fatigue-crack growth resistance. The quenched and tempered 3.5



Ni and 9 Ni steels exhibit low temperature fatigue-crack growth and fracture toughness data trends that are believed to be representative, qualitatively, of ferritic steels in general. Initially, the resistance to crack extension under monotonic loading increases at decreasing temperatures below 295 K, reaching a maximum prior to the ductile-to-brittle transition. The transition for 3.5 Ni steel lies between 172 and 110 K, and the transition for 9 Ni steel lies between 76 and 4 K. Based on observations for these and previously tested nickel steels, the ratios of the peak  $K_{IC}$  values to the minimum  $K_{IC}$  values exhibited near absolute zero are between 2.5:1 and 5:1. The fatigue-crack growth resistance of ferritic steels at room temperature apparently is not measurably influenced by nickel content. Reduced temperatures in the upper shelf range may improve the fatigue-crack growth resistance slightly, but fatigue cracking at sub-transition temperatures is drastically accelerated by cleavage such that the rates at normal temperatures may be exceeded by an order of magnitude.

#### CONCLUSION

The fracture mechanics properties reported here for familiar cryogenic tankage steels are of practical design value for existing and future structural applications. The data clearly illustrate general behavior trends for ferritic steels tested over the complete ambient-to-cryogenic range. In the future, it may be possible to improve the fracture resistance of the 3.5 Ni and 9 Ni steels by applying heat treatments analogous to the austenitized, temperized, and reversion annealing treatment applied to 5 Ni steel [7]. As regards superconducting machinery developments, these steels would not be ideal for use

in tensile-loading (Mode I) applications at 4 K, unless they can be reprocessed to eliminate the fracture transition as discussed by Syn, Jin, and Morris in reference to 9 Ni steel [5].

#### ACKNOWLEDGMENTS

Test materials for this program were donated by the Lukens Steel and Armco Steel Corporations. The program was sponsored by the National Maritime Administration and the Advanced Research Projects Agency of the U.S. Department of Defense. The assistance of Dr. R. P. Mikesell and R. L. Durcholz in conducting tests is gratefully acknowledged.

#### REFERENCES

1. Yeo, R. B. G. and Miller, O. O., "A History of Nickel Steels from Meteorites to Maraging," Sorby Centennial Symposium on History of Metallurgy, ASM, Cleveland, OH, October 21-23, 1963.
2. Properties of Materials for Liquefied Natural Gas Tankage, ASTM STP 579, (Amer. Soc. Test. Mater., Philadelphia, 1975) 1-420.
3. Floreen, S., Hayden, H. W., and Devine, T. M., Cleavage Initiation in Fe-Ni alloys, Met. Trans. 2 (1971) 1403.
4. Huettich, N. J., Pense, A. W., and Stout, R. D., The Toughness of 2 1/4 and 3 1/2% Nickel Steels at Cryogenic Temperatures, WRC Bulletin No. 165 (Welding Research Council, 1974) 1.
5. Syn, C. K., Jin, S., and Morris, J. W., Jr., Cryogenic Fracture Toughness of 9% Ni Steel Enhanced Through Grain Refinement, Met. Trans., submitted for publication.
6. McHenry, H. I. and Reed, R. P., "Fracture Behavior of the Heat-Affected Zone in 5% Ni Steel Weldments," Welding Journal, submitted for publication.

7. Sarno, D. A., Havens, F. E., and Bowley, D. L., Transformations involved in Developing Notch Toughness in a New 5% Nickel Steel for Cryogenic Purposes (ASM Technical Report No. C70-39-2, American Society for Metals, 1970).
8. Johnson, R. J., The Role of Nickel in Carburizing Steels, Metals Eng. Quart., 15 (1975) 1.
9. Pense, A. W. and Stout, R. D., Fracture Toughness and Related Characteristics of the Cryogenic Nickel Steels, WRC Bulletin No. 205 (Welding Research Council, 1975) 1.
10. Standard Method of Test for Plane Strain Fracture Toughness of Metallic Materials, E 399-74 Annual Book of ASTM Standards, Part 10 (Amer. Soc. Test. Mater., Philadelphia, 1976) 471.
11. Tobler, R. L., Mikesell, R. P., Durcholz, R. L., and Reed, R. P., "Low Temperature Fracture Behavior of Iron-Nickel Alloy Steels," Ref. 1, 261.
12. Fowlkes, C. W. and Tobler, R. L., Fracture Testing and Results for a Ti-6Al-4V Alloy at Liquid Helium Temperature, Eng. Fract. Mechs. 8 (1976) 487.
13. Landes, J. D. and Begley, J. A., Test Results from J-integral Studies: An Attempt to Establish a  $J_{IC}$  Test Procedure, in Fracture Analyses, ASTM STP 560 (Amer. Soc. Test. Mater., Philadelphia, 1973) 231.
14. Weston, W. F., Naimon, E. R., and Ledbetter, H. M., "Low Temperature Elastic Properties of Aluminum 5083-O and Four Ferritic Nickel Steels," Ref. 1, 397.
15. Paris, P. C. and Erdogan, F., A Critical Analysis of Crack Propagation Laws, Trans ASME, J. Basic Eng., 85 (1963) 528.

16. Barsom, J. M., Fracture-Crack Propagation in Steels of Various Yield Strengths, Trans. ASME, J. Eng. Ind. (1971) 1190.
17. Barsom, J. M., Imhof, E. J., and Rolfe, S. T., Fatigue Crack Propagation in High Yield Strength Steels, Eng. Fract. Mech. 2 (1971) 301.
18. Wei, R. P., Talda, P. M., and Che-Yu Li, Fatigue Crack Propagation in Some Ultra-High Strength Steels, in Fatigue Crack Propagation, ASM STP 415 (Amer. Soc. Test. Mater., Philadelphia, 1967) 460.
19. Brothers, A. J. and Yukawa, S., Fatigue Crack Propagation in Low Alloy Heat Treated Steels, Trans. ASME, J. Basic Eng., 89 (1967) 19.
20. Miller, G. A., The Dependence of Fatigue-Crack Growth Rate on the Stress Intensity Factor and Mechanical Properties of Some High Strength Steels, Trans. ASM, 61 (1968) 442.
21. Ritchie, R. O. and Knott, J. F., Mechanisms of Fatigue Crack Growth in Low Alloy Steel, Acta Met., 21 (1973) 639.
22. Richards, C. E. and Lindley, T. C., The Influence of Stress Intensity and Microstructure on Fatigue Crack Propagation in Ferritic Materials, Eng. Fract. Mech., 4 (1972) 951.

#### LIST OF TABLES

- Table 1. Mill chemical analyses of test materials.
- Table 2. Tensile properties of test materials.
- Table 3. Fracture toughness results for ASTM A 203 E (3.5% Ni) steel (specimen thickness = 2.54 cm).
- Table 4. Fracture toughness results for ASTM A 553 A (9% Ni) steel (specimen thickness = 3.1 cm).
- Table 5. Comparison of Paris equation parameters for nickel alloy steels.

Table 1. Mill chemical analyses of test materials, wt%.

Material	Fe	Ni	C	Mn	P	S	Si
ASTM A203-E (3.5 Ni steel) quenched and tempered	bal.	3.62	0.10	0.46	0.015	0.013	0.2
ASTM A553-A (9 Ni steel) quenched and tempered	bal.	8.99	0.08	0.62	0.010	0.010	0.1

Table 2. Tensile properties of test materials.

Material	Temperature K	0.2% Yield Strength <sup>a</sup> MPa	Ultimate Tensile Strength <sup>a</sup> MPa	Elongation in 2.54 cm gage <sup>a</sup> %	Reduction of Area <sup>a</sup> %	Young's Modulus <sup>b</sup> GPa	Poisson's Ratio <sup>b</sup>
ASTM A 203-E (3.5 Ni steel)	295	488.2	549.5	33.6	71.8	204	0.287
	111	564.6	659.8	36.2	69.4	213	0.283
	76	776.7	867.7	NA	NA	214	0.282
	4	900.8	911.1	35.1	57.8	215	0.282
ASTM A 553-A (9 Ni steel)	295	740.5	788.7	24	64.1	192	0.292
	111	913.5	1075.2	NA	NA	200	0.287
	76	1028.7	1202	NA	NA	201	0.286
	4	1329.3	1381.7	NA	NA	202	0.286

a. Average values from duplicate tests.

b. Data from Weston, Naimon, and Ledbetter [14].



Table 3. Fracture results for ASTM A 203 E (3.5 Ni) steel (specimen thickness = 2.54 cm).

Temperature K	Specimen	$K_{f1/2}$ MPa·m <sup>1/2</sup>	$a_e/a$	a/W	$P_{\max}/P_Q$	$K_{Q1/2}$ MPa·m <sup>1/2</sup>	J kJm <sup>-2</sup>	$\Delta a$ cm	$J_{IC2}$ kJm <sup>2</sup>	$K_{IC}^a(J)$ MPa·m <sup>1/2</sup>	$K_{IC}$
295	20	48	0.96	0.542	1.7	66	240	0.493			NA
	21	46	0.92	0.546	NA	65	124	0.064			NA
	22	50	0.90	0.552	1.5	69	317	0.838	163+10%	190+5%	NA
	24	48	0.94	0.544	1.6	67	174	0.135			NA
	27	50	0.93	0.552	1.7	60	254	0.457			NA
	27	50	0.93	0.552	1.7	60	254	0.457			NA
172	25	61	0.92	0.571	1.4	86	256	0.363			NA
	26	52	0.95	0.565	1.4	88	332	0.452			NA
	28	53	0.93	0.569	NA	82	70	0.000	193+10%	219+5%	NA
	29	67	0.94	0.585	1.4	89	214	0.150			NA
	30	75	0.93	0.596	1.4	90	231	0.321			NA
	2	40	0.98	0.557	1.0	74.8	NA	NA	NA	NA	Invalid <sup>b</sup>
111	31	45	0.85	0.530	1.4	81.0	NA	NA	NA	NA	Invalid <sup>b,c,d</sup>
76	10	34	0.90	0.582	1.0	63.4	NA	NA	NA	NA	Invalid <sup>g</sup>
	15	31	0.93	0.498	1.0	48.0	NA	NA	NA	NA	Invalid <sup>e</sup>
4	3 <sup>a</sup>	50	0.85	0.475	1.0	60.2	NA	NA	NA	NA	Invalid <sup>d,e,h</sup>
	23 <sup>a</sup>	44	0.88	0.545	1.0	49.9	NA	NA	NA	NA	Invalid <sup>d,e,h</sup>
	33 <sup>a</sup>	32	0.76	0.523	1.0	53.9	NA	NA	NA	NA	Invalid <sup>d</sup>
	36 <sup>a</sup>	29	0.75	0.530	1.0	32.2	NA	NA	NA	NA	Invalid <sup>d,e,f</sup>

a. Calculated using Eq. (3).

b. Insufficient specimen thickness.

c. Excessive  $P_{\max}/P_Q$  ratio.

d. Excessive edge-crack-to-average crack length ratio,  $a_e/a$ .

e. Excessive precracking stress intensity factor,  $K_f$ .

f. Precracked at 76 K.

g. Precracked at 195 K.

h. Precracked at 295 K.

Table 4. Fracture results for ASTM A 553-A (9 Ni) steel (specimen thickness = 3.1 cm).

Temperature K	Specimen	$K_f$ $MPa \cdot m^{1/2}$	$a_e/a$	$a/W$	$\frac{P_{max}}{P_Q}$	$K_Q$ $MPa \cdot m^{1/2}$	J $kJm^{-2}$	$\Delta a$ cm	$J_{IC}$ $kJm^{-2}$	$K_{IC}^a(J)$ $MPa \cdot m^{1/2}$	$K_{IC}$ $MPa \cdot m^{1/2}$
295	3	43	0.96	0.615	1.2	124	188	0.117			NA
	7	43	0.95	0.606	>1.17	120	116	0.043			NA
	11	41	0.94	0.611	NA	115	95	0.0	117±10%	156±5%	NA
	22	41	0.96	0.608	>1.2	113	155	0.100			NA
	23	43	0.96	0.608	>1.3	119	130	0.020			NA
	24	42	0.97	0.609	>1.3	110	153	0.071			NA
111	4	46	0.97	0.617	>1.28	119	130	0.011			NA
	6	48	0.95	0.616	>1.17	142	148	0.023			NA
	9	45	0.95	0.648	>1.25	144	218	0.084			NA
	15	41	0.97	0.607	>1.12	137	162	0.010	140±15%	174±8%	NA
	16	42	0.96	0.618	>1.19	136	232	0.114			NA
	18	45	0.96	0.606	>1.36	116	203	0.006			NA
76	21	40	0.95	0.613	1.07	147	99	NA	99	170	$K_Q \neq K_{IC}^b$
	20	33	0.96	0.612	1.07	145	92	NA	92	164	$K_Q \neq K_{IC}^b$
	17	37	0.97	0.611	1.09	144	97	NA	97	169	$K_Q \neq K_{IC}^b$
4	14 <sup>C</sup>	41	0.97	0.606	1.11	80.5	NA	NA	NA	NA	$K_Q = K_{IC}$
	12 <sup>C</sup>	33	0.98	0.608	1.15	67.3	NA	NA	NA	NA	$K_Q = K_{IC}$
	5	43	0.98	0.617	1.09	78.2	NA	NA	NA	NA	$K_Q = K_{IC}$

a. Calculated using Eq. (3)

b. Insufficient thickness.

c. Precracked at 76 K.

Table 5. Comparison of Paris equation parameters  
for nickel alloy steels (da/dN in mm/cycle).

Material	Temperature K	C	n	$\Delta K$ Region $\text{MPa}\cdot\text{m}^{1/2}$
ASTM A 203-E (3.5 Ni steel) This study.	295	$1.3 \times 10^{-8}$	3.2	18 to 60
	195	$1.3 \times 10^{-8}$	3.2	30 to 70
	172	$1.0 \times 10^{-9}$	3.2	30 to 60
	76	$1.6 \times 10^{-14}$	7.6	20 to 30
ASTM A 645 (5 Ni steel) [11]	295	$1.1 \times 10^{-8}$	2.7	25 to 90
	111	$1.1 \times 10^{-8}$	2.7	25 to 60
	76	$2.0 \times 10^{-10}$	4.0	27 to 80
N-TUF Cr-196 (5.5 Ni steel) [11]	295	$3.7 \times 10^{-9}$	3.0	22 to 85
	111	$3.7 \times 10^{-9}$	3.0	22 to 85
	76	$4.2 \times 10^{-9}$	3.2	25 to 75
ASTM A 553-A (9 Ni steel) [11]	295	$2.3 \times 10^{-7}$	2.0	27 to 100
	76	$3.1 \times 10^{-9}$	3.3	27 to 100
ASTM A 553-A (9 Ni steel) This study.	295	$2.0 \times 10^{-8}$	2.7	16 to 70
	111	$1.0 \times 10^{-9}$	3.4	17 to 80
	76	$4.8 \times 10^{-11}$	4.4	17 to 64
	4	$1.4 \times 10^{-11}$	5.3	25 to 35

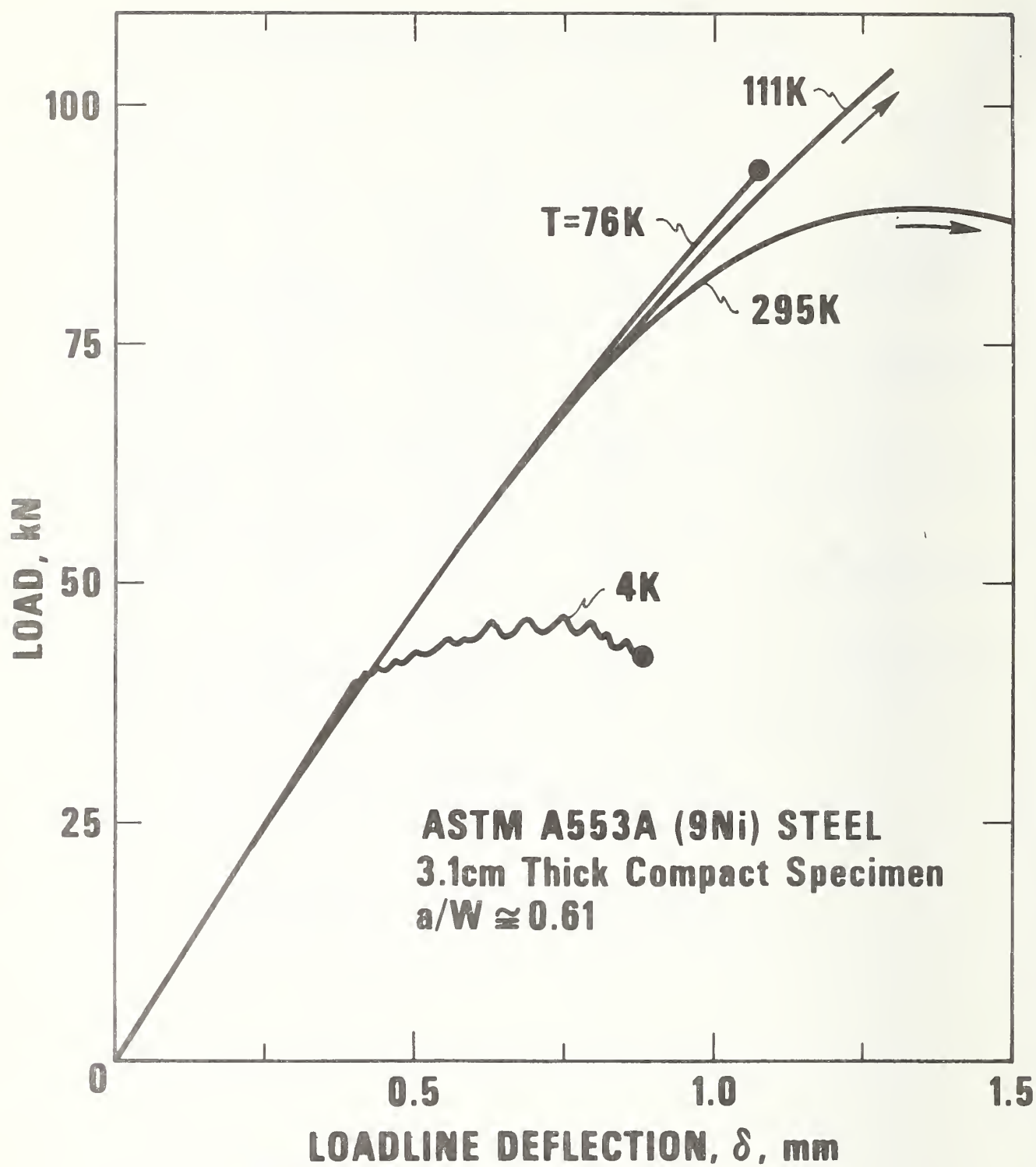


Figure 1. Load-versus-loadline deflection curves for 9 Ni steel.

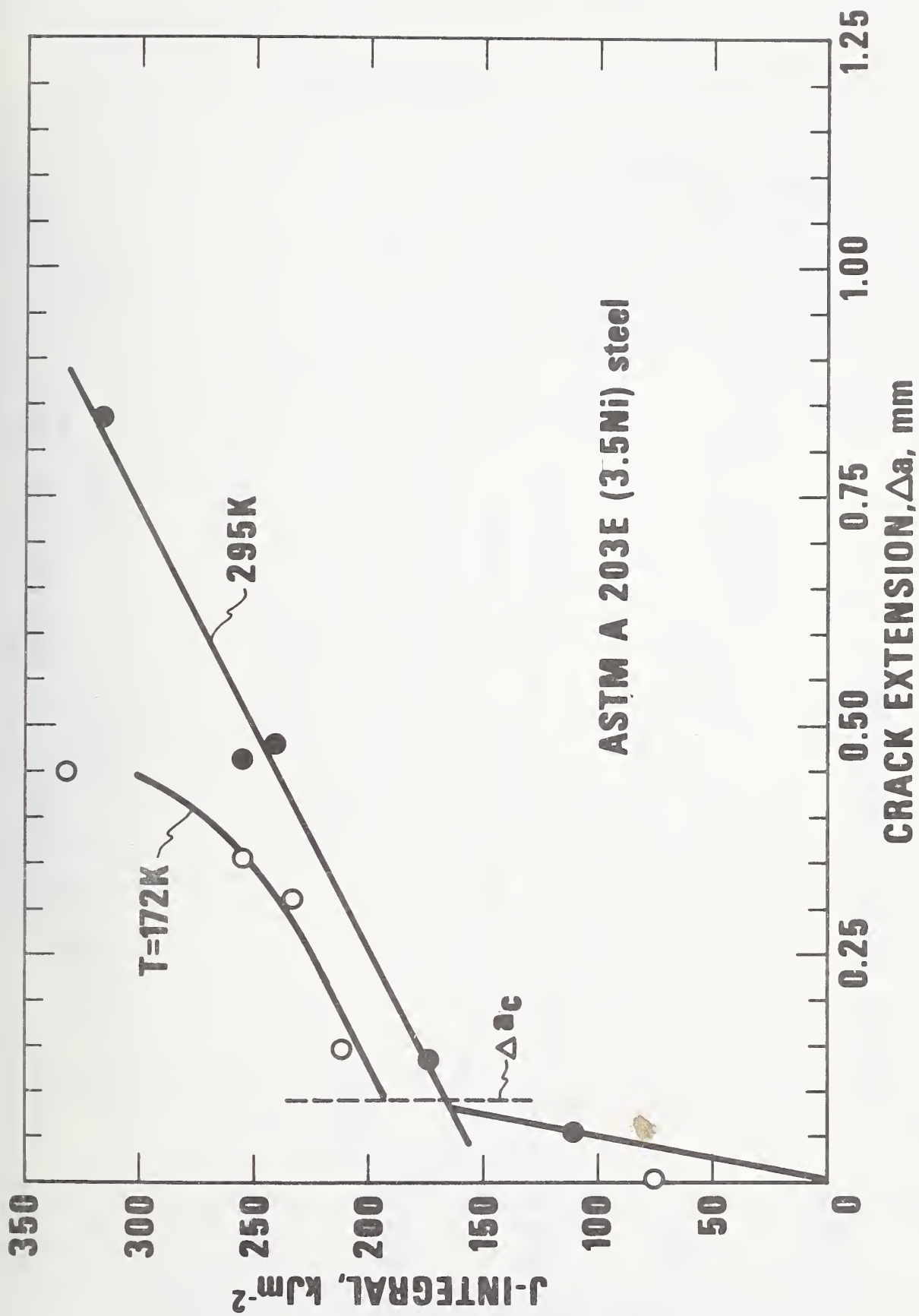


Figure 2. J-resistance curves for 3.5 Ni steel at room temperature (295 K) and the minimum use temperature (172 K).

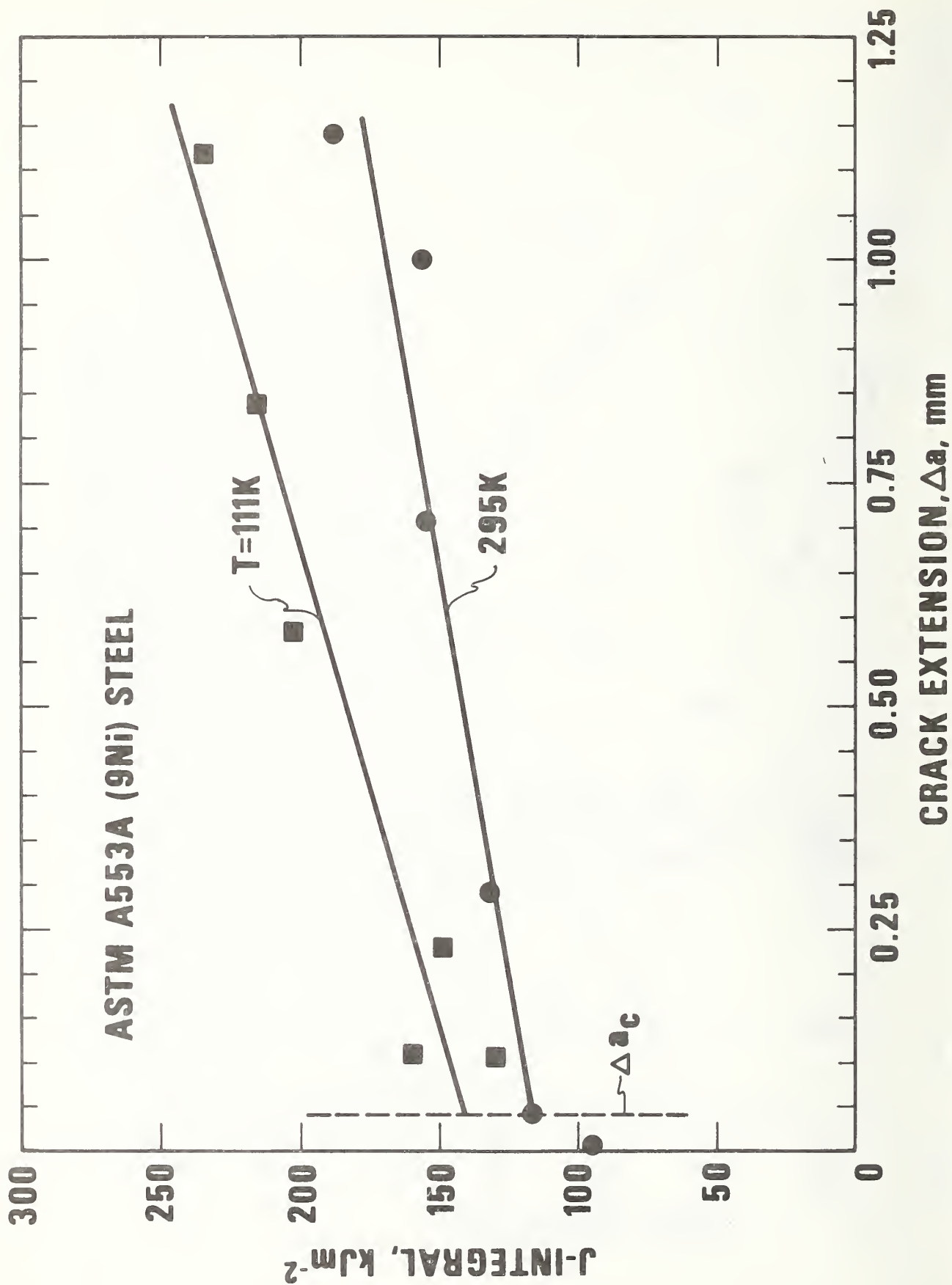


Figure 3. J-resistance curves for 9 Ni steel at room temperature (295 K) and liquefied natural gas temperature (111 K).



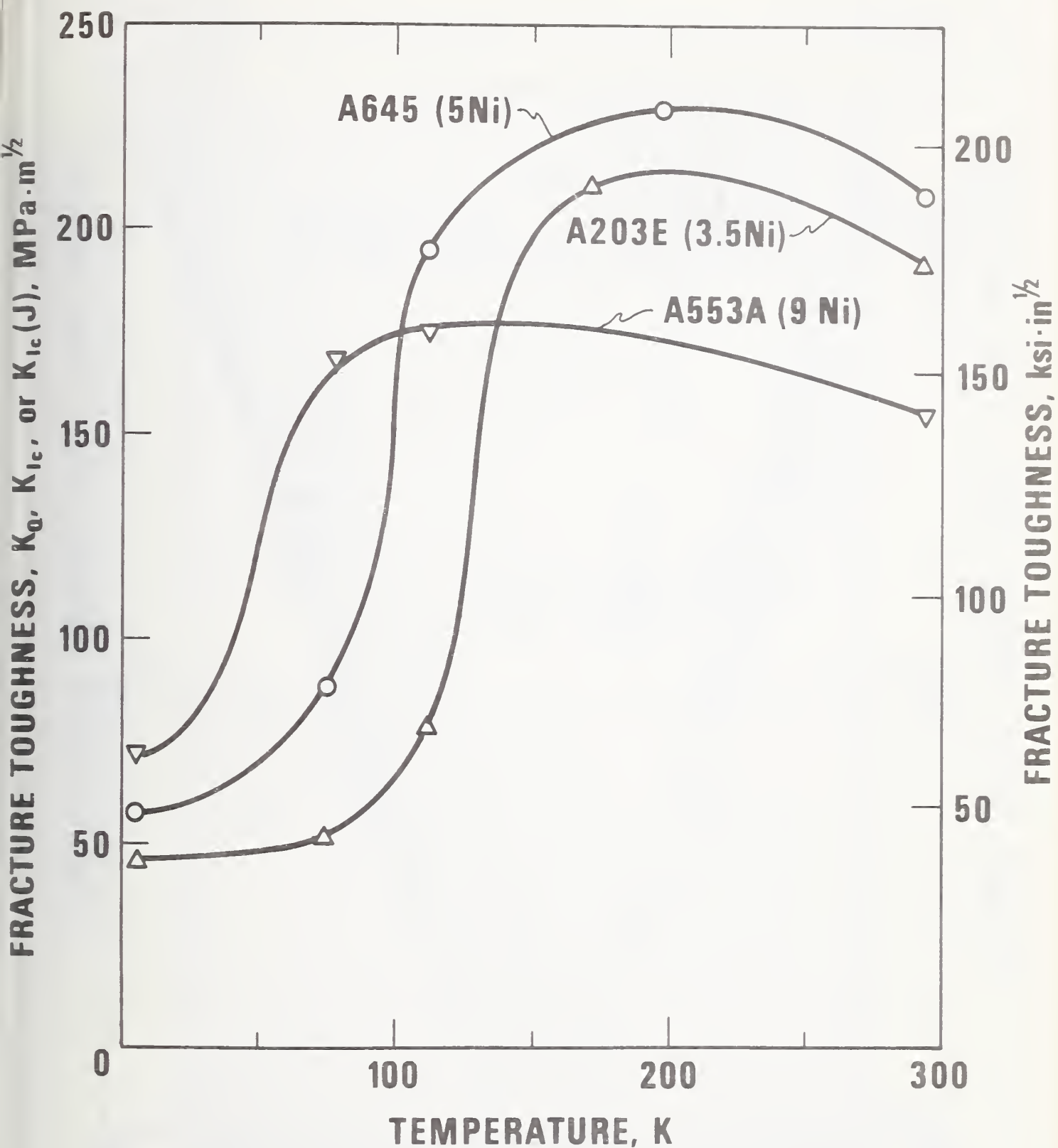


Figure 4. Temperature dependence of  $K_{IC}$  estimates obtained for the 3.5 Ni and 9 Ni steels of this study and the 5 Ni steel of a previous study [11].

FATIGUE CRACK GROWTH RATE,  $da/dN$ , mm/cycle

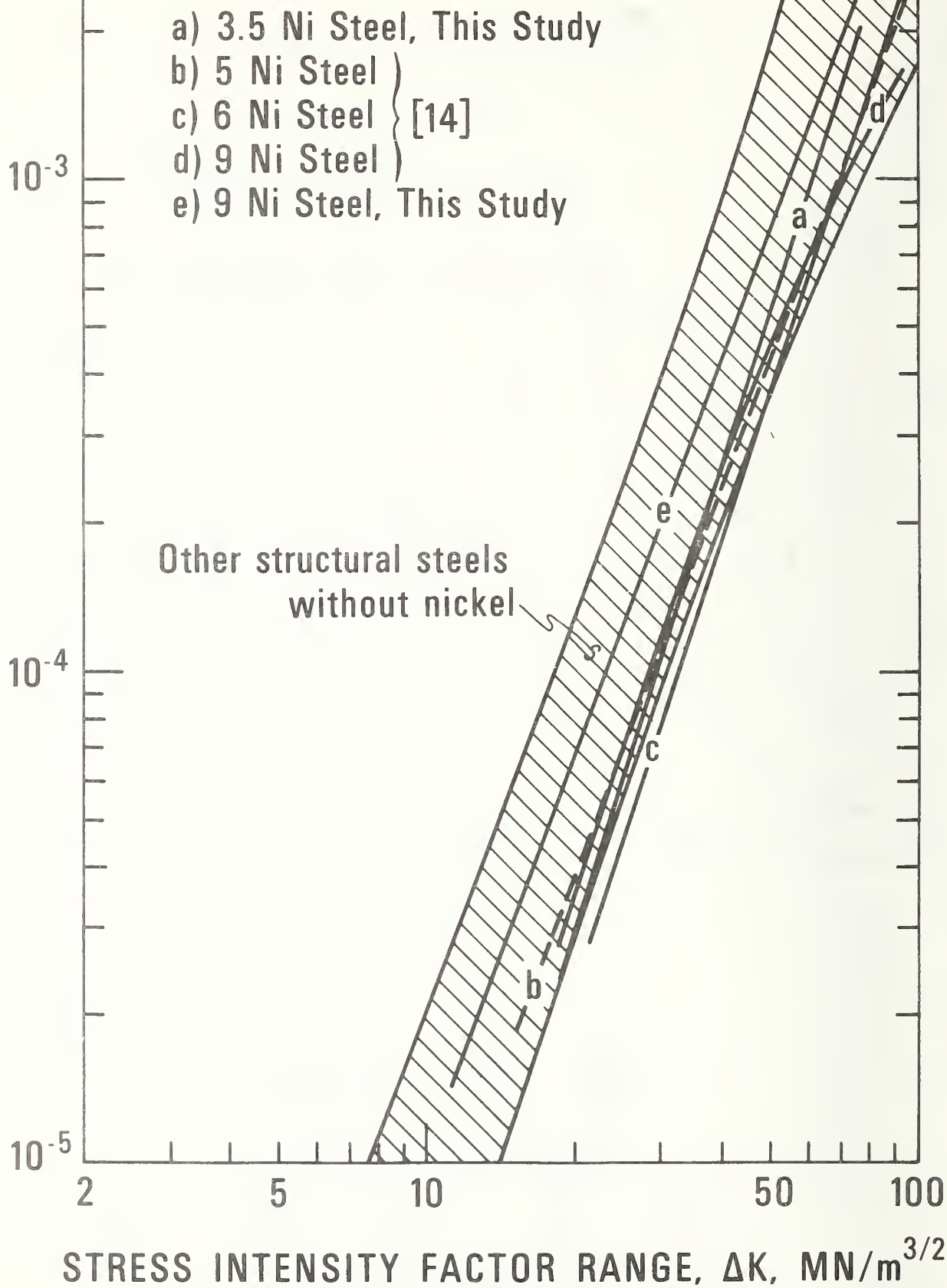


Figure 5. Room temperature fatigue crack growth data for the 3.5 Ni and 9 Ni steels of this study, the 5, 6, and 9 Ni steels of a previous study [11], compared to data for other ferritic structural steels without nickel [16-20].

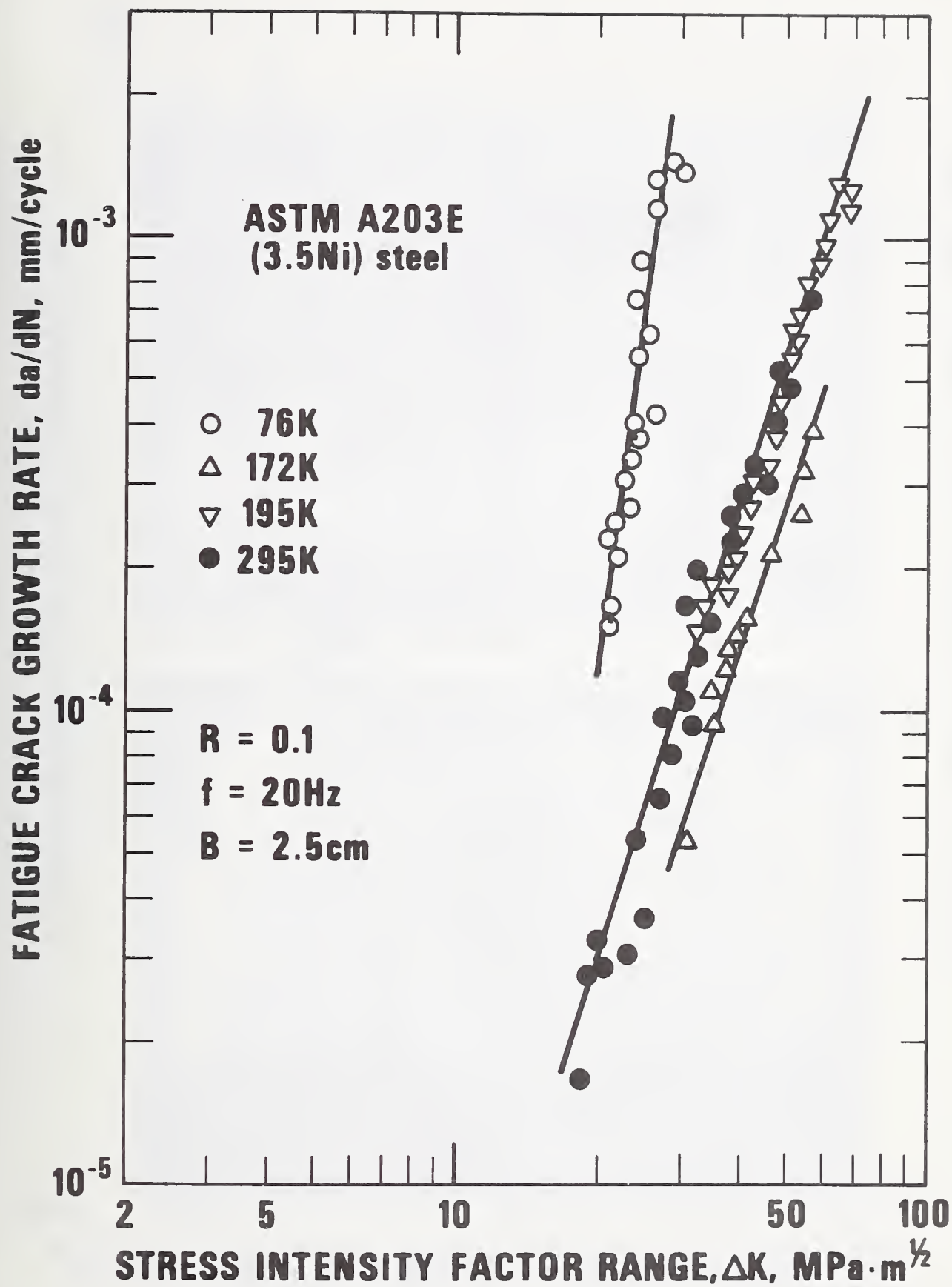


Figure 6. Fatigue-crack growth rates for 3.5 Ni steel at room and cryogenic temperatures.

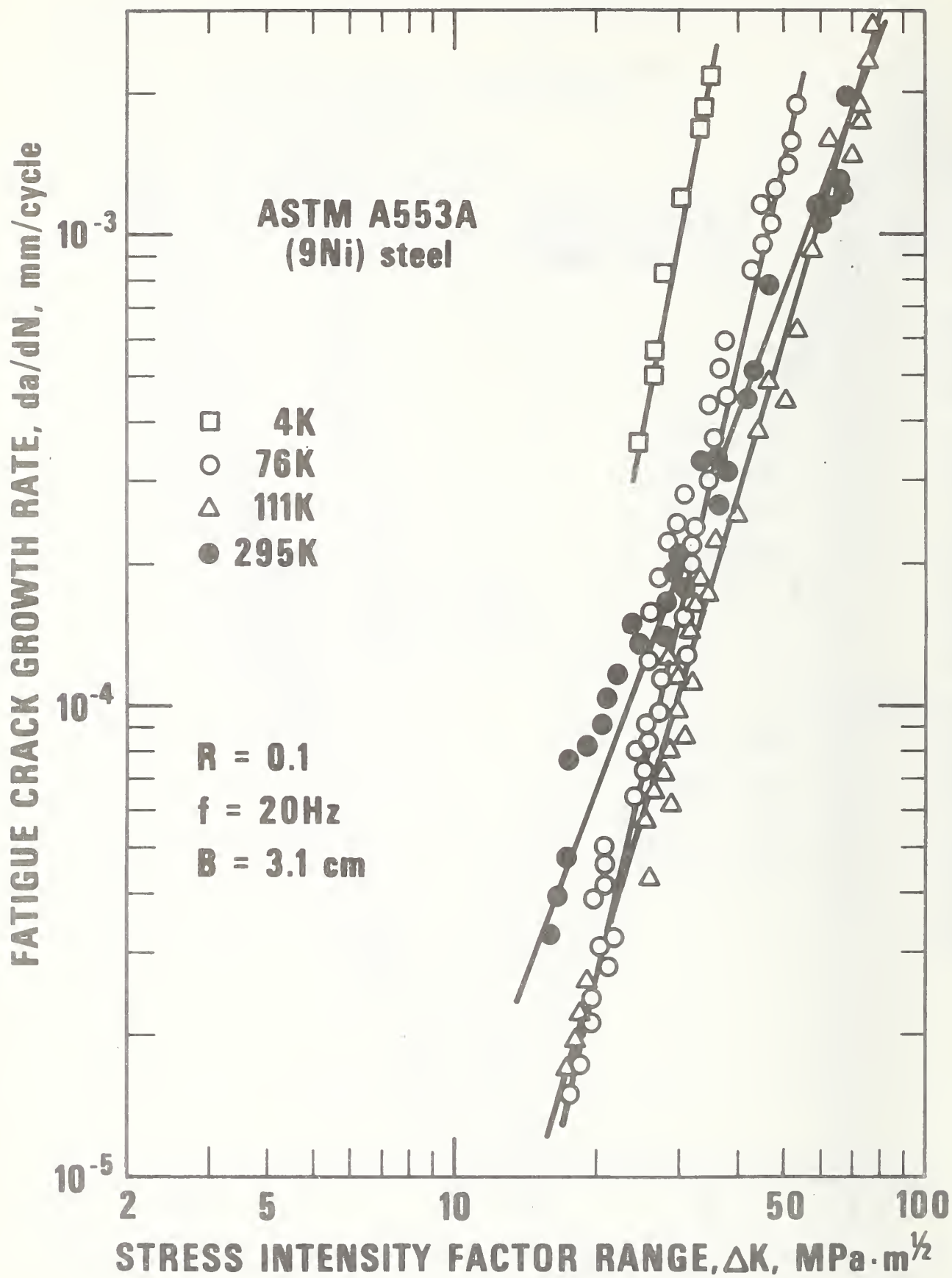


Figure 7. Fatigue-crack growth rates for 9 Ni steel at room and cryogenic temperatures.



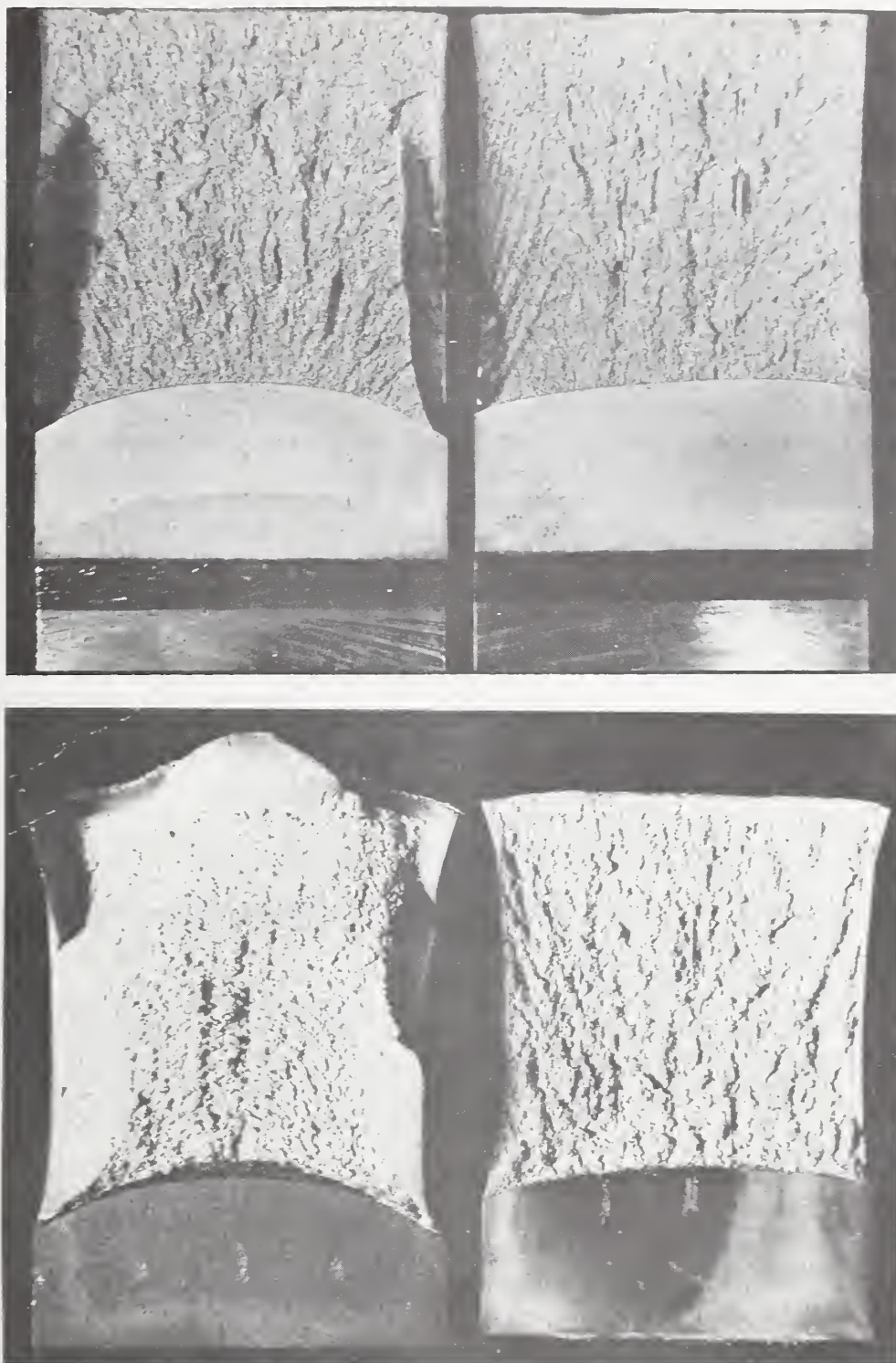


Figure 8. A comparison of the fracture surfaces of two different heats of 9 Ni steel fractured at 295 K (Top) and 76 K (Bottom) reveals heat-to-heat variability. The quenched and tempered 9 Ni steel of a previous study (left) displays a greater proportion of shear fracture at specimen edges, as well as a more pronounced degree of crack-front curvature.

## NOTE ON THE FRACTURE PROPERTIES OF Fe-49Ni AT CRYOGENIC TEMPERATURES

H. I. McHenry and R. E. Schramm

The tensile, fatigue crack growth and fracture toughness properties of Fe-49 Ni were determined at room temperature, 76 K and 4 K. Tensile properties were determined with 25 mm gage length, 6.4 mm diameter specimens using the methods described previously by Reed [1]. Fatigue crack growth rates were determined with 25 mm thick, 51 mm wide compact tension specimens using the compliance method for crack length determinations; the test procedures and equipment were described previously by Fowlkes and Tobler [2]. Fracture toughness was determined with 25 mm thick, 51 mm wide compact tension specimens using the J-integral test procedures of Landes and Begley [3] and the cryogenic testing procedures and equipment described previously by Tobler et al. [4].

The results of the tensile tests are summarized in Table 1. The tensile and yield strengths at room temperature and 76 K are essentially the same as those obtained by Reed [5]. However, at 4 K the strength values obtained in this investigation are approximately 20% higher than those obtained by Reed [5].

The results of the fatigue crack growth tests are summarized in Figs. 1, 2 and 3. For each temperature, the line drawn through the data points has the form

$$\frac{da}{dN} = C(\Delta K)^n \quad (1)$$

where  $da/dN$  is the fatigue crack growth rate in mm/cycle,  $\Delta K$  is the stress intensity range in  $\text{MPa}\cdot\text{m}^{1/2}$ , and  $C$  and  $n$  are empirical constants. The



values for the intercept, C, the slope, n, and the coefficient of determination, R, were determined by least-squares regression analysis:

Temperature	C	n	R
Room Temp	$7.7 \times 10^{-9}$	3.0	.977
76 K	$8.4 \times 10^{-10}$	3.5	.981
4 K	$1.6 \times 10^{-10}$	3.9	.995

A comparison of the data indicate that over the range of crack growth rates measured, the data at 4 K and 76 K are essentially the same and the growth rate at room temperature ranges from 1.4 to 2.5 times faster than the growth rate at the cryogenic temperatures.

The results of the fracture toughness tests are summarized in Table 2 and plotted in Figs. 4, 5 and 6. The J-integral value (J) for each test is calculated using the approximation of Rice, Paris and Merkle [6]:

$$J = \frac{2A}{B(W - a)} \quad (2)$$

where A is the area under the load displacement curve, B is the specimen thickness, W is the width and a is the crack length. For each temperature a curve of J vs  $\Delta a$  (crack extension) is constructed. On the same graph, the line defined by Eq. (3) is drawn:

$$J = 2\sigma_f \Delta a \quad (3)$$

where  $\sigma_f = (\sigma_{ty} + \sigma_{tu})/2$ ,  $\sigma_{ty}$  = .2% offset yield strength and  $\sigma_{tu}$  = ultimate tensile strength. The intersection of the J- $\Delta a$  plot and the  $J/2\sigma_f$  line is defined as  $J_{IC}$ , the value of J at the onset of crack

extension. The values for  $J_{IC}$  are  $1000 \text{ KJ/m}^2$  at 76 K and  $870 \text{ KJ/m}^2$  at 4 K. At room temperature,  $J_{IC}$  was not defined because the curves did not intersect. It is reasonable to say that the room temperature toughness exceeds the  $J$  value for zero crack extension, i.e.  $281 \text{ KJ/m}^2$ .

Specimen size requirements for valid  $J_{IC}$  measurements have not yet been agreed upon by ASTM, however, Landes and Begley [3] suggest use of the following size criteria:

$$a, B, W-a \geq 25 J_{IC}/\sigma_f \quad (4)$$

By these criteria, the measurement capacity of a 2.5 cm thick ( $W = 5 \text{ cm}$ ) compact tension specimen precracked to  $a/W = 0.62$  would be determined by the ligament size,  $W-a = 1.9 \text{ cm}$ . The calculated measurement capacities are 275, 464 and  $568 \text{ KJ/m}^2$  at room temperature, 76 K and 4 K, respectively. At all temperatures, the measured  $J_{IC}$  values exceeded these limits. Thus, the specimen is not sufficiently large to assume that  $J$  characterizes the crack-tip field. If in fact the toughness does exceed the measurement capacity of the specimen, the toughness of Fe-49Ni is very high and not an important consideration in structural design.

Begley and Landes [7] have proposed that the plane strain fracture toughness,  $K_{IC}$ , is related to  $J_{IC}$  as follows:

$$K_{IC}(J) = \left( \frac{J_{IC} E}{1-\nu^2} \right)^{1/2} \quad (5)$$

where  $E$  is Young's modulus and  $\nu$  is Poisson's ratio. The values for  $E$  and

$\nu$  for Fe-49Ni were obtained from Ledbetter [8]: at 76 K  $E = 1.562 \times 10^{11}$  N/m<sup>2</sup> (22.6 x 10<sup>6</sup> psi) and  $\nu = .343$ ; at 4 K  $E = 1.569 \times 10^{11}$  N/m<sup>2</sup> (22.8 x 10<sup>6</sup> psi) and  $\nu = .343$ . The values calculated for  $K_{IC}(J)$  are 423 MPa·m<sup>1/2</sup> (382 ksi√in) at 76 K and 396 MPa·m<sup>1/2</sup> (396 ksi√in) at 4 K. These levels of toughness virtually preclude the possibility of brittle fracture in Fe-49Ni.

1. R. P. Reed, Advances in Cryogenic Engineering, Vol. 7 (Plenum Press, New York, 1962) p. 448.
2. C. W. Fowlkes and R. L. Tobler, Eng. Fract. Mech. 8 (1976) 487.
3. J. D. Landes and J. A. Begley, "Test Results for J-Integral Studies -- An Attempt to Establish a  $J_{IC}$  Testing Procedure," Westinghouse Research Laboratory Scientific Paper 73-1E-7-FMPWR-P3, 1973.
4. R. L. Tobler, R. P. Mikesell, R. L. Durcholz and R. P. Reed, ASTM STP 579, 1975, p. 261.
5. R. P. Reed, National Bureau of Standards, Boulder, CO, to be published.
6. J. R. Rice, P. C. Paris and J. G. Merkle, ASTM STP 536, 1973, p. 231.
7. J. A. Begley and J. D. Landes, ASTM STP 514, 1972, p. 1.
8. H. M. Ledbetter, National Bureau of Standards, Boulder, CO, to be published.

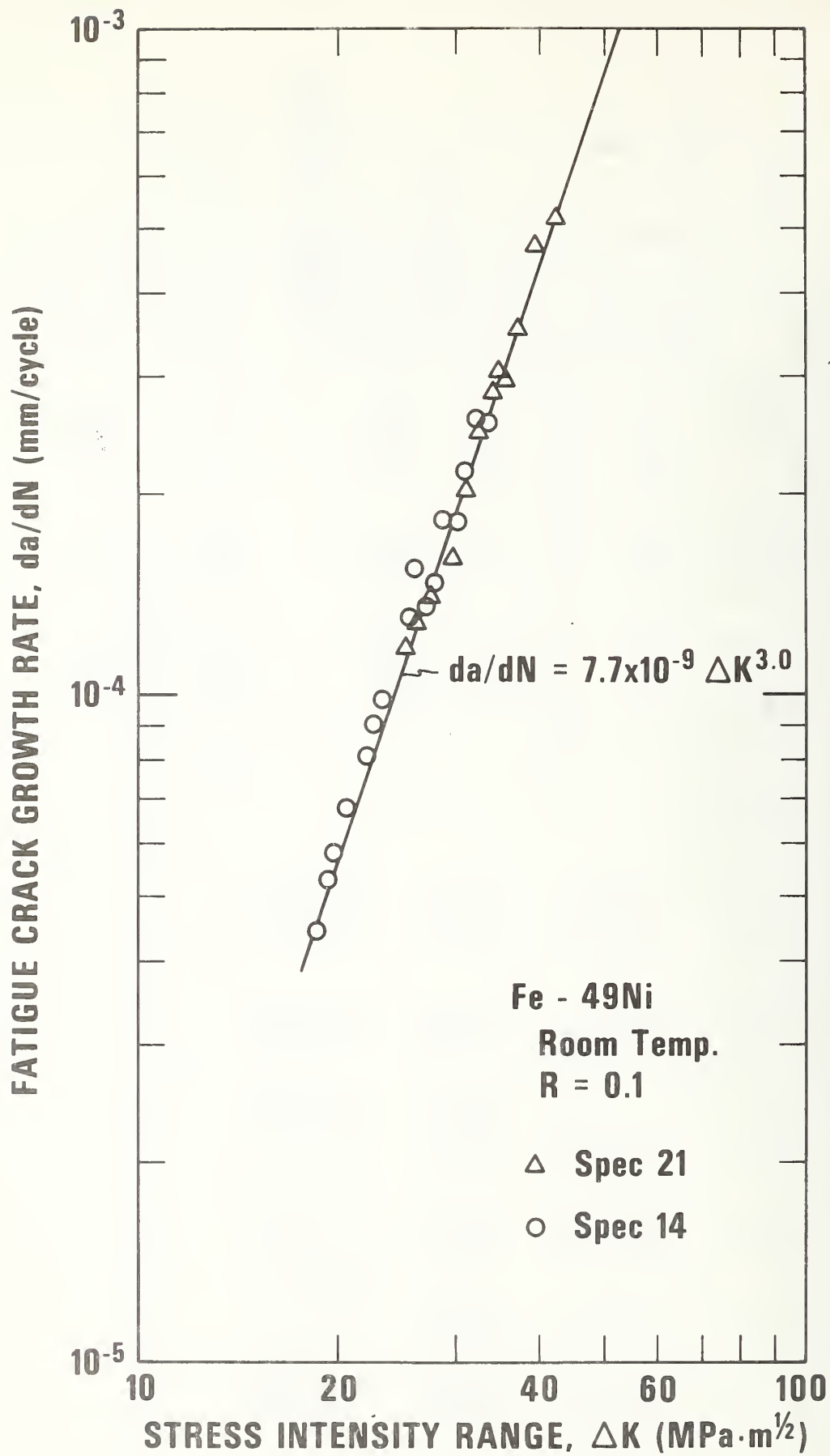
Table 1. Tensile property results for Fe-49Ni

Temperature K	Yield Strength		Ultimate Strength		Elongation % in 25 mm	Reduction of Area %
	MPa	(ksi)	MPa	(ksi)		
298	194	28.2	495	71.9	49	70
298	233	33.8	499	72.5	47	74
Average	214	31.0	497	72.2	48	72
76	351	51.0	841	122	57	72
76	365	53.0	845	123	56	72
Average	358	52.0	843	122	56	72
4	507	73.6	977	142	50	60
4	473	68.7	980	142	49	60
Average	490	71.1	978	142	49	60

Table 2. Fracture toughness results for Fe-49Ni

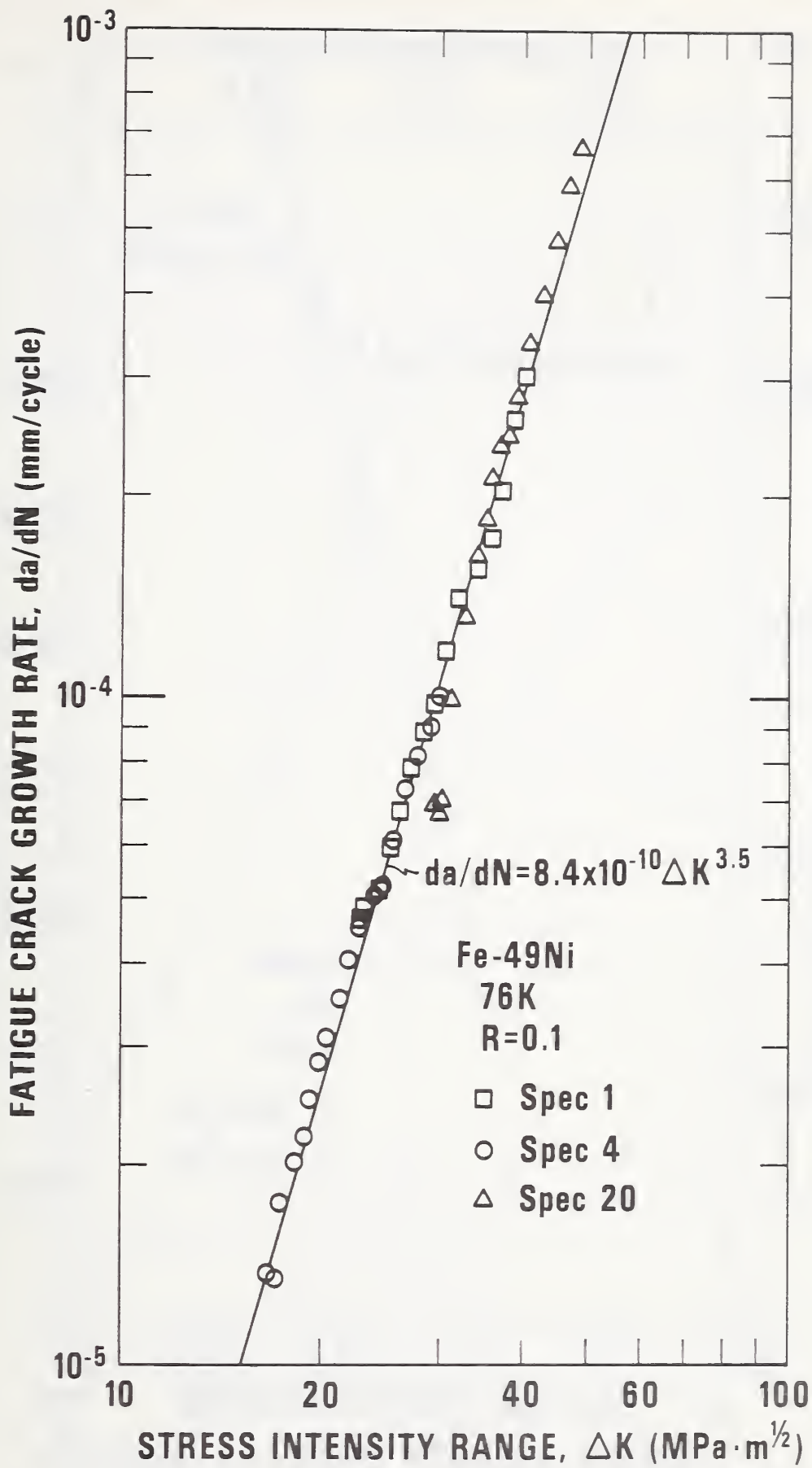
Temp	Spec No	a cm	a in	$\Delta a$ cm	$\Delta a$ in	J kJ/m <sup>2</sup>	J in·lb/in <sup>2</sup>	J <sub>IC</sub> kJ/m <sup>2</sup>	J <sub>IC</sub> in·lb/in <sup>2</sup>	K <sub>IC</sub> (J) MPa·m <sup>1/2</sup>	K <sub>IC</sub> (J) ksi·in <sup>1/2</sup>	Notes
Rm Temp	12	3.03	1.19	.055	.022	849	4840					
	14	3.17	1.25	0	0	281	1600					
	22	3.15	1.24	.027	.011	519	2960					
	23	3.01	1.18	.092	.036	1405	8010					
								Not defined by Landes Begley criterion				
76 K	1	3.16	1.24	.184	.0724	1720	9810					
	4	3.06	1.20	.036	.0143	826	4710					
	6	3.07	1.21	.152	.0598	1350	7680					
	17	3.03	1.19	.054	.0214	1250	7120					$\Delta a$ obliterated
								1000	5700	423	382	
4 K	5	3.12	1.228	.025	.0098	785	4470					
	7	3.06	1.206	.197	.0776	1300	7400					
	9	2.99	1.177	.053	.0207	809	4610					
	15	3.08	1.214	.094	.0372	1306	7740					
	16	3.15	1.242	.050	.0195	815	4640					
								870	4960	396	358	
												Preloaded to 92% P <sub>max</sub> Preloaded to 88% P <sub>max</sub>

Note: In all tests, the toughness exceeded the measurement capacity of the specimen.

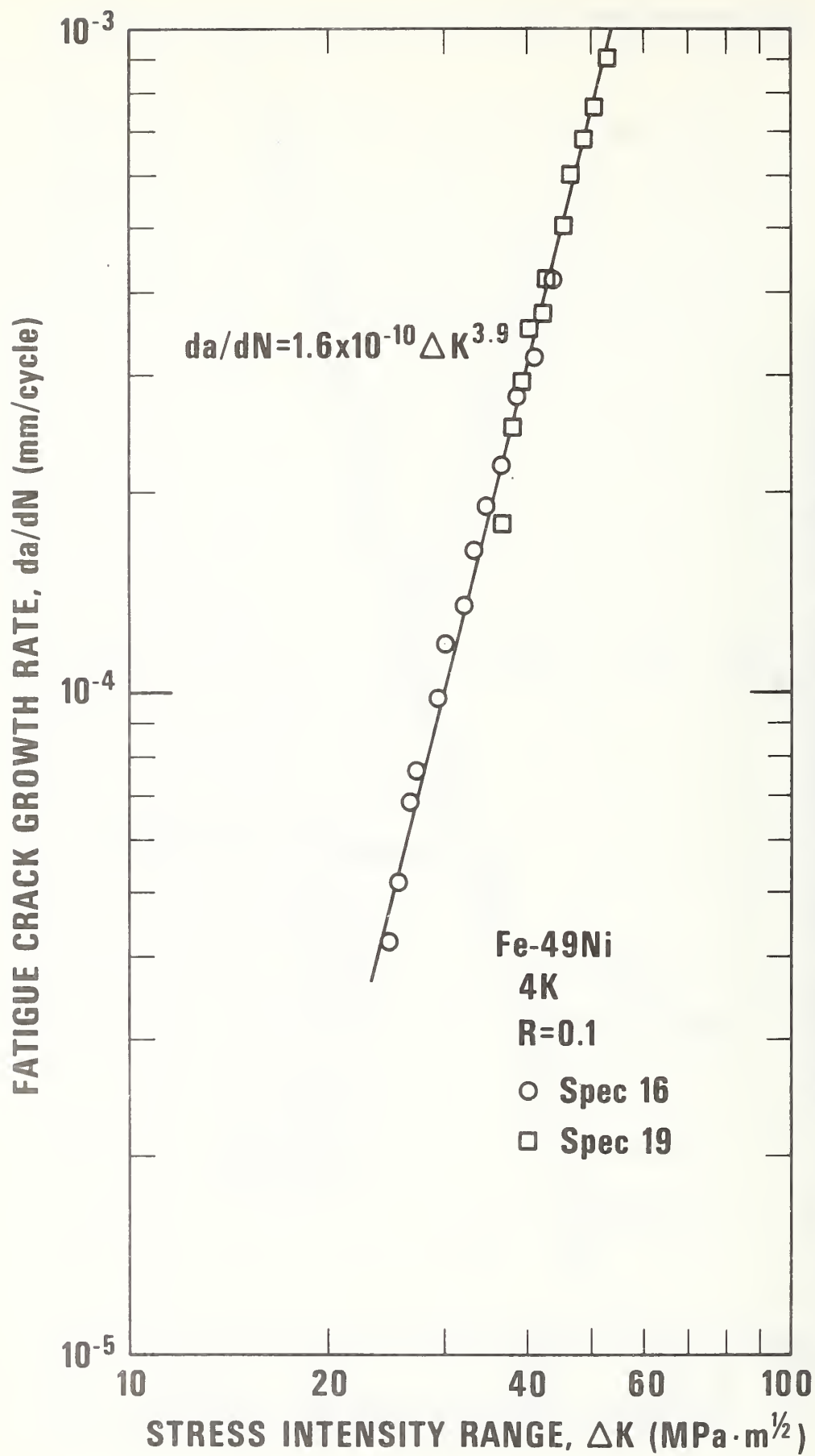


1. Fatigue crack growth rates in Fe-49 Ni at room temperature.

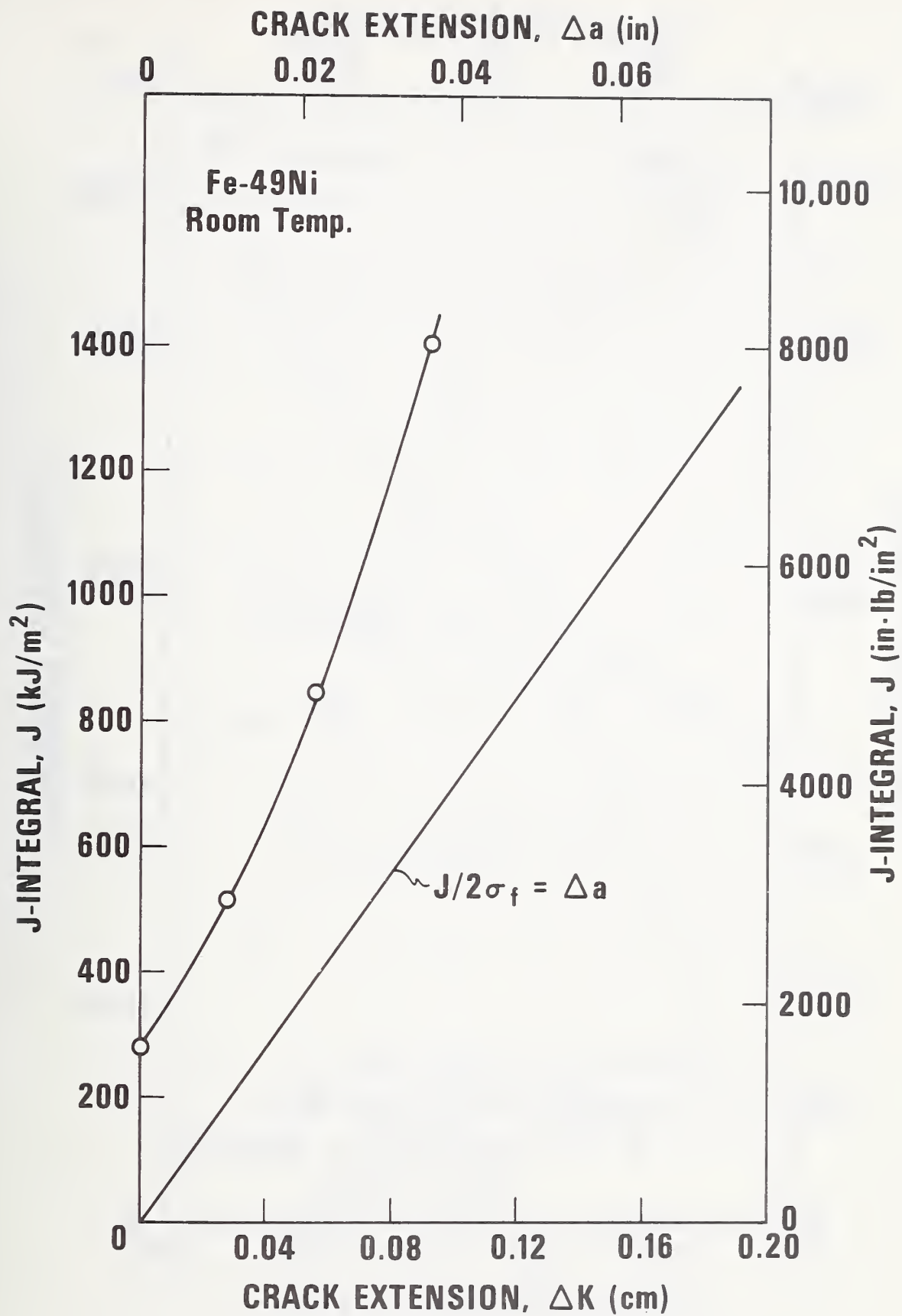




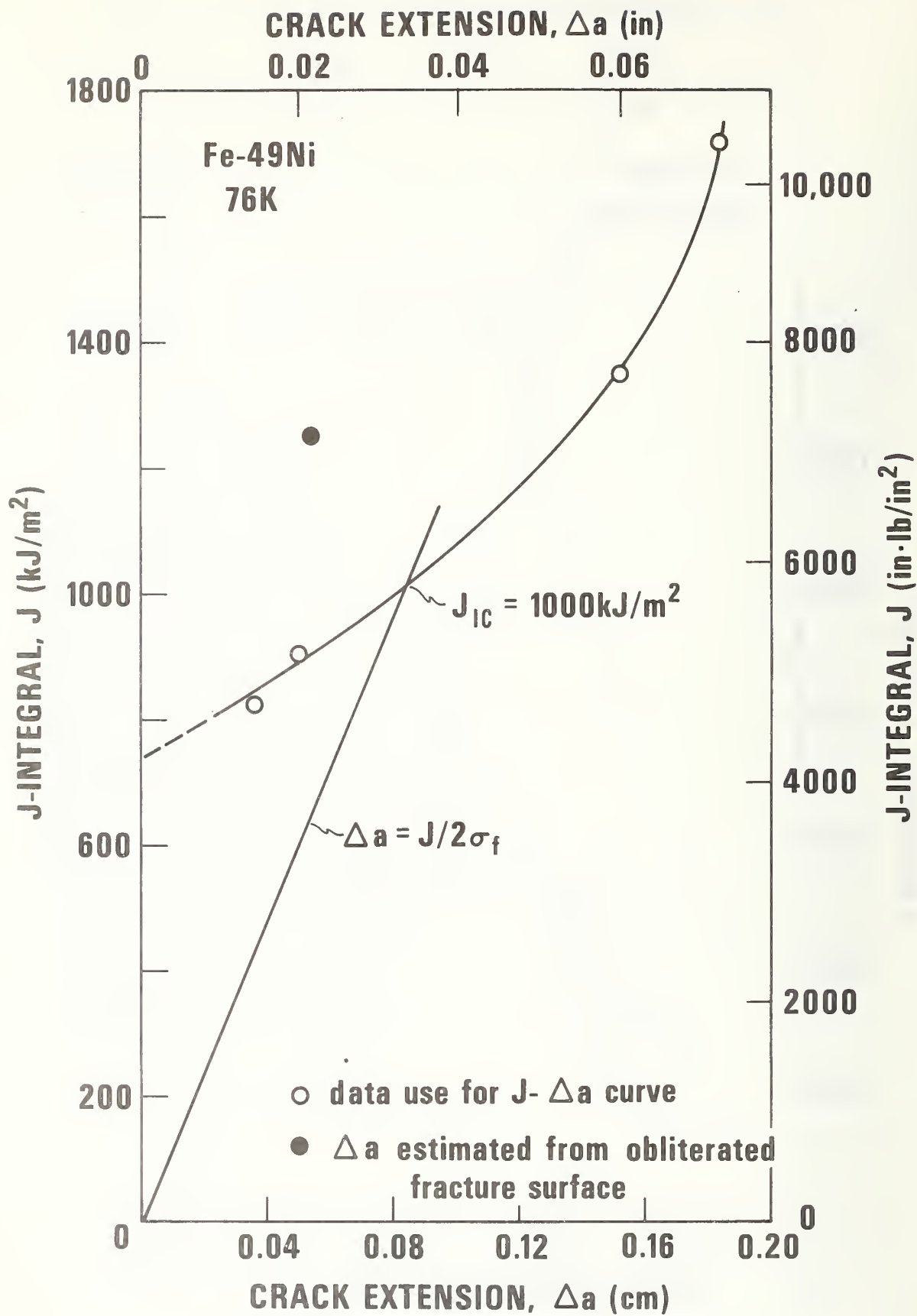
2. Fatigue crack growth rates in Fe-49 Ni at 76 K.



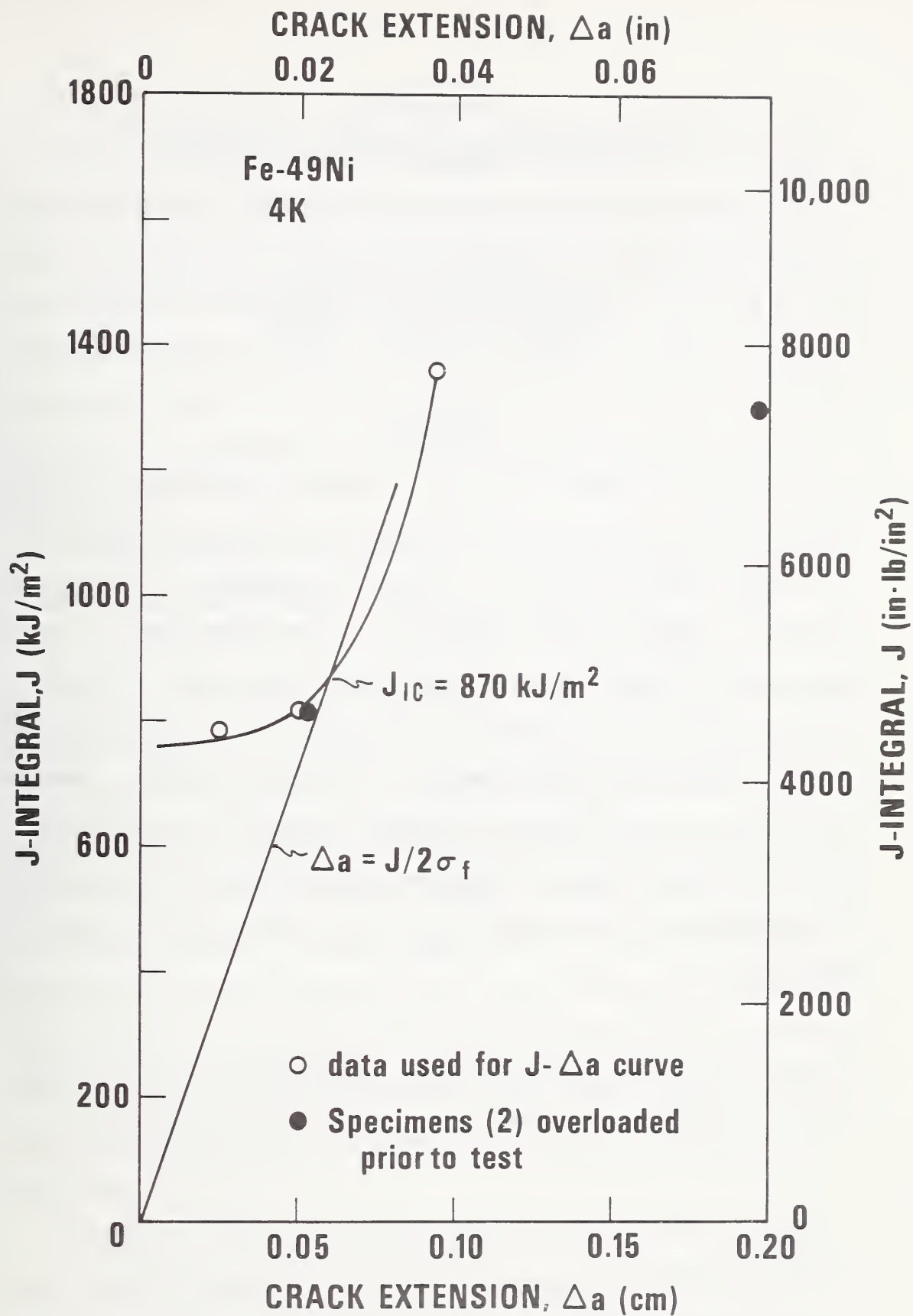
3. Fatigue crack growth rates in Fe-49 Ni at 4 K.



4. J- $\Delta a$  fracture toughness curve for Fe-49 Ni at room temperature.



5. J- $\Delta a$  fracture toughness curve for Fe-49 Ni at 76 K.



6. J- $\Delta a$  fracture toughness curve for Fe-49 Ni at 4 K.

FATIGUE CRACK GROWTH RESISTANCE OF STRUCTURAL  
ALLOYS AT CRYOGENIC TEMPERATURES\*

R. L. Tobler and R. P. Reed

Cryogenics Division  
Institute for Basic Standards  
National Bureau of Standards  
Boulder, Colorado 80302

ABSTRACT

Fatigue crack growth rate data at selected temperatures including 295, 76, and 4 K are presented for a variety of titanium alloys, stainless steels, and Fe-Ni alloys. The results correlate well with crystal structure. Compared to their behavior in a room temperature air environment, stable austenitic face-centered cubic alloys exhibit improved fatigue crack growth resistance at low temperatures. Hexagonal close-packed titanium alloys show temperature-insensitive behavior. Temperature effects on the fatigue crack growth resistance of body-centered cubic Fe-Ni alloy steels are moderate, except below the fracture transition temperature range where fatigue crack growth rates are drastically accelerated.

Key words: Crack propagation; fatigue; low temperature tests; nickel alloys; stainless steels; steels; superalloys; titanium alloys.

\*NBS contribution, not subject to copyright.



## INTRODUCTION

Fatigue failure is a process of crack initiation, crack propagation, and fracture. Fracture occurs when the crack propagates to a critical size, and the structural component is no longer able to support the applied stress. The critical crack size is a function of the fracture toughness of the material and the component geometry, and can be calculated from a fracture mechanics analysis. The fatigue life is determined by the time required to initiate and propagate a crack to critical size.

Fatigue design data are essential to avoid catastrophic failure, overdesign, and inefficient selection of materials. Conventional stress-controlled S-N test data for several alloys at 295, 76, and 4 K are available from the work of Schwartzberg and Kiefer [1] and Nachtigall, Klima and Freche [2]. Nachtigall [3] also reports strain-controlled S-N test data at low temperatures. Such data pertain to smooth or notched bar specimens where the crack initiation phase is important and may account for up to 90% of the total fatigue lifetime, depending on the stress level. However, in many large engineering structures cracks already exist, or are assumed to exist, due to manufacturing and fabrication defects. In such cases, the life of the structure is determined solely by the crack growth rate, and a specific knowledge of fatigue crack growth rates ( $da/dN$ ) is essential for accurate fatigue life predictions.

This paper summarizes our experimental results on the fatigue crack growth resistance of 14 commercial structural alloys tested at selected temperatures between 295 and 4 K. The data presented are

directly applicable to design. Many of the results are reported here for the first time, although some data alloys were previously tested and individually discussed in prior reports []. This collection and comparison of data leads to generalizations showing that temperature effects on  $da/dN$ -versus- $\Delta K$  behavior correlate well with alloy crystal structure.

## EXPERIMENTAL

A list of alloys for which fatigue crack growth rates were measured is shown in Table 1. Included are the material forms, chemical analyses, heat treatments, and specimen orientations according to the ASTM E 399-74 notation [4]. The compact specimen geometry was chosen because it is standardized and much experience with it has been accumulated. Constant amplitude fatigue tests were performed using specimens 20 to 38 mm thick, a sinusoidal load cycle, test frequencies between 20 and 28 Hz, and a constant minimum-to-maximum load ratio,  $R$ , of 0.1. The compliance method of crack growth measurement was employed, using apparatus and techniques that were previously described in detail [5,6], producing fatigue crack growth rate data with uncertainties typically no greater than  $\pm 20\%$ .

## RESULTS AND CONCLUSIONS

Fatigue crack growth rates at intermediate stress intensity factor ranges,  $\Delta K$ , usually conform to Paris equations having the form [7]:

$$\frac{da}{dN} = C(\Delta K)^n \quad (1)$$

where  $C$  and  $n$  are empirical constants that depend on material and test variables. Logarithmic plots of  $da/dN$ -versus- $\Delta K$  data that are in agreement with Eq. (1) reveal linear trends,  $n$  and  $C$  being the slope and

ordinate intercept at  $\Delta K = 1$ , respectively. Room temperature and cryogenic fatigue crack growth rate data for the alloys tested in this study are plotted in Figs. 1-13, and Paris equation parameters for each material/temperature combination are listed in Table 2. There are three distinct alloy groups:

#### I. HCP Titanium Alloys

Of all the alloys having mainly close-packed hexagonal crystal structures, the Ti-5Al-2.5Sn (single phase, HCP) and Ti-6Al-4V (two phase, HCP and some BCC) alloys are the most common for cryogenic service. These alloys offer high strength-to-weight ratios, while retaining adequate low temperature ductility and fracture toughness. As shown in Figs. 1 and 2, the fatigue crack growth data for annealed normal and low-interstitial grade Ti-5Al-2.5Sn alloys demonstrate temperature independent behavior between 295 K and 4 K. The Paris equation exponents for these alloys range from 4.0 to 4.8. Other results for the mill-annealed normal-interstitial and recrystallization-annealed, extra-low-interstitial Ti-6Al-4V alloys described in previous reports [9] also show temperature insensitive behavior. The results for those Ti-6Al-4V alloys are compared with the Ti-5Al-2.5Sn alloys in Fig. 3. Over most of the stress intensity range investigated, the fatigue crack growth resistances offered by the Ti-5Al-2.5Sn alloys are slightly superior to the Ti-6Al-4V alloys.

#### II. BCC Ferritic Steels

Fatigue crack growth rates for three ferritic steels containing 3.5, 5, or 9% nickel are shown in Figs. 4-6. Low temperature effects on this group of alloys are insignificant or slightly beneficial as long as

temperature reductions remain in the "upper shelf" range, which is defined as the region where dimpled rupture or fibrous fractures occur during static fracture toughness tests. However, these ferritic steels exhibit abrupt transitions to low fracture toughness involving cleavage at temperatures determined primarily by the nickel content. Cleavage cracking also leads to a drastic acceleration of fatigue crack growth rates at temperatures in the sub-transition ranges. Accelerated fatigue crack growth rates were observed for 3.5 Ni steel at 76 K (Fig. 4), and for 9 Ni steel at 4 K (Fig. 6). A reduced fatigue crack growth resistance is also evident in the data for 5 Ni steel (Fig. 5) between 111 and 76 K. Due to such adverse trends, ferritic or BCC alloys are of limited use in low temperature tensile applications, and are usually restricted to service temperatures in their upper shelf ranges. Of all alloys tested, the ferritic steels exhibit the most dramatic Paris equation exponent transitions, with the room temperature values near 3.0 increasing to as high as 7.6 at sub-transition temperatures.

### III. FCC Austenitic Alloys

Although more expensive than the less alloyed ferritic steels, austenitic superalloys and stainless steels offer high fracture toughness and constitute the most important class of cryogenic materials. Extensive alloying is possible in austenitic alloys, and a large number of commercially available compositions exist. However, the structures of some alloys are unstable at low temperatures; stress-induced bcc and hcp martensitic phase transformations can occur, affecting fatigue crack growth resistance and other mechanical properties.

Figs. 7-9 illustrate fatigue crack propagation results for Inconel

750\* (ASTM A 637), A-286 (ASTM A 453) and AISI 310 stainless steel, three austenitic alloys that remain stable with respect to martensitic transformations during fatigue tests at room and low temperatures. These alloys exhibit similar behavior: the fatigue crack growth rates at a given stress intensity factor are lower at 76 K and 4 K than at room temperature, but there is no measureable difference in the rates at the two cryogenic temperatures. Other stable FCC alloys such as 5083-0 aluminum and Inconel 718 show similar trends [9]. Logsdon, Wells, and Kossowsky [8] also reported improved rates at 4 K compared to room temperature, in tests of the stable austenitic alloys Kromarc 58 and A-286.

The AISI 304, 304L, and 316 stainless steels and the Fe-21Cr-6Ni-9Mn stainless steel are unstable, undergoing significant martensitic phase transformations during fatigue tests at 76 K and 4 K. Evidence of martensite in crack-tip plastic zones was obtained metallographically, and by detection with a magnetometer. In comparison, the small amounts of martensite formed at 295 K are negligible. It can be assumed that transformations precede crack growth at 76 and 4 K, and that fatigue crack growth at these temperatures represents crack propagation through partially transformed austenite.

It is difficult to generalize regarding the effect of martensitic transformations on fatigue crack growth resistance. The results for AISI 316 and 304 stainless steels, shown in Figs. 10 and 11, reveal no pronounced temperature effects on fatigue crack propagation resistance,

---

\*Tradenames are used for the sake of clarity, and do not imply endorsement or recommendation by NBS.



except perhaps at high rates approaching  $2.5 \times 10^{-3}$  mm/cycle. The AISI 304L stainless steel, having lower carbon content than AISI 304 (0.026C compared to 0.05C), shows behavior analogous to that observed for stable alloys. As shown in Fig. 12, there is a significant decrease in the rates for AISI 304L at cryogenic temperatures compared to room temperature, but the data at 76 K and 4 K are equivalent. The lower carbon content should reduce the stability of AISI 304L relative to AISI 304. Thus, the dissimilar temperature dependences for these alloys may be due to differences in the quantity and properties of the martensites formed.

The fatigue crack growth rates for the Fe-21Cr-6Ni-9Mn alloy are shown in Fig. 13. The rates at 295 K and 76 K are equivalent despite appreciable martensitic transformations occurring at 76 K. This behavior is similar to that observed for AISI 304 and AISI 316. On the other hand, the rates at 4 K are definitely higher than at 295 K and 76 K. Pronounced cleavage-like facets were observed under magnification of the 4 K fatigue surfaces, so that the decreased fatigue crack propagation resistance at 4 K can be attributed to a transition in the fracture mode accompanying the martensitic transformation at this temperature. The results for this alloy represent the only case where the fatigue crack propagation resistance of an (initially) austenitic alloy decreases at cryogenic temperatures.

#### SUMMARY

Temperature effects on the fatigue crack growth resistance of alloys correlate well with crystal structure:

1. HCP titanium alloys exhibit temperature-insensitive behavior between 295 K and 4 K.



2. BCC ferritic steels exhibit weak temperature dependences at in their upper shelf temperature ranges, whereas at sub-transition temperatures fatigue crack growth resistance is markedly decreased, being associated with cleavage microfracture modes.

3. Stable FCC alloys exhibit improved fatigue crack growth resistances at cryogenic temperatures, as compared to their behavior in room temperature air. It is difficult to generalize on the trends for metastable FCC alloys since favorable, adverse, or temperature-insensitive behaviors are observed depending on alloy composition.

#### REFERENCES

1. F. R. Schwartzberg and T. Kiefer, "A Study of Fracture Behavior of Metals for Superconducting Applications," MCR-74-89 (Issue 4), in Materials Research for Superconducting Machinery, IV, R. P. Reed, A. F. Clark, E. C. van Reuth, Eds., (National Bureau of Standards, Boulder, Colorado, October 1975).
2. A. J. Nachtigall, S. J. Klima, and J. C. Freche, J. Mater. JMLSA 3 (1968) 425.
3. A. J. Nachtigall, in Properties of Materials for Liquified Natural Gas Tankage, ASTM STP 579 (Amer. Soc. Test. Mater., Philadelphia, 1975) 378.
4. Standard Method of Test for Plane Strain Fracture Toughness of Metallic Materials, ASTM E 399-74, in 1976 Annual Book of ASTM Standards, Part 10 (Amer. Soc. Test. Mater., Philadelphia, 1976) 471.
5. C. W. Fowlkes and R. L. Tobler, Eng. Fract. Mechs. 8 (1976) 487.
6. R. L. Tobler and R. P. Reed, in Advances in Cryogenic Engineering 22, R. P. Reed, Ed. (Plenum, New York, 1976) 35.
7. P. C. Paris and F. Erdogan, Trans. ASME, J. Basic Eng. 85 (1963) 528.
8. W. A. Logsdon, J. M. Wells, and R. Kossowsky, in Proceedings of the Second International Conference on Mechanical Behavior of Materials (Amer. Soc. Metals, Ohio, 1976) 1283.
9. Materials Research for Superconducting Machinery, Vols. I to V, R. P. Reed, A. F. Clark, H. M. Ledbetter, and E. C. van Reuth, Eds., (National Bureau of Standards, Boulder, Colorado, March 1974 to March 1976) AD780596, ADA004586, ADA012365, ADA019230, ADA030170.

Table 1. Fatigue crack growth rate test materials for the  
ARPA sponsored program ending September 30, 1976.

Material Form and Condition	Specimen Thickness (mm), & orientation	Mill Chemical Analyses, wt%
Ti-5Al-2.5Sn, normal-interstitial annealed bar	38, TS	Ti-5.28Al, 2.46Sn, 0.327Fe, 0.01C, 0.01N, 0.1740, 40 ppm H.
Ti-5Al-2.5Sn, low-interstitial, annealed bar	32, TL	Ti-5.25Al, 2.53Sn, 0.045Fe, 0.012C, 0.009N, 0.1160, 173 ppm H.
Ti-6Al-4V, normal-interstitial, mill-annealed bar	25, TL	Ti-6.24Al, 4.18V, 0.174Fe, 0.035C, 0.011N, 0.1550, 14 ppm H.
Ti-6Al-4V, extra-low-interstitial, recrystallization-annealed bar	20 to 25, TL	Ti-5.91Al, 3.94V, 0.103Fe, 0.018C, 0.014N, 0.110, 52 ppm H.
ASTM A 203 E (3.5 Ni steel), quenched and tempered, 25 mm thick plate	25, TL	Fe-0.10C, 3.62Ni, 0.46Mn, 0.013S, 0.015P, 0.20Si.
ASTM A 645 (5 Ni steel), aus- tenized, temperized and reversion-annealed, 32 mm thick plate	31, TL	Fe-0.08C, 5.03Ni, 0.6Mn, 0.3Mo, 0.08Al, 0.009S, 0.01P, 0.25Si, 0.010N.
ASTM A 553A (9 Ni steel, quenched and tempered, 32 mm thick plate	31, TL	Fe-0.08C, 8.99Ni, 0.62Mn, 0.01S, 0.01P, 0.19Si.
5083-0 aluminum alloy, annealed 43 mm thick plate	32, TL	Al-4.0 to 4.9Mg, 0.3 to 1.0 Mn, 0.05 to 0.25Cr, 0.10Cu max, 0.25Zn max, 0.15Ti max, 0.40Si max, 0.40Fe max, 0.15 others, max.
Inconel 718, solution treated and double-aged forging	31, TS	Ni-18.1Cr, 18.5Fe, 0.90Ti, 0.05C, 0.10Mn, 0.002S, 0.01P, 0.10Si, 0.003B, 0.10Cu, 0.49Al, 0.17Co, 2.95Mo, 5.24 Nb+Ta.
Inconel 750, solution treated and double-aged forging	38, TS	Ni-15.16Cr, 6.58Fe, 2.51Ti, 0.04C, 0.20Mn, 0.007S, 0.25Si, 0.04Cu, 0.78Al, 0.89 Nb+Ta.
A-286, solution treated and aged forging	38, TS	Fe-0.05C, 13.96Cr, 24.97Ni, 1.52Mn, 0.54Si, 0.007S, 0.016P, 1.30Mo, 2.23Ti, 0.004B, 0.30V, 0.19Al.
AISI 310, annealed 38 mm thick plate	38, TL	Fe-0.038C, 24.65Cr, 20.4Ni, 1.41Mn, 0.72Si, 0.016S, 0.023P, 0.13Mo, 0.14Cu.
AISI 316, annealed 38 mm thick plate	38, TL	Fe-0.04C, 17.8Cr, 13.10Ni, 1.72Mn, 0.51Si, 0.019S, 0.019P, 2.18Mo.
AISI 304, annealed 38 mm thick plate	38, TL	Fe-0.052C, 18.33Cr, 9.82Ni, 1.6Mn, 0.75Si, 0.015S, 0.028P, 0.20Mo, 0.13Cu.
AISI 304L, annealed 38 mm thick plate	38, TL	Fe-0.026C, 18.84Cr, 10.18Ni, 1.65Mn, 0.82Si, 0.01S, 0.022P, 0.27Mo, 0.28Cu.
Fe-21Cr-6Ni-9Mn, annealed 38 mm thick plate	38, TL	Fe-0.019C, 19.75Cr, 7.16Ni, 9.46Mn, 0.15Si, 0.003S, 0.004P, 0.28N

Table 2. Paris equation parameters for alloys at room and cryogenic temperatures (da/dN in mm/cycle and  $\Delta K$  in  $\text{MPa}\cdot\text{m}^{1/2}$ ).

Material	Temperature, K	n	C	$\Delta K$ region investigated
Ti-5Al-2.5Sn, annealed				
1. normal-interstitial	295, 76, and 4	4.8	$5.1 \times 10^{11}$	14 to 30
2. low-interstitial	295, 76, and 4	4.0	$4.9 \times 10^{10}$	10 to 60
Ti-6Al-4V				
1. normal-int., mill-annealed,	295, 76, and 4	6.0	$3.1 \times 10^{12}$	14 to 30
2. ELI, recrystallization-annealed	295, 76, and 4	7.0	$1.9 \times 10^{13}$	10 to 20
	295 and 76	3.0	$3 \times 10^8$	20 to 60
ASTM A 203 E (3.5 Ni steel)	295	3.2	$1.3 \times 10^8$	18 to 60
quenched and tempered	195	3.2	$1.3 \times 10^8$	30 to 70
	172	3.2	$1.0 \times 10^9$	30 to 60
	76	7.6	$1.6 \times 10^{14}$	20 to 30
ASTM A 645 (5 Ni steel)	295	2.7	$1.1 \times 10^8$	25 to 90
austenitized, temperized, reversion	111	2.7	$1.1 \times 10^8$	25 to 60
annealed	76	4.0	$2.0 \times 10^{10}$	27 to 80
ASTM A 553 A (9 Ni steel)	295	2.7	$2.0 \times 10^8$	16 to 70
quenched and tempered	111	3.4	$1.0 \times 10^9$	17 to 80
	76	4.4	$4.8 \times 10^{11}$	17 to 64
	4	5.3	$1.4 \times 10^{11}$	25 to 35
5083-0 aluminum	111, 76, and 4	5.2	$1.3 \times 10^{10}$	8 to 28
annealed				
Inconel 718	295	4.0	$8 \times 10^{11}$	20 to 70
solution treated, double-aged	4	4.0	$4.8 \times 10^{11}$	25 to 90
Inconel 750	295	3.0	$2.4 \times 10^9$	26 to 80
solution treated, double-aged	76 and 4	3.8	$6.6 \times 10^{11}$	30 to 92
ASTM A 453 (A-286)	295	3.0	$2.5 \times 10^9$	25 to 90
solution treated, aged	76 and 4	4.0	$2 \times 10^{12}$	32 to 90
AISI 310, annealed	295	4.4	$3.5 \times 10^{11}$	24 to 35
	295	3.0	$4.7 \times 10^9$	35 to 60
	76 and 4	3.7	$1.1 \times 10^{10}$	25 to 80
AISI 316, quenched	295 to 4	3.8	$2.1 \times 10^{10}$	19 to 60
AISI 304, quenched	295 to 4	3.0	$2.7 \times 10^9$	22 to ~ 80
AISI 304L, annealed	295	4.0	$2.0 \times 10^{10}$	22 to 54
	76 and 4	4.0	$3.4 \times 10^{11}$	26 to 80
Fe-21Cr-6Ni-9Mn, annealed	295 and 76	3.7	$1.9 \times 10^{10}$	25 to 80
	4	4.4	$3.6 \times 10^{11}$	25 to 70

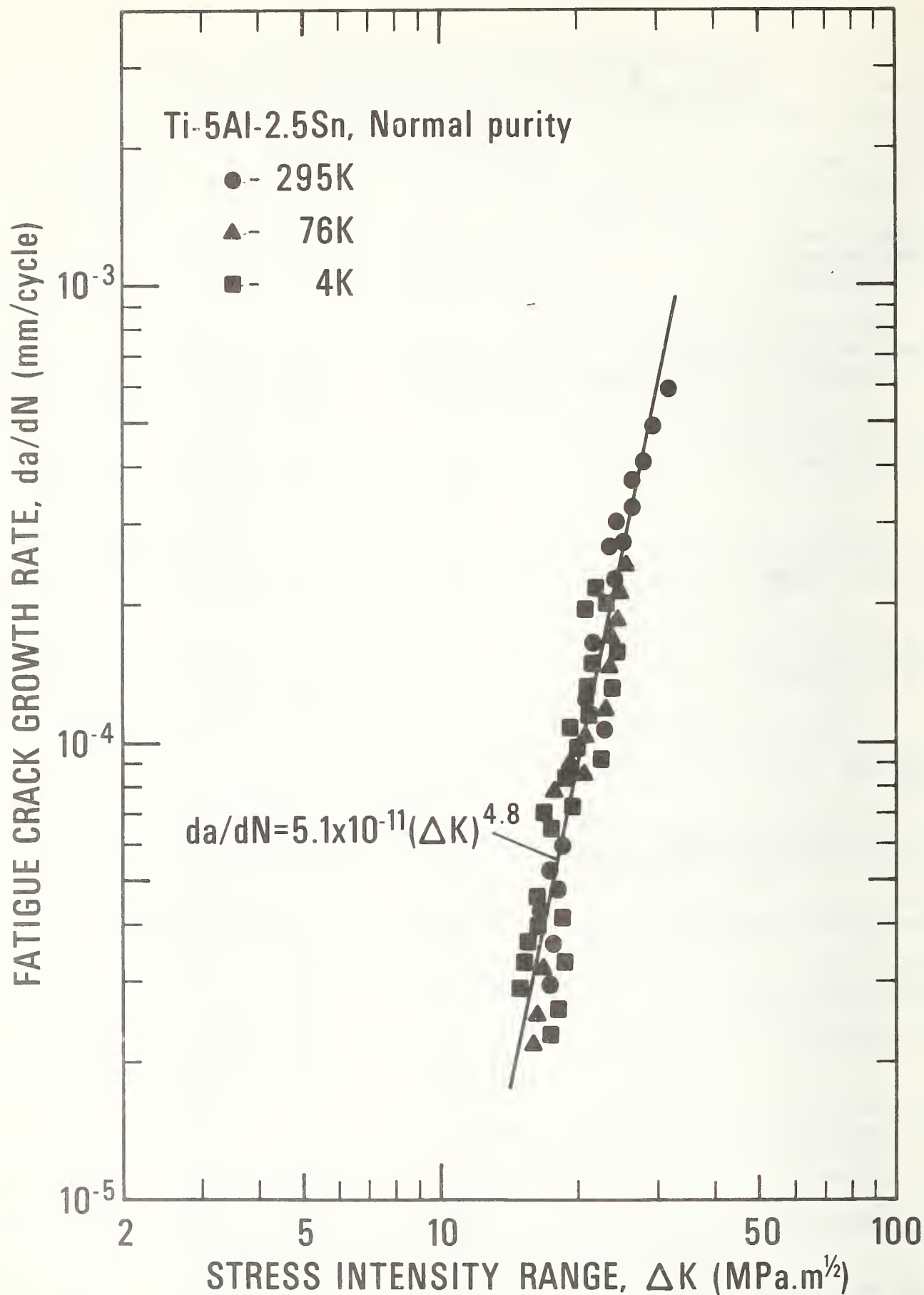


Figure 1. Fatigue crack growth data for a normal interstitial Ti-5Al-2.5 Sn alloy at 295, 76, and 4 K, showing temperature independent behavior.

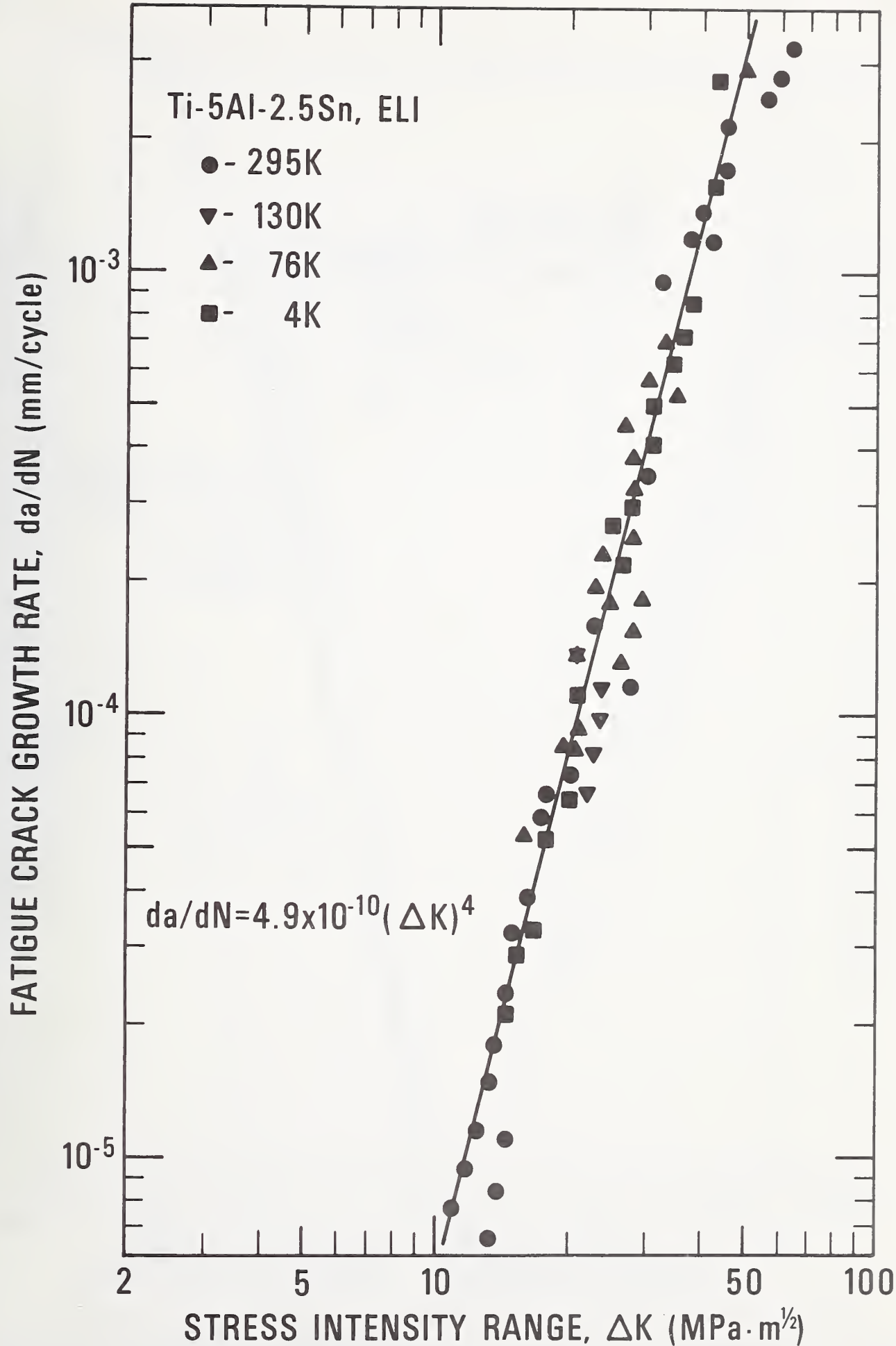


Figure 2. Fatigue crack growth data for a low-interstitial Ti-5Al-2.5Sn alloy at 295, 76 and 4 K, showing temperature independent behavior.



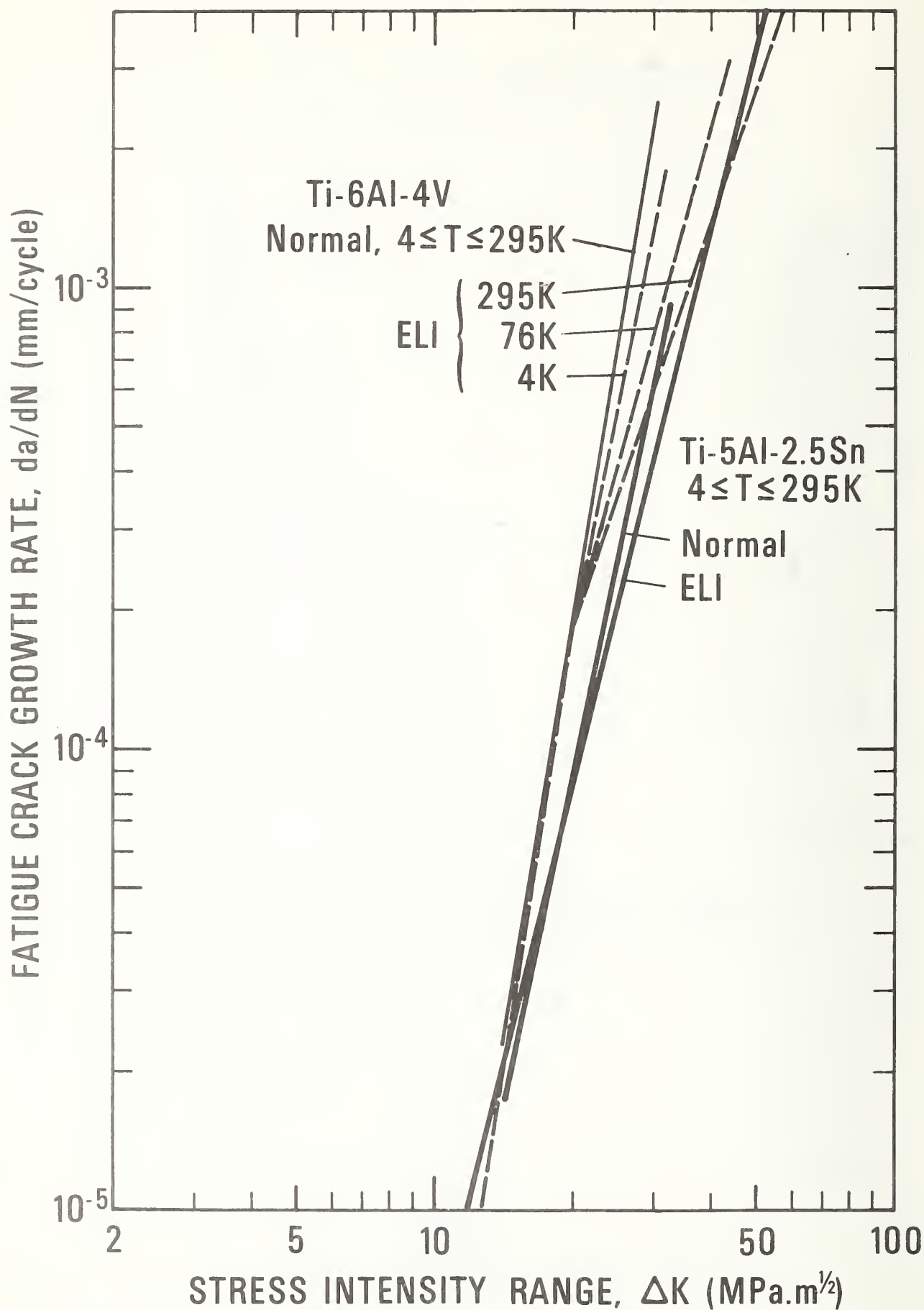


Figure 3. A comparison of fatigue crack growth results for Ti-5Al-2.5Sn and Ti-6Al-4V alloys indicating the slight superiority of Ti-5Al-2.5Sn alloys over most of the  $\Delta K$  regions investigated. 268



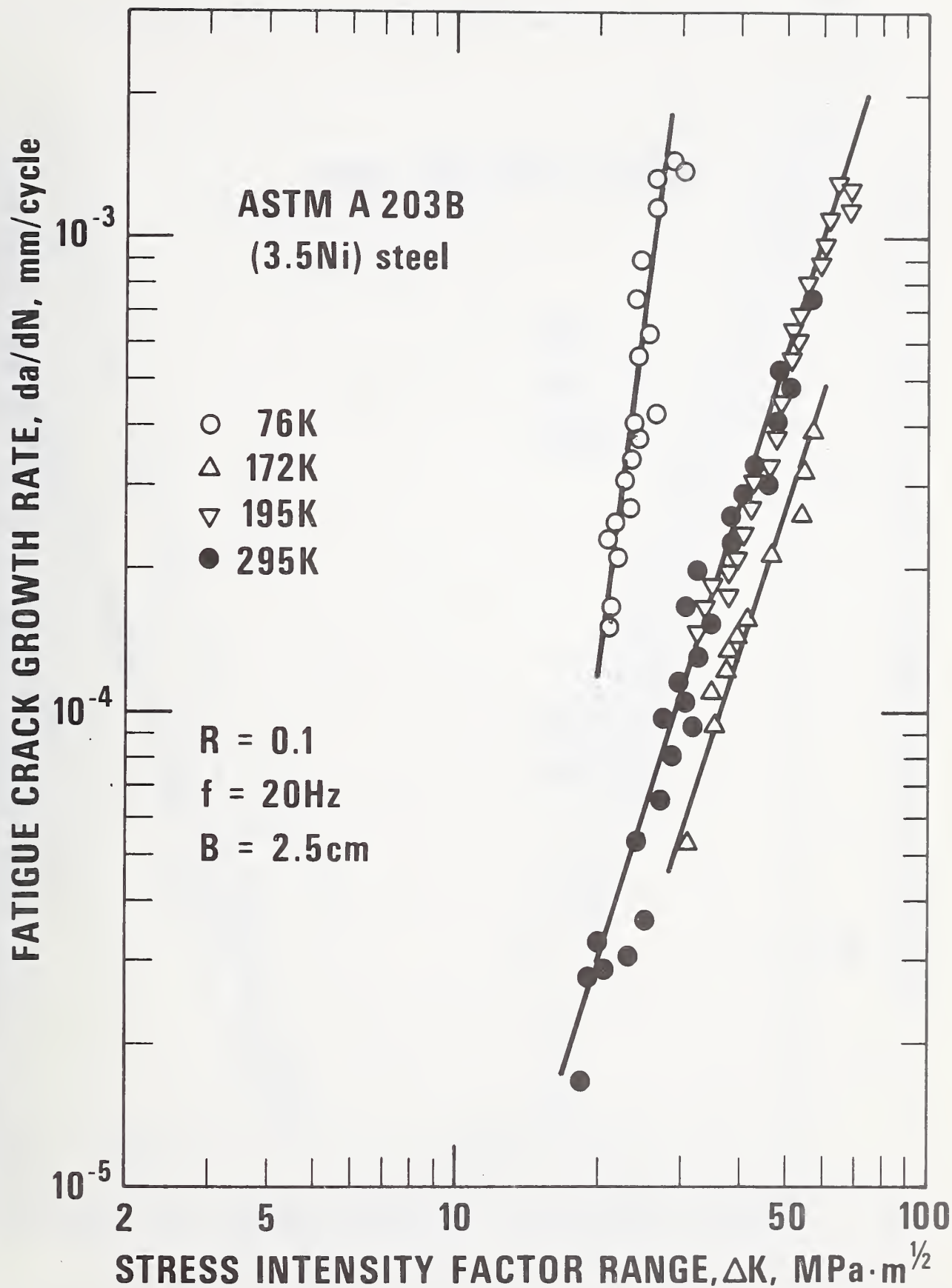


Figure 4. Fatigue crack growth data for a ferritic 3.5 Ni alloy steel at selected temperatures.

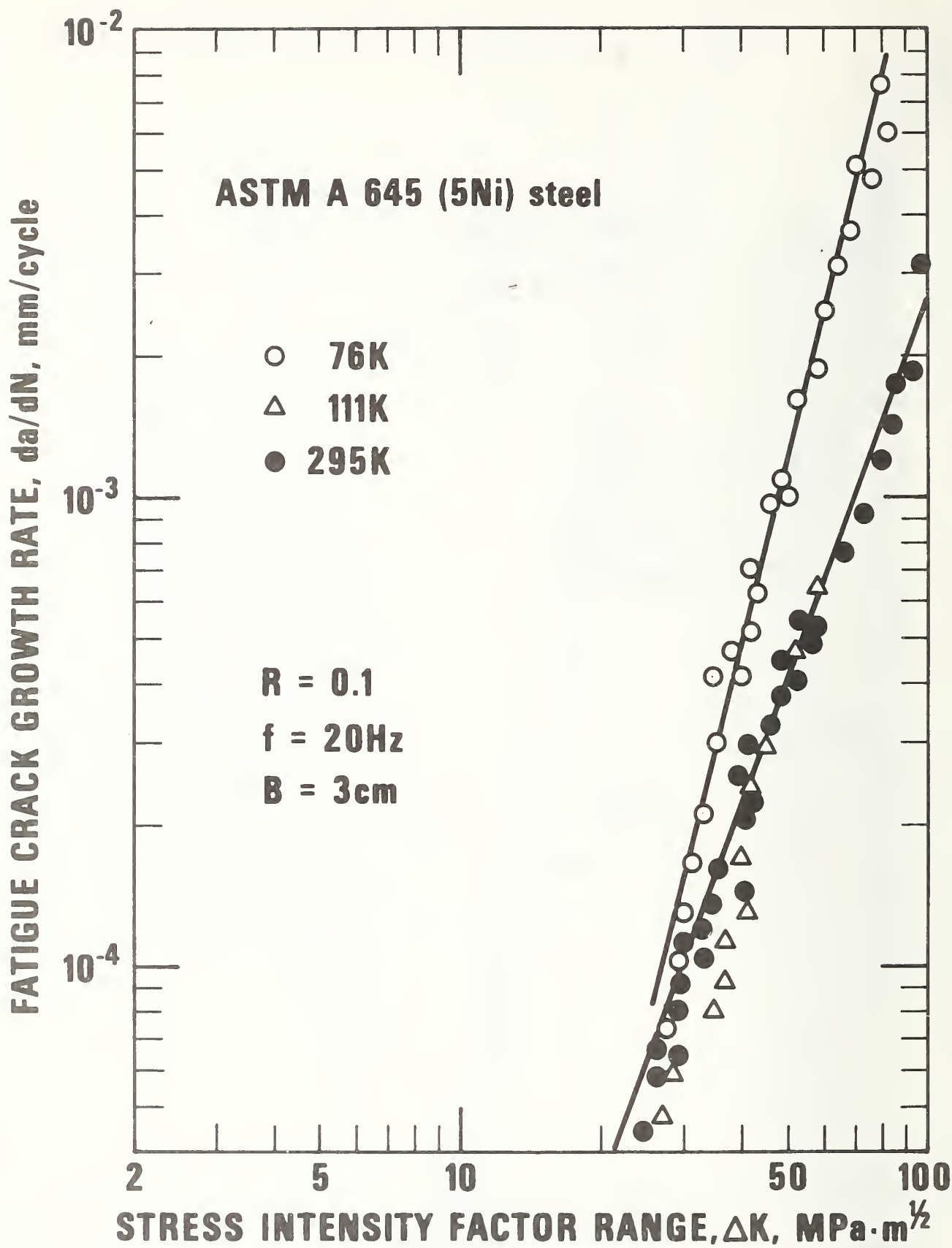


Figure 5. Fatigue crack growth data for a ferritic 5 Ni alloy steel at selected temperatures.

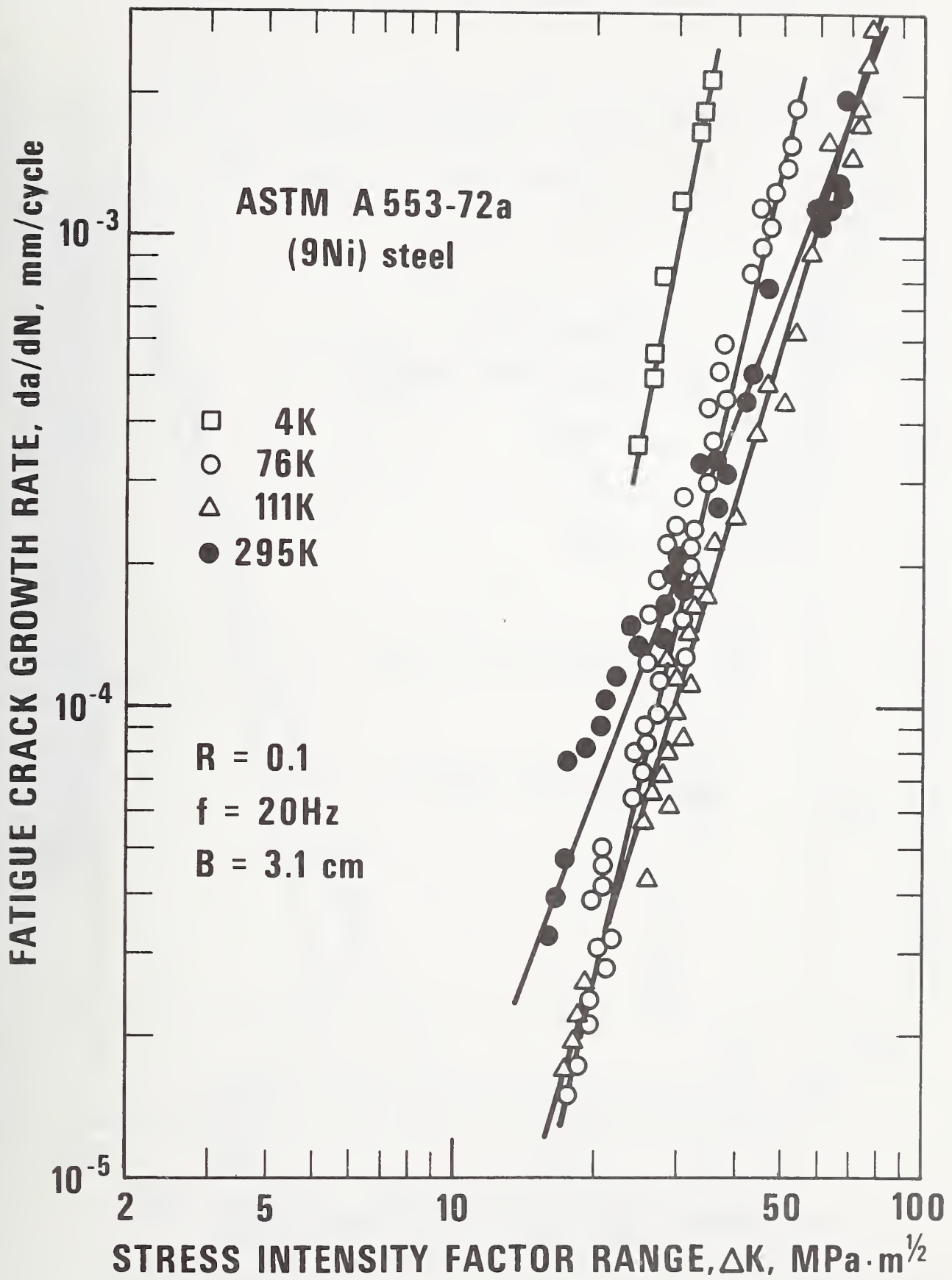


Figure 6. Fatigue crack growth data for a ferritic 9 Ni alloy steel at selected temperatures.

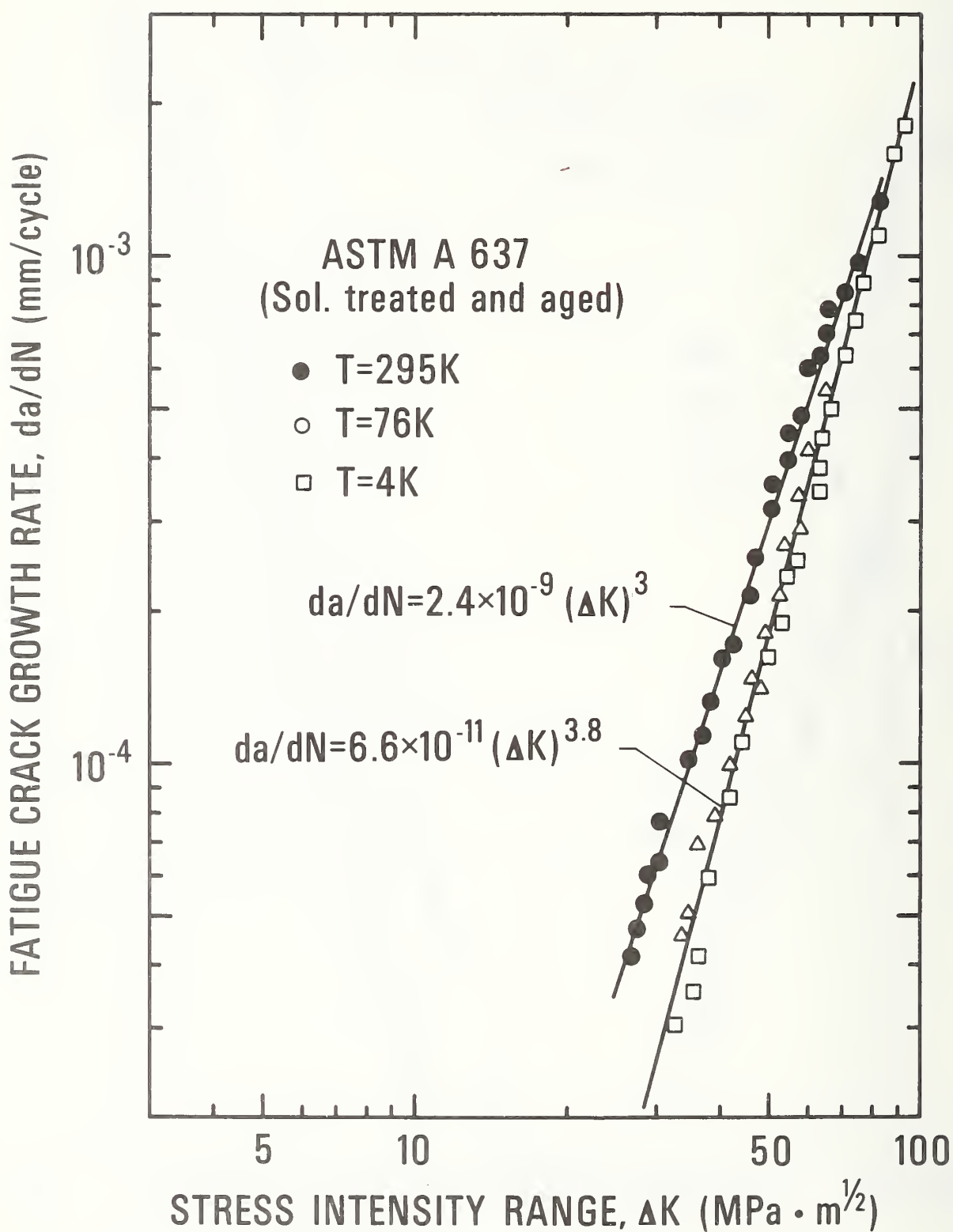


Figure 7. Fatigue crack growth data for a stable nickel-base austenitic superalloy at 295, 76 and 4 K.

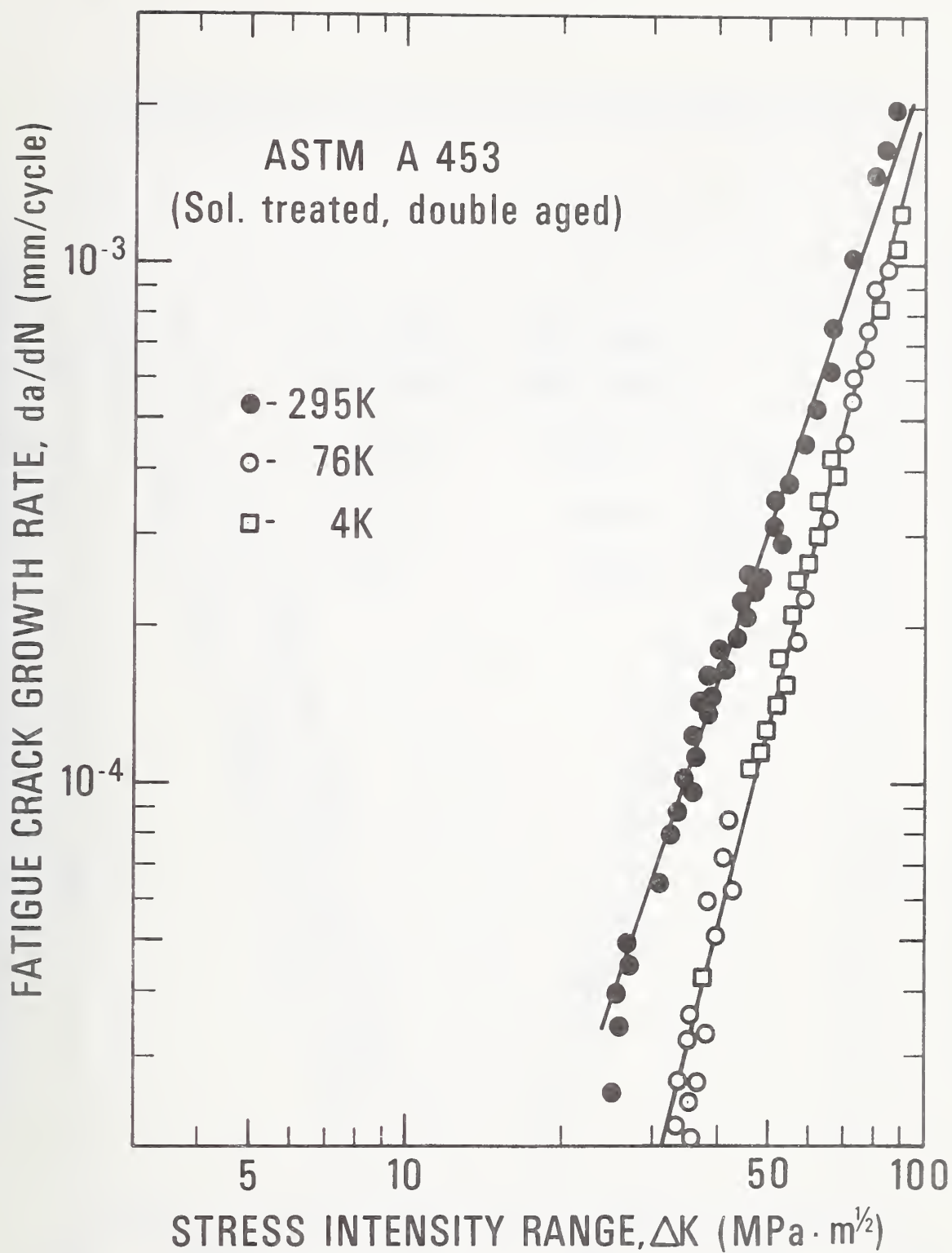


Figure 8. Fatigue crack growth data for a stable iron-base austenitic superalloy and stainless steel at 295, 76 and 4 K.

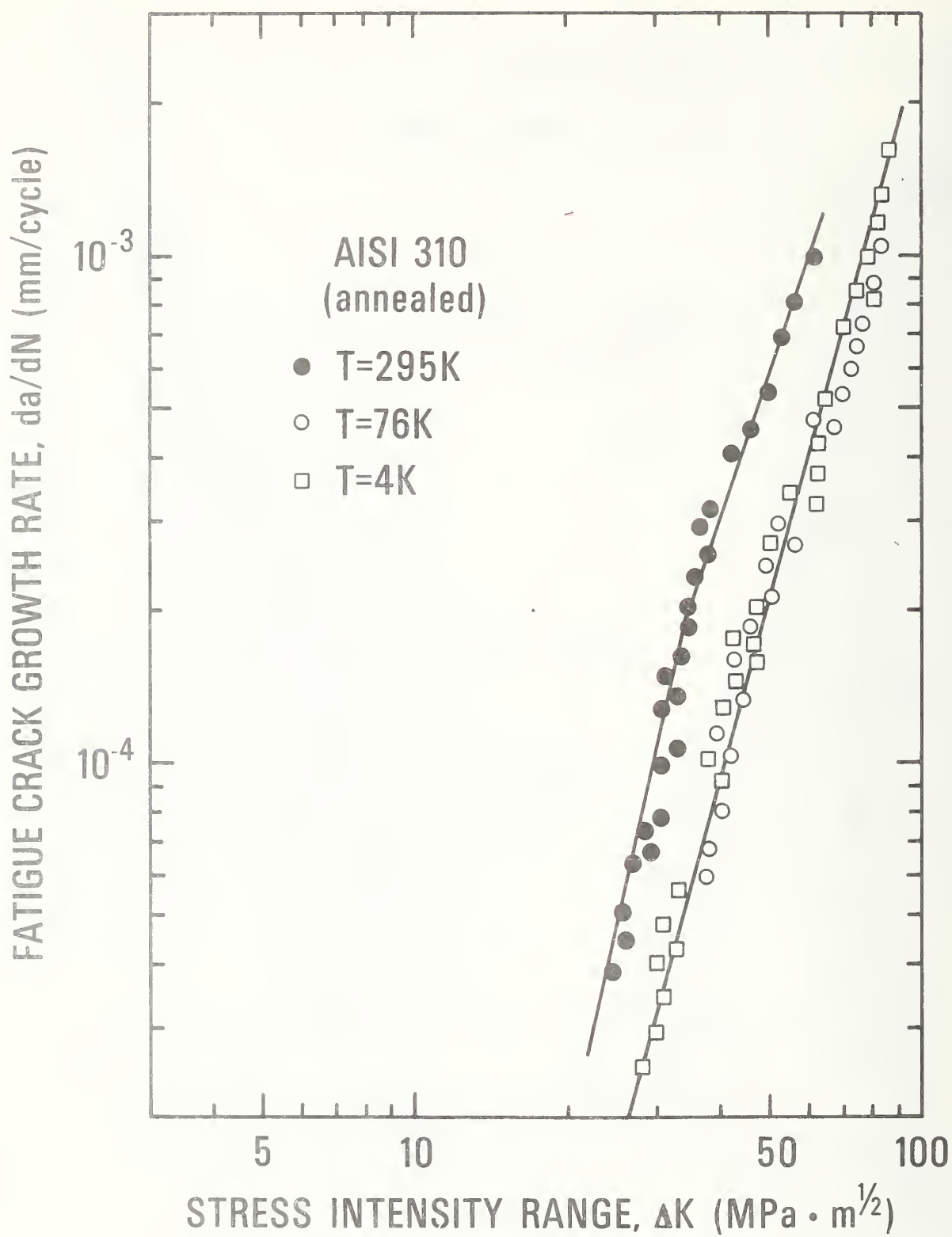


Figure 9. Fatigue crack growth data for a stable AISI 310 austenitic stainless steel at 295, 76 and 4 K.



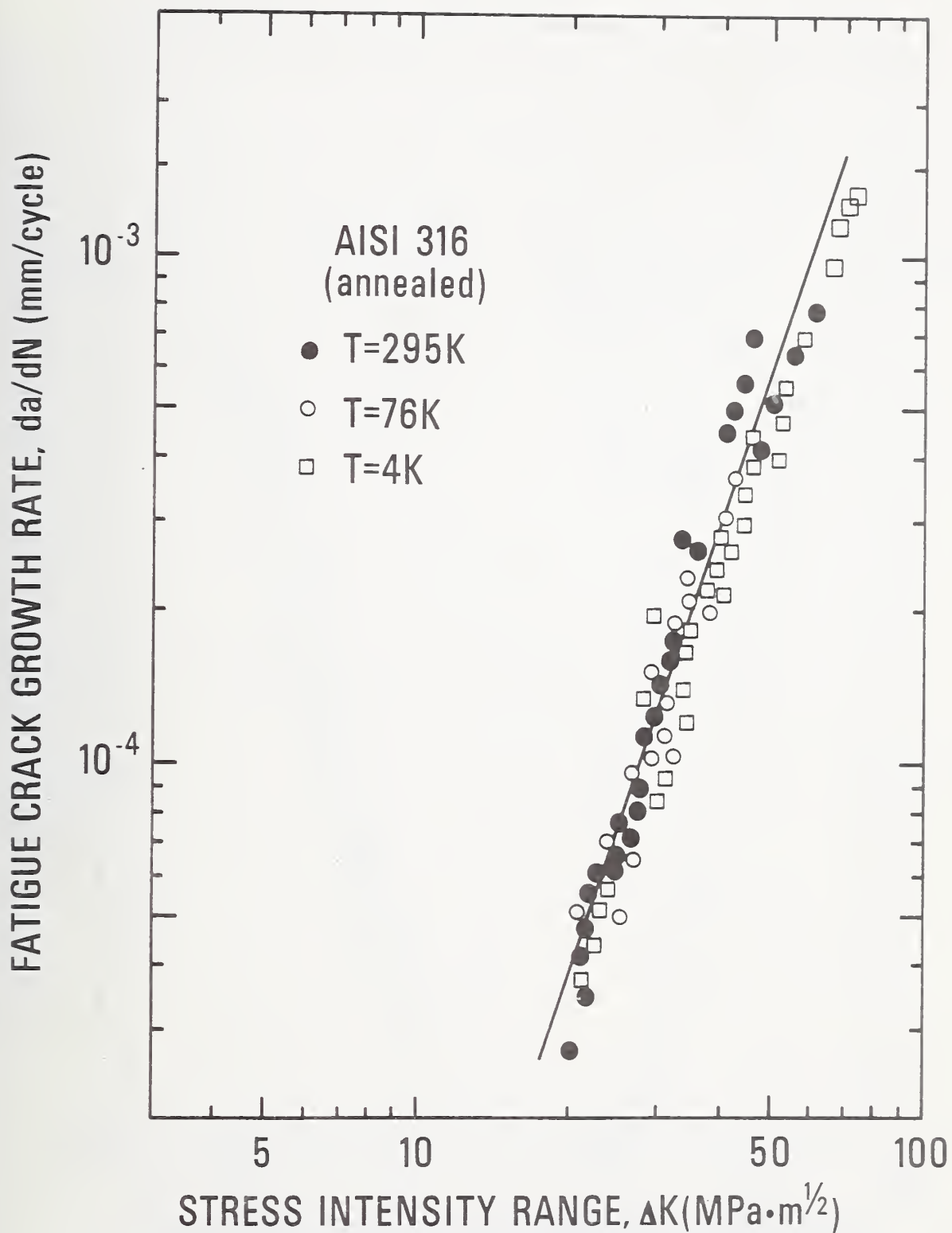


Figure 10. Fatigue crack growth data for a metastable AISI 316 stainless steel which exhibits martensitic transformations during fatigue loading at 76 and 4 K.

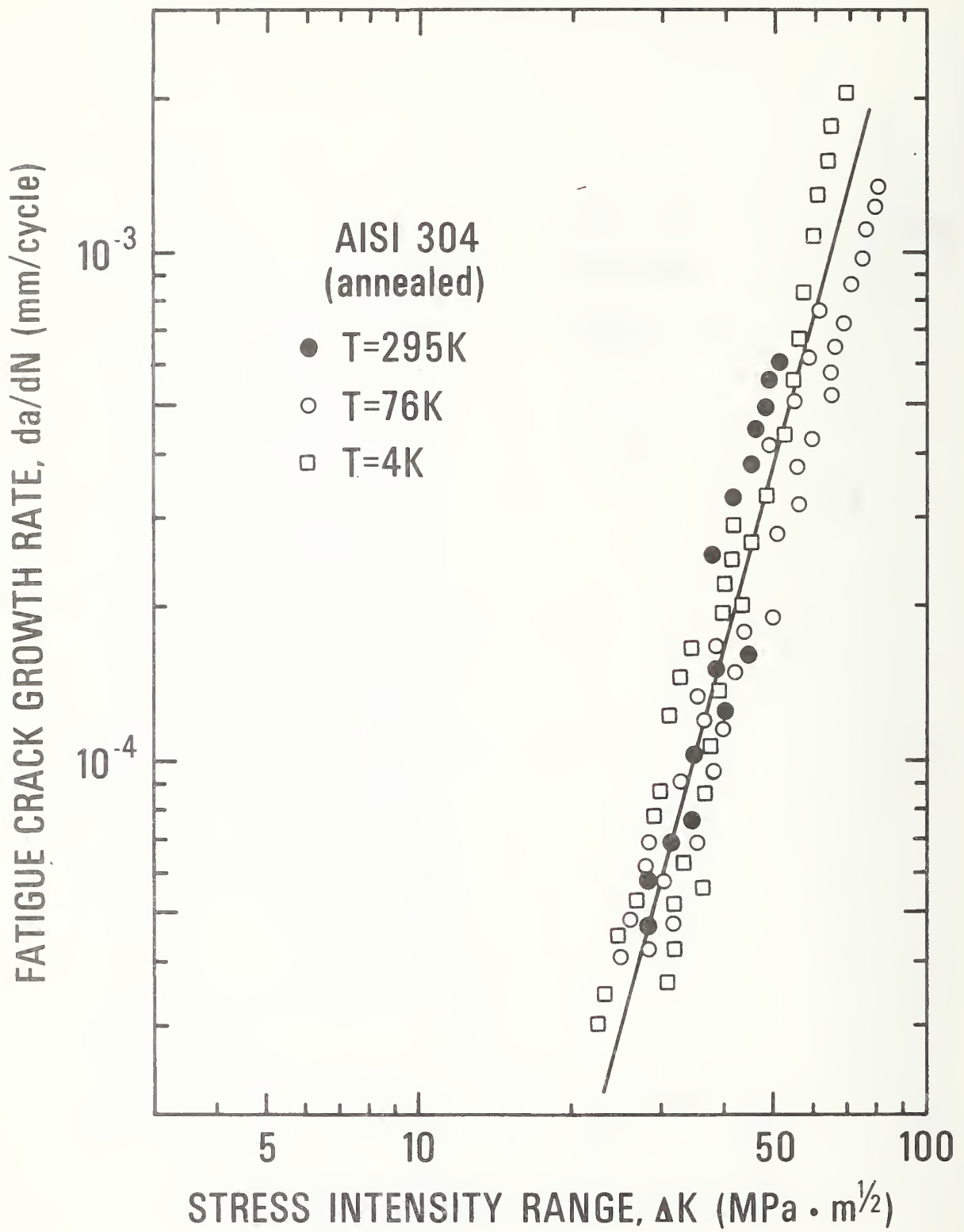


Figure 11. Fatigue crack growth data for a metastable AISI 304 stainless steel which exhibits martensitic transformations during fatigue loading at 76 and 4 K.

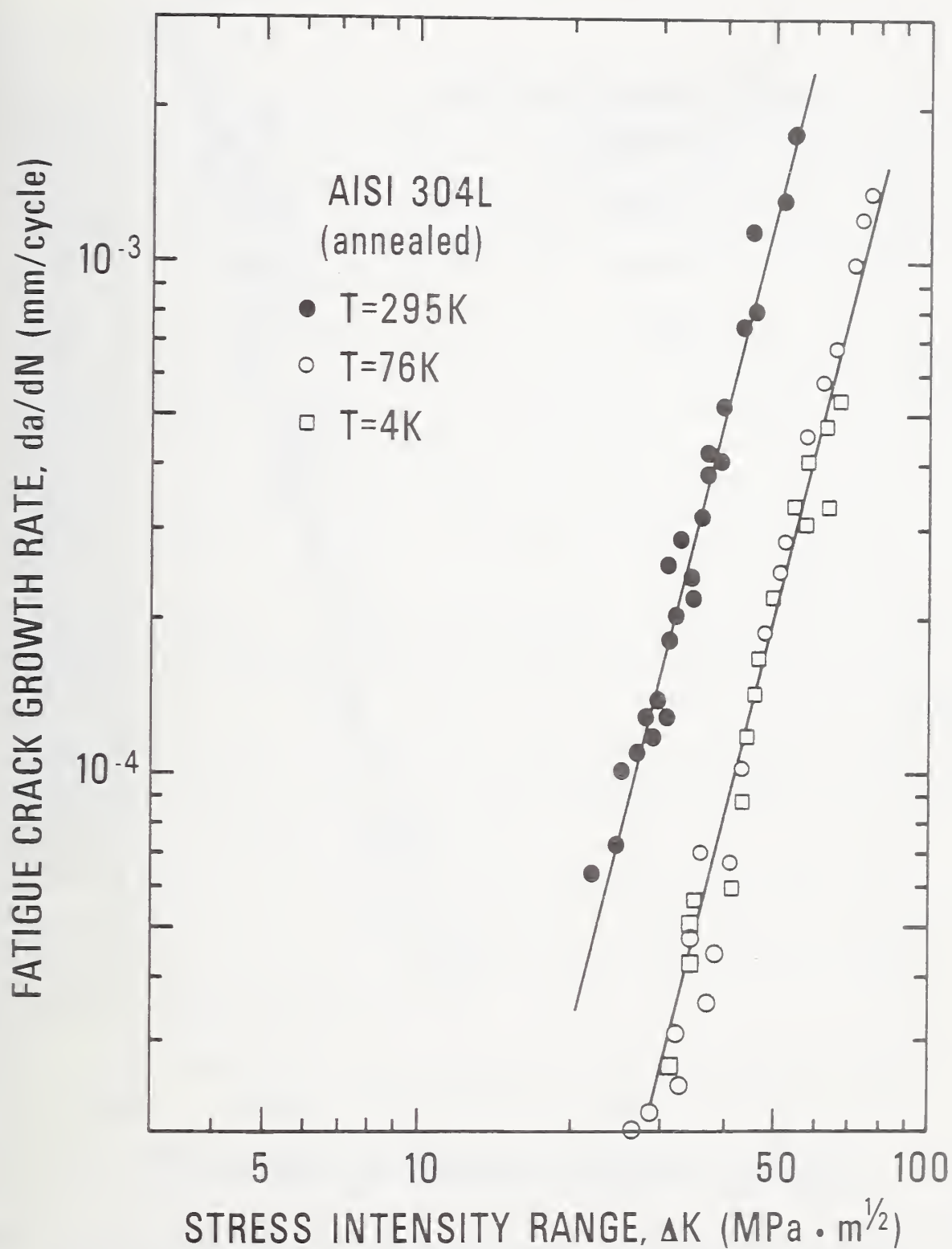


Figure 12. Fatigue crack growth data for a metastable AISI 304L stainless steel which exhibits martensitic transformations at 76 K and 4 K.

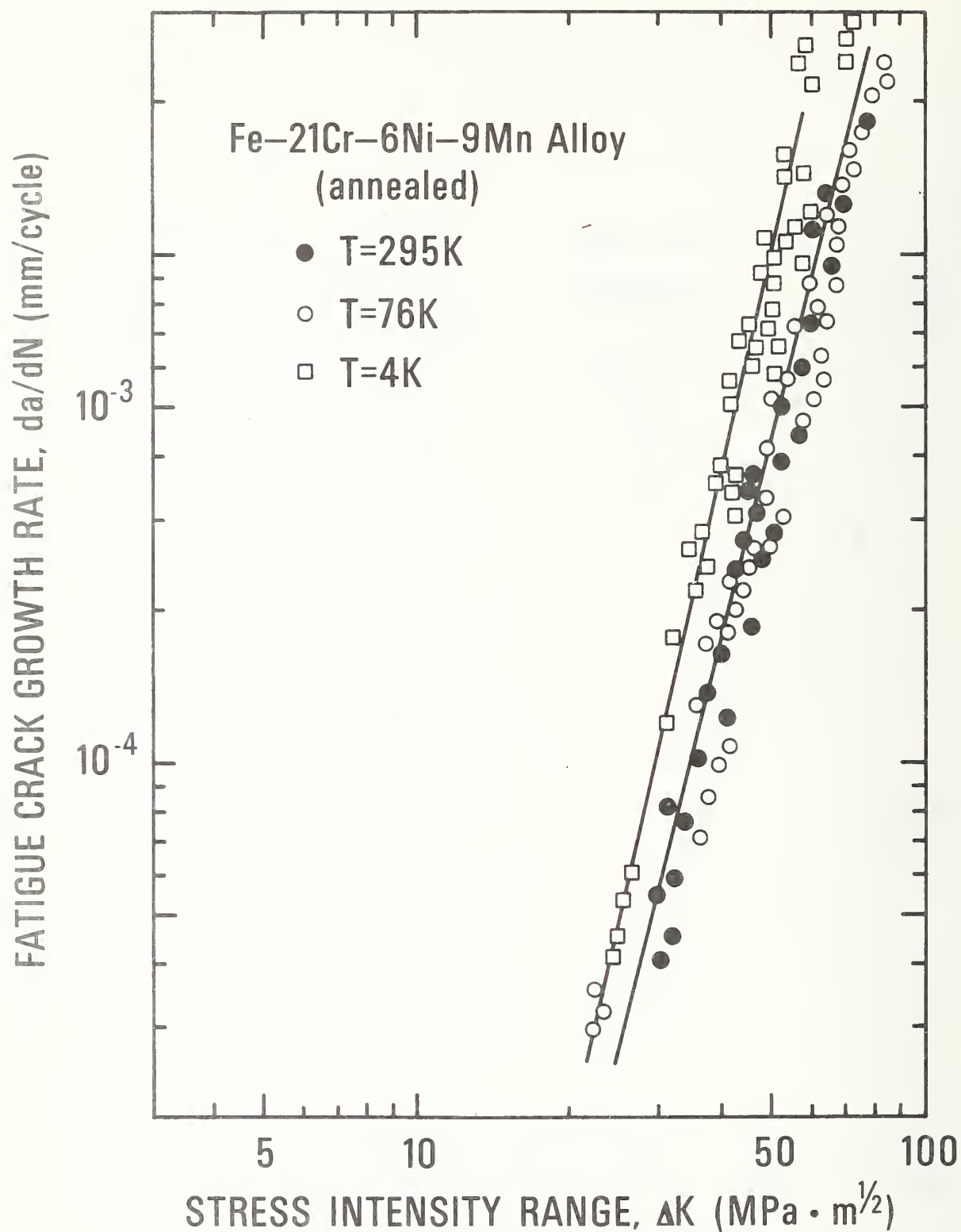


Figure 13. Fatigue crack growth data for a metastable Fe-21Cr-6Ni-9Mn stainless steel which exhibits martensitic transformations at 76 K and 4 K.

# FRACTURE OF STRUCTURAL ALLOYS AT TEMPERATURES APPROACHING ABSOLUTE ZERO\*

R. L. Tobler†

## INTRODUCTION

Plastic deformation and fracture are often viewed as competitive processes. Factors that increase an alloy's resistance to slip usually tend to enhance the probability of brittle fracture. Temperature reductions can lead to pronounced increases in yield strength, while ductility may be decreased, resulting in flaw sensitive mechanical behavior. For this reason, alloys employed at normal temperatures may be unusable at low temperatures, and the fracture toughness of candidate alloys for extreme cryogenic service is a vital design consideration.

With the advent of superconducting electrical machinery we face for the first time a demand for fail-safe, efficiently designed structures that must be cooled with liquid helium to temperatures as low as 4 K. Fracture data are urgently needed to enable judicious material selection for a temperature extreme that previously was rarely experienced. Due to its inertness and proximity to absolute zero, liquid helium at 4 K provides a unique environment where the thermally-activated deformation processes of materials are suppressed, and lattice friction stresses are nearly maximized. Therefore, fracture tests in this environment should provide information of current scientific interest as well as data of engineering utility.

Previous studies of low temperature fracture were hampered by the lack of a quantitative parameter that could be applied to a broad range of material/temperature combinations. The traditional notched tensile and Charpy tests provide only qualitative indications of crack tolerance, while the  $K_{IC}$  test

applies only to high strength alloys which fail in the elastic range. None of these parameters are well suited for characterizing the ductile and tough austenitic alloys, which, as this paper demonstrates, offer maximum fracture resistance at cryogenic temperatures.

In this study, J-integral and  $K_{IC}$  tests were used to characterize the fracture behavior of 14 alloys at temperatures from 295 to 4 K. The parameters measured,  $K_{IC}$  and  $J_{IC}$ , are complementary, being related in the linear-elastic case by the equation:

$$K_{IC}^2 = J_{IC} E (1 - \nu^2)^{-1} \quad (1)$$

where E is Young's modulus and  $\nu$  is Poisson's ratio.

---

\* Contribution of NBS, not subject to copyright.

† Cryogenics Division, National Bureau of Standards, Boulder, CO 80302.



$J_{IC}$  is believed to be a material constant, applicable to either elastic or elastic-plastic fractures. Thus, the  $J_{IC}$  criterion offers a new method for comparing low, medium, and high strength alloys -- a task that was problematic in the past.

## EXPERIMENTAL PROCEDURES

The commercial alloys listed in Table 1 were tested using compact specimens 20 to 38 mm thick. Where possible,  $K_{IC}$  was measured and  $J_{IC}$  was calculated by Eq. (1). Otherwise,  $J_{IC}$  was obtained directly using the resistance

curve method, which required back extrapolation of J-vs- $\Delta a$  data for a series of specimens [1]. Crack extension,  $\Delta a$ , was averaged at 25, 50, and 75% of specimen thickness, and the  $J = 2A/Bb$  approximation was used. Although special cryostats were required to retain liquid helium, the test procedure at 4 K was similar to that at room (295 K) and intermediate temperatures.

The tensile properties of the alloys were also measured, following ASTM Method E8-69, and the elastic constants were obtained by Ledbetter et al., using ultrasonic methods [2]. The chemical analyses of these alloys and other procedural details are available in comprehensive reports [2].

## RESULTS

### Strength Level and Fracture Mode

Table 1 lists selected mechanical property results at 4 K. Following Tetelman and McEvily [3], it is convenient to classify these materials as

low ( $\frac{\sigma_y}{E} < 0.003$ ), medium ( $0.003 < \frac{\sigma_y}{E} < 0.006$ ) and high strength ( $\frac{\sigma_y}{E} > 0.006$ )

alloys. Decreasing the temperature from 295 K to 4 K serves to increase the strength level, with  $\sigma_y/E$  increasing by amounts ranging from 17% for

5083-0 aluminum to 245% for 21-6-9 stainless steel. Most of these alloys were plastic when fractured at 295 K in the thickness stated, necessitating J tests. However, at 4 K, the majority of alloys (all of the ferritic steels and titanium alloys, as well as several precipitation-hardened fcc alloys) were linear-elastic. It was noted that alloys having

$\frac{\sigma_y}{E} > 0.006$  usually satisfied the ASTM E-399-74 specimen thickness requirement; exceptions were the ELI Ti-6Al-4V alloy at 295 K and the 21-6-9 stainless steel at 4 K.

### Strength Versus Fracture Toughness

Although a combination of high yield strength and high fracture toughness would be ideal, in reality these properties are antithetical. It appears that designers must seek an alloy with the optimum combination of strength and toughness for a given application. An inverse relationship between



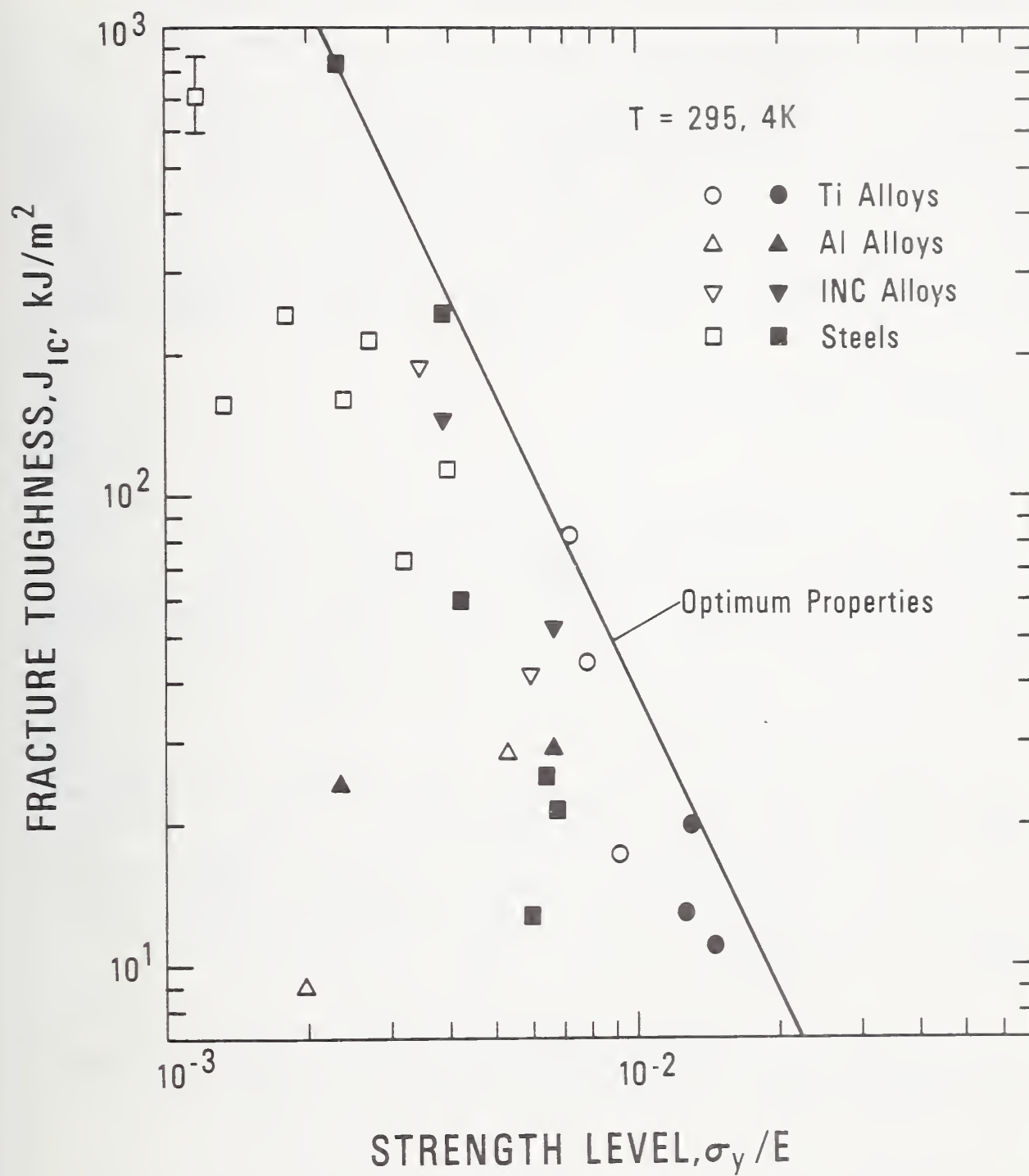


Figure 1. Fracture toughness-versus- $\sigma_y/E$  for commercial structural alloys tested at 295 K and 4 K.

$\sigma_y$  and  $K_{IC}$  at room temperature has been demonstrated for steel, aluminum, and titanium alloys [4]. It must be appreciated that a similar trade-off exists for alloys at cryogenic temperatures, and for elastic-plastic fractures as well.

The  $J_{IC}$  and  $\sigma_y/E$  data at 295 and 4 K are plotted on logarithmic coordinates in Figure 1. These results show that the low strength alloys exhibit a wide variation in toughness, but the spread of observed  $J_{IC}$  values decreases with increasing  $\sigma_y/E$ , following a trend that holds for two orders of magnitude in  $J_{IC}$ . The empirical results for these technologically important materials support the following conclusion: relatively low fracture toughness values are possible at any strength level, but the maximum toughness attainable with commercial alloys is an inverse function of strength throughout the elastic and elastic-plastic ranges.

### The Temperature Dependence of $J_{IC}$

Temperature effects on  $J_{IC}$  correlate well with crystal structure. Figure 2 illustrates three distinct trends for alloys having the fcc, bcc, and hcp structures. The data presented in this figure are representative in that fcc alloys typically exhibit high toughness throughout the ambient-to-cryogenic range, while the hcp alloys are noted for low toughness, and bcc alloys show abrupt transitions to brittle fracture modes involving cleavage. Secondary metallurgical factors such as composition, purity, heat treatment can modify the fracture toughness of alloys within each crystal structure class considerably, as indicated by the following.

#### I. The fcc alloys form three sub-groups:

1. Stable, annealed fcc alloys show sizable increases in toughness as temperature is reduced from 295 to 4 K. The AISI 310 stainless steel and 5083-0 aluminum alloys tested in this study showed  $J_{IC}$  increases amounting to 55% and 175%, respectively.

2. Precipitation-hardened alloys show mild temperature dependences. Included here are Inconel 750\*, Inconel 718, A-286, and 2014-T652 aluminum. The toughness of these alloys either increased, decreased, or remained constant, but the change in  $J_{IC}$  between 295 and 4 K never exceeded 30%.

3. Metastable austenitic alloys undergo martensitic phase transformations during tests at low temperatures. Two such alloys, AISI 316 and 21-6-9 stainless steels, were studied here. Martensitic phases were detected at the fracture surfaces of specimens tested at 4 K, but there was no evidence of transformations at 295 K. AISI 316 shows an increase in  $J_{IC}$

---

\* Tradenames are used for the sake of clarity, and do not imply recommendation or endorsement by NBS.

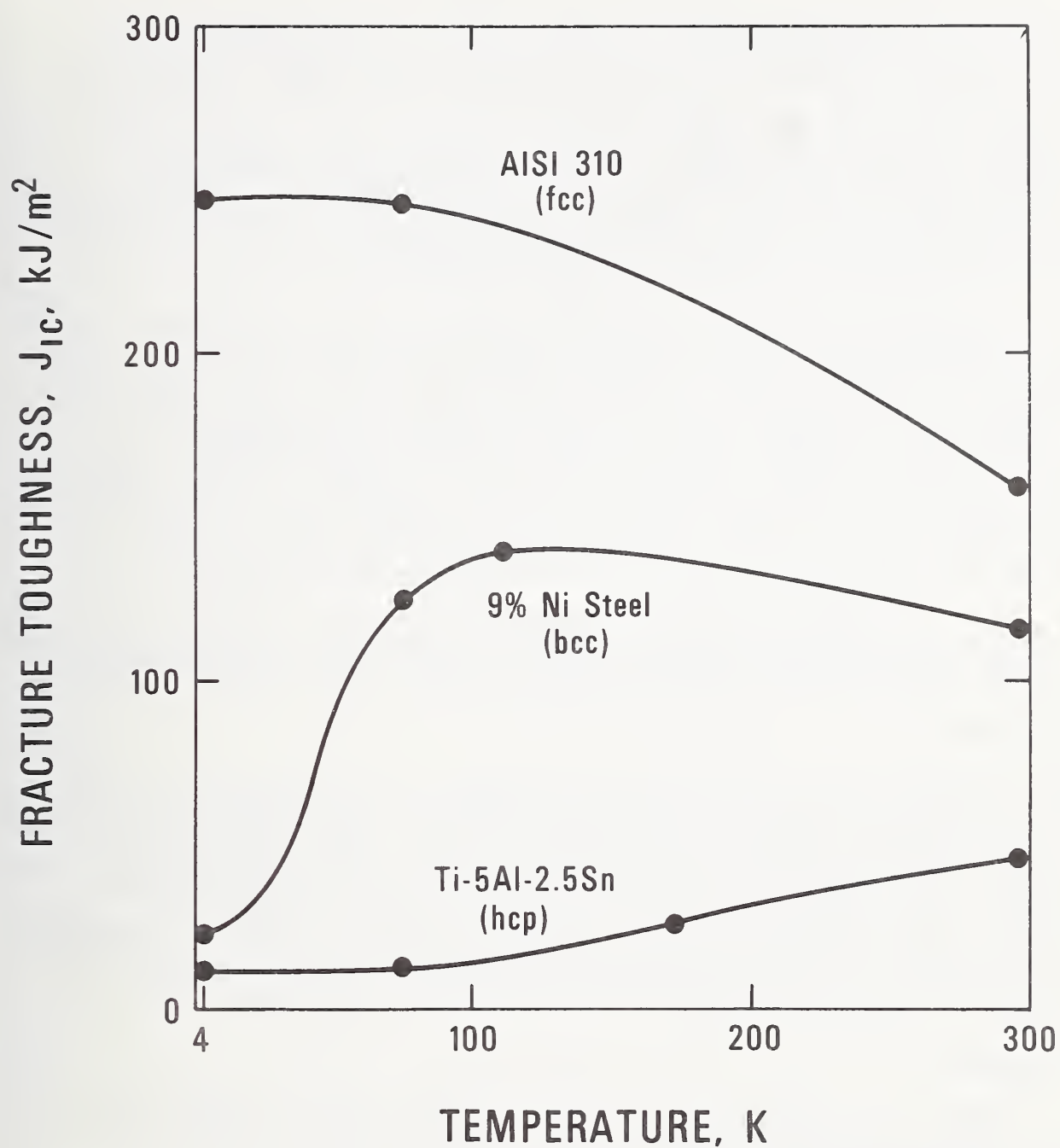


Figure 2. The temperature dependence of fracture toughness for alloys having three different crystal structures.

between 295 and 4 K, whereas 21-6-9 exhibits a sizable decrease. Thus it is difficult to generalize on the effects of phase transformations since favorable as well as adverse effects are possible.

II. The bcc alloys including ferritic steels are of limited use due to their transitional behavior. As a class, the 3.5, 5, and 9% Ni steels exhibited the largest  $J_{IC}$  decreases observed in this study. The transition

for 9% Ni steel occurs between 76 K and 4 K, where  $J_{IC}$  is reduced by 82%. However, note that  $J_{IC}$  actually increases by 20% as the temperature is decreased from 295 to 111 K, just prior to the transition. Similar increases of  $J_{IC}$  in the "upper shelf" regions were observed for 3.5 and 5 Ni steels, but, due to lower Ni content, the transition temperature ranges for these steels were higher in comparison with 9% Ni steel.

III. Although the toughness attainable with hcp alloys is relatively low in comparison with austenitic alloys, some hcp titanium alloys offer unique physical properties, such as superior strength-to-weight and strength-to-thermal conductivity ratios, which guarantee their use in many applications. As indicated in Figure 2, a mildly adverse temperature dependence is accepted as the general trend for the Ti-5Al-2.5Sn and Ti-6Al-4V alloys which are most favored for cryogenic service. Nevertheless, many unalloyed hcp metals (Cd, Zn) display ductile-to-brittle transitions, and tests of an extra-low-interstitial, recrystallization-annealed Ti-6Al-4V alloy revealed a sharp decline of  $K_{IC}$  in the relatively narrow interval  $76 <$

$T < 125$  K. A comparison of data for the ELI and normal Ti-6Al-4V grades (Table 1) confirms that fracture results for these alloys are particularly sensitive to material condition and purity.

## CONCLUSION

The J-integral was used to evaluate and compare the low temperature fracture behavior of 14 commercial structural alloys. These data can be used in fracture mechanics evaluations, and they suggest several generalizations that should aid in predicting the behavior of untested alloys. However, many factors affect fracture behavior, and exceptions to the general trends undoubtedly exist. Moreover, rankings of fracture toughness based on  $J_{IC}$ , a fracture initiation parameter, may not be equivalent to rankings based on initiation/propagation parameters as measured, for example, in dynamic tear tests.

## REFERENCES

1. LANDES, J. D., and BEGLEY, J. A., in Fracture Analysis, ASTM STP 560, Amer. Soc. Test. Mater., 1974, p. 170.
2. Materials Research in Support of Superconducting Machinery, Vol. 5 (and previous volumes), Reed, R. P., Ledbetter, H. M., and van Reuth, E. C., Eds., Nat. Bur. Stds., Boulder, CO.
3. TETELMAN, A. S., and McEVILY, A. J., Fracture of Structural Materials, Wiley, NY, 1967.
4. WOOD, H. A., in Fracture Mechanics of Aircraft Structures, AGARDograph No. 176, Liebowitz, H., Ed., North Atlantic Treaty Organization, 1974, p. 18, AD-777-641.

Table 1. Test Materials and Selected Results

Material and Condition	Spec. Thickness (cm) and Orientation	Yield Strength at 4K, $\sigma_y$ (MPa)	Young's Modulus at 4K (GPa)	Poisson's Ratio at 4K, $\nu$	$K_{IC}$ (MPa $\cdot m^{1/2}$ )	$J_{IC}$ (kJm $^{-2}$ )		
						295K	4K	4K
5083-0 Aluminum (annealed)	3.2 TL	186	81.0	0.318	--	--	9.0	25.0
2014 Aluminum (T652 temper)	3.8, TL	547	83.8	0.330	50.0	53.4	29.2	30.3
Ti-6Al-4V, Normal (mill annealed)	2.5, TL	1792	122.0	0.309	47.0	38.5	17.8	11.0
Ti-6Al-4V, ELI (Recryst. annealed)	2.0, TL	1660	126.0	0.308	--	54.0	86.0	20.9
Ti-5Al-2.5Sn, Normal (annealed)	3.8, TS	1551	123.0	0.311	75.7	42.0	46.1	12.9
Inconel 718 (soln. treated & aged)	2.5, TS	1408	211.0	0.295	96.0	112.0	42.0	54.2
Inconel 750 (soln. treated & aged)	3.8, TS	869	219.0	0.296	--	--	193.0	149.0
A-286 (soln. treated & aged)	3.8, TS	889	212.0	0.281	--	--	74.5	61.2
AISI 310 (annealed)	3.8, TL	765	199.0	0.296	--	--	158.0	245.0
AISI 316 (annealed)	3.8, TL	545	234.0	0.281	--	--	$\sim$ 740.0	875.0
21-6-9 Stainless (annealed)	3.8, TL	1240	--	--	--	--	$\sim$ 245.0	26.3
A203-E (3.5% Ni Steel) (quenched & tempered)	2.5, TL	900	215.0	0.282	--	$\sim$ 30.0	163.0	3.8
A645-74 (5% Ni Steel) (austenitized, tempered, & reversion annealed)	3.1, TL	1200	209.0	0.282	--	$\sim$ 50.0	222.0	13.3
A553-72A (9% Ni Steel) (quenched & tempered)	3.1, TL	1329	202.0	0.285	--	$\sim$ 73.0	117.0	23.2





SEMI-ANNUAL REPORT ON MATERIALS RESEARCH  
IN SUPPORT OF SUPERCONDUCTING MACHINERY

MAGNETOTHERMAL CONDUCTIVITY

L. L. Sparks

Cryogenics Division  
Institute for Basic Standards  
National Bureau of Standards  
Boulder, Colorado 80302

October 1976

MAGNETOTHERMAL-CONDUCTIVITY STUDIES DURING ARPA-  
SPONSORED PROGRAM, SEPTEMBER 1973 TO SEPTEMBER 1976

Material	Unified Numbering System Designation	ARPA Report Number
Inconel 718	N07718	3
AISI 304	S30400	4
AISI 310	S31000	3
Fe-47.5% Ni	--	6
Cu-28% Ni	C71500	6
Cu-0.5% Sn	--	6
OFHC-Cu	C10200	2
Hi Purity Cu	--	3
Al 1100-0	A91100	5
Ti-6Al-4V	--	6

## Summary: Magnetothermal Conductivity

The magnetothermal conductivities have been determined for four alloys: Fe-47.47 wt % Ni, Ti-6Al-4V (ELI), Cu-0.5 at % Sn, and Cu-28 at % Ni. Data are presented in the temperature range 4 to 20 K and for magnetic fields up to 6366 kA/m (80 kOe). The effect of the magnetic field is to reduce the thermal conductivity of the Fe-Ni alloy and the Ti-Al-V alloy. The reduction due to 6366 kA/m field is 4.1% for the Fe-Ni specimen at 5 K and 2.2% at 20 K. The corresponding reductions for the Ti-Al-V specimen are 16% at 5 K and 1.6% at 20 K. Any magnetic field effect on the thermal conductivity of the two copper specimens was below the detectable limits of the system for temperatures below 20 K.

## Contents: Magnetothermal Conductivity

	Page
1. Introduction . . . . .	290
2. Procedures . . . . .	290
2.1 Apparatus . . . . .	290
2.2 Materials . . . . .	290
3. Results and Discussion . . . . .	291
4. References . . . . .	292
List of Figures . . . . .	293

## 1. Introduction

The objective of the magnetothermal conductivity project has been to determine the effect of magnetic fields on the thermal conductivity of technically important metals. The need for this information arises from the development of rotating machinery which operates at cryogenic temperatures. The existing literature on magnetothermal conductivity,  $\lambda(H)$ , deals almost exclusively with pure materials and single crystals. A complete bibliography of the subject was given by Sparks and Fickett in a previous ARPA report [1].

The materials studied in this program are being used or are candidates for use in superconducting motors and generators. Optimum design of these machines, which must operate at low temperatures while in magnetic fields, requires a detailed knowledge of how the thermal properties of the constituent materials are affected by a magnetic field. Test specimens were chosen so that broad categories of materials were represented. The categories and the particular materials tested during the course of the ARPA work were:

- (1) structural alloys -- UNS-N07718, UNS-S30400, UNS-S31000, Fe-47.47 wt % Ni, and Ti-6Al-4V;
- (2) superconductor stabilizing materials -- oxygen-free copper, UNS-A91100, and high purity copper;
- (3) superconductor cable constituents -- Cu-0.5 at % Sn and Cu-28 at % Ni.

Based on these data the magnitude of the magnetic field effect on the thermal conductivity can be estimated for similar materials.

Four specimens, Cu-0.5 at % Sn, Cu-28 at % Ni, Ti-6Al-4V, and Fe-47.47 wt % Ni, have been tested during this reporting period. Results for these materials are included in this report.

## 2. Procedures

### 2.1 Apparatus

The principal components of the  $\lambda(H)$  system are shown schematically in Figure 1. The conventional longitudinal heat flow method of determining thermal conductivity [2] is utilized. A specimen is shown mounted with its axis parallel to the direction of the magnetic field. The longitudinal field effect is determined when the heat current and magnetic field are parallel.

The basic operation of the system has been described in previous reports [1,3], and the details of several system modifications were given in [4].

### 2.2 Materials

An extra low interstitial (ELI) form of Ti-6Al-4V was used for the  $\lambda(H)$  specimen. This alloy was produced to AMS 4930 specifications; it was commercially annealed at 977 K for 2 hours, air cooled and descaled. The microstructure of this stock of material was primary alpha and beta with the average alpha grain diameter being 0.013 mm [5]. The chemical composition of the alloy in weight percent was: Al, 5.91; V, 3.94; Fe, 0.103; O, 0.110; C, 0.018; N, 0.014; H, 52 ppm; Ti, balance. The ratio of the electrical resistivity at the ice point to the electrical resistivity determined at a temperature just above the superconducting critical temperature was  $1.16 \pm 0.02$ . The ratio of area to length (A/l) for this specimen was  $0.89 \pm 0.01$  mm.

A ferromagnetic specimen, Fe-47.47 wt % Ni, with an A/l equal to  $0.852 \pm 0.003$  mm was tested in the hot rolled condition. Mill analysis of this alloy indicated the following composition in weight percent: C, 0.012; Mn, 0.33; Si, 0.25; P, 0.002; S, 0.004; Ni, 47.47; Fe, balance. Grain size, as determined using the intercept method was 0.12 mm, Rockwell hardness was B75, and the specimen density was  $8.19 \times 10^3$  kg/m<sup>3</sup> [6]. The ratio (RRR) of the electrical resistivity at the ice point to that at liquid helium temperature was  $2.40 \pm 0.002$  for this specimen.

Two copper alloys were made at NBS-Boulder using the drop casting technique described by Ekin and Deason [7]. The melting was done in a flowing hydrogen-argon atmosphere. Copper stock used in both alloys was from a 1.9 cm bar of oxygen-free copper (UNS-C10200). The tin content of the Cu-Sn alloy was 0.49 at % and A/l =  $0.87 \pm 0.01$  mm. After machining, the specimen was annealed at 650°C for 2.5 hours at pressures not exceeding  $6.4 \times 10^{-3}$  Pa. The ratio of electrical resistivity at 295 K to the electrical resistivity at 4.2 K was  $1.10 \pm 0.01$ .

### 3. Results and Discussion

The Ti-6Al-4V specimen exhibited a superconducting phase in its electrical resistivity. The onset of superconducting behavior at zero magnetic field occurs when  $5.2 \text{ K} < T < 5.5 \text{ K}$  as shown in Figure 2. The critical transition temperature is lowered as the magnetic field is increased until at 6366 kA/m (80 kOe) no transition is observed. Within the limits of precision of the measurement, the normal resistivity of the specimen was  $1.43 \pm 0.02 \mu\Omega \cdot \text{m}$  and was independent of both temperature ( $T \leq 20 \text{ K}$ ) and magnetic field. Figure 3 shows the resistance of the specimen at 4.2 K as a function of magnetic field. The imprecision of the measurements at  $H = 0$  is quite high as indicated by the scatter shown in the figure. It appears that the critical field is less than 3183 kA/m (40 kOe) when  $T = 4.2 \text{ K}$ .

The thermal conductivity of Ti-6Al-4V is shown in Figure 4 as a function of temperature with magnetic field as a parameter. The relative change in thermal resistivity ( $\Delta W/W_{H=0}$ ) is given by  $(W_H - W_{H=0})/W_{H=0}$ . When  $H = 6366$  kA/m (80 kOe),  $\Delta W/W_{H=0}$  is 19.8% at 5 K and 1.5% at 20 K. The normal to superconducting change is not evident in the thermal conductivity data since the primary mode of heat conduction in this material is due to phonons rather than the electrons. A marked decrease in conductivity would have been expected below the critical temperature ( $T_c$ ) if the primary conduction mode were electronic. Electrons in the superconducting state have zero heat capacity and can, therefore, not carry thermal energy.

The thermal conductivity of the Fe-Ni alloy is shown in Figure 5 as a function of temperature with magnetic field as a parameter. As seen in this figure, essentially all of the reduction in conductivity due to magnetic field occurs when  $H \leq 1592$  kA/m (20 kOe). This saturating tendency is shown in Figure 6. A field of 6366 kA/m (80 kOe) causes  $\Delta W/W_{H=0} = 4.79\%$  at 5 K and  $\Delta W/W_{H=0} = 2.27\%$  at  $T = 20 \text{ K}$ . Hust [8] measured the thermal conductivity of a similar Fe-Ni specimen at zero magnetic field and  $T = 7.42 \text{ K}$ . His data indicate a conductivity of  $1.47 \text{ W/m} \cdot \text{K}$  which is nearly identical to the data taken in the magnetothermal apparatus.

The thermal conductivities of the Cu-0.5 at % Sn and Cu-28 at % Ni at zero field are shown in Figures 7 and 8 respectively. The effect of magnetic field on the conductivity of these specimens is too small to be detected in the present system. Differences between the zero field thermal conductivity



data and the  $H = 3183 \text{ kA/m}$  (40 kOe) and  $H = 6366 \text{ kA/m}$  (80 kOe) data are shown in Figures 9 and 10. The differences in thermal conductivity used in these curves were obtained by subtracting the experimental thermal conductivities for  $H \neq 0$  from the values read from the smooth curves shown in Figures 7 and 8. The electrical resistivity for these copper alloys did not change as a function of magnetic field or temperature for  $H \leq 6366 \text{ kA/m}$  (80 kOe) and  $T \leq 20 \text{ K}$ . This field independence has been observed previously at 4.2 K [9] on specimens from the same melts used for the  $\lambda(H)$  specimens.

#### 4. References

1. L. L. Sparks and F. R. Fickett; in Materials Research in Support of Superconducting Machinery-I; R. P. Reed, A. F. Clark, E. C. van Reuth (Eds.); Nat. Bur. Stds., Boulder, CO; March 1974; AD780596.
2. White, G. K., in Measurement of Solid Conductors at Low Temperatures, Tye, R. P. (Ed.), pages 88-94 (Academic Press, NY, 1969).
3. L. L. Sparks and F. R. Fickett; in Materials Research in Support of Superconducting Machinery-II; R. P. Reed, A. F. Clark, E. C. van Reuth (Eds.); Nat. Bur. Stds., Boulder, CO; October 1974; ADA004586.
4. L. L. Sparks; in Materials Research in Support of Superconducting Machinery-IV; R. P. Reed, A. F. Clark, E. C. van Reuth (Eds.); Nat. Bur. Stds., Boulder, CO; October 1975; ADA019230.
5. R. L. Tobler; in Materials Research in Support of Superconducting Machinery-III; R. P. Reed, A. F. Clark, E. C. van Reuth (Eds.); Nat. Bur. Stds., Boulder, CO; April 1975; ADA012365.
6. H. M. Ledbetter and D. T. Read; in Materials Research in Support of Superconducting Machinery-V; R. P. Reed, H. M. Ledbetter, E. C. van Reuth (Eds.); Nat. Bur. Stds., Boulder, CO; April 1976.
7. J. W. Ekin and V. A. Deason, Technique for Preparing Homogeneous Bulk Samples of Concentrated Alloys, Rev. Sci. Instrum. 46, No. 3, pp. 327 (March 1975).
8. J. G. Hust; in Materials Research in Support of Superconducting Machinery-VI; R. P. Reed, H. M. Ledbetter, E. C. van Reuth (Eds.); Nat. Bur. Stds., Boulder, CO; to be published.
9. F. R. Fickett, Nat. Bur. Stds., Boulder, CO, personal communication.



### List of Figures

- Figure 1. Schematic of magnetothermal conductivity probe and magnet.
- Figure 2. Electrical resistivity as a function of temperature for Ti-6Al-4V (ELI).
- Figure 3. Electrical resistance of Ti-6Al-4V (ELI) as a function of magnetic field at 4.2 K.
- Figure 4. Thermal conductivity of Ti-6Al-4V (ELI) as a function of temperature with magnetic field as a parameter.
- Figure 5. Thermal conductivity of Fe-47.47 wt % Ni as a function of temperature with magnetic field as a parameter.
- Figure 6. Thermal conductivity of Fe-47.47 wt % Ni as a function of magnetic field with temperature as a parameter.
- Figure 7. Thermal conductivity of Cu-0.5 at % Sn as a function of temperature at zero magnetic field.
- Figure 8. Thermal conductivity of Cu-28 at % Ni as a function of temperature at zero magnetic field.
- Figure 9. Deviation of thermal conductivities found in the zero and non-zero field tests on Cu-0.5 at % Sn.
- Figure 10. Deviation of the thermal conductivities found in the zero and non-zero field tests on Cu-28 at % Ni.

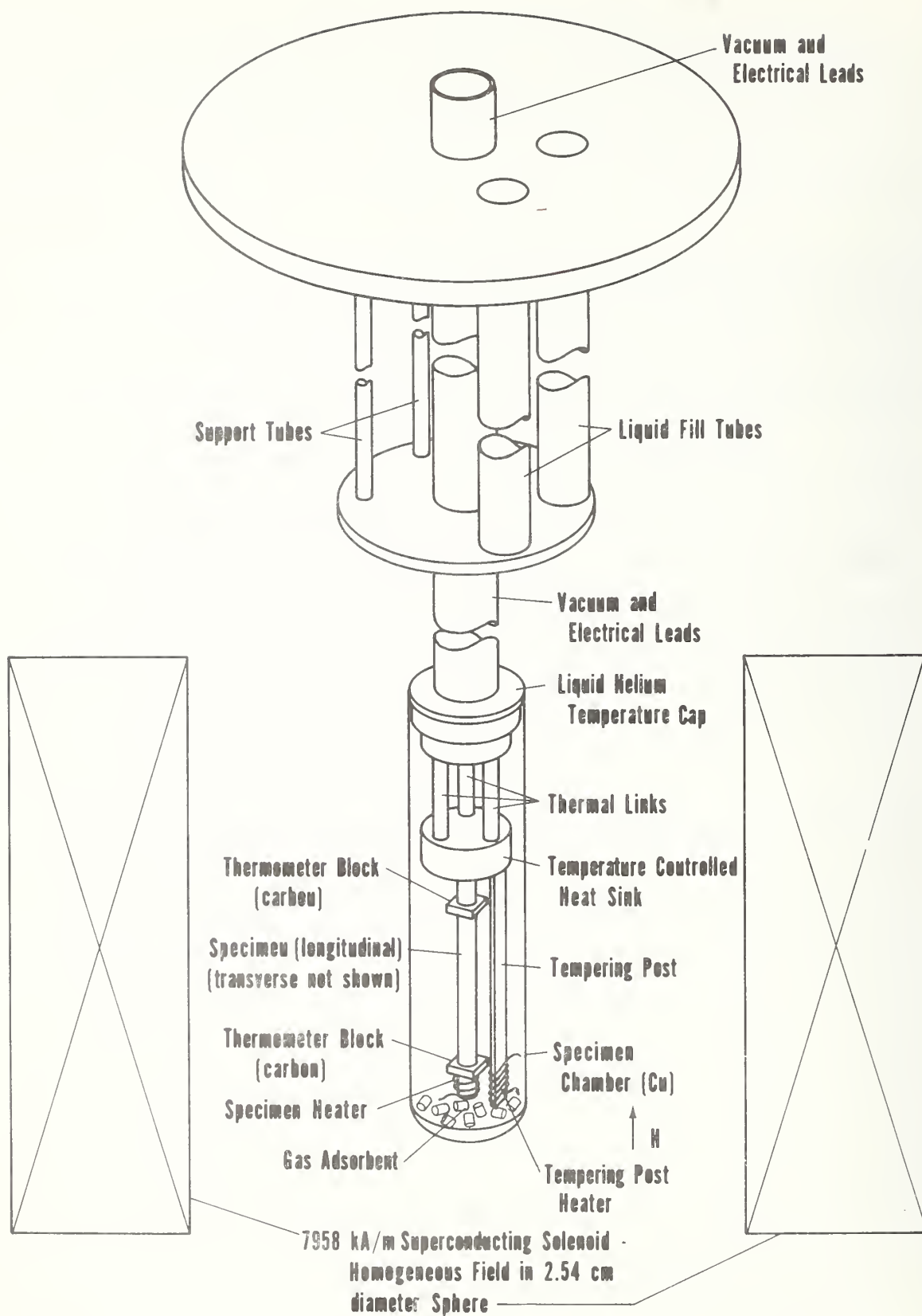


Figure 1. Schematic of magnetothermal conductivity probe and magnet.

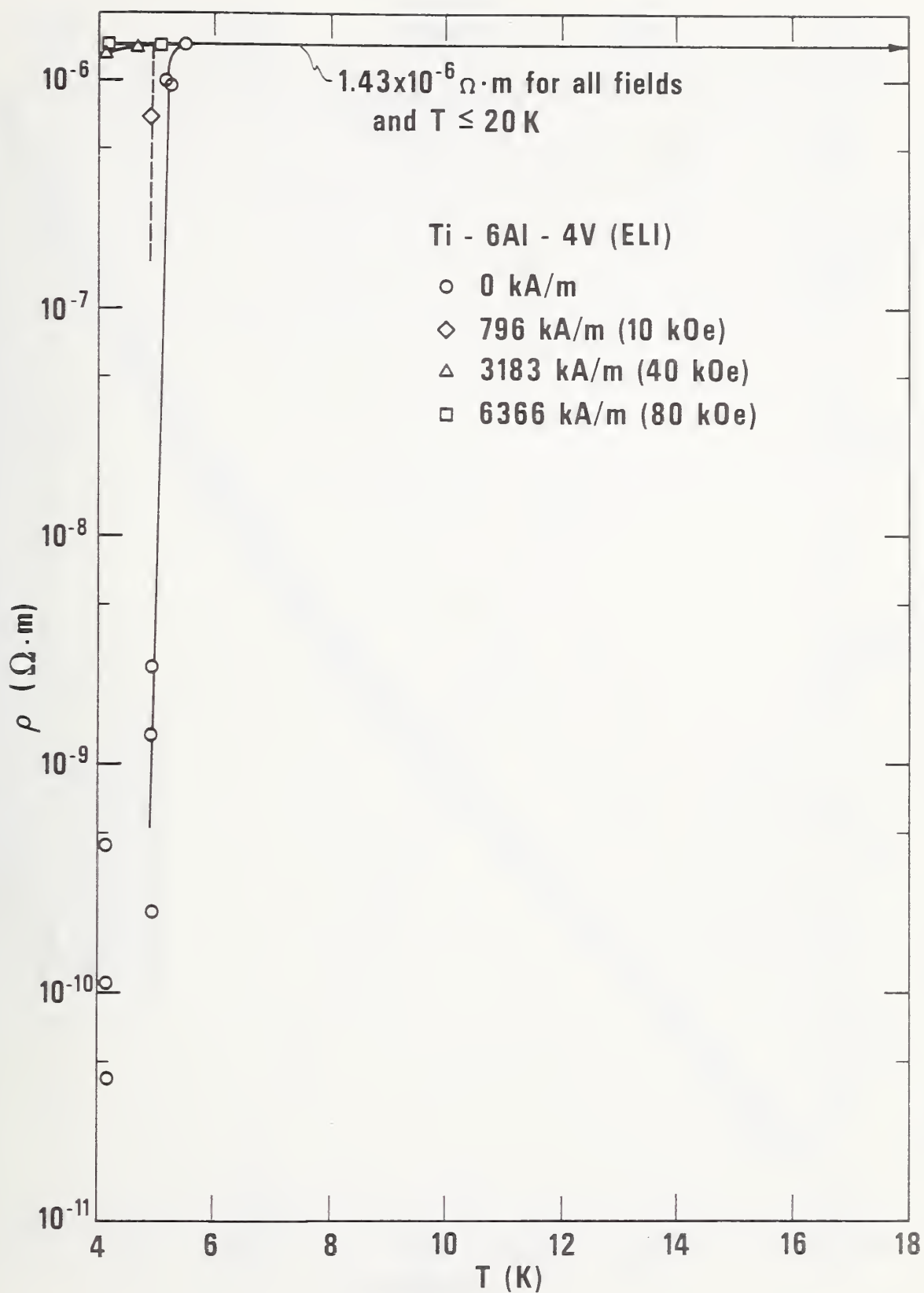


Figure 2. Electrical resistivity as a function of temperature for Ti-6Al-4V (ELI).

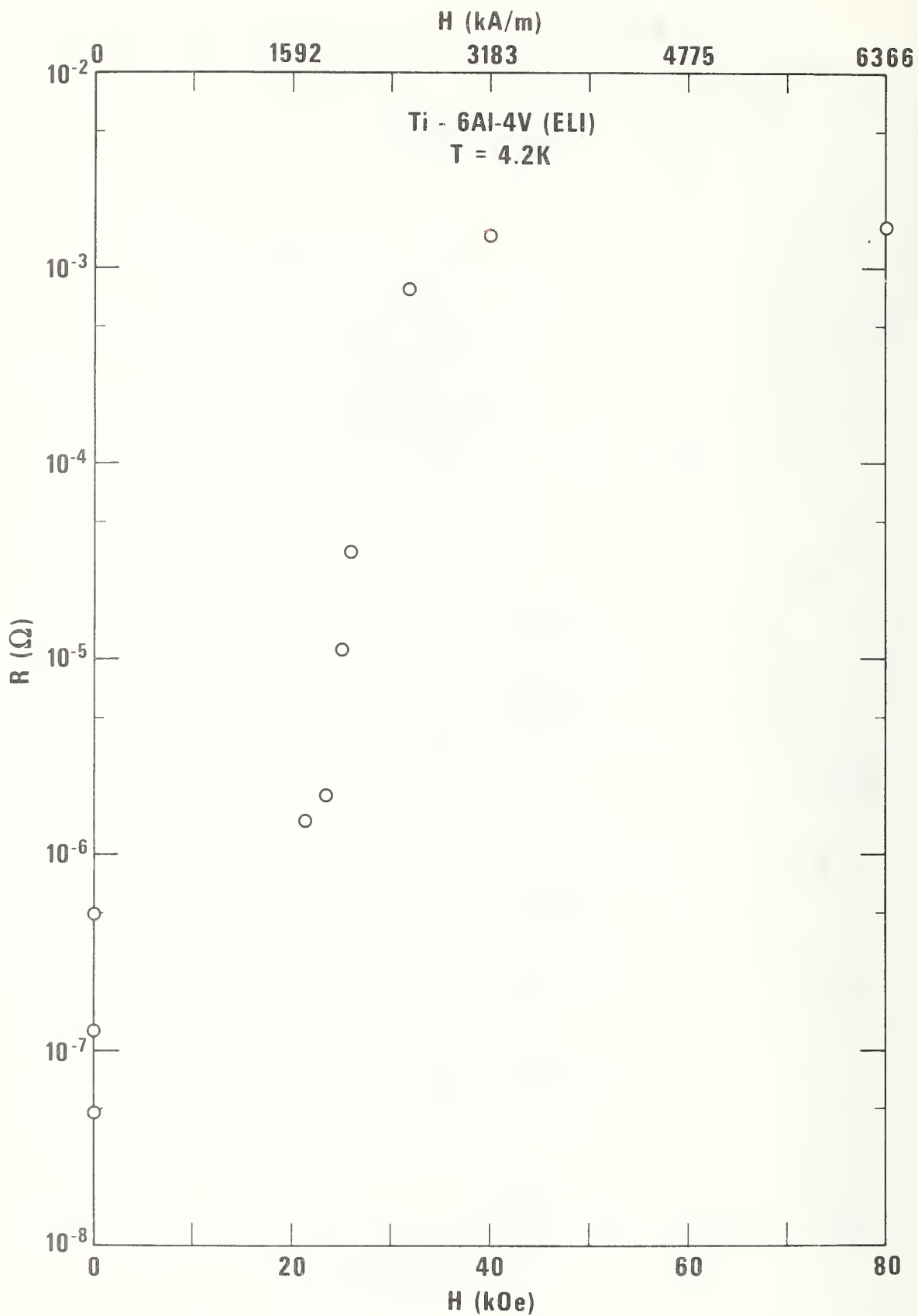


Figure 3. Electrical resistance of Ti-6Al-4V (ELI) as a function of magnetic field at 4.2 K.

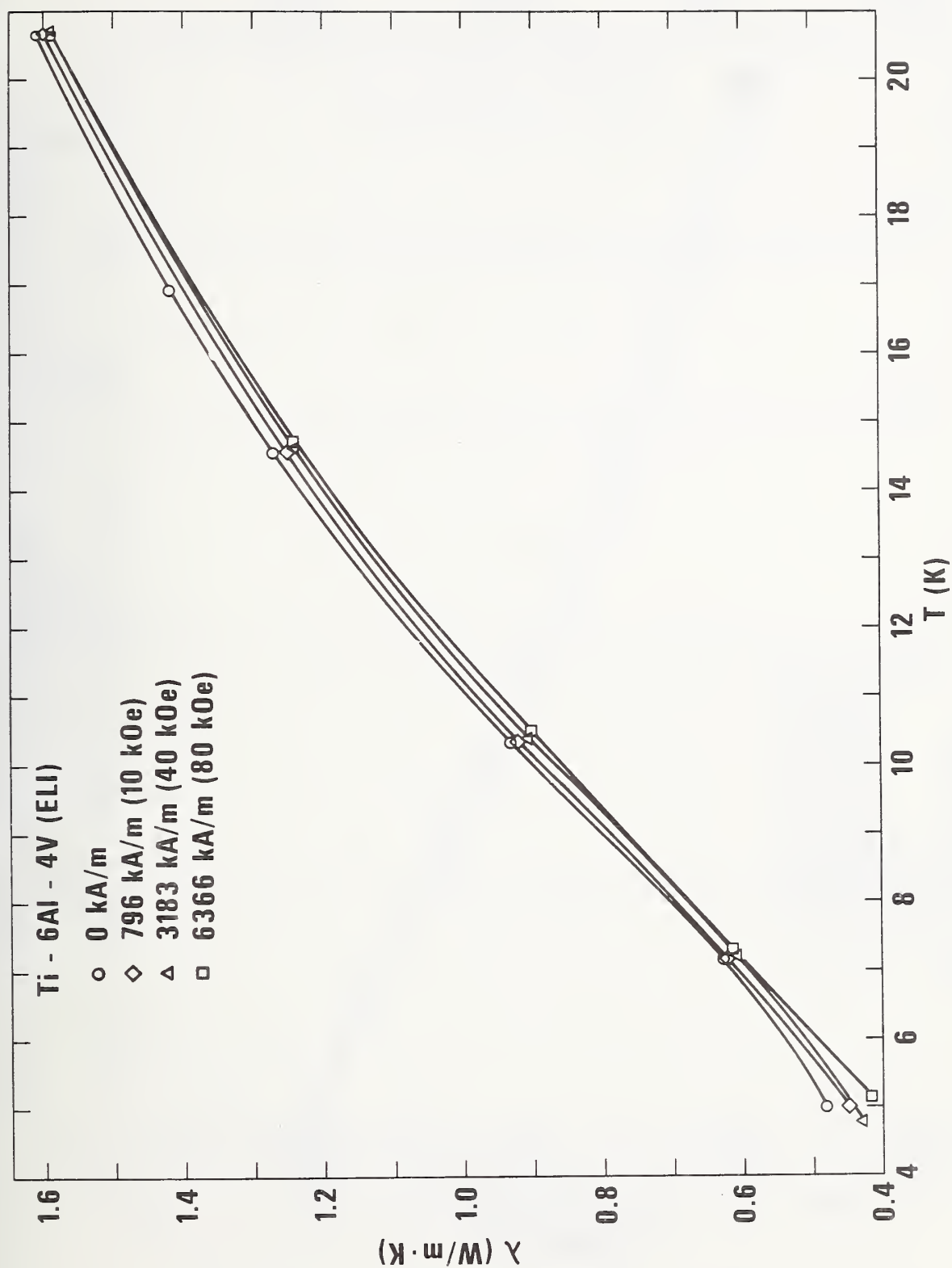


Figure 4. Thermal conductivity of Ti-6Al-4V (ELI) as a function of temperature with magnetic field as a parameter.

77 x 0647

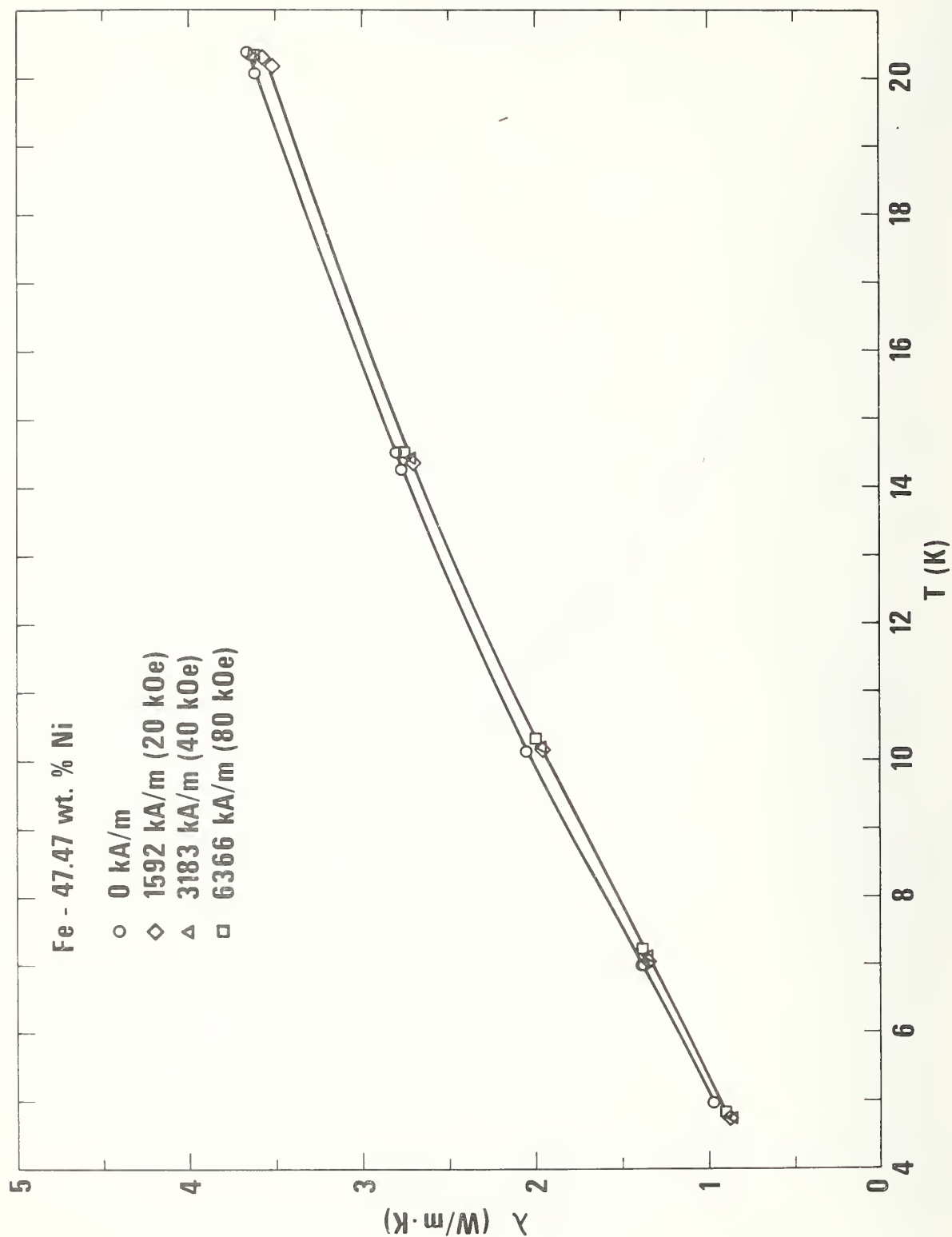


Figure 5. Thermal conductivity of Fe-47.47 wt % Ni as a function of temperature with magnetic field as a parameter.



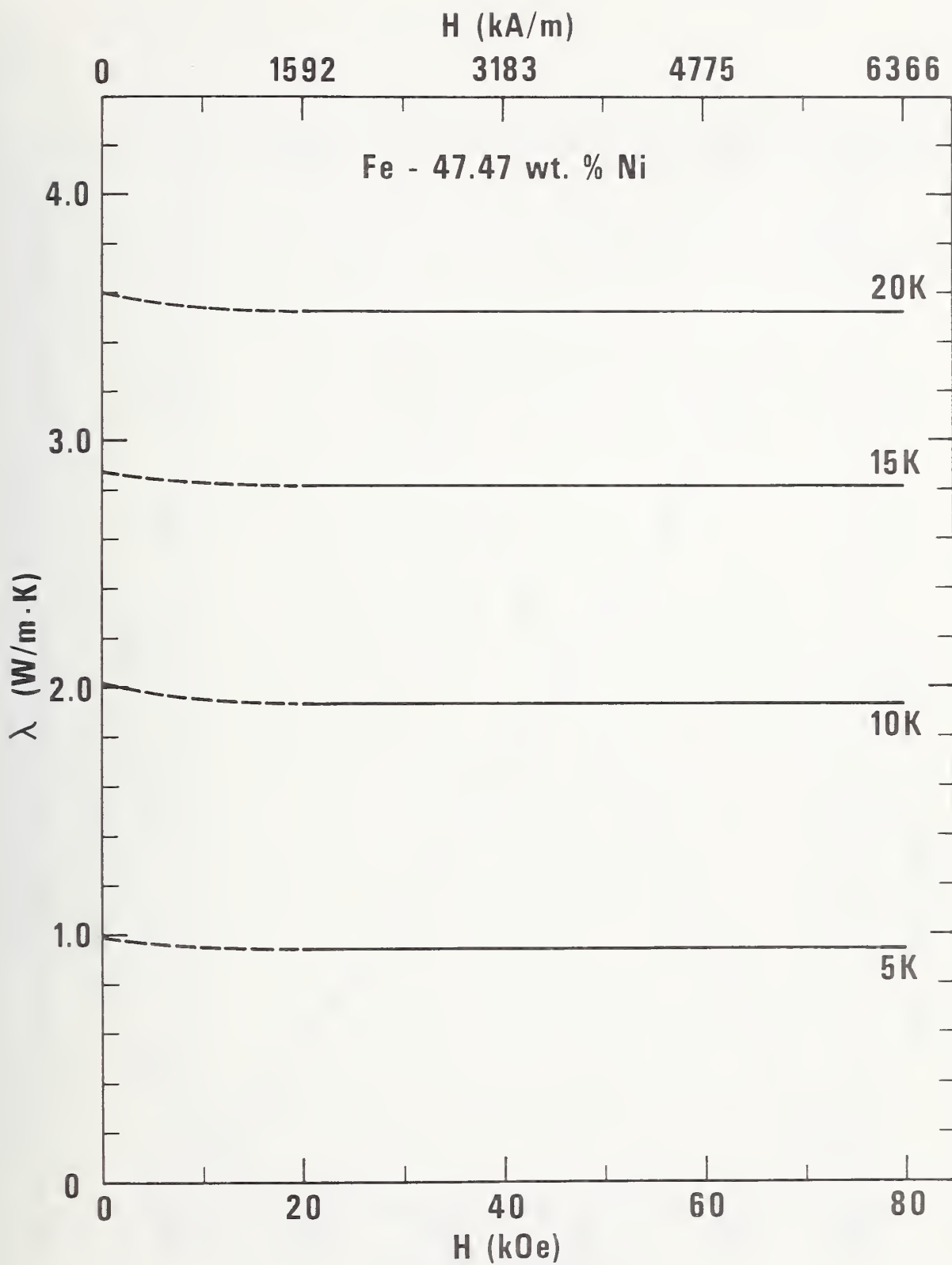


Figure 6. Thermal conductivity of Fe-47.47 wt % Ni as a function of magnetic field with temperature as a parameter.

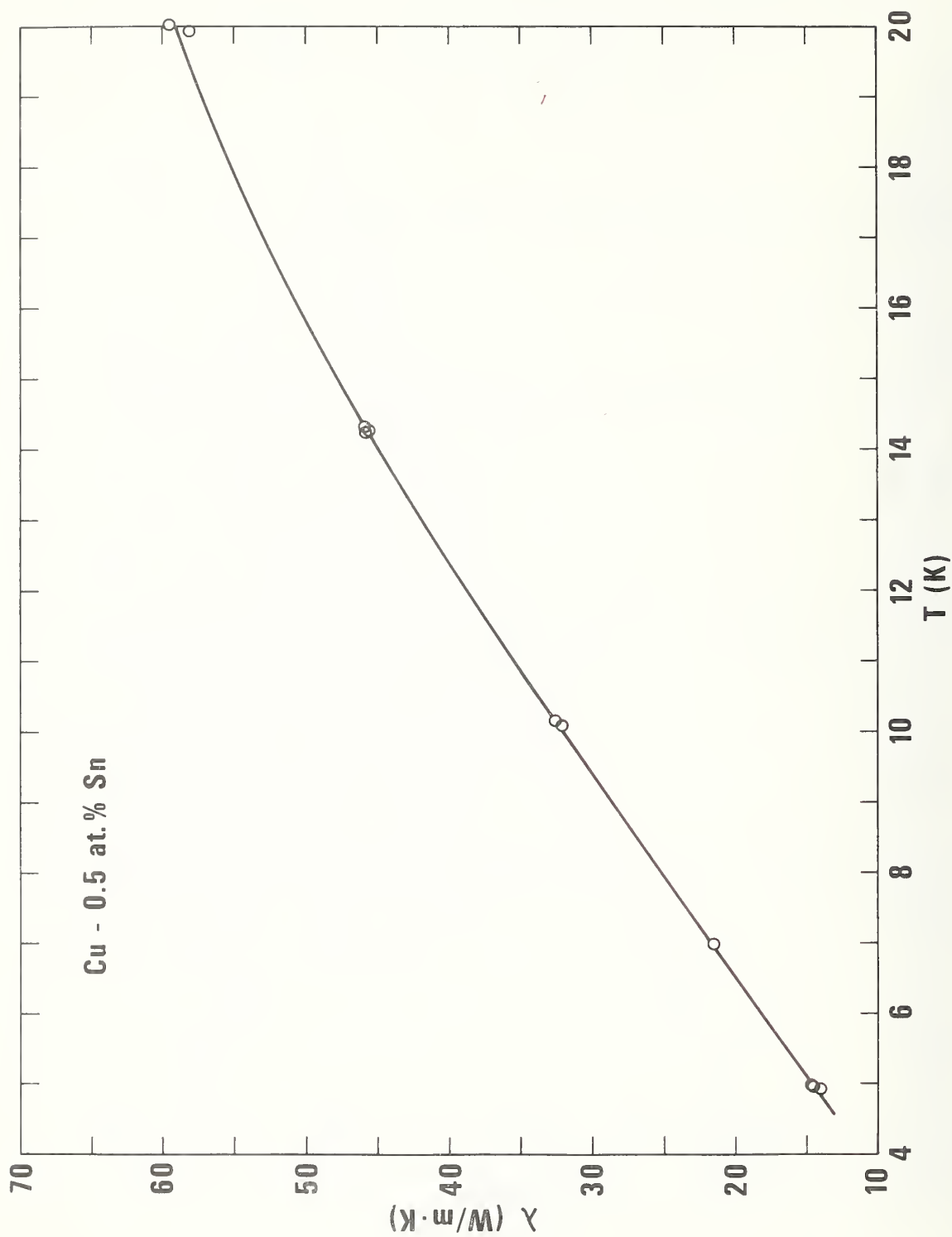


Figure 7. Thermal conductivity of Cu-0.5 at % Sn as a function of temperature at zero magnetic field.

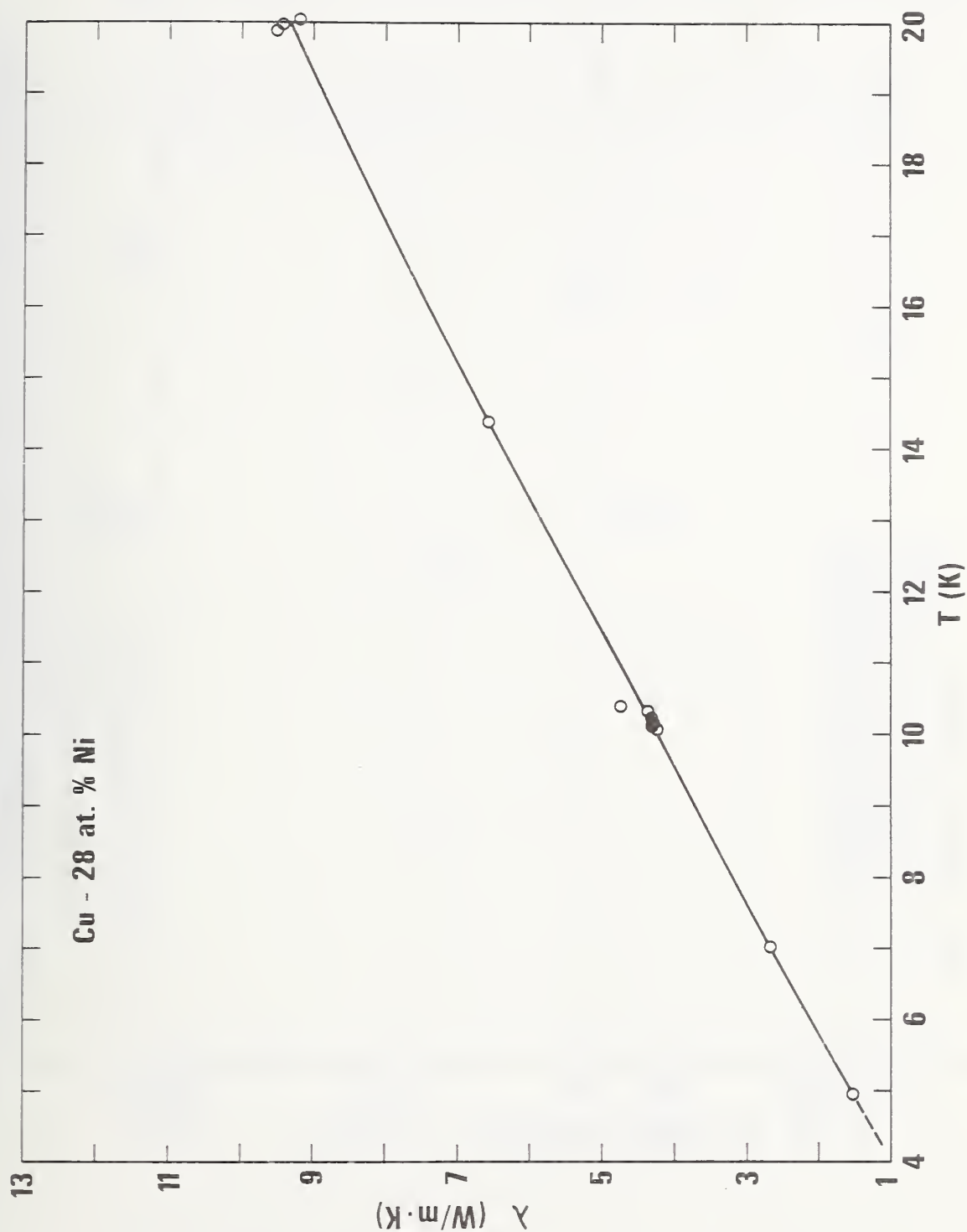


Figure 8. Thermal conductivity of Cu-28 at % Ni as a function of temperature at zero magnetic field.

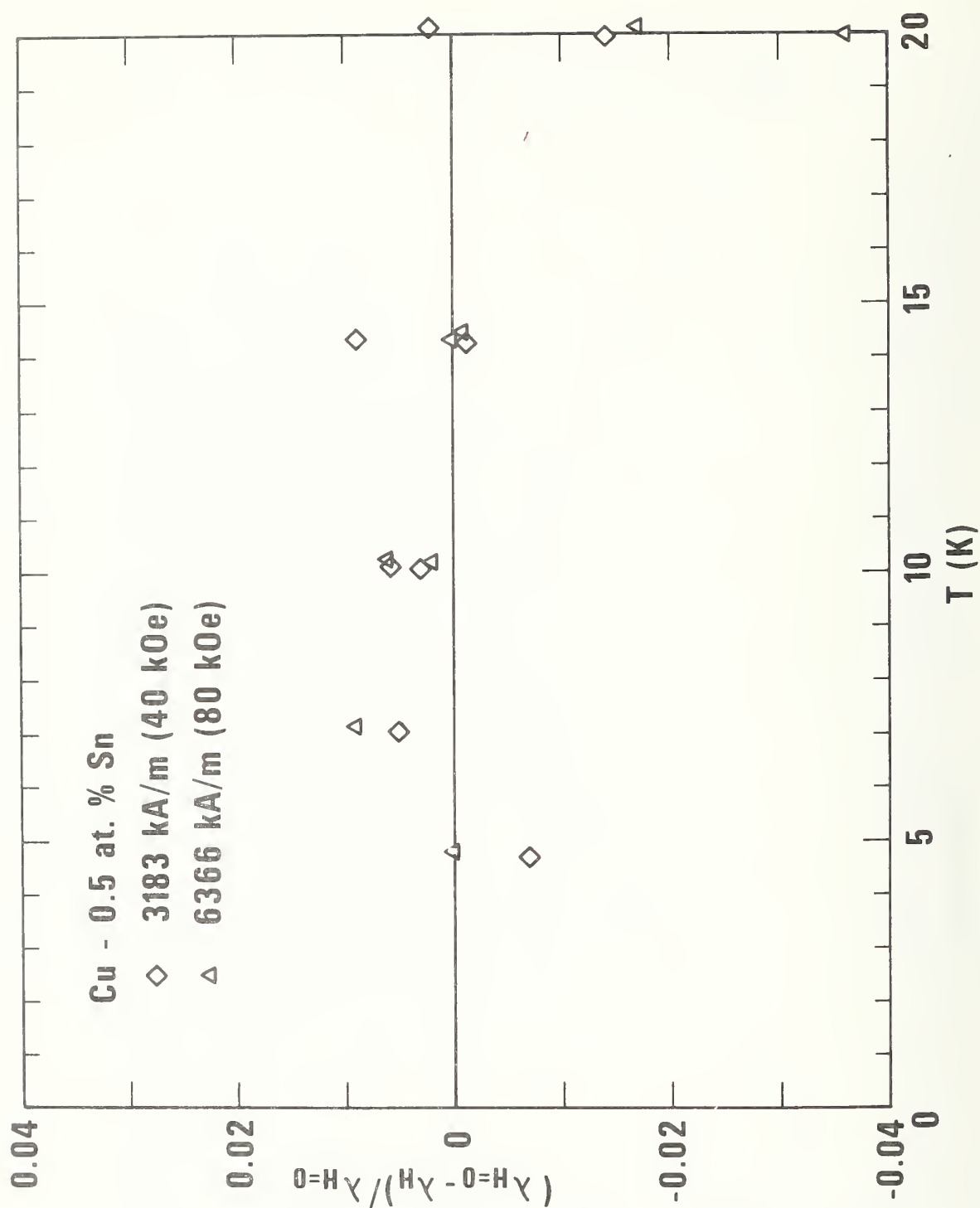


Figure 9. Deviation of thermal conductivities found in the zero and non-zero field tests on Cu-0.5 at % Sn.

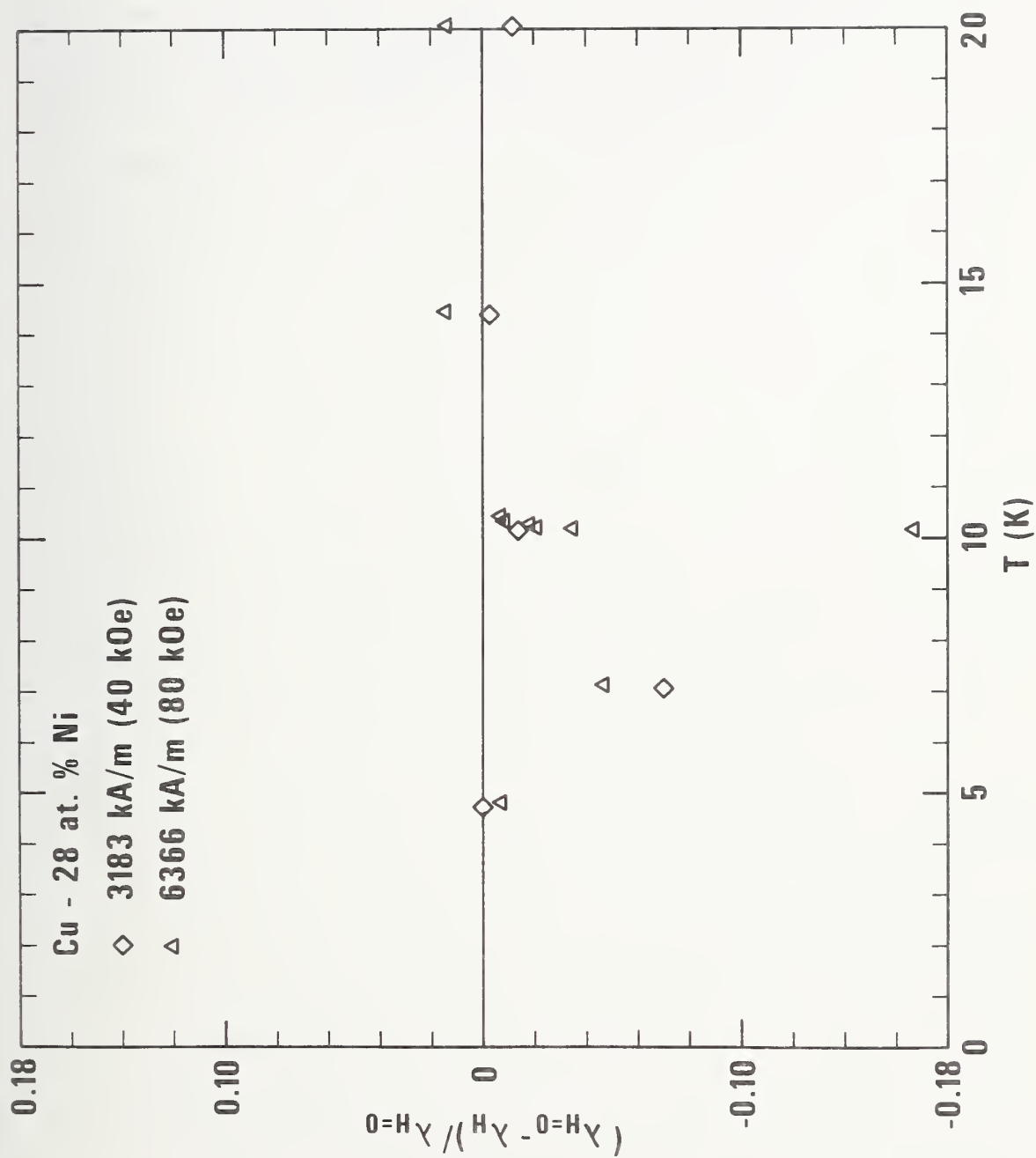


Figure 10. Deviation of the thermal conductivities found in the zero and non-zero field tests on Cu-28 at % Ni.

77x 0646





SEMI-ANNUAL REPORT ON MATERIALS RESEARCH  
IN SUPPORT OF SUPERCONDUCTING MACHINERY

THERMAL CONDUCTIVITY

J. G. Hust

Cryogenics Division  
Institute for Basic Standards  
National Bureau of Standards  
Boulder, Colorado 80302

October 1976

THERMAL-CONDUCTIVITY MEASUREMENTS DURING ARPA-  
SPONSORED PROGRAM, SEPTEMBER 1973 TO SEPTEMBER 1976

Material	ARPA Report No.	Experimental Apparatus
OFHC Copper	2	variable temperature
Inconel X-750 (ST)	2	variable temperature
Inconel X-750 (STDA)	3	variable temperature
INCO LEA	2	variable temperature
Stainless Steel 310-S	2	fixed-point
Stainless Kromarc 58	2	fixed-point
Maraging Steel 300	6	fixed-point
Carpenter 49 Steel	6	fixed-point
Phenolformaldehyde	6	fixed-point
Graphite-epoxy	6	fixed-point
Boron-aluminum	6	fixed-point
Boron-epoxy	4,6	both

### Summary: Thermal Conductivity

Thermal conductivity values are reported for those materials measured during the current reporting period. Specimens were measured of a high permeability steel (Fe-47.5Ni), maraging steel 300 (Fe-18Ni-9Co-5Mo), both in the rolling direction and perpendicular to the rolled plate, boron-aluminum, boron-epoxy, phenolformaldehyde, and graphite-epoxy composites. These data are compared to literature data for similar materials. A new thermal conductivity apparatus is also described. It is a fixed-point apparatus utilizing compressive thermal contacts to circumvent problems encountered with bonded thermal contacts.

## THERMAL CONDUCTIVITY

J. G. Hust  
Cryogenics Division  
Institute for Basic Standards  
National Bureau of Standards  
Boulder, Colorado 80302

### 1. Introduction

Optimum design of superconducting machinery requires a knowledge of thermal properties of technically important materials at low temperatures. But, often, components extend from ambient temperatures to low temperatures, and, therefore, data are needed from 4 K to 300 K. Thermal conductivity of metals is a function of the host metal and its constituent elements and temperature; but it also depends on the microstructure of the material, strain, fatigue, and heat treatment; and in some cases environmental effects are important (e.g. in the case of superconducting machinery, magnetic field intensities may produce significant changes). Specific thermal conductivity data for particular components are required to limit heat losses and thermal stresses in machines. With such a myriad of parameters it is difficult (at best) to determine accurately, by experiment, the thermal conductivity of each machine component. Instead, we often rely on a limited number of measurements on specific types of materials, characterized according to the above parameters. Due to material variability effects these values are generally considered accurate to only about 10%.

It should be noted that accurate thermal conductivity measurements are much more expensive and time consuming relative to many other property measurements. The ease with which high accuracy can be obtained is primarily a function of temperature and the conductivity itself. The extremes of conductivity (both very high, such as in pure metals, and very low, such as in insulating materials) promote inaccuracies in measurement. Generally, low temperature data (below about 100 K) are more readily obtained with accuracy because radiation errors can be minimized.

For the above reasons, various methods of obtaining thermal conductivity data are used. The method used depends primarily on the accuracy dictated by the application. Usually accuracies of 10% are sufficient; in other cases values accurate to 50% suffice. The present state-of-the-art in thermal conductivity measurements is about 1% accuracy, but seldom is this required except in theoretical or standardization work.

In this laboratory three methods of data determination are used:

- (a) A variable-temperature apparatus, capable of measuring at any temperature from 4 to 300 K, with an accuracy of about 2%. This apparatus also simultaneously measures electrical resistivity and thermopower for additional specimen characterization and subsequent predictions of similar materials. This apparatus is used to measure materials that have not been sufficiently measured and characterized previously and for accurate temperature dependence determinations.
- (b) Two fixed point apparatus, capable of measuring near the fixed temperatures of various boiling fluids (such as liquid helium and liquid nitrogen) and melting or subliming solids (such as ice and CO<sub>2</sub>). The accuracy of these apparatus is about 10%, depending mainly on the conductivity of the specimen.

- (c) Predictive methods such as those described by Hust and Clark [1] and Hust and Sparks [2]. The latter paper also contains data for many metals and alloys, necessary to carry out such predictions.

## 2. Apparatus

During the current reporting period the fixed-point apparatus were used to determine thermal conductivity near the fixed-point temperatures of various cryogenic baths. As explained in a later section, difficulty was encountered in accurately measuring composite specimens using the fixed-point apparatus described in a previous report of this series [3]. The difficulty was caused by the differential thermal expansion between the composite specimens and the copper end pieces glued to the specimens for thermal contact. These epoxied bonds apparently cracked during cooldown and resulted in poor thermal contacts. During the last such run with a composite involving NASA resin 2 the end pieces actually fell off during the run. Because of these difficulties a new fixed-point probe was built in which the thermal contact to the specimen was obtained through a compressed indium contact. Otherwise, the operation was identical to the older probe. Figure 1 illustrates this compression type fixed-point apparatus.

The operation of this apparatus is the same as that previously described [3]. Prior to measuring any specimens several calibration runs were conducted to determine the amount of heat conducted by the compression bolts and the measuring wires which pass from the top block to the bottom block. These calibration runs, however, could not be conducted with an empty chamber, as before, because the thermal resistance between the two blocks is dependent on the existence of a force on the compression bolts. Therefore, the system was calibrated using three specimens of phenolformaldehyde rods of decreasing cross-sectional areas. The first was a solid rod of 1.91 cm diameter. The second was of the same outside diameter with a 1.27 cm hole through the center. The third was drilled with a 1.75 cm hole. For each of these specimens, curves of heat flow versus temperature gradient were experimentally determined. These curves were cross-plotted to obtain curves of heat flow versus cross-sectional area at constant gradient. The intersections of these curves (straight lines) with the  $A = 0$  axis were used to determine the heat flow versus temperature gradient of the "empty" chamber. These data, given in Table 1, were used to correct the measured heat flow to obtain the heat flow actually conducted by the specimen at a given gradient.

Table 1. Heat flow of the empty chamber as a function heater block temperature at fixed upper block temperatures, i.e. the bath temperature.

Bath (temp)	$\dot{Q}$ (mW)	T (K)
liquid helium (4 K)	0.00	4.0
	0.44	6.5
	1.32	9.0
	2.89	12.0
	5.70	16.0
	9.05	20.0
liquid nitrogen (76 K)	0.0	76
	36.0	87
	77.7	99
dry ice and alcohol (192 K)	0.0	192
	83.5	204
	176.7	216
ice and water (273.15 K)	0.0	273
	149.0	285
	307.0	297

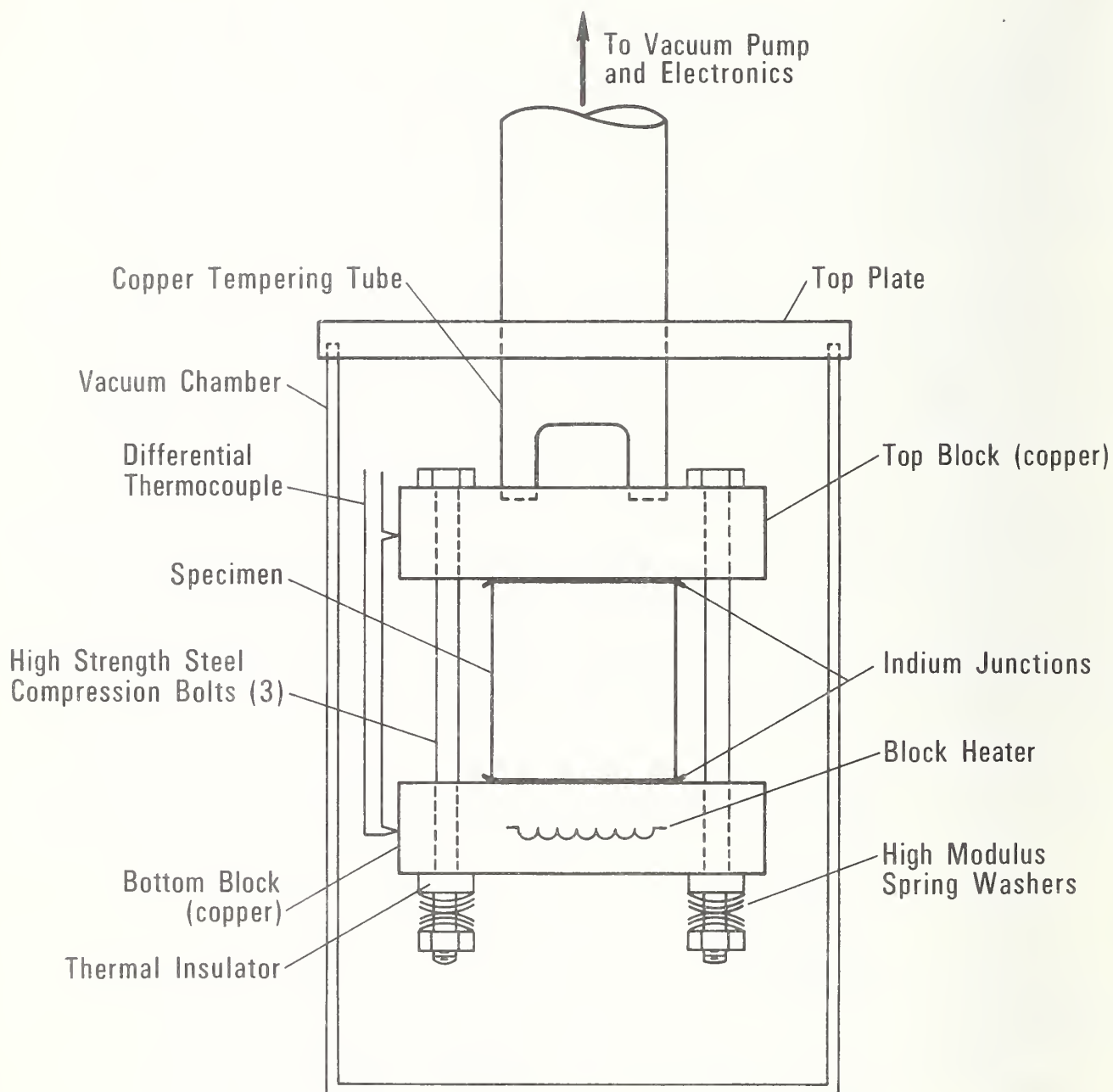


Figure 1. Compressive thermal contact fixed-point thermal conductivity apparatus.



Table 2. Thermal conductivity values for the materials measured during the current reporting period.

Specimen Identification	T (K)	$\lambda$ (W·m <sup>-1</sup> ·K <sup>-1</sup> )	Specimen Identification	T (K)	$\lambda$ (W·m <sup>-1</sup> ·K <sup>-1</sup> )
High Perm 49 Fe-47.5 Ni (in rolling direction)	7.41	1.24	Phenolformaldehyde Compo- site	6	0.055
	84.0	10.4		8	0.070
	200	15.1		10	0.083
	280	16.9		80	0.33
SAME (perpendicular to plate)	7.42	1.47		200	0.58
	84.1	12.8		300	0.54
	199	18.2	Boron-epoxy (longitu- dinal)	5.98	0.248
	280	20.0		7.67	0.380
Maraging Steel-300 (in rolling direction)	85.2	6.93		10.84	0.672
	199	11.8		80.3	2.14
	279	14.4		198	2.24
				277	2.24
SAME (perpendicular to plate)	7.45	0.712	SAME (transverse)	5.96	0.128
	84.5	7.33		80.3	0.612
	199	12.5		196	0.940
	280	15.4		276	0.905
Boron-aluminum compo- site (longitudinal)	7.59	17.7	Graphite-epoxy (longi- tudinal deformed)	6.07	0.0388
	78.4	75.1		80.2	0.702
	195	82.2		196	2.36
	276	89.6		277	3.43
SAME (transverse)	7.60	11.3	Graphite-epoxy (longi- tudinal) (high-temp. resin)	5.97	0.0466
	78.3	51.3		10.82	0.0724
	195	55.7		80.2	0.920
	276	60.6		195	3.19
These data obtained using bonded thermal contact apparatus.			These data obtained using compressive thermal contact apparatus.		

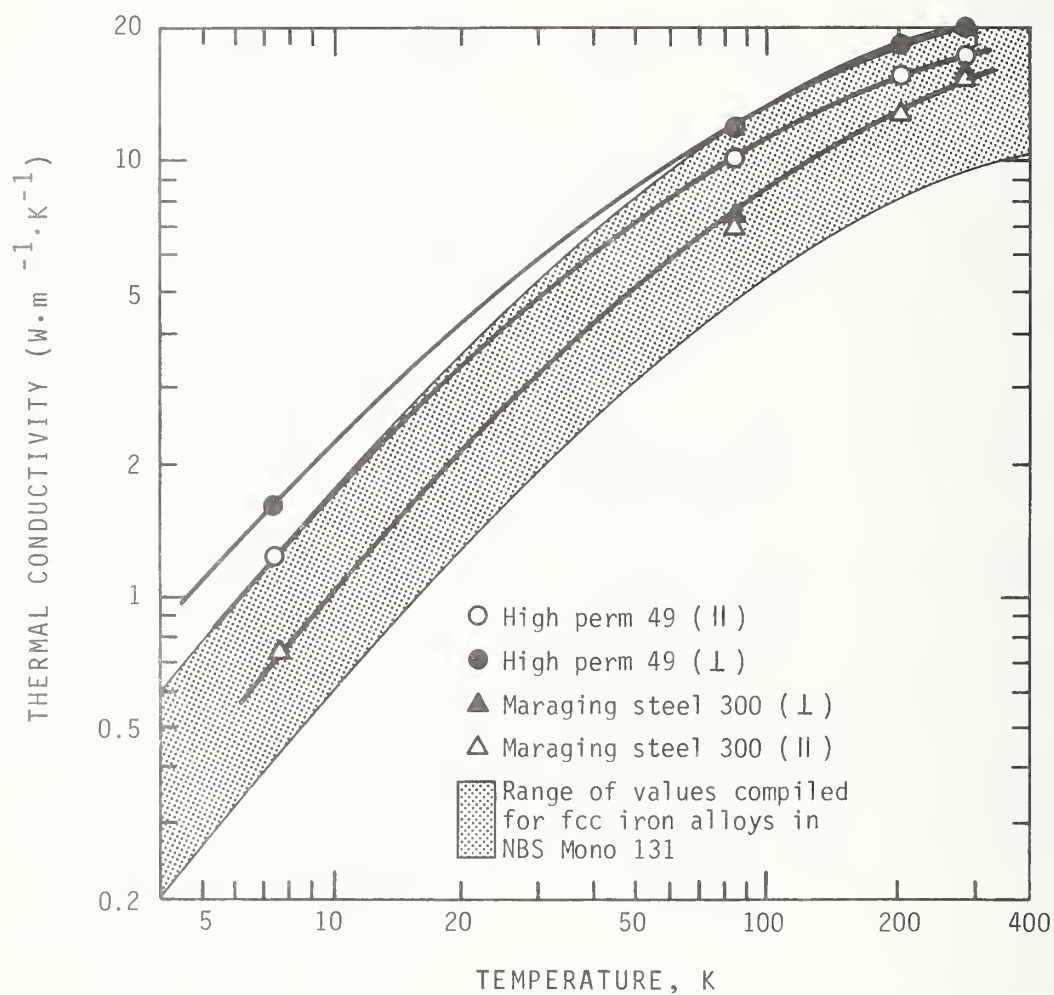


Figure 2. Thermal conductivity of High Perm 49 and Maraging Steel 300 compared to literature data [5] for fcc iron alloys.

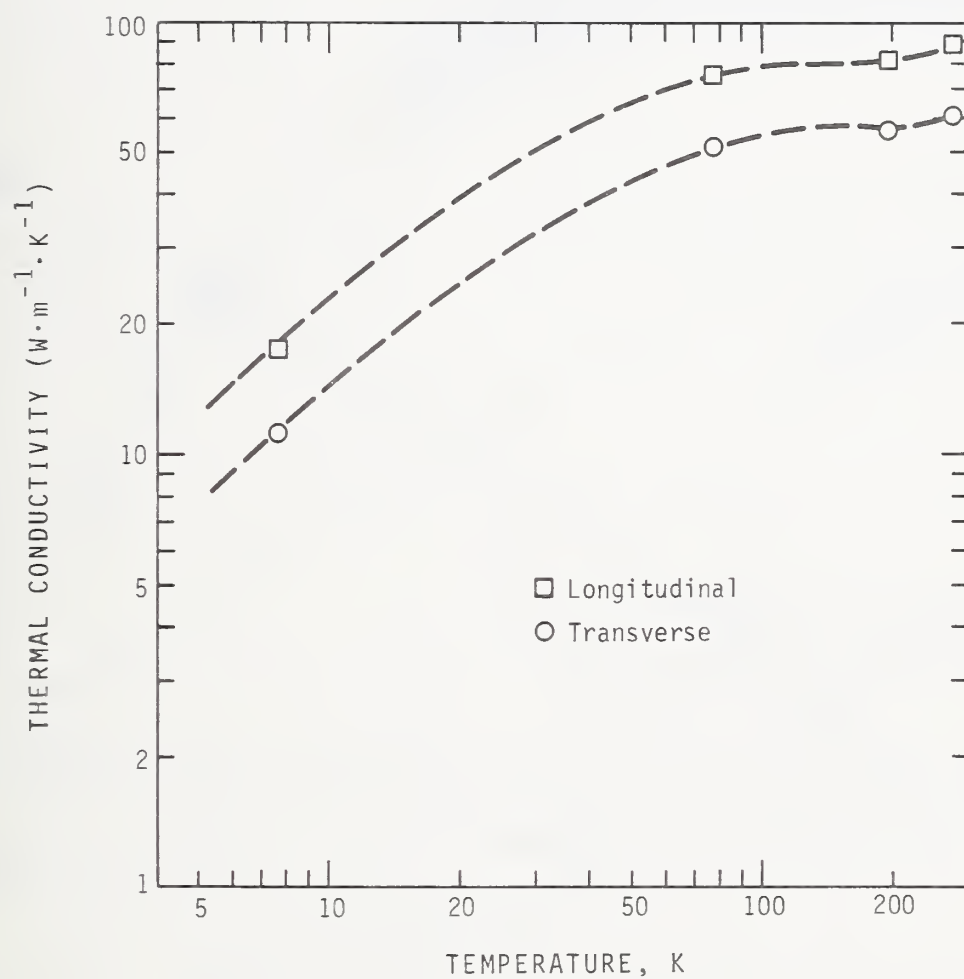


Figure 3. Thermal conductivity of boron-aluminum composite.

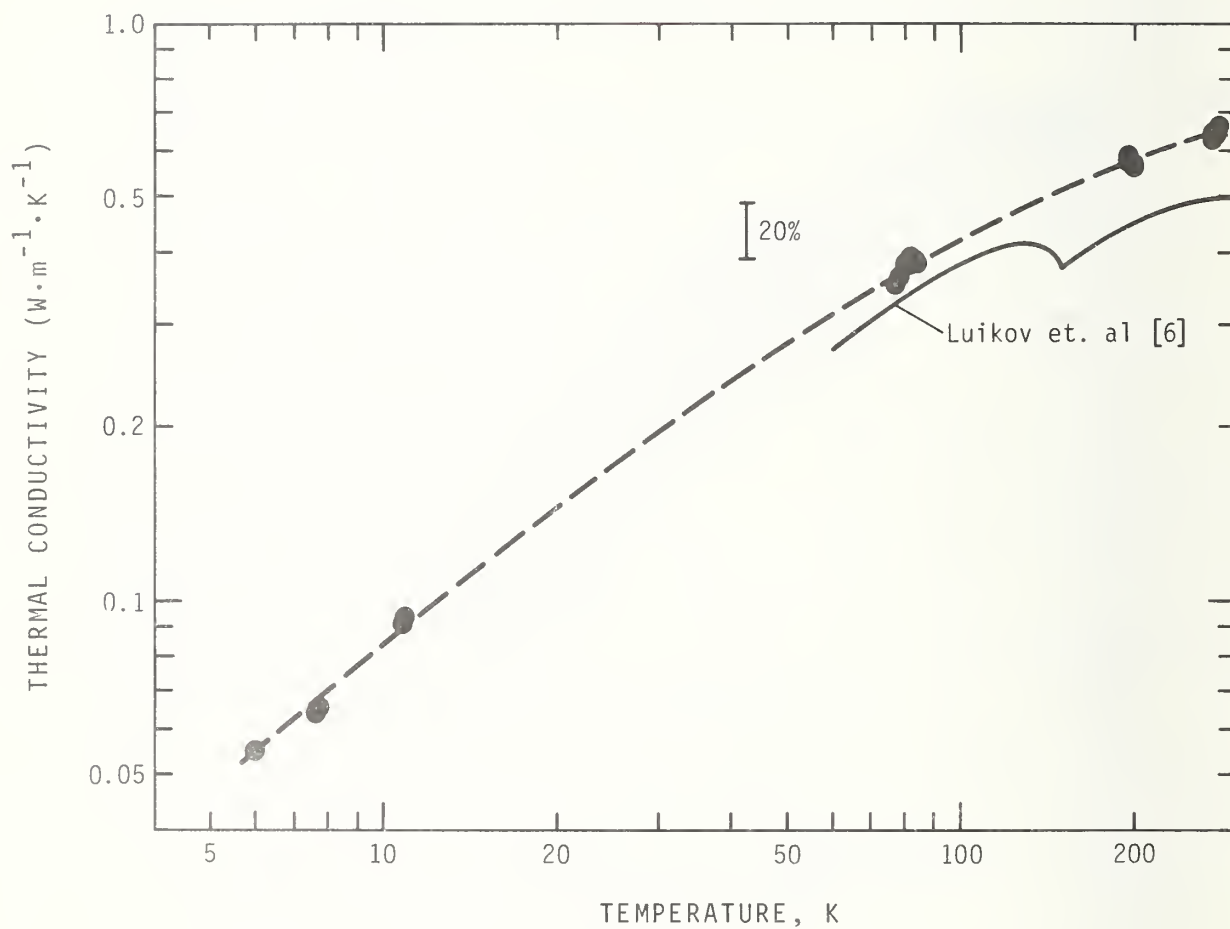


Figure 4. Thermal conductivity of phenolformaldehyde composite.

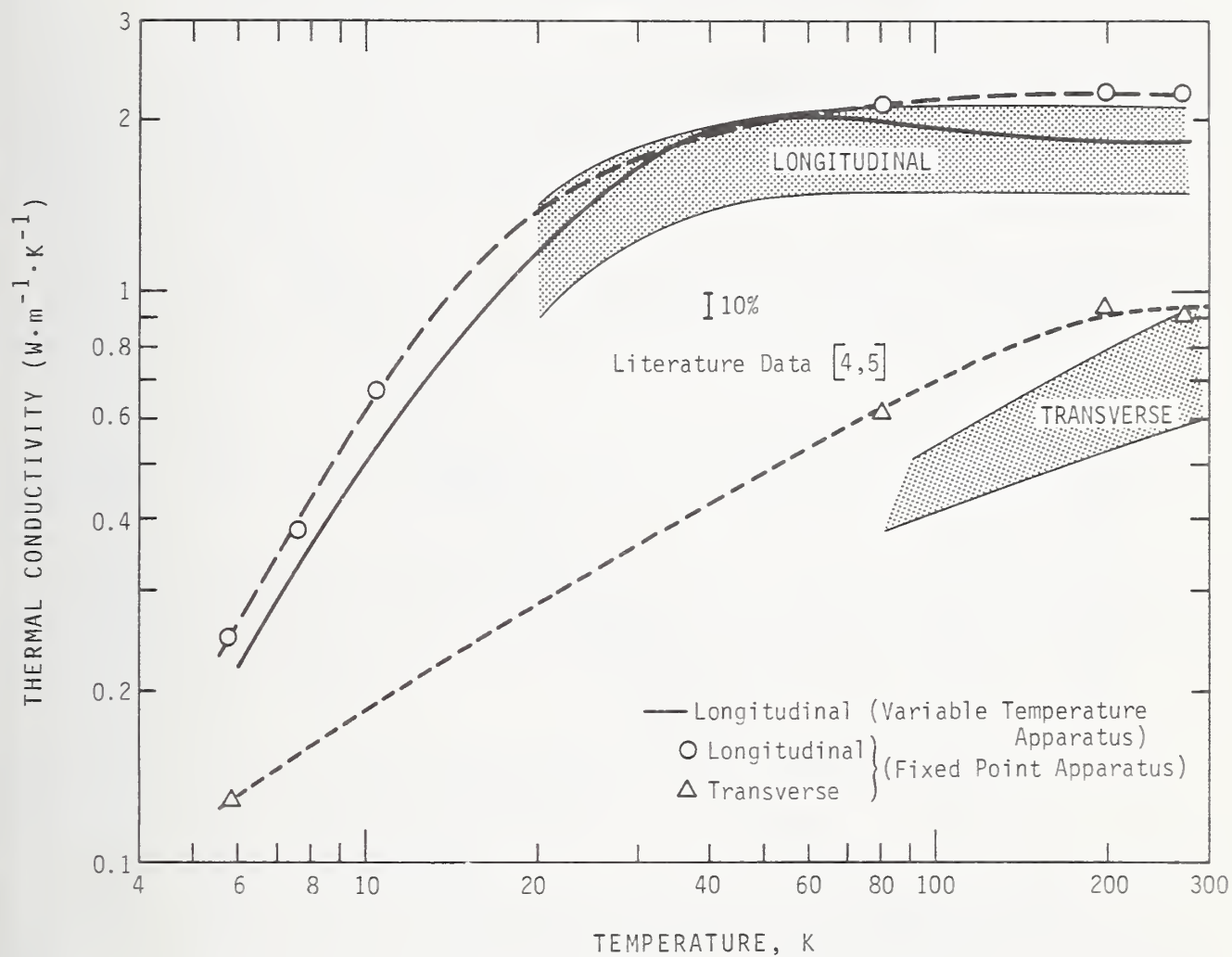


Figure 5. Thermal conductivity of longitudinal and transverse boron-epoxy composite specimens.

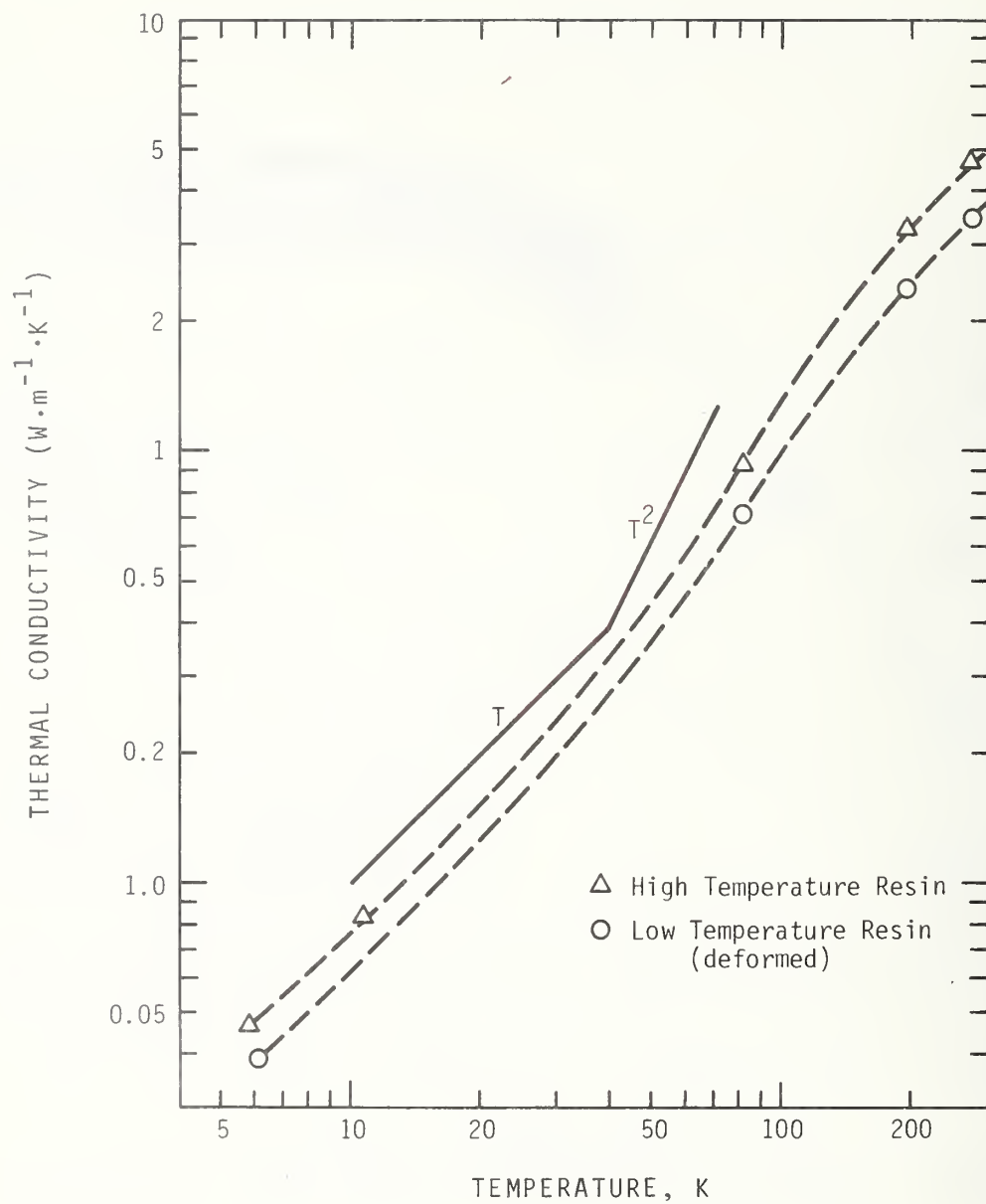


Figure 6. Thermal conductivity of two graphite-epoxy composite specimens (longitudinal).



### 3. Specimen Characterization

During the current reporting period specimens of high permeability steel (Fe-47.5Ni), maraging steel 300 (Fe-18Ni-9Co-5Mo), phenolformaldehyde, boron-epoxy, graphite-epoxy, and boron-aluminum composites were measured.

#### High Perm 49(Fe-47.5Ni):

The chemical composition by weight percent of this material is Fe(bal), Ni(47.47), Mn(0.33), Si(0.25), C(0.012), S(0.004), and P(0.002). The material was hot rolled and ground to a size of 9" X 4" X 20" long. The specimens measured were cut and ground from this plate. The density of the material is  $8.19 \pm 0.02$  g/cm<sup>3</sup> and its Rockwell hardness is B73.

#### Maraging Steel 300:

The chemical composition is Fe(bal), Ni(18.41), Co(9.27), Mo(4.95), Ti(0.59), Al(0.12), Mn(0.01), Si(0.01), P(0.06), S(0.003), and C(0.002). Its density is  $8.06 \pm 0.02$  g/cm<sup>3</sup> and its Rockwell hardness is B105.

#### Boron-Aluminum Composite:

This composite was fabricated with 5.6 mil boron fibers and 6061-F aluminum. The aluminum content by volume is 53% with a void content of less than 2%.

#### Phenolformaldehyde Composite:

This material is uncharacterized rod stock used for apparatus calibration as described earlier.

#### Boron-Epoxy Composite:

This is the same material as described in an earlier report of this series [4]. It was remeasured because of the aforementioned thermal contact problems.

#### Graphite-Epoxy Composite:

Measurements were performed on two graphite-epoxy formulations. One, designated as SP-288-T300, is composed of continuous graphite fibers with a PR-288 resin content of 50% by volume. The other is fabricated with NASA resin 2, also 50% by volume. The latter composite contains a highly flexibilized resin and was difficult to measure, as discussed later.

### 4. Results and Discussion

The results of the measurements conducted during the current reporting period are listed in Table 2 and illustrated in Figures 2 through 6. The uncertainty of these data is estimated to be  $\pm 10\%$ . The data obtained with poor thermal contacts are not listed. However, it may be interesting to note that the discrepancies resulted in values as small as one-third of the correct values. This illustrates the magnitude of the errors which can readily enter into thermal conductivity measurements and emphasizes the care which must be exercised to avoid them.

## High Perm 49 (Fe-47.5Ni) and Maraging Steel 300:

The results of these measurements are plotted in Figure 2. For comparison a shaded area is included which represents the range of reported values for fcc iron alloys [5]. The High Perm 49 values lie at the upper end of this range and the maraging steel values are near the middle. The differences between the longitudinal and transverse High Perm 49 specimens are slightly larger than measurement uncertainty while for maraging steel the differences are within measurement uncertainty. In either case, however, the differences are comparable to that one would expect from material variability.

## Boron-Aluminum Composite:

The measured values of thermal conductivity for the longitudinal and transverse specimens of boron-aluminum composites are shown in Figure 3. An attempt was made to correlate these data with the pure component data. However, no data for aluminum 6061 in the F condition and boron fiber have been reported in the literature. Estimates could be made for both of these, but because of the high uncertainty of such estimates the resulting correlation would be of questionable value. Suffice it to say that the measured values are in reasonable correspondence for a similar aluminum alloy and the results estimated for boron fibers as reported previously in this series [4].

## Phenolformaldehyde Composite:

This material was not measured directly as part of this ARPA program but rather as a calibration material. However, because of its common usage, the results, illustrated in Figure 4, are considered useful. A. V. Luikov, L. L. Vasiliev and A. G. Shashkov [6] measured a similar material; their results are included in Figure 4. The agreement is considered good in view of the uncharacterized nature of these specimens. These results and the following were obtained with the compressive fixed-point apparatus. A smooth (dashed line) has been drawn through the present data, however, the data of Luikov et al [6] indicate there is a phase transition at 150 K. The point spacing of the present data would not reveal this transition but does not conflict with its potential existence.

## Boron-Epoxy Composite:

This material was remeasured with the compressive thermal contact apparatus after the bonded thermal contact problem was discovered. The new results are illustrated in Figure 5 along with the previously reported values for the longitudinal specimen using the variable temperature apparatus. Contrary to the previously reported results using the bonded thermal contact fixed-point apparatus, the two longitudinal specimens are in reasonably good agreement. The poor thermal contacts reduced the apparent thermal conductivity by about 50%. The thermal contact to the transverse specimen was apparently also not good since the previously reported values are low by about 20-30%. The present values are slightly higher than the literature data for both specimen directions.

## Graphite-Epoxy Composite:

As mentioned earlier, considerable difficulty was encountered in measuring this material. The first attempt to measure this material using the bonded thermal contact apparatus resulted in broken thermal contacts. The compressive thermal contact apparatus was then built and measurements attempted. Again, the results were questionable because of the deformation of the highly plasticized resin. Another specimen was fabricated using a less flexible resin and these results are considered reliable. The latter two sets of data are illustrated in Figure 6.

## References

1. Hust, J. G. and Clark, A. F., The Lorenz ratio as a tool for predicting the thermal conductivity of metals and alloys, Materials Research and Standards 11, (No. 8), 22-4 (August 1971).
2. Hust, J. G. and Sparks, L. L., Lorenz ratios of technically important metals and alloys, Nat. Bur. Stand. (U.S.) Tech. Note 634, (February 1973) 133 pp.
3. Hust, J. G., in Semi-annual report on materials research in support of superconducting machinery, NBSIR 74-359 (1974) 308 pp; available from NTIS, AD 780-596/3WM.
4. Hust, J. G., in Semi-annual report on materials research in support of superconducting machinery, NBSIR 75-828 (1975) 186 pp.
5. Childs, G.E., Ericks, L.J., and Powell, R.L., Thermal conductivity of solids at room temperature and below, a review and compilation of the literature, Nat. Bur. Stand. (U.S.) Monograph 131, (1973) 608 pp.
6. Luikov, A.V., Vasiliev, L.L., and Shashkov, A.G., A method for the simultaneous determination of all thermal properties of poor heat conductors over the temperature range 80 to 500 K, Proceedings of the 3rd Symposium on Thermophysical Properties, Purdue University (1965) pp. 314-319.





U.S. DEPT. OF COMM. BIBLIOGRAPHIC DATA SHEET		1. PUBLICATION OR REPORT NO. NBSIR 76-848	2. Gov't Accession No.	3. Recipient's Accession No.
4. TITLE AND SUBTITLE  Semi-Annual Report on Materials Research in Support of Superconducting Machinery			5. Publication Date October 1976	
			6. Performing Organization Code 275.03	
7. AUTHOR(S) R.P. Reed, J.G. Hust, M.B. Kasen, H.M. Ledbetter, H.I. McHenry, D.T. Read, R.E. Schramm, L.L. Sparks, R.L. Tobler			8. Performing Organ. Report No.	
9. PERFORMING ORGANIZATION NAME AND ADDRESS  NATIONAL BUREAU OF STANDARDS DEPARTMENT OF COMMERCE WASHINGTON, D.C. 20234			10. Project/Task/Work Unit No. 2750131	
			11. Contract/Grant No.	
12. Sponsoring Organization Name and Complete Address (Street, City, State, ZIP)  Advanced Research Projects Agency 1400 Wilson Boulevard Arlington, Virginia 22209			13. Type of Report & Period Covered Final	
			14. Sponsoring Agency Code	
15. SUPPLEMENTARY NOTES				
16. ABSTRACT (A 200-word or less factual summary of most significant information. If document includes a significant bibliography or literature survey, mention it here.)  Results are reported of a six-month study, ending September 1976, on candidate materials for superconducting-machinery components. The results cover five areas--advanced composites, elastic properties, fatigue resistance and fracture toughness, magnetothermal conductivity, and thermal conductivity. Material properties were studied over the temperature range 4 to 300 K. Materials studied include: aluminum alloy 5083, copper-0.3 cadmium-0.3 tin, copper-28 nickel, iron-48 nickel, 3.5 Ni and 9 Ni steels, titanium-4 aluminum-6 vanadium, titanium-5 aluminum-2.5 tin, stainless steel 21-6-9, several austenitic stainless steels of the 300 series, 300-grade maraging steel, phenolformaldehyde, and the composites boron/aluminum, boron/epoxy, graphite/epoxy, and niobium-titanium/copper. Some notable results of the study are: anomalous elastic properties of stainless steel 21-6-9 due to a Néel transition; complete sets of elastic constants for two composites, B/Al and NbTi/Cu; thermal conductivities of Ti-6Al-4V and Fe-48Ni are reduced by a magnetic field while those of Cu-0.5 Sn and Cu-28Ni are unaffected; a screening method for composites of possible cryogenic use; general trends regarding temperature effects on the fracture toughness and fatigue-crack-growth resistances of structural alloys are correlated with crystal structure class; and the tensile-yield-strength and fracture-toughness data for fourteen commercial structural alloys at 4 K and 295 K are compared demonstrating an inverse relationship between these properties and indicating the optimum combination of properties that are technologically possible. Also, the materials and properties studied experimentally during the three-year program are summarized.  This work was supported by the Advanced Research Projects Agency of the U.S. Department of Defense.				
17. KEY WORDS (six to twelve entries; alphabetical order; capitalize only the first letter of the first key word unless a proper name; separated by semicolons) Aluminum alloys; composites; elastic properties; engineering materials; fatigue; fracture; iron alloys; cryogenic temperatures; maraging steels; mechanical properties; nickel alloys; phenolformaldehyde; stainless steels; superconducting machinery; thermal conductivity; titanium alloys.				
18. AVAILABILITY  <input type="checkbox"/> Unlimited  <input type="checkbox"/> For Official Distribution. Do Not Release to NTIS  <input type="checkbox"/> Order From Sup. of Doc., U.S. Government Printing Office Washington, D.C. 20402, SD Cat. No. C13  <input checked="" type="checkbox"/> Order From National Technical Information Service (NTIS) Springfield, Virginia 22151		19. SECURITY CLASS (THIS REPORT)  UNCLASSIFIED	21. NO. OF PAGES  320	
		20. SECURITY CLASS (THIS PAGE)  UNCLASSIFIED	22. Price  \$9.75	





